

FACULDADE DE ENGENHARIA DA UNIVERSIDADE DO PORTO

Control and cooperation of marine vehicles

Bruno Miguel Mateus Ferreira



Doctoral Program in Electrical and Computer Engineering

Supervisor: Aníbal Castilho de Coimbra Matos

Co-supervisor: António Paulo Gomes Mendes Moreira

February 28, 2014

Control and cooperation of marine vehicles

Bruno Miguel Mateus Ferreira

Doctoral Program in Electrical and Computer Engineering

February 28, 2014

Abstract

This thesis addresses the problem of controlling and coordinating autonomous marine vehicles. Distributed systems has become a standard solution for a large number of engineering problems. Marine robotics has also followed the same trend: coordinated surface and underwater vehicles have been used as a means to distribute possibly heterogeneous equipment over regions of interest. The work presented throughout this document has been motivated by recent challenges and constraints intrinsic to marine environments.

Firstly, a control application example is presented to stabilize a hovering autonomous underwater vehicle (AUV) in the vertical pose, that is, pitching up or down. This pose is specially appreciated for fast and efficient descent (or ascent) maneuvers. Moreover, a guidance law to drive the vehicle horizontally when it is in the vertical pose is proposed, envisioning potential positioning corrections when the vehicles is diving or surfacing.

Then, two methods to solve the problem of homing a vehicle to a given reference based on range-only measurements are provided, inspired from acoustic ranging applications. This rather simple task can be seen as a basic exercise of coordination between a vehicle and a, possibly moving, beacon. The first method is built from a combination of estimation and guidance while the second approach is based on the sensor, where only the range measurements are used to guide the vehicle towards its reference. These address the problem at kinematic level, presuming the existence of a lower level velocity control law which is subsequently formalized.

Local automatic control of vehicles and coordination are addressed here at different levels. Coordination of vehicle relies on the local control of each vehicle. The coordination scheme presented is composed of three main control layers. At the dynamics level, the vehicle velocity is stabilized around a desired reference vector, which is subsequently used in a guidance law. These then constitute the basic layers on which the coordination algorithm builds upon. For all these layers, special attention is given to practical problems that arise from model uncertainties and tracking errors. Following a bottom-up development, upper bounds on tracking errors are derived for both velocity and position in order to assess the achievable performances of the control method and also to ensure that the tracking task is satisfactorily fulfilled. As a by-product, a compilation of results is provided for error boundedness in velocity and position tracking.

Coordination of a team of autonomous marine vehicles is finally applied to tracking and estimation of a sound source located underwater based on time-of-arrival (TOA) measurements only. As the uncertainty of the estimate depends on the relative positions of the receivers, a solution that optimally places the receivers in space is proposed by taking advantage of the motion capabilities of a coordinated formation of vehicles.

Keywords: Marine vehicles, Underactuated vehicles, Homing, Vertical pose, Nonlinear control, Formation keeping, Target localization, Coordination, Communication constraints

Resumo

A presente tese aborda o controlo e a coordenação de veículos marinhos autónomos. Os sistemas distribuídos têm-se tornado uma solução comum para um grande número de problemas de engenharia. A robótica marinha tem seguido a mesma linha: veículos de superfície e submarinos têm sido utilizados como meios para distribuir equipamento, possivelmente heterogéneo, em regiões de interesse. O trabalho apresentado neste documento é motivado por desafios recentes e restrições intrínsecas ao meio marinho.

Primeiro, apresenta-se um exemplo de aplicação de método de controlo para a estabilização de um veículo submarino autónomo na pose vertical, isto é, inclinado para baixo ou para cima. Esta pose é particularmente interessante em cenários de descida (ou subida) rápida. Por outro lado, propõe-se uma lei de controlo para guiar o veículo horizontalmente, quando este se encontra na pose vertical, antecipando possíveis correções de posição aquando da submersão ou da emersão.

De seguida, inspirados em aplicações que usam medições acústicas, propõem-se dois métodos baseados apenas em medições de distância para resolver o problema de condução de um veículo para uma dada referência. Esta simples tarefa pode ser vista como um exemplo básico de coordenação entre um veículo e uma baliza acústica, a qual pode também ser móvel. O primeiro método é construído a partir de uma combinação de estimação e controlo enquanto a segunda abordagem baseia-se apenas no sensor, na qual são usadas apenas as medições de distância para guiar o veículo até à sua referência. Estes abordam o problema ao nível da cinemática, assumindo a existência de um nível mais baixo de controlo de velocidade que é posteriormente formalizado.

O controlo automático local dos veículos e a coordenação são resolvidos a diferentes níveis. A coordenação baseia-se no controlo local destes veículos. O esquema de coordenação apresentado é composto por três camadas principais de controlo. Ao nível da dinâmica, estabiliza-se a velocidade do veículo à volta de um vetor de referência, que é ulteriormente usado por uma lei de condução que dita referências de velocidade para posicionamento. Estas constituem as camadas básicas nas quais assenta o algoritmo de coordenação. Para todas essas camadas, dá-se uma atenção reforçada a problemas práticos originados por incertezas nos modelos e erros de seguimento (*tracking*). Seguindo um desenvolvimento de baixo para cima, determinam-se limites superiores nos erros de velocidade e posicionamento, de forma a avaliar o desempenho alcançável pelos métodos de controlo e também para garantir que a tarefa de seguimento seja cumprida de forma satisfatória. Assim, apresenta-se uma compilação de resultados sobre limites de erros de velocidade e de seguimento de uma referência de posição.

Por fim, a coordenação de uma equipa de veículos marinhos autónomos é aplicada ao seguimento e à estimação da posição de uma fonte sonora, baseados apenas nos tempos de chegada. Tendo em conta que a incerteza da estimativa depende das posições dos recetores relativas ao alvo, propõe-se uma solução que posiciona os recetores de forma ótima no espaço, tirando partido da capacidade de movimento de uma formação de veículos.

Palavras-chave: Veículos marinhos, Veículos sub-atuados, *Homing*, Pose vertical, Controlo não linear, Formação de veículos, Localização de alvo, Coordenação, Restrições de comunicação

Acknowledgements

This has been a long but enthusiastic journey trying to figure out solutions to several problems in robotics. I really feel lucky for being surrounded of great people and for the support and encouragements that I received over the last four years. Without these, everything would be much more difficult and it very likely would not come to this end. I am also very glad for having worked and for having met very talented people that brought so many ideas and challenges to my mind.

First, I would like to thank to my thesis supervisor, Professor Aníbal Matos, for his guidance, his patience, his encouragements and his friendship. He has supported me from the very beginning of my research, for more than four years now, continuously offering me many good advices. I am grateful for the numerous discussions about many subjects related to this thesis, for the sharing of his unique vision and impressive knowledge on a broad spectrum of subjects that we have approached. He met all the best expectations I had when I enrolled in the PhD program and I hope that the work compiled in this thesis meets his. He was the person who influenced the most the development of my work. I am also indebted to my thesis co-supervisor, Professor A. Paulo Moreira, for his insightful comments, discussions and ideas. These were very important at different stages of this thesis.

My special thanks go to Professor Nuno Cruz for his help in many parts of my work, for his enthusiasm, for his availability and his fellowship. The countless discussions we have had since I came to the OceanSys lab have contributed in many ways to this thesis. His capability to understanding and simplifying problems are remarkable and inspiring. He was also of great help in the several trials we have done thus far.

I am grateful to Professor Jerome Jouffroy for his contributions during his stay in Porto and also for having accepted to be part of my thesis research and final PhD committees. His comments, advices and encouragements during his short stay were of great importance as they have contributed to defining clearer objectives and draft the final thesis. Working with him and learning from him have been a privilege. I would also like to thank to Professor Luís Almeida for having kindly accepted to participate in my thesis research and final PhD committee, and for his useful comments. I am indebted to Professor António Pascoal and Professor A. Pedro Aguiar for having cordially accepted to be part of the final PhD committee.

I would like to thank Daniele Spaccini and Roberto Petroccia for their contributions on acoustic communications in our joint work. I am grateful to Helder Campos for his enthusiasm, his interest and his important help, accompanying me over several hours of work. His contributions in acoustic sensing have made the experiments, in the last part of this thesis, possible.

I acknowledge all my colleagues and visiting researchers who have been in the lab for their friendship, help and availability, whenever it was needed. I would like also to thank to my closest friends in FEUP, David and Xınca, for many conversations about everything. I also thank Haider for many discussions over lunches.

My biggest appreciations go to Suzy, my mother, my father and my brother for their unconditional support. Suzy always supported me in everything I was doing with an inexhaustible patience

and motivation, making everything much easier and happier. I can not express how grateful I am. The encouragements from my parents have always been fundamental over my entire life. They are my best examples. To my brother go my thanks for simply being the best brother I could have.

Finally, I would like to thank FCT (Fundação para a Ciência e Tecnologia) for supporting this work through the PhD grant SFRH/BD/60522/2009.

Bruno Ferreira

Project "NORTE-07-0124-FEDER-000060" is financed by the North Portugal Regional Operational Programme (ON.2 – O Novo Norte), under the National Strategic Reference Framework (NSRF), through the European Regional Development Fund (ERDF), and by national funds, through the Portuguese funding agency, Fundação para a Ciência e a Tecnologia (FCT).

Contents

| | | |
|----------|-------------------------------------------------------|-----------|
| 1 | Introduction | 1 |
| 1.1 | Marine robotics | 2 |
| 1.1.1 | Surface vehicles | 2 |
| 1.1.2 | Underwater vehicles | 3 |
| 1.2 | Control and coordination | 4 |
| 1.3 | Motivation | 5 |
| 1.4 | Contributions | 6 |
| 1.5 | Organization of the thesis | 7 |
| 2 | Overview | 9 |
| 2.1 | Notation | 9 |
| 2.2 | Dynamic and kinematic models | 10 |
| 2.3 | Control tools | 12 |
| 2.3.1 | Exact feedback linearization | 13 |
| 2.3.2 | Lyapunov direct method | 13 |
| 2.3.3 | Backstepping | 14 |
| 2.4 | Estimation background | 15 |
| 2.4.1 | Kalman filter and extended Kalman filter | 15 |
| 2.4.2 | Particle filter | 17 |
| 2.5 | Underwater localization technology | 18 |
| 2.5.1 | Dead-reckoning localization | 18 |
| 2.5.2 | Absolute and relative localization | 20 |
| 2.6 | Experimental setup | 23 |
| 2.6.1 | The MARES AUV | 24 |
| 2.6.2 | The TriMARES AUV | 25 |
| 2.6.3 | The Zarco and Gama ASVs | 26 |
| 2.6.4 | BASV | 26 |
| 2.6.5 | LASV | 26 |
| 3 | Control of a hovering AUV in the vertical pose | 27 |
| 3.1 | Motivation and related works | 27 |
| 3.2 | Reduced models | 29 |
| 3.3 | Pose stabilization | 31 |
| 3.3.1 | Control law | 32 |
| 3.3.2 | Constraint on the desired velocity | 33 |
| 3.4 | Horizontal guidance | 35 |
| 3.4.1 | Roll dynamics | 35 |
| 3.4.2 | Guidance | 36 |

| | | |
|----------|------------------------------------------------------------------------|------------|
| 3.5 | Results | 38 |
| 3.5.1 | Simulation | 38 |
| 3.5.2 | Experiments | 39 |
| 3.6 | Conclusions | 41 |
| 4 | Homing using range-only measurements | 43 |
| 4.1 | Motivation and related works | 43 |
| 4.2 | Reduced models and cylindrical coordinates | 45 |
| 4.3 | Homing using an estimation based approach | 46 |
| 4.3.1 | Estimating the position: extended Kalman filter | 47 |
| 4.3.2 | Estimating the position: particle filter | 48 |
| 4.3.3 | Initialization | 50 |
| 4.3.4 | Control | 51 |
| 4.3.5 | Results | 53 |
| 4.4 | Homing using a sensor-based approach | 60 |
| 4.4.1 | Control method | 61 |
| 4.4.2 | Stability analysis | 65 |
| 4.4.3 | Homing with practical constraints on input | 66 |
| 4.4.4 | Results | 69 |
| 4.5 | Conclusions | 72 |
| 5 | Local control for marine vehicles | 73 |
| 5.1 | Velocity control | 74 |
| 5.1.1 | Bounded velocity under bounded actuation | 74 |
| 5.1.2 | Inner velocity loop | 77 |
| 5.1.3 | Error boundedness | 78 |
| 5.1.4 | Combinations of degrees of freedom (DOFs) and guidance | 83 |
| 5.2 | Target tracking and station keeping | 86 |
| 5.2.1 | Guidance law | 89 |
| 5.2.2 | Steady state orientation for station keeping | 91 |
| 5.2.3 | Target tracking under unknown drifts and velocity errors | 93 |
| 5.3 | Experimental results | 96 |
| 5.3.1 | Setup description | 96 |
| 5.3.2 | Static target tracking and station-keeping | 96 |
| 5.4 | Conclusions | 98 |
| 6 | Coordination of marine vehicles | 101 |
| 6.1 | Related works and motivation | 101 |
| 6.1.1 | Coordinated control | 103 |
| 6.1.2 | Biased comparison of methods | 106 |
| 6.2 | Formation keeping | 106 |
| 6.2.1 | Background | 107 |
| 6.2.2 | Generalization | 108 |
| 6.2.3 | Particular method | 110 |
| 6.2.4 | Convergence under bounded tracking error and communication constraints | 111 |
| 6.3 | Experimental results | 113 |
| 6.3.1 | Operation using radio communications | 113 |
| 6.3.2 | Operation using acoustic communications | 119 |
| 6.4 | Conclusions | 121 |

| | | |
|----------|------------------------------------------------------------|------------|
| 7 | Cooperative localization and tracking | 123 |
| 7.1 | Related works and motivation | 123 |
| 7.2 | Unconstrained optimal positioning of sensors | 125 |
| 7.2.1 | Background | 125 |
| 7.2.2 | Unconstrained optimal 3D localization | 127 |
| 7.2.3 | Positioning and estimation | 131 |
| 7.2.4 | Results | 134 |
| 7.3 | Plane-constrained optimal 3D localization | 137 |
| 7.3.1 | Plane constrained optimal positions | 137 |
| 7.3.2 | Case with four sensors and same noise variance | 141 |
| 7.4 | Coordinated placement of sensors | 143 |
| 7.4.1 | Coordination of autonomous vehicles | 143 |
| 7.4.2 | Homing to target | 144 |
| 7.4.3 | Estimation-based positioning | 144 |
| 7.5 | Field trials | 145 |
| 7.5.1 | Assets | 145 |
| 7.5.2 | Operation | 146 |
| 7.5.3 | Performances | 146 |
| 7.6 | Conclusions | 147 |
| 8 | Conclusions | 151 |
| 8.1 | Main contributions | 151 |
| 8.2 | Publications | 153 |
| 8.3 | Future work | 157 |
| A | Guidance laws for other DOFs combinations | 159 |
| A.1 | Controlled surge, heave and yaw rate | 159 |
| A.2 | Controlled heave, pitch rate and yaw rate | 160 |
| A.3 | Controlled surge, heave, pitch rate and yaw rate | 160 |
| B | Efficiency considerations | 161 |
| C | MARES model | 163 |
| D | TriMARES model | 167 |
| E | Zarco and Gama model | 169 |
| F | BASV model | 173 |
| G | LASV model | 175 |
| | References | 177 |

List of Figures

| | | |
|------|-------------------------------------------------------------------------------------------------------------------------------------------------------------------------------------------------------------------------------------------------------------------------------|----|
| 2.1 | Frames and position vector | 10 |
| 2.2 | Sequence of rotations from the inertial frame $\{I\}$ to the body-fixed frame $\{B\}$. Sequence: yaw \rightarrow pitch \rightarrow roll ($\psi \rightarrow \theta \rightarrow \phi$) | 11 |
| 2.3 | Attenuation of acoustic waves in seawater. Parameters: salinity = 3.54%, temperature = 20°C, sound speed = 1500m/s, pH = 8. | 23 |
| 2.4 | Multipath originated by refraction and reflections | 24 |
| 2.5 | Autonomous underwater vehicles | 24 |
| 2.6 | Autonomous surface vehicles | 25 |
| 3.1 | MARES thrusters configuration | 28 |
| 3.2 | Sequence of rotations from the inertial frame $\{I\}$ to the body-fixed frame $\{B\}$. Sequence: roll \rightarrow pitch \rightarrow yaw ($\phi \rightarrow \theta \rightarrow \psi$) | 31 |
| 3.3 | The function $f_\rho(\tilde{\phi}(t))$ | 37 |
| 3.4 | Simulation results: pitch and yaw angles | 39 |
| 3.5 | Simulation results: depth | 39 |
| 3.6 | Simulation results: horizontal position evolution | 40 |
| 3.7 | MARES in vertical pose | 41 |
| 3.8 | Experimental results: pitch and yaw angles | 42 |
| 3.9 | Experimental results: roll angle | 42 |
| 3.10 | Experimental results: depth | 42 |
| 4.1 | Comparison between the particle filter and the extended Kalman filter estimates . | 54 |
| 4.2 | Evolution of the 1000 particles for an initialization with the vehicle starting at (x, y) = ($-150, -170$). The vehicle velocity is $u = 1\text{m/s}$ and the currents are (v_x, v_y) = ($-0.2, 0.1$). | 56 |
| 4.3 | Position and current velocity estimations | 57 |
| 4.4 | Homing at 2m/s | 58 |
| 4.5 | Evolution of the covariance as a function of the minimum switching period and of the switching covariance. The results were obtained from several simulations performed with the same initial conditions. | 59 |
| 4.6 | Ground truth (blue solid line) and estimated trajectories (red dots) as functions of the minimum switching period and of the switching covariance. Surge velocity reference is $u = 1\text{m/s}$ and the current velocity is (v_x, v_y) = ($-0.2, 0.1$) | 60 |
| 4.7 | Homing method | 62 |
| 4.8 | Illustration of the intervals of angles for stability analysis | 66 |
| 4.9 | Upper bound of the invariant set | 67 |
| 4.10 | Results obtained for homing with surge velocity 1.0 meter per second (estimated) and desired approach rate $\beta = 0.6$ (log20110729142857) | 70 |

| | | |
|------|---------------------------------------------------------------------------------------------------------------------------------------------------------------------------------------------------------------------------------|-----|
| 4.11 | Results obtained for homing with surge velocity 1.5 meter per second (estimated) and desired approach rate $\beta = 0.7$ (log20110803142434) | 71 |
| 5.1 | Controlled states during a hovering maneuver of TriMARES | 85 |
| 5.2 | Position errors and relative angles | 88 |
| 5.3 | Target tracking trajectory. The arrows show the heading of the vehicle plotted at intervals of 10 seconds. | 97 |
| 5.4 | Evolution of the horizontal coordinates | 97 |
| 5.5 | Tracking error: center of gravity (CG) and bow relative distances | 98 |
| 5.6 | Relative position of the vehicle (center of gravity (CG)) and relative position of bow with regard to the position reference | 100 |
| 5.7 | Yaw angle | 100 |
| 6.1 | Coordinated mission of Zarco and Gama in La Spezia | 114 |
| 6.2 | Positions of Zarco and Gama resulting from the coordinated mission in La Spezia. The circles indicate the positions of the vehicles at intervals of 30 seconds. | 115 |
| 6.3 | Relative positioning error between Zarco and Gama for the trajectory of figure 6.2 | 115 |
| 6.4 | Coordinated mission of Zarco and Gama | 117 |
| 6.5 | Relative distance error of Zarco and Gama along the coordinated operation | 117 |
| 6.6 | Coordinated mission of Zarco and Gama | 118 |
| 6.7 | Relative distance error of Zarco and Gama along the coordinated operation | 119 |
| 6.8 | Discrete position references and trajectories of the two autonomous surface vehicles (ASVs). The circles indicate the position references. | 120 |
| 6.9 | Real and reference relative positions of the two ASVs. Upper: North component. Lower: East component. | 120 |
| 6.10 | Time difference between two consecutive successful transmissions of state to the virtual leader | 121 |
| 7.1 | Optimal positions of receivers (circles). The target (cross) is located at the origin. The parameters considered are $\sigma_i = 10^{-4}$ s $\forall i$. | 128 |
| 7.2 | Metric value as a function of target position as a function of the target position in the plane defined by $z_t = 0$. The parameters considered are $c_s = 1500$ m/s, $\sigma_i = 10^{-4}$ s $\forall i \in \{1, \dots, N\}$. | 128 |
| 7.3 | Error evolution | 133 |
| 7.4 | Step increment | 133 |
| 7.5 | Optimal positioning ($\sigma = 10^{-4}$ s) | 135 |
| 7.6 | Estimate error ($\sigma = 10^{-4}$ s) | 135 |
| 7.7 | Optimal positioning ($\sigma = 10^{-2}$ s) | 136 |
| 7.8 | Estimate error ($\sigma = 10^{-2}$ s) | 136 |
| 7.9 | Influence of ρ on the metric | 142 |
| 7.10 | Formation of four heterogeneous vehicles | 145 |
| 7.11 | Mean estimated position over a window of 60 sequential estimates | 147 |
| 7.12 | Standard deviation of the estimate | 148 |
| 7.13 | Mean position of the formation and estimated position of the target | 149 |
| B.1 | Comparison of trajectories for control law variants | 162 |

List of Tables

| | | |
|-----|---------------------------------------------------------|-----|
| 2.1 | Characteristics of navigation sensors/systems | 26 |
| C.1 | Added mass coefficients | 165 |
| C.2 | Viscous damping coefficients | 165 |
| C.3 | Parameters | 166 |
| C.4 | Inertia tensors | 166 |
| D.1 | Added mass coefficients | 167 |
| D.2 | Viscous damping coefficients | 168 |
| D.3 | Parameters | 168 |
| D.4 | Inertia tensors | 168 |
| E.1 | Added mass coefficients | 170 |
| E.2 | Viscous damping coefficients | 171 |
| E.3 | Parameters | 171 |
| E.4 | Inertia tensors | 171 |
| F.1 | Added mass coefficients | 173 |
| F.2 | Viscous damping coefficients | 174 |
| F.3 | Parameters | 174 |
| F.4 | Inertia tensors | 174 |
| G.1 | Added mass coefficients | 175 |
| G.2 | Viscous damping coefficients | 176 |
| G.3 | Parameters | 176 |
| G.4 | Inertia tensors | 176 |

Chapter 1

Introduction

Currently, the world demands for the inclusion of robotics in several domains, a demand that has been increasing each day. Motivated by such need, robotics has evolved considerably over the last decades in which intensive and enthusiastic works have been developed by many researchers. Although it is based on a core where electrical and mechanical engineering constitute the elementary sciences, the multidisciplinary nature of robotics makes this domain even more challenging.

In a historical perspective, humans have always made use of tools to help themselves to accomplish an extensive number of tasks. Nowadays, the technology has become an important (indispensable) tool for humans and has evolved, answering to new needs and challenges. By following the same trend, robots have been employed as means of performing undesired or impossible tasks. They have replaced humans in numerous risky tasks, protecting them from injuries and ultimately saving lives. Several examples can be found in land robotics (space and hearth) (Squyres et al., 2004), industrial robotics (Fukuda and Nakagawa, 1988) and underwater robotics (Antonelli et al., 2008), covering a large number of distinct applications from exploration, monitoring and surveillance to transportation, intervention and rescue. The latter references are, of course, just illustrative examples of many works in the different branches of robotics. Not only professional needs have originated robotics solutions but also entertainment and domestic needs have contributed for an important growth of robotic systems.

Nevertheless, the expansion of robotics is yet restrained since most robots are operated only by their designers, experienced specialists or closely related people. However, as the interest of the general public and non-related professionals increases, the interface with the robot must be simple while its operation must be strongly robust and autonomous. These characteristics imply considerable effort during the design process.

Different needs have originated different types of solutions with heterogeneous operation methods specially specified to each problem. Land robots include wheeled and legged robots while water environments have originated surface and underwater vehicles. In the present thesis, a special focus will be given on marine robotics but most of the subjects tackled here are not constrained to this specific domain.

The underlying subject of the current work is on control and coordination of multiple robots

that suffer from real practical constraints. Motivated by scenarios in which the navigation of robots commonly depends on auxiliary equipment coherently deployed on the region of interest, the control and coordination of robots are addressed in order to achieve more dynamic and versatile behaviors.

1.1 Marine robotics

The domain of application of mobile marine robots is broad, comprehending fields that go from science to defence. As for robotics in general, their tasks include operations that require skills that humans do not compile, as well as operations in hazardous or intolerable environments. A large number of specific tasks in different environments has given rise to several types of marine robots. Marine robots can be divided in two large families: surface and underwater robots. The most common applications of marine robots include archaeology, mapping, inspection, environmental data sampling and defence.

Marine robots have taken an important role in underwater archaeology. Common operations require large coverage and the observation of numerous interesting objects with historical relevance lying on the bottom of the seas or rivers. The intrinsic constraints of underwater environment such as limited visibility and acoustic attenuation/refractions make vision systems and sonars useless at large distances. The observation of such an environment demands for precise localization and positioning. Underwater vehicles play an important role in this context thanks to their ability to approach the site as close as required in order to obtain sufficiently refined data.

The sea floor topology has been studied through bathymetry and mapping in which surface and underwater vehicles have served as platforms to carry the respective payload. Combined with precise localization data, three-dimensional maps can be build for the purpose, thus cultivating the knowledge on the sea bottom and contributing for topography of oceans.

Inspection of moving and stationary platforms has attracted the attention of the industry and of the military community by understanding the capability of robots to perform such a task. Several works have motivated the use of robots for inspection of ship hulls as well as the inspection of offshore oil platforms. The versatility and the sensing capability make the robots instruments of relevant value for those applications.

Not less important is the scientific data harvesting. Oceans, and underwater environments in general, possess unique resources that are probably underexplored because of the particularly hostile conditions. Today, several underwater robots are serving the scientific community by navigating over large regions while collecting meaningful data through on-board sensors.

Within the military context yet, marine robots have applications in surveillance, recognition and demining, just to cite a few.

1.1.1 Surface vehicles

Autonomous surface vehicles include autonomous surface crafts (ASCs) and autonomous sailboats. The first ones are self-propelled by means of thrusters physically coupled to the craft body.

For ocean applications, their design makes them large enough to remain stable under adverse conditions that are caused by wind, currents and waves. Their dimensions are usually above three meters long by one meter large, depending on their shape (monohull, catamaran, trimaran). These dimensions generally leave free space for carrying a relatively large amount of batteries, or fuel, for propulsion and power for electronics. Besides power, ASCs usually employ a set of sensors for measuring velocity, position, wind speed, angles, and are commonly endowed with communication devices.

For what concerns equipment, autonomous sailboats are similar to ASCs. However, instead of using thrusters, their motion relies on the force originated by the wind blowing on one or more sails. Heading is controlled by a combination of one or more rudders placed under the hull and by the orientation of the sails. Although their maneuverability is generally poorer than that of the ASCs, the low power consumption constitutes a major advantage for long trajectories.

The domain of application of autonomous surface vehicles is, at least, as large as the fields that are covered by boats and floating platforms, including (just to cite a few) monitoring, surveillance, rescue and inspection.

1.1.2 Underwater vehicles

There exist two classes of underwater vehicles, namely autonomous underwater vehicles (AUVs) and remotely operated vehicles (ROVs). As their name suggest, AUVs operate autonomously and generally do not contemplate any physical connection to control stations when they navigate. In opposition to AUVs, one or more operators control the ROVs by means of communications that a tether usually grants. A large variety of ROVs exists nowadays, mainly differing on dimension, actuation and payload. Their characteristics are determined according to their missions. The dimensions and weight of common commercial ROVs range from few centimeters with few kilograms to few meters and a few tons. ROVs for intervention and deep operation typically have larger dimensions and weight than shallow water inspection ROVs. ROVs are usually designed to navigate in confined regions where on-line observations and remote intervention are required. On the surface, an operator commands the motion of the robot and other actuation tools, which are carried along, by means of a connecting tether that can also be used to supply power to the ROV. A tether can have considerable diameter and length. Since the reachable area is limited by the length of the cable, its presence makes the operation of this type of robots conditioned. In addition, the drag forces become significantly large with long tethers and the corresponding weight induces forces and moments on the robot.

AUVs, also known as unmanned underwater vehicles (UUVs), have been conceived to access underwater environments and overcoming some of the limitations of ROVs. According to Antonelli et al. (2008), there are approximately 200 different AUVs operating in the world. Their shapes differ on details but commonly converge to streamlined bodies such as torpedoes, spheres, ellipsoids or flat shapes because of their low damping characteristics in viscous environments. AUVs include propelled and buoyancy driven vehicles. The motion of the first ones is driven by propellers and (possibly) control surfaces while the seconds make use of fins and a compartment

where a gas is compressed and decompressed in order to vary the buoyancy of the body. During ascent and descent, the fins are controlled in a way that makes them induce lift and therefore create longitudinal motion. This type of vehicles are commonly referred to as gliders. While their power consumption is very low, the low speed at which they are able to move (typical speeds are about 0.3m/s) make their operation difficult under large currents or turbulent waters.

1.2 Control and coordination

The motion of vehicles is guaranteed by means of actuators. In unmanned vehicles, actuation commands are either given remotely or automatically by means of controllers that are used to ensure that the desired motion of the vehicle is obtained. Nevertheless, it is frequent to find combinations of these in order to reduce the operation complexity and/or to improve performances according to any given performance metric that may consider precision, efficiency or stability, for example. Besides performance improvement, deterministic behaviors and robustness over long time operations are some of their additional characteristics that are particularly appreciated.

In the context of marine vehicles, nonlinear controllers have the capability to warrant all such characteristics. Provided that the dynamics of marine vehicles is strongly nonlinear, it is expected that nonlinear controllers have some advantages over linear and artificial intelligence based controllers. In the former case, linear automatic controllers can not ensure stability and performing operation over a broad state range. In many cases, artificial intelligence based controllers, which include neural networks and fuzzy controllers, are not supported by a theoretical background that enables stability analysis and therefore can not warrant the same determinism as that of nonlinear controllers.

Robotic coordination, and more generally cooperation, are means of taking advantage of several distributed robots that may have different and complementary capabilities. A multitude of applications and motivating examples can be found in the literature to emphasize the need for coordination in robotics. Coordination is used to obtain coherent motion of vehicles that makes the overall system, which is composed of the robots in the team, perform according to the objectives of a given mission.

In coordinated operations, robots require exchanging information on relevant quantities that define their states with regard to the operation objectives. This exchange is obtained from sensing or communications, or a combination of both. The stability and the robustness of the coordinated operations under constraints imposed by current technological solutions, which contemplate delayed, low rate and intermittent exchange of information, has attracted the attention of several researchers recently, encouraged by the current challenges and needs posed in robotics and especially in marine robotics.

1.3 Motivation

The intrinsic characteristics of marine environment frequently make the operations risky, especially underwater. There is no, and there will not be, totally secure operations in the water but a recent trend stimulated by several researchers has shown that it is possible to improve the navigation through distributed, cooperating robots.

Parker (2008) summarizes the following:

“The most common motivations for developing multirobot system solutions are that:

1. the task complexity is too high for a single robot to accomplish;
2. the task is inherently distributed;
3. building several resource-bounded robots is much easier than having a single powerful robot;
4. multiple robots can solve problems faster using parallelism; and
5. the introduction of multiple robots increases robustness through redundancy. ”

One can quickly identify several items that correspond to cooperative improvement of navigation of vehicles, namely items 2, 3 and 5. To our knowledge, there is yet no solution that cooperatively solves the problem of navigation of underwater vehicles with bounded error for an unlimited region without human intervention. Moreover, very interesting results have been obtained for cooperation of ground, and more generally surface, robots but the most of these methods can not be directly applied to underwater robotics mainly due to communication constraints. Taking such constraints into consideration, the need to develop new methods has emerged. Those methods would solve cooperative, bounded error navigation.

The natural constraints found in underwater environments makes the navigation of autonomous robots difficult. In opposition to surface, land and aerial robots whose localization problems are generically easier to solve thanks to the broad current sensing technology, underwater navigation poses several challenges especially when accurate, bounded error localization is required. As previously stated, most current state-of-the-art solutions for precise bounded error underwater navigation are time-consuming and sometimes expensive when they imply the deployment of several equipments, such as beacons. Additionally, the localization precision varies according to the relative position of the AUV with respect to the beacons.

The energy autonomy of underwater vehicles has been growing and it is now possible to address several scenarios that require long range/large area missions. In those cases, static acoustic beacons are of limited use and perception-based navigation is extremely complex due to the featureless nature of many underwater environments.

Robot cooperation becomes a valid option to overcome such constraints. By exploring the concept of navigation aid systems, the human intervention can be significantly reduced. Ultimately, deployment could be reduced to launching a small group of robots from the coast/margin.

Additionally, the operation area would be limited only by the energy autonomy available in each robot.

The present work is established around control and coordination of marine robots. Motivated by navigation aided robotics applications, for which navigation aid robots have to coordinate their operations to provide meaningful measurements or data to one or more survey robots, robust control methods and coordination schemes must be derived for the team of robots. The intrinsic practical constraints found in underwater environments should be regarded with particular attention. These generally make the navigation problems more challenging than in surface, aerial or ground robotics mainly because of the sensing limitations and of the communication constraints.

Different robots with different shapes and different actuator configurations originate different dynamics. Each robot must be regarded singularly and its motion must be governed by proper, well defined control laws. Although different, the control algorithms can be built upon a common framework. This type of approach enables the possibility of common interactions and quick reconfigurations for defining new roles. Moreover, the definition of a set of common elementary motion primitives makes it possible to achieve coordination at a (desired) higher level. The capability of coordinated vehicles to distribute resources over a region of interest can then be exploited to cooperatively accomplish goals that may include cooperative tasking or performances improvement according to any given metric.

1.4 Contributions

This thesis builds upon the background of control, coordination and navigation. Mainly motivated by robust control of marine vehicles, multi-vehicle operations and robot aided navigation, several steps towards fully autonomous coordinated operations and coordinated localization are made. The contributions of this thesis are summarized as follows:

- Design of a control law to stabilize hovering AUVs in the vertical pose - as a demonstration of the capabilities of the application of nonlinear control tools to achieve desired behaviors, a control law is derived to stabilize a hovering AUV at pitching angles of $\pm 90^\circ$.
- Development of a new localization method using range-only measurements combined with homing of a vehicle - using estimation, an extended Kalman filter (EKF) and a particle filter (PF) are implemented to solve the localization problem. The estimate is then combined with a control law that drives the vehicle to the beacon. The estimate confidence is used to modify the trajectory of the vehicle, intending to improve the estimate.
- Design of a gradient-tracking guidance law to home a vehicle using range-only measurements - localization is dispensable to home a vehicle to a beacon to which it is able to measure ranges. A guidance law is derived to home the vehicle with surge and yaw degrees of freedom (DOFs) and its stability is proven .

- Development of a generic control framework for coordinated autonomous vehicles - by adopting a layer perspective, three control loops are proposed to stabilize velocity, position and the configuration and position (center of mass) of the formation.
- Derivation of a set of tools to compute velocity and position errors boundedness - in the presence of model uncertainties and measurements errors, it is expectable that model-based control and guidance laws can not guarantee null error in steady state. As such, relevant results have been derived to assess such tracking errors.
- Extension and adaptation of the coordination scheme proposed by Egerstedt and Hu (2001) - the centralized control method is made tolerant to communication intermittences and is adapted so that the formation can hold its position. Moreover, the method is built so that, if the local control and guidance laws warrant appropriate tracking, the relative positioning errors are upper bounded and configurable.
- Derivation of the three-dimensional optimal positions of sensors in time-of-arrival (TOA)-based localization of a sound source underwater - two cases are addressed for this problem: 1) the optimal unconstrained positions of sensors to minimize the volume of the confidence region around the sound source; 2) the plane-constrained optimal positions of sensors to estimate the three-dimensional position of a sound source underwater.

1.5 Organization of the thesis

The remainder of this thesis is organized as follows. Chapter 2 gives a brief overview on control tools and estimation algorithms to support the following chapters. Additionally, and to motivate several solutions adopted in this thesis, a technological overview on the current navigation solutions is provided and the autonomous vehicles that have been employed throughout the development of the work presented in this thesis are introduced. Chapter 3 presents an application example where the control of a hovering AUV at pitching angle $\pm 90^\circ$ is addressed. At the kinematics level, the localization and the homing of an autonomous vehicle with controllable surge and yaw rate are addressed in chapter 4 as basic exercise of coordination. Two methods are proposed for homing the vehicle resorting only to range measurements. Firstly, homing is obtained by means of combined estimation and control. Then, following a sensor-based approach, a guidance law is derived to home the vehicle without any position estimate. Both the methods presume the existence of a lower loop that is capable of tracking the velocity reference provided. This velocity control loop is formalized in chapter 5. This chapter presents a model-based control law where possible modelling errors may be introduced. The upper bounds on velocity tracking are derived. The velocity inner loop is then employed in a target tracking and station-keeping guidance law for autonomous marine vehicles. These two basic layers are subsequently used to track references given by a coordination scheme presented in 6 that is capable of handling communication constraints and ensures an upper bounded relative position error under appropriate tracking of the vehicles. Finally, the

coordination of marine vehicles is applied to the coordinated tracking and localization of an underwater sound source in chapter 7, where the optimal positions of acoustic receivers are derived. Two cases are addressed: unconstrained positioning of sensors in three-dimensional space and plane-constrained positioning for three-dimensional optimal estimation.

Whenever it is convenient, at the beginning of each chapter, the main background and the related works are presented. Results of simulations, experimental data and the respective analysis are provided at the end of each chapter.

Chapter 2

Overview

Before addressing specific problems of marine vehicle automatic guidance and control, it is important to expose the main tools used in this thesis. Firstly, this chapter aims at providing a brief overview on mathematical dynamic and kinematic models and on control tools closely related to the solutions adopted in the next chapters. Secondly, the *fusion*¹ of measurements is addressed. In real applications, sensors provide meaningful measurements on a multitude of variables that are subsequently *fused* to guess the state estimate. This fusion has to be performed for two main reasons: noise affects the measurements and the direct utilization of measurements to determine the state may lead to very noisy state estimates, which may significantly degrade the control performances; or, the state is not directly measurable (there is no closed, direct relationship between the state and the observations) and a *filter* that uses (fuses) the relevant measurements has to be employed to infer the state. In robotics, these filters are commonly utilized for both smoothing and state estimation. For completeness and to support the forthcoming chapter, the main concepts and formulation for two widely-used filters are presented, specifically, the extended Kalman filter (EKF) and the particle filter (PF). In a more technological perspective, this chapter ends with an overview on the commonly employed solutions in marine localization, and on their constraints, as well as a brief presentation of autonomous vehicles that have served as development and testing platforms.

2.1 Notation

Throughout this document, the following notation is adopted for simplicity and compactness. For brevity, as in Fossen (1994), the trigonometric functions are denoted $s \cdot = \sin(\cdot)$, $c \cdot = \cos(\cdot)$ and $t \cdot = \tan(\cdot)$. For vectors, the notation $[\cdot]_i$ denotes the i th entry, $[\cdot]_{ij}$ denotes the entry of a matrix on the i th row and j th column. The representation $|\cdot|$ is used to denote the absolute value of a scalar or a vector. In the latter case, all the resulting entries are the absolute values of the components of the vector. The notation $(\cdot)^T$ is used to express the transpose of a matrix or vector. Similarly,

¹fusion of measurements is the process of combining different or similar measurements obtained from different sensors with the aim of reaching a better estimate for a given quantity

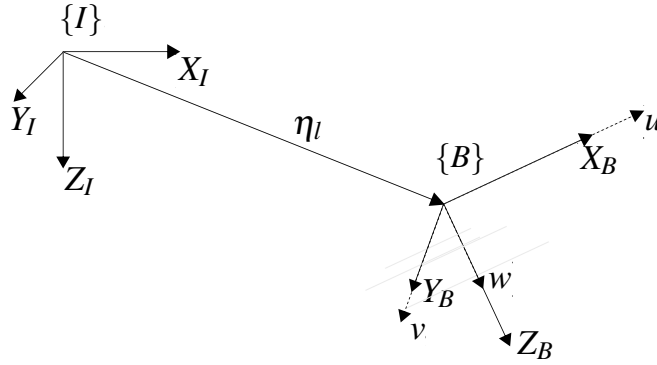


Figure 2.1: Frames and position vector

$(\cdot)^\dagger$ is used to denote the pseudo or Moore-Penrose inverse matrix, that is, for a given matrix $Q \in \mathbb{R}^{m \times n}$, its pseudo-inverse is defined to be given through the singular value decomposition (SVD) as $(Q)^\dagger = V \Sigma^\dagger U^T$ where the columns of $V \in \mathbb{R}^{n \times n}$ and $U \in \mathbb{R}^{m \times m}$ are respectively the right-singular and the left-singular vectors of Q , and the diagonal of $\Sigma \in \mathbb{R}^{m \times n}$ is composed of the singular values of Q (Katayama, 2005).

2.2 Dynamic and kinematic models

Let us consider the motion of a mobile robot in the three-dimensional space. Define $\{I\} = \{X_I, Y_I, Z_I\}$ as the inertial reference frame and $\{B\} = \{X_B, Y_B, Z_B\}$ as the body fixed referential frame with origin coincident with the center of gravity and the x and y axes being coincident with the surge and sway axes as depicted in figure 2.1. Adopting the same widely used notation as in (Fossen, 1994), the robot absolute position in $\{I\}$ is denoted by the vector $\eta_l = [x, y, z]^T \in \mathbb{R}^3$, while $\eta_a = [\phi, \theta, \psi]^T \in \mathbb{R}^3$ denotes the vector of Euler angles as depicted in figure 2.2. The relative linear and angular velocity vectors of the robot, with regard to the fluid velocity, expressed in the $\{B\}$ frame, are given by $v_l = [u, v, w]^T \in \mathbb{R}^3$ and $v_a = [p, q, r]^T \in \mathbb{R}^3$, respectively. During operation, the robot is assumed to be subject to the effects of *constant or at least slowly-varying* drifts that are represented by $v_{ld} = [v_x, v_y, v_z]^T \in \mathbb{R}^3$, expressed in the inertial frame $\{I\}$ (Fossen, 1994). Introducing the rotation matrix $J_l(\eta_a)$ ($J_l^{-1}(\eta_a) = J_l^T(\eta_a)$) from $\{B\}$ to $\{I\}$ parametrized by η_a , the velocity vectors in both referential frames $\{I\}$ and $\{B\}$ are related through the following expression, from (Fossen, 1994, pp. 86-87):

$$\dot{\eta}_l = J_l(\eta_a)v_l + v_{ld}.$$

Similarly, the relation between the angular velocities expressed in $\{B\}$ and the angle rates (time-derivative of the angles) expressed in $\{I\}$ is given through the transformation matrix $J_a(\eta_a)$ (see (Fossen, 1994; Diebel, 2006) for further details):

$$\dot{\eta}_a = J_a(\eta_a)v_a.$$

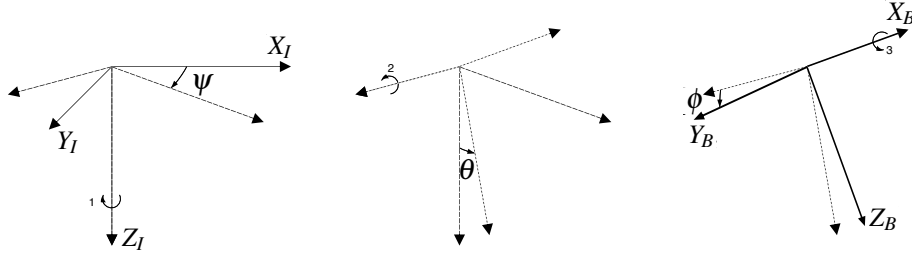


Figure 2.2: Sequence of rotations from the inertial frame $\{I\}$ to the body-fixed frame $\{B\}$. Sequence: yaw \rightarrow pitch \rightarrow roll ($\psi \rightarrow \theta \rightarrow \phi$)

In opposition to the relation between linear velocities and the time-derivative of the position, the matrix $J_a(\eta_a)$ is not a rotation matrix. Moreover, this matrix has singularities for any sequence of rotations chosen. For the sequence illustrated in figure 2.2, the matrix is singular for $\theta = \pm 90^\circ$ (see (Diebel, 2006)).

A more compact notation can be obtained by defining the pose vector η , which is the concatenation of the linear and angular positions into a single vector. Define the block diagonal matrix $J(\eta)$ that maps the velocity vector expressed in $\{B\}$ into $\{I\}$, given by

$$J(\eta) = \begin{bmatrix} J_l(\eta_a) & 0_{3 \times 3} \\ 0_{3 \times 3} & J_a(\eta_a) \end{bmatrix} \in \mathbb{R}^{6 \times 6}.$$

Additionally, define the concatenated velocity vector, expressed in the body frame $\{B\}$ as

$$\mathbf{v} = \begin{bmatrix} \mathbf{v}_l \\ \mathbf{v}_a \end{bmatrix} \in \mathbb{R}^6,$$

and the augmented drift vector

$$\mathbf{v}_d = \begin{bmatrix} \mathbf{v}_{ld} \\ 0_{3 \times 1} \end{bmatrix} \in \mathbb{R}^6.$$

Note that it has been assumed that the drift is irrotational, that is, the angular components of the drift vector are null. The mapping of the velocity vector, expressed in the body frame $\{B\}$, into the inertial frame $\{I\}$ is given by

$$\dot{\eta} = \begin{bmatrix} \dot{\eta}_l \\ \dot{\eta}_a \end{bmatrix} = J(\eta) \mathbf{v} + \mathbf{v}_d \in \mathbb{R}^6. \quad (2.1)$$

As for many mechanical systems, mobile robots are governed by a second order differential equation which incorporates the effects of damping, added mass, restoring and applied forces and moments. The relation between these forces and the rigid body dynamics is given by the following six degrees of freedom (DOFs) equation (Fossen, 1994):

$$M\dot{\mathbf{v}} = -C(\mathbf{v})\mathbf{v} - D(\mathbf{v})\mathbf{v} - g(\eta) + \tau \quad (2.2)$$

where $\tau \in \mathbb{R}^6$ is the vector of actuation forces and moments, $M, C(\cdot), D(\cdot) \in \mathbb{R}^{6 \times 6}$ and $g(\cdot) \in \mathbb{R}^6$. The square matrix M is a positive definite matrix, that is $x^T M x > 0 \forall x \in \mathbb{R}^6 \setminus \mathbf{0}$ that contains the acceleration multiplicative terms related to rigid-body and added mass forces and moments, $C(\cdot)$ is a skew-symmetric matrix originated by the Coriolis and centripetal effects, $D(\cdot)$ contains the terms related to viscous damping and $g(\cdot)$ is the vector of restoring forces and moments originated by the weight and the bouyancy forces.

The derivation of the parameters composing the entries of the dynamics expression matrices is beyond the scope of this thesis. The reader is referred to (Prestero, 2001; Fossen, 1994; Hoerner, 1965; Faltinsen, 2005; White, 2003) for a complete overview on the derivation hydrodynamic models.

In robotics, for simplicity reasons, it is a common practice to decouple vertical and horizontal motions to ensure independent manipulation of the respective state variables. For example, while moving, underwater vehicles are often required to keep pre-set distances from the bottom or from the surface, independently of the horizontal motion. Thus, several authors consider simplified dynamics and kinematics models assuming that the cross-influences of the resulting models are small enough. Previous works have already proven the validity and the satisfactory performance of this approach in underwater vehicles (Fossen, 1994). In ground robotics, several works do not even consider the vertical motion since the robots are constrained to lie in a two-dimensional subspace.

Decoupling of motions or model order reduction is often carried out to reduce the complexity of the dynamics. Cross related forces between decoupled or neglected DOFs are commonly regarded as disturbances that must be accommodated by the controllers.

2.3 Control tools

Robots are governed through control laws that permit tracking reference signals whose values represent desired angular or linear positions, velocities or accelerations. The correct operation of the controllers is, at least, as important as a good localization for navigation. This fact leads us to present some of the most common techniques used for stabilization of nonlinear systems.

Important and very interesting works have been developed in the domain of robot control using a diversity of methods to achieve desired behaviors in a large variety of robotics platforms. Robotic systems are commonly nonlinear. Therefore, high performances control of robots requires nonlinear control techniques, otherwise leading to poorer, or even unstable, behaviors. In most cases, traditional linear control theory is not sufficient to ensure stability of robotic systems over the full range of operation.

Several books on nonlinear systems and nonlinear control theory can be found in the literature. Undeniable references are the books by Khalil (2002) and Slotine and Li (1991). Additionally, the reference book by Fossen (1994) presents a multitude of control techniques as well as models for marine vehicles. The reader is referred to those books for further details. In this section,

it is intended to cover some of the feedback control techniques found in the literature and used throughout this document.

For the sake of illustration, let us consider the general nonlinear system

$$\dot{x} = f(t, x, u), \quad (2.3)$$

where $x \in \mathbb{R}^n$ is the state vector, $u \in \mathbb{R}^p$ is the input vector and $t \in \mathbb{R}$ is the time variable.

Below, three of the most common tools in nonlinear control are briefly presented, namely exact feedback linearization, Lyapunov direct method and backstepping.

2.3.1 Exact feedback linearization

Nonlinear systems can be linearized by employing exact feedback linearization technique. Considering now the more specific system

$$\dot{x} = f(x) + g(x)u, \quad (2.4)$$

the problem is now related with the possibility of deriving a feedback control law of the form $u = \alpha(x) + \beta(x)v$ and a change of variables given by a diffeomorphism² $z = T(x)$ such that the system above can be transformed in the following form

$$\dot{z} = Az + B\beta^{-1}(x)(u - \alpha(x)), \quad (2.5)$$

with $\beta(x)$ nonsingular and (A, B) controllable.

The general solution is such that the term $\alpha(x)$ in the control law cancels the undesired nonlinearities and the term $\beta(x)v$ is designed so that the system is stabilized. Exact feedback linearization techniques are particularly interesting since the implicit solution allows for inducing specific performances of convergence, such as exponential convergence, by properly defining v .

2.3.2 Lyapunov direct method

Besides linearization techniques, Lyapunov-based methods are tools for designing suitable control laws in nonlinear systems. Lyapunov methods are dual since they serve as tools for analyzing the system stability and for designing the respective control law. Stability is evaluated by investigating the evolution of the Lyapunov function. This important feature permits assessing the stability of a given system, after having properly chosen the corresponding Lyapunov function, and is of particular interest for determining regions of attraction as well as invariant sets for uncertain and/or complex nonlinear systems.

The Lyapunov direct method can be summarized in two steps: definition of a continuously differentiable positive definite Lyapunov function $V(x) > 0, \forall x \in D \setminus \{0\}$, verifying $V(0) = 0$, and derivation of the control input u such that $\frac{dV(x)}{dt} < 0, \forall x \in D \setminus \{0\}$, where the domain $D \subseteq \mathbb{R}^n$

²a diffeomorphism is a continuously differentiable map that has a continuously differentiable inverse

contains the origin. This control law implies that x converges to zero in the domain D . Further results, such as Lyapunov redesign (Khalil, 2002), were extended from this method. In particular, the latter allows for defining a control law that stabilizes the system in the vicinity of the origin, in the presence of bounded uncertainties with respect to the nominal model. Such methods are useful in practical applications, since exact mathematical models are impossible to obtain for most systems. Hence, the existence of a bounded uncertainty or disturbance implies that the origin of the system is not asymptotically stable, that is, x does not converge asymptotically to zero, but, in some cases, an invariant set in the vicinity of the origin can be derived, guaranteeing an upper bound on the steady state error.

2.3.3 Backstepping

Backstepping method is particularly interesting for the purpose of deriving control laws for strict-feedback systems, that is, systems that take the form

$$\begin{aligned}\dot{x}_1 &= f_1(x_1) + g_1(x_1)x_2 \\ \dot{x}_2 &= f_2(x_1, x_2) + g_2(x_1, x_2)x_3 \\ &\vdots \\ \dot{x}_n &= f_n(x_1, x_2, \dots, x_n) + g_n(x_1, x_2, \dots, x_n)u.\end{aligned}\tag{2.6}$$

To illustrate the method, let us consider the simpler integrator system

$$\begin{aligned}\dot{x}_1 &= f(x_1) + g(x_1)x_2 \\ \dot{x}_2 &= u.\end{aligned}\tag{2.7}$$

and define a Lyapunov function $V(x_1)$ which is positive definite. Suppose that a function α that, if $x_2 = \alpha(x_1)$, the time derivative of the Lyapunov function is made negative definite over a domain D containing the origin, that is,

$$\frac{dV(x)}{dt} = \frac{dV(x)}{dx} (f(x_1) + g(x_1)\alpha(x_1)) < 0, \quad \forall x_1 \in D \setminus \{0\}.\tag{2.8}$$

Hence, let us introduce the tracking error $z = x_2 - \alpha(x_1)$ and re-write the system as

$$\begin{aligned}\dot{x}_1 &= f(x_1) + g(x_1)\alpha(x_1) + g(x_1)z \\ \dot{z} &= u - \frac{d}{dt}\alpha(x_1).\end{aligned}\tag{2.9}$$

The definition of this new error is introduced to explicitly relate x_2 and the function $\alpha(x_1)$, which can be seen as a virtual (desired) control input. This error will be introduced in the system and reduced to zero next.

Hence, by defining a new augmented Lyapunov function candidate as $V_1 = V + \frac{1}{2}z^T z$, the time

derivative of this new positive-definite function results

$$\begin{aligned}\dot{V}_1 &= \dot{V} + z^T \dot{z}, \\ &= \frac{dV}{dx} (f(x_1) + g(x_1)\alpha(x_1)) + \frac{dV}{dx} g(x_1)z + z^T (u - \frac{d}{dt}\alpha(x_1)), \\ &< \frac{dV}{dx} g(x_1)z + z^T (u - \frac{d}{dt}\alpha(x_1)),\end{aligned}\tag{2.10}$$

where \dot{z} has been expanded for convenience in order to show the dependence on the input u . This latter can then be designed to guarantee negative definiteness of \dot{V}_1 .

The method follows the same steps for higher order systems, such as the one in (2.6). Under appropriate assumptions on the functions $f_i(\cdot)$ and $g_i(\cdot)$, the backstepping method recursively seeks for functions of the type $x_i = \alpha_i(x_{i-1})$, $i = 2, \dots, n$, introducing error variables $z_i = x_i - \alpha_i$ in the recursively augmented Lyapunov function candidates.

2.4 Estimation background

In robotics it is common to tackle problems in which state variables can not be measured directly due to sensing constraints. Instead, sensors provide important information from which it is possible to determine the current state but, due to noise and biases, analytical methods may not be suitable. Therefore, estimation becomes the only solution. Several methods have been developed and employed in robotics, from Kalman filters (KFs) (Kalman, 1960) to nonlinear observers (see the example in (Khalil, 2002)).

Position estimation in robotics usually employs recursive methods. The literature is vast on this subject. The reader is referred to Gelb (1999) for an overview on estimation or Thrun et al. (2005) for application to robotics. The following sections summarize the KF and PF algorithms, based on Thrun et al. (2005).

2.4.1 Kalman filter and extended Kalman filter

KFs have become standard tools in estimation and are very common in robotics. This filter was first designed for linear systems and has posteriorly been adapted to nonlinear systems through linearizations resulting in the so-called EKF.

The KF formulation assumes linear evolution of the state, that is, it assumes that the dynamics of the state vector and the output can be expressed in the form:

$$\begin{aligned}x(t_k) &= A_k x(t_{k-1}) + B_k u(t_k) + w(t_k), \\ z(t_k) &= C_k x(t_k) + v(t_k),\end{aligned}\tag{2.11}$$

where $x(t_k) \in \mathbb{R}^N$ is the state vector at time t_k , $u \in \mathbb{R}^M$ is the input vector, $z \in \mathbb{R}^L$ the output vector and $w \sim \mathcal{N}(0, R_k)$, with $R_k \in \mathbb{R}^{N \times N}$ and $v \sim \mathcal{N}(0, Q_k)$, with $Q_k \in \mathbb{R}^{L \times L}$, are noise vectors that follow Gaussian distributions. In robotics in general, $z(t_k)$ is a vector of measured variables, obtained directly from sensors. The remaining elements are matrices of appropriate dimensions.

For brevity, in what follows, the notation $(\cdot)_k$ will be used to denote $(\cdot)(t_k)$. The KF algorithm considers two steps: prediction and update.

Denoting the expected value of the state x_k as $\bar{\mu}_k$, after the prediction step, and as μ_k after the measurement update, the KF algorithm is given by the following expressions:

Prediction

$$\bar{\mu}_k = A_k \mu_{k-1} + B_k u_k \quad (2.12)$$

$$\bar{P}_k = (A_k P_{k-1} A_k^T + R_k)^{-1} \quad (2.13)$$

Update

$$P_k = (C_k^T Q_k C_k + \bar{P}_k^{-1})^{-1} \quad (2.14)$$

$$K_k = P_k C_k^T Q_k^{-1} \quad (2.15)$$

$$\mu_k = \bar{\mu}_k + K_k (z_k - C_k \mu_k). \quad (2.16)$$

In the absence of measurements or between two consecutive measurements, the prediction step is executed iteratively. Whenever a new measurement is available, the update step is executed.

For the nonlinear case, assume that the dynamics can be written in the following form:

$$\begin{aligned} x_k &= f_k(x_{k-1}, u_k) + w_k \\ z_k &= h_k(x_k) + v_k \end{aligned} \quad (2.17)$$

where $f_k(\cdot, \cdot)$ and $h_k(\cdot)$ are nonlinear functions of their arguments. Then, defining the Jacobian of the functions f and h , evaluated at x_{k-1} and x_k , respectively

$$F_k = \frac{\partial f(x, u)}{\partial x} \Big|_{x=x_{k-1}}, \quad (2.18)$$

$$H_k = \frac{\partial h(x)}{\partial x} \Big|_{x=x_k}, \quad (2.19)$$

the EKF algorithm results from adaptation of (2.12)-(2.13) and (2.14)-(2.16):

Prediction

$$\bar{\mu}_k = f_k(\mu_{k-1}, u_k) \quad (2.20)$$

$$\bar{P}_k = (F_k P_{k-1} F_k^T + R_k)^{-1} \quad (2.21)$$

Update

$$P_k = (H_k^T Q_k H_k + \bar{P}_k^{-1})^{-1} \quad (2.22)$$

$$K_k = P_k H_k^T Q_k^{-1} \quad (2.23)$$

$$\mu_k = \bar{\mu}_k + K_k (z_k - h_k(\mu_k)). \quad (2.24)$$

For the derivation details, the reader is referred to [Thrun et al. \(2005\)](#).

The EKF was classified as suboptimal (Gelb, 1999) for nonlinear systems since it approximates the nonlinear functions by the corresponding first order truncated Taylor series expansion. It is important to note that the KF algorithms needs for an initialization of μ_0 and P_0 , that is, initial guesses of the state vector and of the covariance matrix.

Despite their high robustness in several problems with non-Gaussian noises, after an appropriate tuning of parameters, KFs are optimal only for Gaussian noises corrupting the dynamics and the observations. For applications that do not verify the existence of such noises, enlarging the process and the measurement noise covariances is a common practice. Several works have employed EKF algorithm to determine the state estimate on-line. Examples of implementation of EKF can be found in (Baccou and Jouvencel, 2002; Ferreira et al., 2010b; Folk et al., 2010; Olson et al., 2006; Rui and Chitre, 2010), for example.

2.4.2 Particle filter

In opposition to KFs, PFs do not make any assumption on the process and measurement noise distributions (Thrun et al., 2005). Instead of defining the posterior in a parametric way, a finite set of particles approximate the posterior distribution function through their distribution over the state space. The method is based on the Markov sampling: particles are vectors with the same dimension as the estimate, and they represent possible states whose evolutions are driven according to a given dynamics. Such a dynamics usually includes propagation based on the state model and spreading according to a provided distribution. Recursively, the importance of each particle is determined based on the measurements. Some algorithms, such as the sequential importance sampling (SIS) (Arulampalam et al., 2002), resample around the most important particles in order to keep the number of particles sufficiently small. Actually, this allows for concentrating the particles over the regions of interest, which also permits to reduce the total number of particles while keeping a good representation of the probability density in those regions. Even though, PFs are known to be computationally more demanding than KFs due to the need for evaluating the entire set of particles.

After initialization, PF algorithms generally consist of three steps: prediction, measurement update and resampling. Let us consider the general, possibly nonlinear, system (2.17) and a set of n particles $\chi_k = \{x_k^1, x_k^2, \dots, x_k^n\}$, where x_k^i are of the same dimension as that of the state x_k . A set of importance weights $\mathcal{W}_k = \{w_k^1, w_k^2, \dots, w_k^n\}$, $w_k^i \in \mathbb{R}$, is associated with the particles. Accordingly, the state estimate can simply be obtained by the weighted sum of the particles.

The prediction is obtained by drawing the particles according to their prior value and to the input of the system:

$$x_k^i \sim p(x_k | x_{k-1}^i, u_k). \quad (2.25)$$

In a practical perspective, this step results in driving the particles according to the dynamics and the input and spreading them according to a given process noise. Measurement updates affect only the weights by modifying their values according to the probability of the corresponding

particle to generate the measurement z_k :

$$\bar{w}_k^i \propto p(z_k | x_k^i), \quad (2.26)$$

$$w_k^i = \frac{\bar{w}_k^i}{\sum_{i=1}^n \bar{w}_k^i}. \quad (2.27)$$

For the purpose of resampling, let us define a set of indices $\mathcal{J} = \{i^1, i^2, \dots, i^n\}$ and the discrete density of probability $p(i) = w_k^i$. Sample the indices of the set \mathcal{J} as follows:

$$i^j \sim p(i) \quad (2.28)$$

Finally, resampling is achieved by setting:

$$\mathcal{X} = \{x_k^{i^1}, x_k^{i^2}, \dots, x_k^{i^n}\} \quad (2.29)$$

and the weights $w_k^i = 1/n$.

Resampling too often, however, may reduce the diversity of particles and may increase computational requirements. It is common to adopt alternatives that reduce the resampling frequency by doing so only when $\frac{1}{\sum_{k=1}^n w_k^{i^2}}$ is above a given threshold (Arulampalam et al., 2002).

One of the most infamous issues in PFs is the deprivation: due to their nature, PFs may fail to cover the vicinity of relevant regions. This happens because of the finite number of particles used to approximate the posterior. Indeed, the impossibility of having an infinite number of particles due to computational constraints is a major drawback in PFs. This can lead to lack of representativity of the posterior in the state space.

2.5 Underwater localization technology

Localization is essential in mobile robotics applications since it constitutes one of the two fundamental components of navigation along with control. In robotics, localization aims at determining the current position by means of collected measurements.

The following subsections focus on the problem of robot position estimation, with emphasis on marine robotics. As the localization problems can not be decoupled from the current technology available, some of the most important equipment used for position estimation will be covered.

2.5.1 Dead-reckoning localization

Intuitively, one could infer about the own current position based on previous knowledge and a collection of estimates or pose measurements. Defining η as the current position and v the absolute velocity in the same frame, the actual position could be directly obtained through the well known relation:

$$\frac{d}{dt} \eta = v. \quad (2.30)$$

Moreover, define the acceleration in the absolute frame a , then the following relation is established:

$$\frac{d}{dt^2}\eta = \frac{d}{dt}v = a. \quad (2.31)$$

However, it may be difficult to assess all the variables composing the acceleration, velocity or position vectors due to the sensing limitations. Furthermore, in the case where accelerations and velocities are accessible they may be corrupted by unpredictable noise and biases which make the integration of (2.30) or the double integration of (2.31) unreliable over extended periods of time. By considering the equations above, there exists a trade-off between resolution, precision, accuracy of inertial measurements and long term accuracy of the position estimate.

Linear accelerations are usually obtained by means of accelerometers. These devices are generally grouped into a single device that possesses three independent accelerometers along three orthogonal axes. They are usually inexpensive and are frequently found in robots together with other equipments in all-in-one solutions. However, the presence of biases and noise constrains their wide integration in robotic platform.

Rate gyroscopes measure angular velocities of the body they are attached to. As for accelerometers, commercial solutions generally combine the three angular rates into a single device. Complementary to rate gyroscopes, compasses measure heading through magnetic fields and are commonly used in mobile robotics. Tilt sensors measure the inclination in orthogonal axes of the body.

The technological solutions described above can be found in inertial measurement unit (IMU) (see for example Xsens (2011); Hol et al. (2010)) which combine the measurements of each subdevice in order to get more precise information on angles, angular velocities and linear accelerations. IMUs generally result in better solutions than having each single device separately: the proper fusion of different measurements commonly yields more reliable estimates. In other words, instead of interpreting the raw data provided by each sensor, they can be combined (fused) for better performances.

Besides inertial and angular measurements, the determination of the position based on the traveled distance through the use of appropriate sensors is particularly desired for mobile robotics applications. Such a process is referred to as odometry³. While, in land robots, odometry can be directly assessed from a simple odometer such as a hall sensor coupled to the wheel shaft (assuming there is no slip), in marine robotics, and aerial robotics as well, the problem results more complex since there is no solid mechanical coupling between the robot's body and the environment. Therefore, alternative sensing solutions have been developed and implemented in marine robots. The velocity with respect to the water can be obtained by a simple flow meter using a paddle wheel (Airmar Technology, 2011b), for example. The main issue concerning this type of equipment is poor performance at slow speeds. As a consequence, wheel-less sensors have been developed to overcome this limitation and ultrasonic speed sensors (Airmar Technology, 2011a)

³the term odometry is more related with land robotics in the literature

constitute valid alternatives, since they are able to measure speeds as low as 0.05m/s. The operation of this class of sensors explores the Doppler effect, which allows for the determination of the speed based on the analysis of emitted and reflected signals. Their principles of operation relies on an emitted wave, with a well established frequency, and posterior reception of the same signal, after having been reflected on a given surface or particle. The frequency shift then permits determining the relative speed.

Doppler velocity loggers (DVLs) use the same principle as that of ultrasonic speed sensors. DVLs typically operate at low frequencies (300 to 1200 kHz) (Instruments, 2011; Linkquest, 2011) and are engineered for bottom-lock or surface-lock applications, although relative water velocity can also be measured. In bottom-lock operations, the emitted acoustic pulses are reflected directly on the bottom while in surface-lock mode they are reflected on the surface. Bottom-lock mode makes it possible to obtain absolute velocity measurements. Nonetheless, their range of operation is limited: the maximum altitude ranges from 30 to 500 meters. In opposition to ultrasonic speed sensors, DVLs provide the discriminated components of linear velocity along the three orthogonal axes. The measurement precision of these equipments is generally below the impressive 1% of the actual velocity (Instruments, 2011).

2.5.2 Absolute and relative localization

The use of sensors such as the ones referred above provide inertial and velocity measurements. As already stated, the presence of unpredictable biases on their outputs makes the resulting estimate error unbounded for large scale or long term operations. As a result, precise localization can not be guaranteed through dead-reckoning of inertial and velocity measurements. Inertial navigation systems (INSs) are *of limited utility in the low-speed, low-acceleration regime typical for oceanographic robotic vehicles* (Whitcomb et al., 1999). Therefore, complementary equipments are often used to assess the position.

Artificial vision has been used in robotics for relative localization of robots. However, most of the applications remain within structured environments where familiar shapes can be recognized. One interesting exception is the work by Pfingsthorn et al. (2010) where pictures from the bottom are taken and cooperatively shared by several vehicles for simultaneous localization and mapping (SLAM). Vision based localization methods present some issues related with the low visibility underwater, low natural brightness for deep scenarios and absence of features on the observed surface.

Sonar based technologies can also be included in this context since they produce an array of information obtained through the reflection of acoustic waves. Relative localization is possible by matching maps of features over the trajectory (see also (Pfingsthorn et al., 2011) for a cooperative approach example).

At the surface, general positioning system (GPS) are probably the most suited technologies for localization and positioning of a large range of autonomous marine robots due to their accuracy and coverage. Nevertheless, GPS may have some limitations in occluded zones close to marine structures or because of hills close to rivers margins that occlude signals from satellites,

for example. GPS devices use the concept of trilateration to determine their position. Satellites are constantly emitting coded messages via electromagnetic waves, providing time-stamps and other relevant information. Based on the time that the message is sent and on the propagation speed of electromagnetic waves, a GPS device is able to determine its horizontal positions and altitude by using the information from four satellites to determine the three-dimensional position and the current time. Nonetheless, GPS is unavailable underwater because of the strong attenuation of electromagnetic waves and reflections on the surface. The study in Al-Shamma'a et al. (2004) showed that the attenuation for antennas located 1 meter away from each other is close to 80dB for a signal frequency of 66MHz propagating in the water. For the typical 1.4GHz carrier frequency of GPS signals, the attenuation is larger.

In order to overcome these constraints in relative and absolute localization, some solutions were engineered by taking advantage of the sound propagation characteristics in the water. The solutions are built upon the time of flight (travel time) of acoustic waves. Generally, acoustic transducers, thereafter referred to as beacons, are deployed on the area of interest and are able to emit acoustic pulses. The localization process is similar to GPS. While assuming that the velocity of propagation of sound is known along the path followed by the wave, a robot is able to compute the travelled distance of the acoustic pulse and assess its current position. A minimum of three beacons is required for unambiguous localization (assuming, of course, that there is no ambiguity on the subspaces delimited by the plane composed by the position of the three beacons). However, the number of beacons can be reduced by using a depth (pressure) sensor. The problem lies on the ambiguity that this configuration creates with respect to the side where the vehicle is. Depth sensors are usually inexpensive and provide accurate information at relatively high rates.

For the purpose of underwater localization through acoustic ranging, two solutions are commonly employed: long baseline (LBL) and ultra-short baseline (USBL). The first one operates by means of trilateration, measuring ranges to each beacon. The idea is finding the point of intersection of spheres centered at the beacons with radii equal to the respective range. The beacons can be deployed on the surface (Cruz et al., 2001), on the seafloor (Kussat et al., 2005) or a mixture of both can also be utilized. The USBL solution generally requires a single beacon only while the robots carry an array of, at least two, transducers closely located. The distance is assessed in the same way as in LBL but, in opposition to that solution, relative position is not determined through the intersection of spheres. Instead, the angle relative to the beacon is obtained by determining the phase shift of the received carrier on the array of transducers. Other approaches explore the use of a single beacon (Ferreira et al., 2010b; Casey et al., 2007; Baccou and Jouvencel, 2002) where the range and an estimate of the velocity (possibly measurements) are used to estimate the relative position of the beacon. This type of solutions solves a particular problem of simultaneous localization and mapping (SLAM), where the beacon is mapped while the robot try to localize itself with respect to the beacon.

For static beacon operations, the robots commonly know the position of the beacons and are able to determine their own relative position. In some scenarios, the localization accuracy and precision depends on the relative positions of the vehicles with regard to the beacons. As such,

moving the beacons enables new capabilities such as unbounded operation area and bounded error navigation. Moving baseline operation was explored in Vaganay et al. (2004) and Folk et al. (2010). Unless explicit communications are used, in those scenarios, the robots are unable to determine their absolute position on-line, with bounded error, based only on LBL (or USBL) information.

Acoustic based solutions, such as the ones described above, use two types of ranging methods. One is the two-way travel time (TWTT) method (see Cruz et al. (2001) for example), based on the query-response scheduling: a robot queries the beacon which is listening to interrogations (pings). The beacon responds immediately (or after an established time) while the robot await for the response. By computing the time-of-flight of both emitted and received pings, the robot determines the distance to the beacon. These steps must be repeated for each beacon and for each sampling iteration. The second method is the one-way travel time (OWTT) (see Eustice et al. (2011) for example), for which an established emission schedule is shared in advance by the beacons and the robots. Each beacon pings at a scheduled time while the robots passively listen to the acoustic channel. Such an approach implies synchronized clocks with very low drifts in order to achieve reasonably low errors for extended periods of time. The OWTT approach has therefore several important advantages over TWTT: firstly, robots do not need to query the beacons; secondly and consequently, there is no need to allocate time periods for each robot to measure ranges; thirdly, in OWTT, the maximum update rate is independent of the number of robot in the team (for TWTT, the fix rate for a team is inversely proportional to the number of robots); fourthly, the fix (ping) rate can be naturally higher since there is no need to query the beacons.

LBL systems for areas in the order of few hundreds of meters to some kilometers employ relatively low frequencies between 10-12kHz (Desset et al., 2003; Whitcomb et al., 1999; Eustice et al., 2011) and 37 kHz (Sgorbini et al., 2002; ACSA, 2011b,a). Commercially available solutions such as (ACSA, 2011b) enable an announced localization over an area as broad as 2km by 2km with precision in the order of 1m (one standard deviation). The set of equipments consists of four moored buoys (beacons) on the surface. The system described in Whitcomb et al. (1999); Eustice et al. (2011) allows for a wider range of operation (up to 10 km but no information is given on the geometry of the baseline) for precision ranging from 1cm to 10m. It is implicit that the beacons are precisely moored on the seafloor or on some kind of structure to achieve such a precision. The EXACT LBL system described in (Whitcomb et al., 1999; Bingham, 2003) uses a 300kHz carrier pulse to achieve precision in the order of few millimeters. Nevertheless, the coverage area is much smaller than the one provided by the former equipment (square area of 100m side length).

The use of acoustics for localization is not straightforward. One of the major issues is the presence of noise whose frequencies are close to the carrier used by the localization system. Furthermore, several phenomena such as multipath, reflections and attenuation introduce less intuitive problems that are frequently difficult to solve.

Attenuation of acoustic waves is originated by the natural loss of energy along the traveled path which is a consequence of the geometric spreading and the absorption of energy in the form

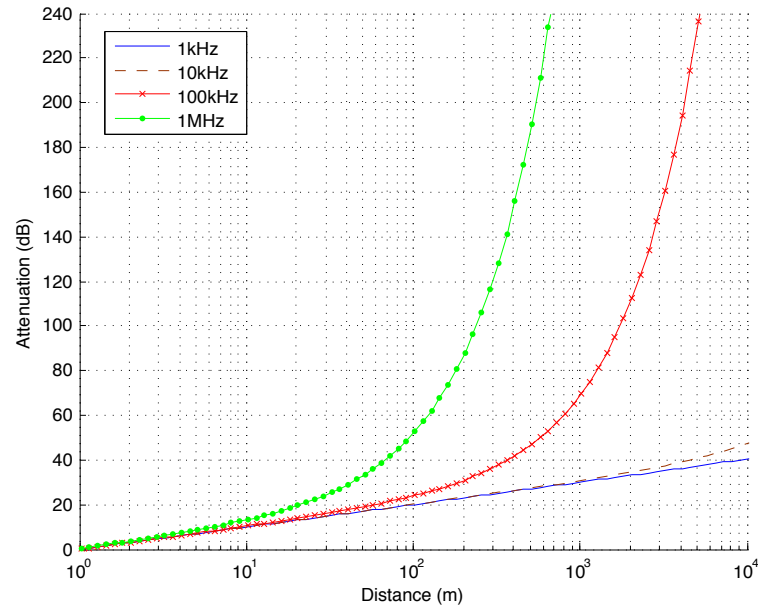


Figure 2.3: Attenuation of acoustic waves in seawater. Parameters: salinity = 3.54%, temperature = 20°C, sound speed = 1500m/s, pH = 8.

of heat (Aparicio et al., 2011). For further details, an overview on underwater acoustics is given in Domingo (2008). Assuming that the acoustic waves propagate within a cylinder in shallow water, figure 2.3 show how the waves attenuate according to the travelled distance and their frequencies.

The multipath effect is originated by reflections and refractions. Let us simply assume that the acoustic waves propagate as lines in space. At a given a point in space, different from the emission one, the first ping received usually (this may not always true because it depends on the sound speed profile) corresponds to the direct path between the reception and emission points (as far as the reception point is not in a shadow zone). Afterwards, secondary waves are received due to reflections on the surface and on the bottom. The multipath effect is also originated by the refraction since the acoustic waves travel along regions where the sound speed varies. Ray tracing is often used in order to better understand the phenomena. Figure 2.4 illustrates the effects originated by multipath, reflections and refraction by simulating the trajectories of a set of rays with angles comprised between -20 and 20 degrees over the vertical plane. The sound speed profile from Kussat et al. (2005) (San Diego coast) was used for ray tracing. The rays correspond to the idealization of path of acoustic waves assuming they do not spread and are emitted as infinitesimal section beams. Multipath effects can be seen at the intersections of the rays.

2.6 Experimental setup

Throughout this document, different autonomous vehicles are either used as case-studies or validation platforms. This set of heterogeneous vehicles includes surface and underwater vehicles. Brief descriptions of these systems are provided below.

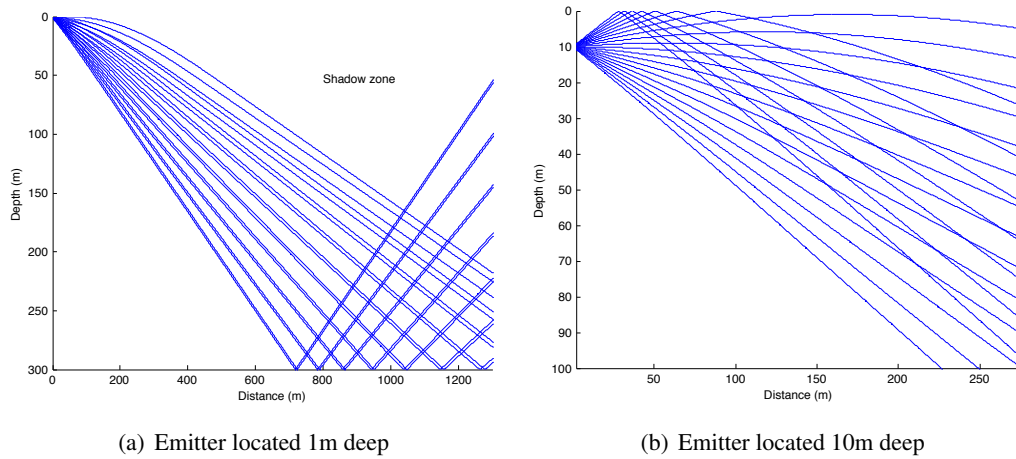


Figure 2.4: Multipath originated by refraction and reflections

Common to all vehicles are the computational devices and the communication capabilities (when they are at the surface). Sensing capabilities may vary from a vehicle to another. The types of sensors used for the purpose of navigation and their characteristics are summarized in table 2.1. The presented values are taken from the manufacturers datasheets, or are typical values observed in practice for the case of LBL. However, the experience from their use suggests that these values are frequently affected by the environmental conditions and calibration. In particular, angular measurements are typically affected by magnetic fields existing on board, while the precision of LBL estimates depends on the relative position of the vehicle with regard to the beacons.

2.6.1 The MARES AUV

The MARES AUV (figure 2.5(a)) is a small-sized, torpedo-shaped AUV with 1.7 meters of length and 20 centimeters of diameter. This vehicle was developed by the OceanSys group at INESC TEC, University of Porto. Besides the modularity feature, MARES differs from most of current AUVs since it has no fins and is capable of hovering. Its four thrusters provide four DOFs: two thrusters located at the stern provide surge and yaw DOFs while two through-hull thrusters enable

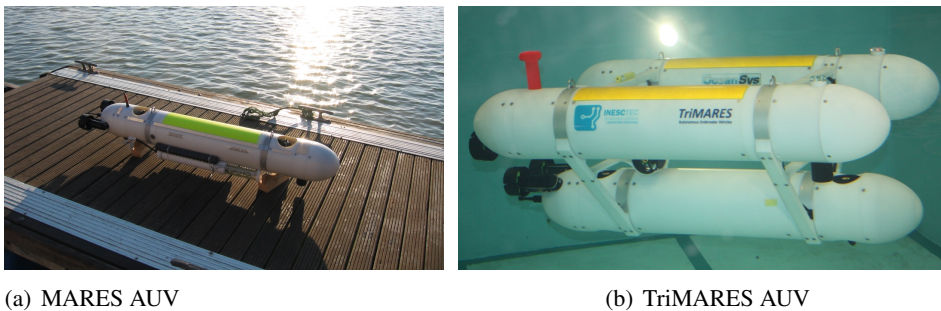
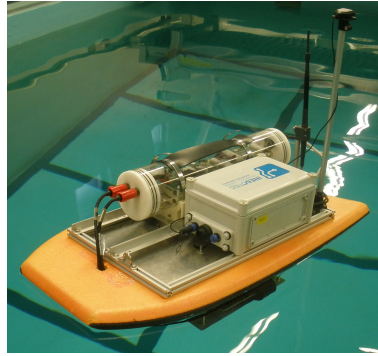


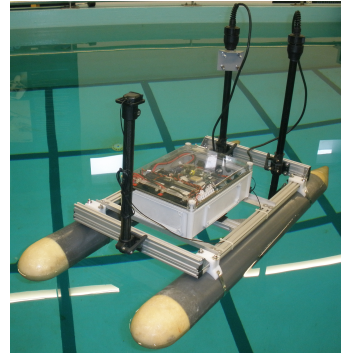
Figure 2.5: Autonomous underwater vehicles



(a) Zarco and Gama autonomous surface vehicles (ASVs)



(b) BASV



(c) LASV

Figure 2.6: Autonomous surface vehicles

controlling heave and pitch. Each thruster is capable of generating up to 35N of force. Additionally, the vehicle can control all the DOFs independently as long as the actuator remain unsaturated. This feature enables the vehicle to decouple motion primitives such as the ones in the vertical and in the horizontal planes.

On board, a computer is responsible for generating the commands for the thruster and fuse the information from the sensors. The basic sensing equipment includes a depth sensor, an altimeter, an IMU, a GPS for use at the surface and a transponder for long baseline (LBL) localization. Other sensors can occasionally be carried by taking advantage of the modular characteristic.

2.6.2 The TriMARES AUV

TriMARES is a hybrid AUV (figure 2.5(b)) that can also be operated in remotely operated vehicle (ROV) mode (Cruz et al., 2011). This vehicle was inspired on MARES and possesses three bodies to carry larger amounts of payload. Seven thrusters, each exerting forces up to 35N, ensure five DOFs. Four thrusters, frontward directed, at the stern provide control on surge, yaw, and possibly pitch. As for MARES, two through-hull thrusters, downward directed, in the lower body are responsible to create motion along heave direction and pitch. Finally, a lateral thruster between the three bodies creates sway motion. TriMARES weights about 75 kilograms in air and its length is 1.3 meters.

Table 2.1: Characteristics of navigation sensors/systems

| | MARES | TriMARES | Zarco | Gama | BASV | LASV |
|------------------------------|-------|----------|-------|------|------|---------|
| GPS | | | | | | |
| horiz. accuracy (m) | 5.0 | 5.0 | 1.5 | 1.5 | 2.5 | 2.5 |
| update rate (Hz) | 1 | 1 | 10 | 10 | 4 | 10 |
| Angular | | | | | | |
| accuracy (deg) | 2.0 | 2.0 | 1.5 | 3.0 | 1.5 | 2.0 |
| rate gyro accuracy (deg/sec) | 0.3 | 0.3 | - | 0.3 | - | unknown |
| update rate (Hz) | 10 | 10 | 40 | 10 | 40 | 10 |
| LBL | | | | | | |
| typical precision (m) | 2.0 | 2.0 | - | - | - | - |
| update rate (Hz) (typ.) | 0.25 | 0.25 | - | - | - | - |
| Depth sensor | | | | | | |
| accuracy (m) | 0.06 | 0.06 | - | - | - | - |
| update rate (Hz) | 40 | 40 | - | - | - | - |

2.6.3 The Zarco and Gama ASVs

Zarco and Gama (figure 2.6(a)) ASVs have been used to test control, guidance and coordination schemes. Zarco and Gama ASVs are similar vehicles with 1.5 meters of length and weighting slightly over 50 kilograms in their basic configuration. Their shapes and payload can be adapted depending on the mission requirements and carried sensors. They are actuated by two thrusters located at the stern granting control on the surge (longitudinal axis) and yaw (heading) DOFs. Each thruster is capable of generating 50N of force. The basic set of navigation sensors include a GPS receiver and an IMU.

2.6.4 BASV

The BASV (figure 2.6(b)) is a small-sized surface vehicle with approximately 70 centimeters of length and weighting about 11 kilograms. Computational and sensing devices are similar to those used by Zarco and Gama ASVs. Two horizontal thrusters exerting forces up to 28N, located underneath, grant surge and yaw DOFs.

2.6.5 LASV

Similarly to Zarco, Gama and the BASV, the LASV (figure 2.6(c)) is actuated by two frontward directed thrusters, located at stern, providing the same DOFs as the referred vehicles. Each thruster is capable of generating up to 50N. This vehicle, whose weight is about 25 kilograms and whose length is approximately 1.3 meters, has been designed in the context of the work presented in chapter 7.

Chapter 3

Control of a hovering AUV in the vertical pose

The nonlinear nature of both dynamics and kinematics of marine vehicles demands for robust controllers, which are typically nonlinear. The linear control theory may not apply to certain systems since it can not guarantee stability or, at least, can not guarantee satisfactory performances over all the range of operation. Control of marine vehicles have been an enthusiastic subject where several researchers have applied efforts to guarantee appropriate motion. As an exercise and to demonstrate the capabilities of nonlinear control tools, the stabilization of a streamlined hovering AUV in the vertical pose is addressed in this chapter. These vehicles are commonly built so that they are stable when they are in the horizontal pose as it commonly is the most used mode. However, the vertical pose may be beneficial under some scenarios such as the fast descent or ascent in deep waters since this can lead to more efficient motion. This poses a challenging problem since the AUVs are typically unstable in the vertical pose. By using the MARES AUV as a case-study, a control law is derived to stabilize the vehicle in the vertical pose. Additionally, motivated by the underlying challenge of guiding the vehicles horizontally when the vehicle is in the vertical pose, a guidance law is proposed to drive the vehicle to any horizontal point.

3.1 Motivation and related works

Control of AUVs is a subject that has attracted the attention of several researchers over the last decades. The nonlinearity and the uncertainty of the corresponding mathematical models have originated several challenges in both control theory and design. Some examples can be found in (Aguilar and Hespanha, 2007; Aguiar and Pascoal, 2007; Borhaug et al., 2007) or in (Antonelli et al., 2008) for an overview. In this section, the problem of stabilizing MARES in the vertical plane while pitching up or down (referred to as vertical pose or vertical orientation hereinafter) is addressed. While holding the vertical pose, the motion over the horizontal plane is further explored by determining a guidance law to enable the vehicle to reach any horizontal position. Although MARES was used as a case-study, the method presented in this section applies to a large range of

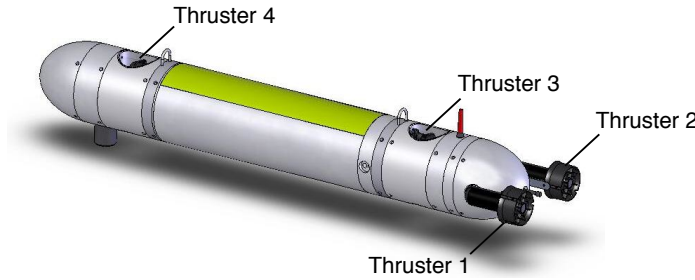


Figure 3.1: MARES thrusters configuration

hovering AUVs, that is, AUVs that are capable of controlling the vertical motion independently of the horizontal one.

The two vertical thrusters of MARES (see figure 3.1) make it possible to control heave independently of the surge motion. Beyond depth control, the pitch and yaw angles can also be controlled independently. Only few AUVs hold this capability. The Girona 500 (Ribas et al., 2012), the ODIN III (Zhao and Yuh, 2005; Choi et al., 2003) and the TriMARES (Cruz et al., 2011) are some examples of hovering AUVs. The restoring moments, which are a consequence of non-coincident center of gravity (CG) and center of buoyancy (CB), naturally stabilize MARES by *driving* the pitch and roll angles to zero, when it is properly trimmed. By actuating on the vertical thrusters, the vehicle can be controlled so that the pitch angle is different from its natural equilibrium point. Ultimately, the vehicle can even travel with composed motions with relatively large pitch angle while maintaining its depth constant. Such a feature is particularly appreciated in scenarios in which maneuverability or precise and even immobile positioning is required. Some examples can be found in intervention (Ribas et al., 2012), archaeology (Bingham, 2003) or inspection of underwater structures (Cruz et al., 2011) using AUVs.

The approach presented in this chapter takes advantage of the thruster configuration to control the vehicle in unusual modes of operation for most AUVs. Motivated by scenarios that demand for large vertical velocities and/or navigation in confined horizontal sections, a control law is developed to make the vehicle stabilize in the vertical pose, that is, with the nose pointing either downwards or upwards ($\theta = -\pi/2$ or $\theta = \pi/2$). Stability and convergence is achieved both when the vehicle is static or moving. In fact, the control law stabilizes the vehicle independently of the heave motion. Nonlinear control tools are used to derive an appropriate control law (refer to (Khalil, 2002) and (Slotine and Li, 1991) for a broad coverage on the subject) and base our analysis on the dynamics model of MARES.

Furthermore, the approach is extended to control the vehicle in the horizontal plane when it is pitching up or down. The periodic rotation of MARES along the x -axis is exploited to drive the vehicle to any desired position. In fact, the actuation of the stern thrusters creates a moment along the x -axis (often undesired in normal operation, see, for example, (Petrich and Stilwell, 2011)) that makes MARES roll. This effect is due to asymmetric stern propellers that, when actuating in

steady state, make the roll stabilize at an angle different from zero when it is in the horizontal pose (that is, pitch angle equal to zero). The stability is achieved because of a restoring moment induced by a non-null distance between the center of gravity and the center of buoyancy. However, such a moment along the x -axis no longer exists when the vehicle is in the vertical pose. Consequently, the roll dynamics model shows that the vehicle continuously rotates when subject to constant actuation on the stern thrusters.

By taking advantage of this behavior, it is possible to drive the vehicle to any horizontal point. A method similar to the one derived in Jouffroy et al. (2011) will be used in this approach. Originally used in the context of efficient motion of Lagrangian profilers using tidal currents and different depth layers, the method is extended to the motion of MARES when it takes a vertical pose. Roughly speaking, MARES activates its through-hull thrusters only when they are aligned with the general direction (sector-of-sight) of the desired horizontal position.

3.2 Reduced models

Consider the problem of stabilizing an AUV with four DOFs. Assume that the surge, heave, pitch and yaw DOFs are controlled and that sway and roll are constant and approximately null, that is, $v = 0$ and $\phi = p = 0$, respectively, using the same notation as in section 2.2, whose correspondence of angles will be modified later on for this chapter. This assumption is made because there is no actuation along these DOFs and possible deviations from zero are originated by cross-coupling effects, which are considered negligible in this chapter.

Based on the model (2.1)-(2.2), the kinematics and the dynamics expressions are simplified assuming that the drift vector is null $v_{ld} = 0$ and are respectively given by

$$\dot{\eta} = J(\eta)v, \quad (3.1)$$

$$\dot{v} = A(v)v + h(\eta) + T\tau_M. \quad (3.2)$$

Recall that $\eta \in \mathbb{R}^6$ is the pose vector, $v \in \mathbb{R}^6$ is the velocity vector, $J \in \mathbb{R}^{6 \times 6}$ is a matrix that maps the linear and angular velocities expressed in the body-fixed frame into the earth-fixed, inertial referential frame. The matrix $A(v) = M^{-1}(-C(v) - D(v)) \in \mathbb{R}^{6 \times 6}$ results from the hydrodynamic forces applied on the body of the vehicle when it is moving at a velocity v . The term $A(v)v$ compiles the effect of added mass, Coriolis, centripetal and viscous damping forces and moments. The vector $h(\eta) = M^{-1}g(\eta) \in \mathbb{R}^6$ includes the effects of the restoring forces and moments, while T maps the forces and moments exerted by the four thrusters, whose actuation forces are given in the vector $\tau_M \in \mathbb{R}^4$ and expressed in the body-fixed frame.

For the purpose of stabilizing MARES in the vertical pose, the order of the system is now reduced by projecting the pose and the velocities in a lower dimension subspace. The focus is on controlling the depth, and the pitch and yaw angles using the four controllable DOFs. Therefore,

define the reduced order system as follows:

$$\eta_z = P^{356} \eta, \quad (3.3)$$

$$v_l = P^{1356} v, \quad (3.4)$$

where

$$P^{356} = \begin{bmatrix} 0 & 0 & 1 & 0 & 0 & 0 \\ 0 & 0 & 0 & 0 & 1 & 0 \\ 0 & 0 & 0 & 0 & 0 & 1 \end{bmatrix},$$

$$P^{1356} = \begin{bmatrix} 1 & 0 & 0 & 0 & 0 & 0 \\ 0 & 0 & 1 & 0 & 0 & 0 \\ 0 & 0 & 0 & 0 & 1 & 0 \\ 0 & 0 & 0 & 0 & 0 & 1 \end{bmatrix}.$$

are projection matrices that capture the depth position, pitch and yaw angles and the surge, heave, pitch rate and yaw rate, respectively. This type of projection matrices will be further explored and generalized in chapter 5.

Recall that sway and roll rate are considered to be null. Therefore the velocity vector can be written as

$$v = \begin{bmatrix} u & 0 & w & 0 & q & r \end{bmatrix}^T.$$

Denote the Moore-Penrose inverse of a matrix as $(\cdot)^\dagger$ (Katayama, 2005). Then, by noting that $P^{1356\dagger} = P^{1356T}$, it is easy to prove that

$$P^{1356} B v = P^{1356} B P^{1356T} v,$$

for any matrix $B \in \mathbb{R}^{6 \times 6}$, and using (3.1)-(3.2) and (3.3)-(3.4) we can write the projected system as follows:

$$\dot{\eta}_z = \bar{J}(\eta) v_l(t), \quad (3.5)$$

$$\dot{v}_l = \bar{A}(v) v_l(t) + \bar{h}(\eta) + \bar{T} \tau_M, \quad (3.6)$$

where $\bar{J}(\eta) = P^{356} J(\eta) P^{1356\dagger}$, $\bar{A}(v) = P^{1356} A(v) P^{1356\dagger}$, $\bar{h}(\eta) = P^{1356} h(\eta)$ and $\bar{T} = P^{1356} T$. It should be stressed that this projection holds and this reduced model is valid only if the sway and the roll are assumed to be null. Although it is not the case in reality, these can be regarded as disturbances in this new model.

Rotation sequence

For this problem, the sequence of rotations ZYZ (also known as 323, see figure 3.2) is chosen. This composition of rotations is formed by a sequence of rotations along the z -, the y - and again

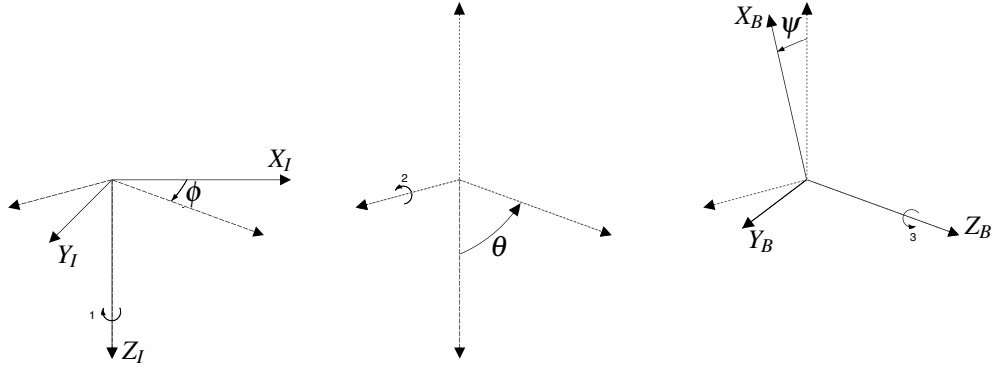


Figure 3.2: Sequence of rotations from the inertial frame $\{I\}$ to the body-fixed frame $\{B\}$. Sequence: roll \rightarrow pitch \rightarrow yaw ($\phi \rightarrow \theta \rightarrow \psi$)

the z -axes. The body-fixed referential frame is obtained by a sequence of three rotations of an inertial earth-fixed frame rotation: firstly, a rotation of an angle ϕ about the z -axis; secondly, a rotation of θ about the y -axis and; thirdly, a rotation of an angle ψ about the z -axis. Recall that the trigonometric functions are denoted $s \cdot = \sin(\cdot)$, $c \cdot = \cos(\cdot)$ and $t \cdot = \tan(\cdot)$. The J matrix results

$$J(\eta) = \begin{bmatrix} s\phi c\psi c\theta - s\phi s\psi & -c\psi s\phi - c\phi c\theta s\psi & c\phi s\theta & 0 & 0 & 0 \\ c\phi s\psi + c\psi c\theta s\phi & c\phi c\psi - s\psi c\theta s\phi & s\phi s\theta & 0 & 0 & 0 \\ -c\psi s\theta & -c\psi s\phi - c\phi c\theta s\psi & c\phi s\theta & 0 & 0 & 0 \\ 0 & 0 & 0 & c\psi/t\theta & -s\psi/t\theta & 1 \\ 0 & 0 & 0 & s\psi & c\psi & 0 \\ 0 & 0 & 0 & -c\psi/s\theta & s\psi/s\theta & 0 \end{bmatrix}.$$

Note that this representation is not unique. Other sequences of rotations can also be applied (Waldron and Schmiedeler, 2008). However, this one is considered the most appropriate in the context of this work, as it likely is the most intuitive sequence of rotation and consequently allows for a simple definition of the reference angles. This representation is used throughout the following developments in this chapter only.

3.3 Pose stabilization

The problem of stabilizing MARES at a general pose reference $\eta_z^*(t)$ is now addressed. At the end of this section, it will become clear that, when the vehicle is in a vertical pose, a velocity reference can be used to guide the vehicle horizontally.

3.3.1 Control law

Let $\eta_z^* : \mathbb{R} \rightarrow \mathbb{R}^3$ be a smooth desired pose vector of the vehicle and define the error vector as

$$\tilde{\eta}_z(t) = \eta_z(t) - \eta_z^*(t). \quad (3.7)$$

Similarly, let us define $v_l^* : \mathbb{R} \rightarrow \mathbb{R}^4$ to be a desired velocity reference. This vector is constrained to lie in a manifold that depends on the orientation of the vehicle as it will be seen later on. For now, assume that it does not influence the stability of the system and define the velocity error vector as follows:

$$\tilde{v}_l(t) = v_l(t) - v_l^*(t). \quad (3.8)$$

By noting that $\eta_z(t) = \tilde{\eta}_z(t) + \eta_z^*(t)$, $v_l(t) = \tilde{v}_l(t) + v_l^*(t)$ from (3.7) and (3.8), respectively, the system (3.5)-(3.6) can be rewritten as

$$\dot{\tilde{\eta}}_z(t) = \chi_1(\eta, t) + \bar{J}(\eta) \tilde{v}_l(t), \quad (3.9)$$

$$\dot{\tilde{v}}_l(t) = \chi_2(v, \eta, t) + \bar{T} \tau_M, \quad (3.10)$$

where

$$\begin{aligned} \chi_1(\eta, t) &= -\dot{\eta}_z^*(t) + \bar{J}(\eta) v_l^*(t), \\ \chi_2(v, \eta, t) &= \bar{A}(v) \tilde{v}_l(t) + \bar{A}(v) v_l^*(t) - \dot{v}_l^*(t) + \bar{h}(\eta). \end{aligned}$$

Based on the backstepping method (see section 2.3.3 or Khalil (2002)), consider the virtual control law $\alpha : \mathbb{R}^6 \times \mathbb{R} \rightarrow \mathbb{R}^3$, defined as

$$\alpha(\eta, t) = \bar{J}^\dagger(\eta) (-\chi_1(\eta, t) - K_\eta \tilde{\eta}_z(t)), \quad (3.11)$$

where $K_\eta \in \mathbb{R}^{3 \times 3}$ is a positive definite gain matrix. This control method is natural choice for the strict-feedback system (3.9)-(3.10) because it formally derives a control solution while it analytically ensures the stability of the controlled system. Let us include this virtual control input, by adding and subtracting it in (3.9) as follows:

$$\begin{aligned} \dot{\tilde{\eta}}_z(t) &= \chi_1(\eta, t) + \bar{J}(\eta) (\tilde{v}_l(t) + \alpha(\eta, t) - \alpha(\eta, t)) \\ &= -K_\eta \tilde{\eta}_z(t) + \bar{J}(\eta) (\tilde{v}_l(t) - \alpha(\eta, t)). \end{aligned}$$

The objective becomes now to drive $\dot{\tilde{\eta}}_z(t)$ to zero. In this sense, $\tilde{v}_l(t)$ has to be indirectly controlled so that $\tilde{\eta}_z(t) \bar{J}(\eta) z_2 < 0$, being $z_2 = \tilde{v}_l(t) - \alpha(\eta, t)$ a new error variable. Again, rewrite

the system (3.9)-(3.10) as

$$\dot{\tilde{\eta}}_z(t) = -K_\eta \tilde{\eta}_z(t) + \bar{J}(\eta) z_2, \quad (3.12)$$

$$\begin{aligned} \dot{z}_2 &= \dot{\tilde{v}}_l(t) - \dot{\alpha}(\eta, t) \\ &= \chi_2(v, \eta, t) - \dot{\alpha}(\eta, t) + \bar{T} \tau_M, \end{aligned} \quad (3.13)$$

and choose the control law

$$\tau_M = \bar{T}^{-1}(\chi_2(v, \eta, t) + \dot{\alpha}(\eta, t) - \bar{J}(\eta)^T \tilde{\eta}_z(t) - K_v z_2), \quad (3.14)$$

where $K_v \in \mathbb{R}^{4 \times 4}$ is a positive definite gain matrix. The choice of this control law makes the system (3.12)-(3.13) result into

$$\begin{aligned} \dot{\tilde{\eta}}_z(t) &= -K_\eta \tilde{\eta}_z(t) + \bar{J}(\eta) z_2, \\ \dot{z}_2 &= -\bar{J}(\eta)^T \tilde{\eta}_z(t) - K_v z_2. \end{aligned}$$

The subsequent proof of stability is based on the analysis of a Lyapunov function. For this purpose, define the Lyapunov function candidate

$$V = \frac{1}{2} \tilde{\eta}_z(t)^T \tilde{\eta}_z(t) + \frac{1}{2} z_2^T z_2, \quad (3.15)$$

whose time derivative results

$$\begin{aligned} \dot{V} &= \tilde{\eta}_z(t)^T \dot{\tilde{\eta}}_z(t) + z_2^T \dot{z}_2 \\ &= \tilde{\eta}_z(t)^T K_\eta \tilde{\eta}_z(t) + \tilde{\eta}_z(t)^T \bar{J}(\eta) z_2 - z_2^T \bar{J}(\eta)^T \tilde{\eta}_z(t) - z_2^T K_v z_2 \\ &= -\tilde{\eta}_z(t)^T K_\eta \tilde{\eta}_z(t) - z_2^T K_v z_2 \\ &< 0, \forall \tilde{\eta}_z(t) \neq 0, z_2 \neq 0. \end{aligned} \quad (3.16)$$

The negative definiteness and the form of the time derivative of the Lyapunov function ensures that the system is uniformly exponentially stable (Khalil, 2002).

The dynamics was projected to a four-dimension space in (3.6) with the intention of handling the *free* DOF, heave, when the vehicle is in the vertical pose. The desired velocity $v_l^*(t)$ was assumed not to disturb the stability of the pose. Indeed, this velocity reference can not collide with the control objective for the pose, otherwise the exponential tracking of the pose reference is not guaranteed. The following development gives a necessary condition to ensure the pose tracking exponential stability.

3.3.2 Constraint on the desired velocity

The influence of the DOFs in the pose of the vehicle is illustrated hereafter by expanding their relationship. The necessary condition will then be derived to ensure appropriate performances of the pose tracking control.

First, notice that

$$\begin{aligned} P^{356} &= \begin{bmatrix} P^3 & 0_{1 \times 3} \\ 0_{2 \times 3} & P^{56} \end{bmatrix} \quad \text{and} \quad P^{356\dagger} = P^{356T} = \begin{bmatrix} P^{3T} & 0_{3 \times 2} \\ 0_{3 \times 1} & P^{56T} \end{bmatrix}, \\ P^{1356} &= \begin{bmatrix} P^{13} & 0_{2 \times 3} \\ 0_{2 \times 3} & P^{56} \end{bmatrix} \quad \text{and} \quad P^{1356\dagger} = P^{1356T} = \begin{bmatrix} P^{13T} & 0_{3 \times 2} \\ 0_{3 \times 2} & P^{56T} \end{bmatrix}, \end{aligned}$$

where

$$P^3 = \begin{bmatrix} 0 & 0 & 1 \end{bmatrix}, \quad P^{13} = \begin{bmatrix} 1 & 0 & 0 \\ 0 & 0 & 1 \end{bmatrix}, \quad P^{56} = \begin{bmatrix} 0 & 1 & 0 \\ 0 & 0 & 1 \end{bmatrix}.$$

Moreover, from section 2.2, it was seen that the matrix $J(\eta)$ can be written in the block diagonal form:

$$J(\eta) = \begin{bmatrix} J_l(\eta) & 0_{3 \times 3} \\ 0_{3 \times 3} & J_a(\eta) \end{bmatrix}. \quad (3.17)$$

Defining $\eta_z = [\eta_{z1} \ \eta_{z2}]^T = \bar{J}(\eta)v_l$, with $v_l = P^{1356}v$ and $\eta_{z1} = z$, $\eta_{z2} = [\theta \ \psi]^T$, yields

$$\begin{aligned} \begin{bmatrix} \dot{\eta}_{z1} \\ \dot{\eta}_{z2} \end{bmatrix} &= P^{356}J(\eta)P^{1356\dagger}v_l \\ &= \begin{bmatrix} P^3 & 0_{1 \times 2} \\ 0_{2 \times 1} & P^{56} \end{bmatrix} \begin{bmatrix} J_1(\eta) & 0_{3 \times 3} \\ 0_{3 \times 3} & J_2(\eta) \end{bmatrix} \begin{bmatrix} P^{13T} & 0_{3 \times 2} \\ 0_{3 \times 2} & P^{56T} \end{bmatrix} \begin{bmatrix} v_{l1} \\ v_{l2} \end{bmatrix} \\ &= \begin{bmatrix} P^3 J_1(\eta) P^{13T} & 0_{1 \times 2} \\ 0_{2 \times 2} & P^{56} J_2(\eta) P^{56T} \end{bmatrix} \begin{bmatrix} v_{l1} \\ v_{l2} \end{bmatrix} \\ &= \begin{bmatrix} -c\psi s\theta & c\theta & 0 & 0 \\ 0 & 0 & c\psi & 0 \\ 0 & 0 & s\psi/s\theta & 0 \end{bmatrix} \begin{bmatrix} u \\ w \\ q \\ r \end{bmatrix}, \end{aligned} \quad (3.18)$$

where $v_{l1} = [u \ w]^T$ and $v_{l2} = [q \ r]^T$ are the vectors of linear and angular velocities, respectively.

It is now possible to see that for the vehicle pitching up or down ($\theta = \pm\pi/2$), the heave velocity, w , has no influence on the vertical pose and can therefore be handled independently of the remaining DOFs. This simple example serve as a basis for the following developments in this section.

As it is desired that $v_l^*(t)$ has no influence in the vertical pose stabilization, the following expression must hold:

$$\bar{J}(\eta)v_l^*(t) = \mathbf{0}, \quad \forall \eta(t). \quad (3.19)$$

Since $\bar{J}(\eta)$ is the transformation matrix *projected* in the new “vertical pose subspace”, this expression means that the reference velocity does not impact on this subspace.

In the next section, special focus is given to setting the linear velocity reference in order to control the horizontal motion. Obviously, the angular velocity references must remain unchanged in order not to disturb the orientation stability. Define $\mathbf{v}_{l1}^*(t) = [u^*(t) \ w^*(t)]^T$ and $\mathbf{v}_{l2}^*(t) = [q^*(t) \ r^*(t)]^T$ ($\mathbf{v}_l^*(t) = [\mathbf{v}_{l1}^*(t) \ \mathbf{v}_{l2}^*(t)]^T$) and let us focus on the linear velocity dynamics.

By combining (3.18) and (3.19), the linear velocity sub-vector of the equation above becomes

$$P^3 J_1(\eta) P^{13T} \mathbf{v}_{l1}^*(t)^T = \begin{bmatrix} -c\psi s\theta & c\theta \end{bmatrix} \begin{bmatrix} u^*(t) \\ w^*(t) \end{bmatrix} = 0. \quad (3.20)$$

In order to satisfy this equality, it must be verified that

$$u^*(t) = \frac{w^*(t)}{\tan\theta c\psi}, \quad (3.21)$$

to ensure the stability of the control law in (3.14).

3.4 Horizontal guidance

So far in this section, it has been assumed that \bar{T} has full rank. From a practical point of view, this means that the considered DOFs (surge, heave, pitch and yaw) are controllable. Now, let us extend the study to the roll dynamics and on how this can be used to guide MARES in the horizontal plane.

3.4.1 Roll dynamics

The rotation of propellers induce a torque when generating the desired lift (Petrich and Stilwell, 2011). This is a natural consequence coming from the fact that the blades are inclined with regard to the plane that is perpendicular to the thruster axis of rotation. A practical way to cancel such a moment is to use symmetric inclinations of blades, for symmetrically located thrusters with respect to the CG. In this case, for the same force, the propellers rotate in opposite directions, thus cancelling each other torques. However, here it is assumed that the inclinations of the stern thrusters are the same, thus inducing a moment on the x -axis.

In previous works (see, for example Ferreira et al. (2010, 2012)), this effect was neglected as its influence is residual when compared to the moment created by non-coincident vertical position of the CB and the CG. Nevertheless, this restoring moment no longer exists when the vehicle is pitching up or down ($\pm\pi/2$) and the moment induced by the stern thrusters does influence the roll dynamics and can not be neglected. Actually, its presence is used here to drive the vehicle to a horizontal position.

Mathematically, the roll dynamics can be written as a scalar differential equation (see appendix C), where the effect of the moment originated by the stern thrusters is added:

$$\dot{p} = f_p(\mathbf{v}) - d_p(p)p - g_p(\eta) + (f_\tau(\tau_s))^T \tau_s, \quad (3.22)$$

where $f_p : \mathbb{R}^6 \rightarrow \mathbb{R}$ is a function containing the added mass, Coriolis, centripetal and cross-related viscous damping effects. The scalar function $d_p : \mathbb{R} \rightarrow \mathbb{R}$ represents the direct viscous damping effect, while $g_p : \mathbb{R}^6 \rightarrow \mathbb{R}$ is the restoring moment in roll. It is assumed that there exists a positive definite function $f_\tau : \mathbb{R}^2 \rightarrow \mathbb{R}^2$ that relates the moment generated by the thruster with the actual lift force of the stern thrusters that compose the entries of the vector $\tau_s \in \mathbb{R}^2$. Note that the function $g_p(\eta)$ is positive definite for all non-null p and verifies $d_p(p) = 0$ if and only if $p = 0$. It is assumed that $f_\tau(\tau_s) = \mathbf{0}$ if and only if $\tau_s = \mathbf{0}$. These facts are used in the forthcoming analysis.

At equilibrium (see section 3.3) with $\theta = \pm\pi/2$, it is possible to prove that $f_p(v) \approx 0$ and $g_p(\eta) = 0$ for the case of MARES. Hence the roll dynamics results

$$\dot{p} \approx -d_p(p)p + (f_\tau(\tau_s))^T \tau_s, \quad (3.23)$$

which, for a constant τ_s , gives $d_p(p)p \approx (f_\tau(\tau_s))^T \tau_s$ in steady state. This means that the roll angular velocity is different from zero in steady state, when $\theta = \pm\pi/2$.

This result is particularly interesting since a constant actuation on the stern thrusters implies that the vehicle will keep rotating along the x -axis. Note that, under a given condition, it is not necessary the vehicle to be moving to have a constant actuation on the stern thrusters. Indeed, a positive (or negative) buoyancy would make the vehicle actuate on the stern thrusters to maintain the depth constant.

3.4.2 Guidance

The problem of guiding the vehicle to a given desired static position in the horizontal plane is now addressed. For the purpose, define the horizontal position of MARES $\eta_h(t) = [x \ y]^T$ and $\eta_h^*(t) = [x^* \ y^*]^T$ to be a constant horizontal position reference. The error vector is defined as

$$\tilde{\eta}_h = \begin{bmatrix} \tilde{x}(t) \\ \tilde{y}(t) \end{bmatrix} = \eta_h(t) - \eta_h^*(t). \quad (3.24)$$

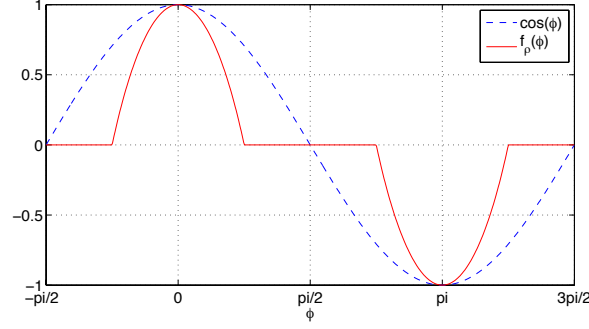
The guidance objective is to drive the error vector to zero.

For convenience, let us make a change of coordinates to the polar coordinate system and write the equivalent equation in (3.24) as

$$\begin{aligned} \rho(t) &= \|\tilde{\eta}_h\| \\ \gamma(t) &= \angle(\tilde{\eta}_h) = \text{atan2}(\tilde{y}(t), \tilde{x}(t)), \end{aligned} \quad (3.25)$$

where $\angle(\tilde{\eta}_h)$ is the angle of the vector $\tilde{\eta}_h$ with respect to the x -axis, given in the reference frame. The function $\text{atan2}(\cdot, \cdot)$, whose counter-domain is the interval $]-\pi, \pi]$, stands for the variant of the arctangent function $\text{atan}(\cdot)$. The guidance objective now becomes driving the distance from the reference $\rho(t)$ to zero.

With the vehicle in the vertical pose, the orientation of the body-fixed z -axis expressed in the horizontal plane of the inertial reference frame is given by $\phi(t)$. In order to find suitable guidance

Figure 3.3: The function $f_\rho(\tilde{\phi}(t))$

law, differentiate the system (3.25) with respect to time:

$$\begin{aligned}\dot{\rho}(t) &= \frac{\dot{\tilde{\eta}}_h(t)^T \tilde{\eta}_h}{\rho(t)} \\ \dot{\gamma}(t) &= \frac{d}{dt} \text{atan2}(\tilde{y}(t), \tilde{x}(t)),\end{aligned}$$

which, after algebraic manipulation, results

$$\begin{aligned}\dot{\rho}(t) &= w(t) \cos(\tilde{\phi}(t)) \\ \dot{\gamma}(t) &= \frac{1}{\rho(t)} (w(t) \sin(\tilde{\phi}(t))),\end{aligned}\tag{3.26}$$

where $\tilde{\phi}(t) = \gamma(t) - \phi(t)$ and recall that w is the heave velocity, which can be handled “independently” of the remaining DOFs when the vehicle pose verifies $\theta = \pm\pi/2$. A suitable guidance law has to be found to drive the vehicle towards its reference point by using $w(t)$ as the input. Implicitly, the derivation of the control law in section 3.3, suggests that the heave velocity reference $w^*(t)$ must be differentiable. Hence, the following guidance law is proposed:

$$w^*(t) = -\text{sat}(\rho(t), \beta) \cdot f_\rho(\tilde{\phi}(t)),\tag{3.27}$$

where $\beta > 0$ and $\text{sat}(\cdot, \cdot)$ being the saturation function defined as

$$\text{sat}(\rho(t), \beta) = \begin{cases} \rho(t), & \text{if } |\rho(t)| \leq \beta \\ \beta \frac{\rho(t)}{\|\rho(t)\|}, & \text{otherwise} \end{cases}.$$

The continuous function $f_\rho(\tilde{\phi}(t))$ (illustrated in figure 3.3), reminiscent of the sector-of-sight, is given by

$$f_\rho(\tilde{\phi}(t)) = \begin{cases} \frac{\cos(2\tilde{\phi}(t))}{\cos(\tilde{\phi}(t))}, & \text{if } \cos(2\tilde{\phi}(t)) > 0 \\ 0, & \text{otherwise} \end{cases}.\tag{3.28}$$

Hence, when $w(t) = w^*(t)$, the time derivative of the distance to the desired position is given

by

$$\dot{\rho}(t) = \begin{cases} -\text{sat}(\rho(t), \beta) \cos(2\tilde{\phi}(t)), & \text{if } \cos(2\tilde{\phi}(t)) > 0 \\ 0, & \text{otherwise} \end{cases} \quad (3.29)$$

Note that $\dot{\rho}(t)$ is negative semi-definite and negative definite under the condition $\cos(2\tilde{\phi}(t)) > 0$. Since, it was assumed that $\phi(t)$ is periodical, one has only need to ensure that the difference $\tilde{\phi}(t) = \gamma(t) - \phi(t)$ does not verify $\cos(2\tilde{\phi}(t)) < 0$ for all time. By contradiction, suppose that this condition is verified. From (3.27), $w(t) = 0$ (see (3.28)) and hence, from (3.26) it is possible to conclude that $\dot{\gamma}(t) = 0$. Therefore, it is straightforward to see that the difference $\tilde{\phi}(t)$ changes over time if the inequality $\cos(2\tilde{\phi}(t)) < 0$ holds, since $\phi(t)$ is periodical. Thus, it is possible to conclude that the position error vector $\tilde{\eta}_h$ converges to zero.

Remark 3.1. *The choice of the function $f_\rho(\tilde{\phi}(t))$ is not restricted to the one presented here. In fact, the function must only be differentiable and verify two conditions: 1) $f_\rho(\tilde{\phi}(t)) = 0$ if $\tilde{\phi}(t) = \pm\pi/2$ and; 2) $f_\rho(\tilde{\phi}(t)) \cos(\tilde{\phi}(t)) \geq 0$ for all $\tilde{\phi}(t) \neq \pm\pi/2$ and verify $f_\rho(\tilde{\phi}(t)) \cos(\tilde{\phi}(t)) > 0$ in a non-empty interval $\Omega \subset [-\pi, \pi] \setminus \{\pm\pi/2\}$*

Remark 3.2. *In the guidance law (3.27), the saturation function has been introduced for practical reasons as any real actuator have a limited force, which consequently limits the heave velocity. The constant β plays the role of an upper bound on the absolute value of the heave velocity w .*

3.5 Results

To illustrate and validate the approach to stabilize MARES in the vertical pose and guide it to an horizontal position, hereinafter the results of simulations and experiments are presented. The first ones show the simulation of a six DOFs model of MARES (see appendix C) stabilized in the vertical pose and horizontally guided to a reference point. Afterwards, experimental results collected from tests in a tank validate the control law derived earlier.

3.5.1 Simulation

In order to assess the performances and the behavior of the system using the derived controllers, a simulation of the vehicle was ran prior to real experiments. For this purpose, the gain matrices were set such that $K_\eta = \text{diag}([1, 1, 1])$, $K_v = \text{diag}([1, 10, 1, 1])$, where $\text{diag}(\cdot)$ denotes a diagonal matrix whose diagonal entries are the ordered entries of its argument. Figure 3.4 shows the evolution of the pitch (θ) and yaw (ψ) angles for a desired pose defined by the vector $\eta_z^*(t) = [4 \ \pi/2 \ 0]^T$. The depth is shown in figure 3.5. The initial conditions were set to $\eta(0) = [0 \ 0 \ 3 \ 0 \ 0 \ 0]^T$ and $v(0) = \mathbf{0}$.

Figures 3.4-3.5 show that the control law in (3.14) stabilizes MARES in the vertical pose in less than ten seconds. Note that the pitch angle starts decreasing to negative values and posteriorly starts increasing to the assigned reference. This is the result of a relatively large gain for the depth. The control law makes the heave velocity be large during the first instants thus influencing the pitch dynamics. Although not included, simulation results using smaller values for the gain

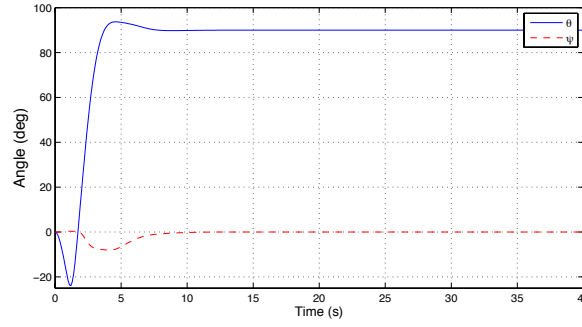


Figure 3.4: Simulation results: pitch and yaw angles

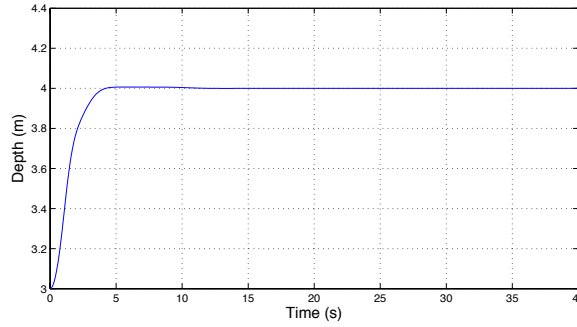


Figure 3.5: Simulation results: depth

corresponding to the depth error show that the initial deviation of θ becomes smaller during the initial instants. The same can be verified with larger gains for pitch.

Figure 3.6 shows the trajectory of the vehicle for the application of the guidance law derived in the section 3.4.2. The desired horizontal position was set to $\eta_h^*(t) = [10 \ 10]^T$. The initial conditions remained the same as the ones above. The simulation shows successful tracking of the target.

3.5.2 Experiments

In order to test the approach, the control algorithm was implemented in the MARES AUV and tests have been carried out in a tank. The current control software interprets and sequentially executes mission scripts where maneuvers and parameters (desired depth, angles, duration, etc.) are defined. The controller has been implemented in the computer aboard MARES. Although MARES may include a large set of sensors, for the purpose of this implementation only depth and IMU sensors have been used to measure relevant data to control MARES in the vertical pose. From the IMU, angles and angular rates have been read and directly used to feedback the controller. In practice, the expected angle errors are below few degrees (typically less than 4 degrees). Depth measurements are fairly precise with errors in the order of few millimeters.

The gain matrices used in the control law (3.14) were set to $K_\eta = \text{diag}([2 \ 0.7 \ 1])$ and $K_v = \text{diag}([0.01 \ 0.01 \ 1 \ 1])$. In order to make the mission more challenging than in the simulation, a time varying reference for both pitch and depth was provided to the controller. The mission

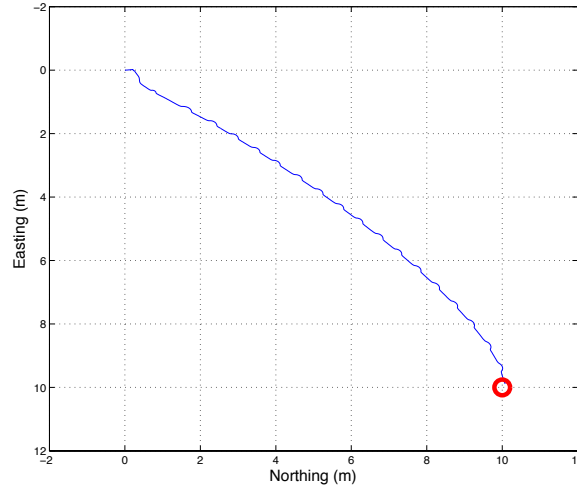


Figure 3.6: Simulation results: horizontal position evolution

script included a sequence of three maneuvers that are completely defined by the desired pose and the time they should be executed: 1) $\eta_z^* = [z^* \ \theta^* \ \psi^*] = [1 \ \pi/2 \ 0]$ during the first 30 seconds; 2) $\eta_z^* = [2.5 \ \pi/2 \ 0]$ for the subsequent 60 seconds and; 3) $\eta_z^* = [2.5 \ -\pi/2 \ 0]$ for the final 60 seconds. In order to ensure that there is no abrupt variations in the pose references, their values were smoothed by bounding their change rate.

The results of the mission are shown in figures 3.8-3.10. Figure 3.8 shows the pitch and the yaw angles, figure 3.9 presents the evolution of the roll angle and figure 3.10 shows the depth over time. Despite the natural disturbances, in general, the control law ensures stability of MARES with satisfactory performances.

It can be noticed that the pitch angle suffers from a relatively large oscillation before stabilizing around $\theta^* = \pi/2$. This is due to the restoring moment that made MARES rapidly rotate around the body-fixed x -axis when pitch was greater than $\pi/2$. The fast evolution of the roll angle can be verified in figure 3.9 for the corresponding interval. The discontinuity at time $t \approx 100$ s on θ and ψ is caused by the singularity at $\theta = 0$ (see section 3.2). The small deviation of θ (typically less than three degrees) is mainly induced by mismatches on the mathematical model of MARES used in the control law. Later, in chapter 5, an analysis on the effects of the model mismatches in the control performances will be given. On the contrary, the oscillation in ψ was likely caused by a small offset in the corresponding measurements also inducing roll oscillation. Notice that the pitch rotation from $\theta = \pi/2$ to $\theta = -\pi/2$ impacts on the depth for the corresponding interval. The cause for this comes from the hydrodynamic coupling of pitch and heave, from the uncertainties in the hydrodynamic model and on the thrusters model as well as non-instantaneous thrust command execution (in opposition to what it is assumed), which are particularly noticeable during transient. Nevertheless, the depth stabilizes afterwards. It is expectable that slower pitch variations contribute less for depth deviations. Similarly, a larger depth-related gain would make the depth control more accurate.

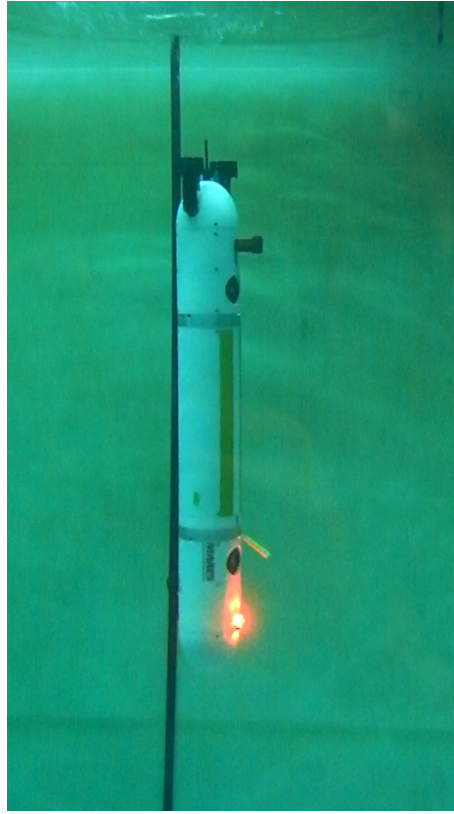


Figure 3.7: MARES in vertical pose

As expected, a positive trend on ϕ (roll angle) is visible when the vehicle stabilizes at $\theta = \pm\pi/2$. Recall from section 3.4.1, that the actuation on the stern thrusters makes the vehicle rotate about the x -axis. Indeed, the stabilization of the depth implies non-null actuation since the slightly positive buoyancy of MARES creates a force that leads it to the surface. The oscillation of the roll angle is caused by the moment about the x -axis created by a non-null yaw.

3.6 Conclusions

A control example application has been considered to stabilize MARES in the vertical pose. Based on the nonlinear control theory, and more specifically on backstepping, a control law that ensures exponential stability for the vertical pose has been derived. In order to explore the capabilities of MARES, a guidance law that enables the vehicle to reach any horizontal reference by using a sector-of-sight-like controller has been designed. Both guidance and control law convergence to the desired pose were verified. The approach shows to be effective and both simulations and experiments have validated the approach, originating very encouraging results. Although the derivation was based on this specific vehicle, this approach can be easily extended to other hovering AUVs.

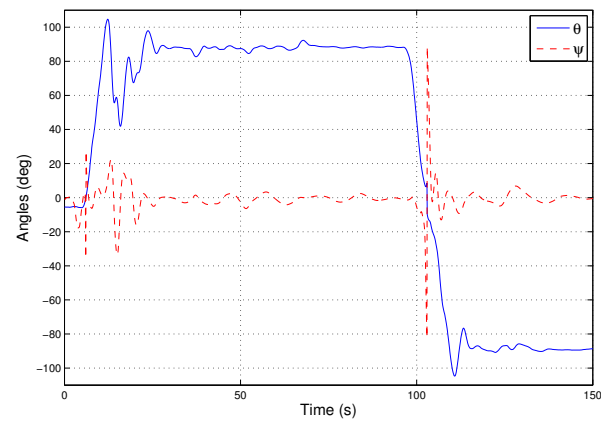


Figure 3.8: Experimental results: pitch and yaw angles

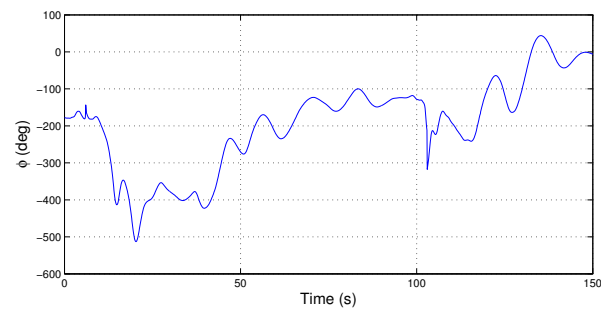


Figure 3.9: Experimental results: roll angle

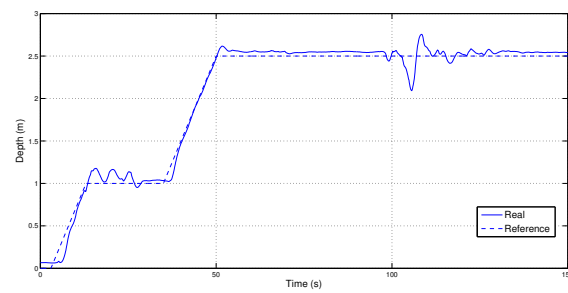


Figure 3.10: Experimental results: depth

Chapter 4

Homing using range-only measurements

Coordination of robots is a broad area that ranges from simple tasks such as keeping within a given relative range to more complex coordination tasks such as robotic soccer. It is important to clarify what *coordination* is. According to (Oxford Dictionaries), *coordination* stands for

“the organization of the different elements of a complex body or activity so as to enable them to work together effectively”.

In this chapter, a basic coordination scheme is presented to *home* a robot, that is guiding a robot to a reference point. This reference point can be either static or dynamic, thus enabling coordinated motion of two robots in which the reference robots interacts with the homing robot via sensing. Only range measurements are used to drive the homing robot towards the reference point. Two approaches are presented: the first one relies on estimation to infer the position of the homing robot with regard to the reference; the second approach employs a sensor-based controller to generate a heading rate reference. In both methods, the guidance problem is tackled at the kinematic level by assuming that the velocities can be controlled directly.

The next sections are organized as follows: after a brief introduction on the homing subject, a reduced dynamic and kinematic models for the horizontal plane are given in section 4.2. Then, based on the estimation tools background given in section 2.4, section 4.3 derives a position estimator and a guidance law that utilizes the estimated position to set the vehicle heading, while the section 4.4 presents a guidance law to drive the vehicle to the vicinity of the beacon based on range measurements provided by a sensor.

4.1 Motivation and related works

Along with the advances in sensing, several techniques for navigation have been developed for AUVs. The navigation using only DVL, IMU and a compass constitutes a suitable solution even though the error grows with time due to the inherent drifts of the first two sensors and due to

possible angular errors for the last one. The use of effective equipment in large scale, or long time, operations makes it possible to achieve drift errors below 10 meters per hour (Eustice et al., 2007). Similarly, feature based navigation using acoustic imaging from sidescan sonars or multi-beam echosounder has attracted the attention of several research groups (see Barkby et al. (2011) for a SLAM application, for instance) thus leading AUVs toward the concept of standalone platform. The use of acoustic beacons is compatible with those techniques but may be unavailable for some scenarios such as large scale operation, deep waters (Hegrenaes et al., 2009) or under-ice (Ferguson, 2009) navigation.

Common to most operations underwater is the recovery of AUVs. One may imagine several scenarios where there is a low confidence on the position estimate and safe recovery close to a beacon is required. At the end of a mission, the vehicle may not have a sufficiently accurate position estimate and the recovery point may be placed anywhere. Still, if ranges to the recovery reference point are measurable, then the homing procedure is feasible by adopting a suitable method.

Homing of AUVs requires a method that robustly drives the robot to an assigned position. This is a simple task when both home and vehicle positions are perfectly known by this latter but becomes a challenging problem when such information is not available. The problem is even more complex when only ranges to home are measured and disturbances affect the vehicle trajectory or the home position. Therefore, a complete method that considers the undesired - and often neglected - external effects is needed to robustly home an AUV.

In underwater robotics, absolute and relative localization and positioning of autonomous vehicles are mainly constrained by the intrinsic strong attenuation of electromagnetic waves and by the poor visibility conditions found in the environment. Thus, the research efforts completed by several researchers over the last decades (see (Cruz et al., 2001; Stojanovic et al., 2002; Eustice et al., 2011; Vaganay et al., 2004), just to cite a few) has led to a common solution that explores the trilateration concept for bounded error navigation. The method is based on ranges, indirectly obtained from times-of-flight (TOFs) of acoustic waves between two or more coordinated entities (for example, an AUV and a navigation beacon). Such systems employ a minimum set containing one (Ferreira et al., 2010a) to three acoustic beacons carefully placed in the operation area (Bingham, 2003). The number of deployed beacons can be greater in cases that require more precise navigation.

Vision-based homing has been widely implemented in ground and aerial robotics (e.g. Argyros et al. (2005)) and its concepts have been translated to underwater robotics in some works such as Negre et al. (2008). Although this approach is interesting for accurate positioning and docking in particular, it constraints the vehicle to be relatively close the target (typically below a few meters) to be able to home. An alternative homing method was proposed by Feezor et al. (2001) using electromagnetic waves emitted and received by means of large coils placed in both the docking station and the AUV. The overall system makes it possible to compute bearing to the dock at distances up to 35m in sea water. Bearing was also employed by Singh et al. (2001) using an USBL sensor carried on the vehicle. The control law derived just has to ensure that the bearing angle is null along the trajectory to home. However, it is well known that, in USBL systems, the

angle resolution decreases with the distance and the sensor may not be omnidirectional, thus being possible to measure angles and ranges only when the beacon is located at a given angular position, with regard to the USBL sensor. Recently, Batista et al. (2010) presented a method which only takes into account raw measurements obtained from an USBL system for deriving a control law to home the vehicle. In Bezruchko et al. (2011), an extremum-seeking algorithm was introduced to find the maximum approach rate to the beacon. Nevertheless, the method requires initialization otherwise the AUV may be driven to a stable equilibrium point in the opposite direction of the beacon. A priori information on the area is used by Jantapremjit and Wilson (2007) to generate an artificial potential field combined with a sliding mode control law to home an AUV to its docking station.

In the context of range-only-based homing, Vaganay et al. (2000) and Baccou and Jouvencel (2002, 2003) have proposed a method that exploits an EKF for vehicle localization using range measurements only, where kinematic variables are taken into consideration along with the water current velocity components and a possible speed bias. The use of EKF requires an initialization procedure to ensure fast convergence of the estimate. To overcome this problem, Baccou and Jouvencel (2002, 2003) have adopted a nonlinear least mean squares method that is composed of a two step procedure which first does not consider currents and secondly improves the complete state estimate with the remaining current components, while relying on kinematic and dynamic models. A similar approach was presented by Casey et al. (2007). The localization problem is also addressed by Newman and Leonard (2003) for relative navigation. A sequence of non-collinear positions and respective ranges relative to a beacon are assumed to be known in order to estimate the position of the latter using nonlinear least mean squares recursively. Additionally, Jouffroy and Reger (2006) presented an algebraic solution for determining the position an AUV that measures course, velocity over the ground and ranges to a beacon. Along with the algebraic solution, a filtering method is employed to smooth the output. Furthermore, the work theoretically supports some intuitive facts on observability, namely: the system is not locally observable when the vehicle is stopped, that is, when the velocity over the ground is zero, and when the course has the same or the opposite direction of that of the vector that joins the beacon and the vehicle.

4.2 Reduced models and cylindrical coordinates

Throughout this section, some assumptions will be made in order to simplify the development of the methods presented. These simplifications can be performed as long as it is assumed that certain state variables remain stable. Thus, let us consider the reduced bi-dimensional model of a vehicle with *horizontal pose* vector $\eta_h = [x \ y \ \psi]^T$ and linear and angular velocities $v_h = [u \ v \ r]^T$, expressed in the body frame. The pitch θ and the roll ϕ angles have been neglected and are assumed to be null. Additionally, it is also assumed that the heave motion, w , is null and that the depth is kept constant. The kinematics and dynamics equations are respectively given, by simple derivation

from (2.1) and (2.2), by

$$\dot{\eta}_h = J_h(\eta_h)v_h + v_{c_h} \quad (4.1)$$

$$\dot{v}_h = A_h(v_h)v_h + h(\eta_h) + T\tau_h, \quad (4.2)$$

where the matrices and vectors result from the reduced order model for the horizontal pose derived similarly to method presented in section 3.2. This simplification results after order reduction by suppressing the cross-related terms of the unconsidered DOFs. The simplification is made assuming that the remaining DOFs are stable and that their influences are negligible. Since this chapter essentially focuses on guidance, no emphasis on the reduced dynamics model will be given. Suppose only that any sufficiently smooth velocity reference can be tracked by means of an inner-loop controller.

Let us now focus on kinematics. Expand (4.1) in the form:

$$\begin{bmatrix} \dot{x} \\ \dot{y} \\ \dot{\psi} \end{bmatrix} = \begin{bmatrix} \cos(\psi) & -\sin(\psi) & 0 \\ \sin(\psi) & \cos(\psi) & 0 \\ 0 & 0 & 1 \end{bmatrix} \begin{bmatrix} u \\ v \\ r \end{bmatrix} + \begin{bmatrix} v_x \\ v_y \\ 0 \end{bmatrix}, \quad (4.3)$$

where it has been assumed that the external disturbances, such as currents, do not influence the angular dynamics.

As the intention is to home the robot to an unknown position from which it is able to range, let us consider the cylindrical coordinates and denote the range and the angle between the beacon and the robot, respectively, as

$$\begin{aligned} \rho &= \rho(x, y) = \sqrt{x^2 + y^2}, \\ \psi_p &= \angle(x, y). \end{aligned} \quad (4.4)$$

Their time derivatives are given by

$$\begin{aligned} \dot{\rho} &= u \cos(\psi - \psi_p) - v \sin(\psi - \psi_p) + v_x \cos \psi_p + v_y \sin \psi_p, \\ \dot{\psi}_p &= \frac{1}{\rho} (u \sin(\psi - \psi_p) - v_x \sin \psi_p + v_y \cos \psi_p). \end{aligned} \quad (4.5)$$

Based on this model, a homing method using estimators is presented in the next section.

4.3 Homing using an estimation based approach

In this section, the homing problem is solved by means of localization using estimators. KFs and PFs seem to be promising approaches for this scenario. In order to verify their performances and compare the two methods, both were developed. Their formulations are shown in the following subsections. Initialization and guidance are addressed afterwards.

4.3.1 Estimating the position: extended Kalman filter

The KF is an optimal estimator for linear systems subjected to white noise in measurements and state. Its performance in the nonlinear case degrades and the filter becomes suboptimal (Gelb, 1999). However, it has been implemented in several works (see (Newman and Leonard, 2003; Olson et al., 2004; Baccou and Jouvencel, 2002), for example) with satisfactory results even in the presence of non-Gaussian, non-null mean noise. The first approach presented here contemplates an EKF to estimate the horizontal position $\eta_h = [x y]^T$ and the water current velocities $v_{lh} = [v_x v_y]^T$.

The range measurement at time t_k is given by

$$h(t_k) = h_k = \rho(\eta_h(t_k)) + l_k, \quad (4.6)$$

where $l_k \in \mathbb{R} \sim \mathcal{N}(0, R_m)$ is a noise variable assumed to follow a normal distribution with variance $R_m \in \mathbb{R}$.

Define the state vector as $X = [\eta_h^T v_{lh}^T]^T = [x y v_x v_y]^T$, with the corresponding estimate $\hat{X} = [\hat{x} \hat{y} \hat{v}_x \hat{v}_y]^T$ and, from (4.1), it is possible to write (Casey et al., 2007):

$$\begin{bmatrix} \dot{x} \\ \dot{y} \\ \dot{v}_x \\ \dot{v}_y \end{bmatrix} = \begin{bmatrix} 0 & 0 & 1 & 0 \\ 0 & 0 & 0 & 1 \\ 0 & 0 & 0 & 0 \\ 0 & 0 & 0 & 0 \end{bmatrix} \begin{bmatrix} x \\ y \\ v_x \\ v_y \end{bmatrix} + \begin{bmatrix} \cos(\psi) & -\sin(\psi) \\ \sin(\psi) & \cos(\psi) \\ 0 & 0 \\ 0 & 0 \end{bmatrix} \begin{bmatrix} u \\ v \end{bmatrix} + w \quad (4.7)$$

where $w \in \mathbb{R}^4 \sim \mathcal{N}(0, Q)$ is the process noise vector, which is assumed to follow a Gaussian distribution with zero mean and variance $Q \in \mathbb{R}^{4 \times 4}$.

The formulation of the EKF follows from section 2.4.1. Whenever a new measurement h_k is available, the state estimate update is given by

$$\hat{X}_{k|k} = \hat{X}_{k|k-1} + K_k [h_k - \rho(\hat{x}_{k|k-1}, \hat{y}_{k|k-1})]$$

where K_k is the so-called Kalman gain at instant t_k which is obtained through the following expression:

$$K_k = P_{k|k-1} H_k^T (H_k P_{k|k-1} H_k^T + R_k)^{-1},$$

where H_k is the Jacobian of $\rho(\cdot)$ evaluated at $[\hat{x}, \hat{y}]$. The matrix P is the estimation error covariance, which is updated at each new range measurement through

$$P_{k|k} = (I - K_k H_k) P_{k|k-1}.$$

The last equations standing for the update step. The prediction step is easily obtained from (4.7)

as

$$\begin{bmatrix} \hat{x}_{k|k-1} \\ \hat{y}_{k|k-1} \\ \hat{v}_{x_{k|k-1}} \\ \hat{v}_{y_{k|k-1}} \end{bmatrix} = \begin{bmatrix} \hat{x}_{k-1|k-1} \\ \hat{y}_{k-1|k-1} \\ \hat{v}_{x_{k-1|k-1}} \\ \hat{v}_{y_{k-1|k-1}} \end{bmatrix} + \int_{t_{k-1}}^{t_k} \left(\begin{bmatrix} 0 & 0 & 1 & 0 \\ 0 & 0 & 0 & 1 \\ 0 & 0 & 0 & 0 \\ 0 & 0 & 0 & 0 \end{bmatrix} \begin{bmatrix} \hat{x}_{k-1|k-1} \\ \hat{y}_{k-1|k-1} \\ \hat{v}_{x_{k-1|k-1}} \\ \hat{v}_{y_{k-1|k-1}} \end{bmatrix} + \begin{bmatrix} \cos(\psi_k) & -\sin(\psi_k) \\ \sin(\psi_k) & \cos(\psi_k) \\ 0 & 0 \\ 0 & 0 \end{bmatrix} \begin{bmatrix} \hat{u}_{k-1} \\ \hat{v}_{k-1} \end{bmatrix} \right) dt. \quad (4.8)$$

Note that the velocities \hat{u} and \hat{v} can be obtained either by estimation through dead-reckoning or direct measurements, if available. In this last expression, errors may be introduced because of the assumption that the heading, the body velocities and the drifts are constant in the interval $[t_k, t_{k+1})$. Nevertheless, these errors can be made smaller if shorter intervals are considered. These errors are considered disturbances here.

At each prediction step, the covariance matrix evolves as follow:

$$P_{k|k-1} = F_{k-1} P_{k-1|k-1} F_{k-1}^T + Q_k \quad (4.9)$$

where F is the Jacobian of (4.7) evaluated at \hat{X} and $Q_k = \int_{t_k}^{t_{k+1}} Q dt$ is the noise variance integrated over the interval $[t_k, t_{k+1}]$.

One of the major issues with the EKF is the initialization. To avoid divergence and guarantee fast convergence of the estimate, the initial positions and water current velocities have to be adequately initialized. This question will be addressed later in subsection 4.3.3. The next subsection present a valid alternative to EKF which can also be used as an initialization method, as will be seen later on.

Boutayeb et al. (1997) has proven that, under appropriate choice of process noise and observation error covariance matrices, the estimate of EKF does not diverge. Convergence is guaranteed if a sequence of measurements makes the system observable. Here, the vehicle trajectory depends on the estimate and wrong estimates may lead to a locally unobservable system and thus the estimate may diverge.

4.3.2 Estimating the position: particle filter

While EKFs assume the presence of Gaussian noises affecting the observations and the process, PFs do not make any assumption on the noise probability distribution (Arulampalam et al., 2002; Gustafsson et al., 2002). In fact, the posterior probability distribution is discretized into a finite number of particles, which are vectors that represent probable state estimates.

Although PF is a promising approach it is usually more demanding than the EKF in terms of computational requirements. Generally, the number of particles is large in order to guarantee a

good coverage of the belief distribution and grows substantially with the number of state estimate variables (Gustafsson et al., 2002). Since computational resources are naturally limited, there is a trade-off between accuracy and processing requirements. This makes the processing time available for PF estimation narrower which leads us to consider and estimate only horizontal positions while water currents are considered disturbances.

According to section 2.4.2, consider the set of particles $\mathcal{X}_k = \{X_k^1, X_k^2, \dots, X_k^n\}$, where $X_k^i = [x_k^i, y_k^i]^T \in \mathbb{R}^2$ and n is the number of particles. Associated to these particles, a set of weights $\mathcal{W}_k = \{w_k^1, w_k^2, \dots, w_k^n\}$, $w_k^i \in \mathbb{R}$, assign an importance to the corresponding particle. For initialization, the vehicle is stopped and the range is measured several times. The mean \bar{R}_{ini} of consecutive consistent measurements (consistent measurements are those that obey to a given condition on their difference, for example) is computed and each particle is sampled according to

$$\begin{bmatrix} x_0^i \\ y_0^i \end{bmatrix} = \begin{bmatrix} (\bar{R}_{ini} + r_s^i) \cos(\psi_s^i) \\ (\bar{R}_{ini} + r_s^i) \sin(\psi_s^i) \end{bmatrix}, \quad (4.10)$$

where $r_s^i \sim \mathcal{U}(-\delta_r, \delta_r)$ and $\psi_s^i \sim \mathcal{U}(-\pi, \pi)$ are sampled from uniform probability distributions.

At each time step, each particle is propagated through dead-reckoning similarly to (4.8). The propagation differs only in an added sample s_k^i drawn from the process noise probability density function p_f , assumed to be piecewise constant in the intervals $[t_k, t_{k+1})$, resulting into:

$$X_k^i = \begin{bmatrix} x_{k-1}^i \\ y_{k-1}^i \end{bmatrix} + \int_{t_{k-1}}^{t_k} \left(\begin{bmatrix} \cos(\psi_k) & -\sin(\psi_k) \\ \sin(\psi_k) & \cos(\psi_k) \end{bmatrix} \begin{bmatrix} \hat{u}_{k-1} \\ \hat{v}_{k-1} \end{bmatrix} + s_k^i \right) dt. \quad (4.11)$$

Whenever a new range measurement is available, the update is performed and the weights are computed according to

$$w_k^i = w_{k-1}^i q(h_k | X_k^i), \quad (4.12)$$

where q is an importance function that approximates the likelihood. For this particular case, $q = q(|\|X_k^i\| - h_k|)$. Likelihood resemblance is of special importance since it impacts on the performances of the filter. For acoustic range measurements, it might be difficult to find an *appropriate* function to play this role. Our intuition and practice suggest that a monotonically decreasing function would be an adequate choice.

After computing the weights, normalization follows: $w_k^i = w_k^i / \sum_i^n w_k^i$. The state estimate is then obtained using the weighted summation of the particles:

$$\hat{X}_k = \sum_{i=1}^n w_k^i X_k^i. \quad (4.13)$$

Due to their nature, after some iterations, it is common that PFs weight a set of few particles considerably more than the remaining ones. In the single beacon localization problem, this happens when a small set of particles is recursively consistent with the range measurements. Their

weights will increase while the remaining ones will decrease. In such a scenario, the reliability on the estimate decreases, since the estimation relies on a small number of possible states. This phenomenon is known in the literature as *degeneracy* and can be attenuated by resampling. This method consists of spreading the particles over regions around the most weighted particles and setting the weights uniformly as $w_k^i = 1/n$. Resampling can be achieved by sampling from an accumulative weight function (see Arulampalam et al. (2002), for example). Nevertheless, resampling should not be performed at every iteration but only when the degeneracy is considered too large. As introduced in 2.4.2, a common metric for degeneracy is the summation of the squared weights (Arulampalam et al., 2002; Gustafsson et al., 2002). Thus, resampling has to be performed whenever the following inequality holds:

$$\frac{1}{\sum_i^n w_k^i{}^2} < N_{th}, \quad (4.14)$$

where $N_{th} \in [1, n]$ is a preset threshold.

Although PFs provide an estimate based on vectors spread in space, it may diverge. Divergence, in this case, may be due to deprivation. Indeed, when the particles are resampled, they likely concentrate in a region and may originate lack of *representativity*. Of course, this can be overcome by increasing the number of particles and/or tuning the user-defined distribution function p_f so that the particles are propagated within a broader range. Nevertheless, the first option may be undesirable because of the computational requirements.

4.3.3 Initialization

Although PFs include a step for initialization, the same does not apply to the EKF algorithm. Hence, in order to guarantee fast convergence of the KF to the real position, it is necessary to provide a reasonably good guess of the initial position while reducing the values of the covariances of the corresponding variables, as performed by Baccou and Jouvencel (2002). Unfortunately, the speed of convergence is not the only issue: without adequate initialization, the EKF would possibly diverge or converge to local minima. Baccou and Jouvencel (2002) implemented an iterative least mean square estimator for the initial position. However, the estimator relies on an accurate model for dead-reckoning or accurate knowledge on vehicle velocities. A previous implementation and simulation of least mean square method revealed that the initialization is very sensitive to model uncertainties. Similarly, Casey et al. (2007) defined an intuitive estimator, also based on least mean square errors but relying on very accurate dead-reckoning.

Here, the proposed approach takes advantage of the PF properties: the PF estimates the initial position of the vehicle which in turn is used to set the initial estimate of the EKF. The initialization includes the following sequential steps:

1. Spreading particles on a circle: with the vehicle stopped, the PF is initialized as described in section 4.3.2;

2. Constant heading: the vehicle starts moving with an arbitrary orientation describing a line during a pre-established time at constant velocity;
3. Constant heading rate: while keeping the same surge velocity, the vehicle describes a distorted arc of circumference (typically a quarter or a half of a circle), by setting the yaw rate constant and non-null;
4. Initialization of the EKF: the initial estimate of the KF is set according to the PF estimate.

Clearly, this does not ensure accurate initialization. Henceforth, if a measure of the estimate coherency is available and if the estimates are inconsistent, the initialization step may have to be performed again.

Divergence of the EKF can be easily detected through observation of the covariance matrix terms or large value of the norm of the water current velocities. Therefore, in the case of divergence, the KF has to be re-initialized using the procedure above.

4.3.4 Control

If the actual position of the vehicle and the currents were known over the operation, the control law would be simple and would make the vehicle move in a straight line to the origin. However, it is easy to verify that this linear motion makes the system unobservable (Jouffroy and Reger, 2006). Indeed, even with a very accurate initialization, the uncertainty would grow over time, which could make the filters diverge from the actual position. A possible solution is described by Feder et al. (1999), making it possible to compute the optimal control at each time step such that a given criterion of observability is maximized. However, the method is computationally expensive, relying on optimization algorithms. Here, as in (Baccou and Jouvencel, 2002), a curvilinear motion is considered to approach the beacon. A heading offset with regard to the orientation of the vector that joins the vehicle and the beacon solves the problem.

Throughout the following developments, the reference position will be considered to be coincident with the origin of the horizontal plane, that is $\eta_d = \{[x_d, y_d, \theta_d]^T : x_d = y_d = 0, \theta_d \in [-\pi, \pi]\}$, enabling the use of the form (4.4). Therefore the control law must stabilize the origin of the vector $[x, y]^T$, which is equivalent to stabilizing the origin of ρ . The approach presented here is based on backstepping (see Khalil (2002)). Although a simple control law can be almost empirically derived, taking u and r as inputs of the system, Lyapunov theory and the backstepping technique provide a framework to analyze and to guarantee stability.

Consider the system

$$\begin{aligned}\dot{\rho} &= u \cos(\psi - \psi_p) - v \sin(\psi - \psi_p) + v_x \cos \psi_p + v_y \sin \psi_p \\ \dot{\psi} &= r\end{aligned}\tag{4.15}$$

Relying on the estimate, let us assume that the angle between the beacon and the vehicle position is equal to the estimated $\psi_p = \hat{\psi}_p = \angle(x, y)$.

Define the Lyapunov function candidate as $V(\rho) = \rho$. Its time derivative results

$$\dot{V} = \dot{\rho} = u \cos(\psi - \psi_p) - v \sin(\psi - \psi_p) + v_x \cos \psi_p + v_y \sin \psi_p. \quad (4.16)$$

Setting $u > 0$, the following implication holds: $u \cos(\psi_p - \psi) < 0 \Rightarrow \psi \in]\psi_p + \pi/2, \psi_p + 3\pi/2[$.

Considering that the lateral velocity is small compared to the longitudinal one and that the difference $\psi - \psi_p$ is sufficiently small, yields

$$\dot{\rho} \approx u \cos(\psi - \psi_p) + v_x \cos \psi_p + v_y \sin \psi_p. \quad (4.17)$$

From this last equation, the constraint on the forward velocity is straightforward:

$$u \cos(\psi_p - \psi) < -v_x \cos(\psi_p) - v_y \sin(\psi_p). \quad (4.18)$$

Suppose that $\psi = \xi(\psi_p)$, along with the condition (4.18), stabilizes the system (4.5) and makes the Lyapunov function satisfy the inequality $\dot{V} \leq -W(\rho)$, where W is a positive semi-definite function. A simple example is

$$\xi(\psi_p) = \psi_p + \pi + \psi_o, \quad (4.19)$$

where $\psi_o \in (-\pi/2, \pi/2)$ is an offset angle that makes the trajectory curvilinear during the approach to the origin. Defining the error variable $z_1 = \xi - \psi$, the system (4.15) can be re-written as

$$\begin{aligned} \dot{\rho} &= u \cos(\xi - z_1 - \psi_p) + v_x \cos(\psi_p) + v_y \sin(\psi_p) \\ \dot{z}_1 &= r - \dot{\xi} \end{aligned}$$

Note that for each z_1 , there exist a δ such that $\cos(\xi - z_1 - \psi_p) \leq \cos(\xi - \psi_p) + \delta \|z_1\|$. In fact, assuming that $z_1 \in [-\pi, \pi]$, it is easy to show that δ belongs to the interval $[0, 1/\pi]$. Using $V_2 = V + 1/2 z_1^2$ as the new augmented Lyapunov function, which is obviously positive definite, its time derivative is given by:

$$\begin{aligned} \dot{V}_2 &= u \cos(\xi + z_1 - \psi_p) + v_x \cos(\psi_p) + v_y \sin(\psi_p) + z_1 \dot{z}_1 \\ &\leq -W(\rho) + \delta \|z_1\| + z_1(r - \dot{\xi}). \end{aligned}$$

Choosing $r = \dot{\xi} - K z_1 - K' \text{sign}(z_1)$, being K' chosen such that the term $\delta \|z_1\|$ is cancelled, stability would be ensured. Note that the control law is discontinuous which is undesirable. Making $K' = 0$ makes the control law continuous but at the cost of making \dot{V}' positive for some values of $\|z_1\|$. Nevertheless, using theorem (Khalil, 2002, th. 4.18, pp. 172), it is possible to prove that the system converges to the vicinity of $\rho = 0$ with an error that can be made arbitrarily small by manipulating the gain K , if the product $\delta \|z_1\|$ remains bounded. The same result can be derived for the neglected sway velocity v , if its norm is upper bounded.

Remark 4.1. *Thus far in this subsection, it has been considered that the position of the vehicle is perfectly known. Although with PFs it is not trivial to assess the confidence on the estimate, the KF provides a notion of the uncertainty through its covariance matrix P . In general, the bigger the values of its entries, the less the confidence on the estimate is. In such scenarios it could be useful to modify the trajectory. Here, the change of approach side is a valid choice in order to try to reduce the estimate uncertainty. Thus, our method makes use of the offset angle introduced in (4.19): whenever the elements of the error covariance matrix grow above a preset threshold, the approach side is switched by simply setting $\psi_o(t_{k+1}) = -\psi_o(t_k)$ in the control law. Note that such a change introduces discontinuities in the control law but bounding its slope would be sufficient to overcome the problem.*

4.3.5 Results

Implementation of the approach is demonstrated by realistic simulations using a six DOF model of the dynamics, whose accuracy was already proved through comparisons in Ferreira et al. (2010b), and a non-gaussian noise for the time-of-arrival (TOA). For simulation, an uniform distribution $\mathcal{U}(0, \bar{e}_l)$, $\bar{e}_l > 0$, is used. The measurements have been simulated to occur every two seconds.

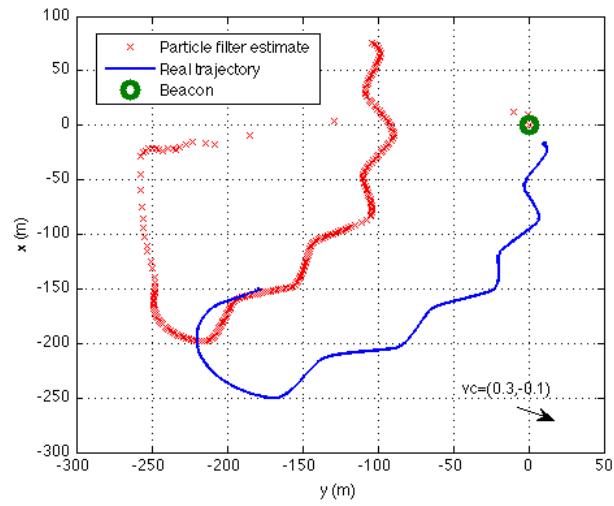
In order to imitate the real behavior of the dynamics and the constraints in real operations, the estimation and control software are tested in their final version as they are implemented in real vehicle. Beyond validation of algorithms, this way enables performance evaluation and parameters tuning, as well. While the implementation code runs in its final version, the dynamics and the sensors are emulated accurately by a model implemented in Simulink. A communication interface in the middle grants connection between the two modules. This approach makes code porting totally transparent when implementing in real vehicles.

In this section, the results from both PF and EKF approaches are presented. A comparison of the results under the same conditions is given and a more focused analysis on the performances of the EKF is provided.

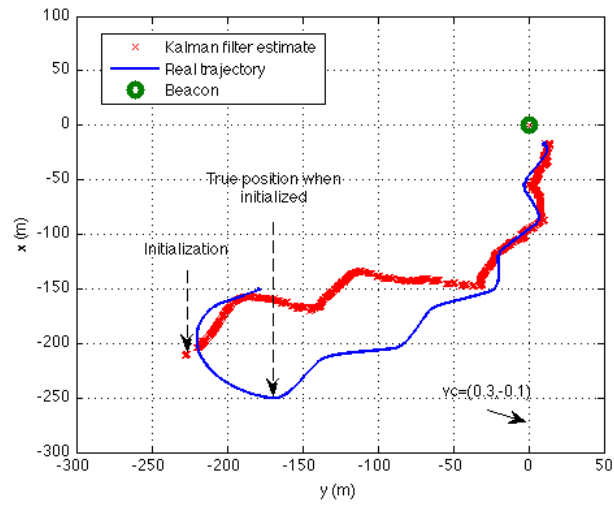
4.3.5.1 Comparison

To find the best approach, the two estimators were implemented. The results obtained from simulations with different initial positions and different water currents are similar to the one addressed here in terms of behavior. In order to make clear the algorithm followed for this simulation, let us recall the main steps:

1. the vehicle is set in a unknown random position, with an arbitrary heading
2. initialization is performed by the particle filter while describing a line during few seconds (30 seconds in this case) followed by an arc of circumference
3. Kalman filter is initialized with the last estimate of the particle filter after the initial trajectory
 - whenever the diagonal elements of the covariance matrix P grow above a pre-set threshold, the approach side is switched



(a) PF estimate



(b) EKF estimate

Figure 4.1: Comparison between the particle filter and the extended Kalman filter estimates

4. the homing process ends when the vehicle is close to the beacon (20 meters in this simulation)

The homing trajectory shown in figure 4.1 starts at point $[x\ y]^T = [-150, -180]^T$ with an arbitrary heading. The water current variables were set to $[v_x\ v_y]^T = [0.3\ -0.1]^T$. The controller uses the estimates of the EKF to generate the trajectory, while moving at a constant forward speed of 1m/s. In figure 4.1(a), the result of the PF estimation are shown. The estimate starts at approximately $[0\ 0]^T$ and iteratively approximates the real position. However, it can be seen that the particle filter diverges after some steps. The cause of this divergence is the lack of coverage of the particles: after re-sampling several times, the particles occupy a small area and their propagation is not enough to prevent divergence. After divergence, the particles are basically driven by dead-reckoning. Propagation can be made larger with an adequate choice of the distribution p_f from which the of “propagation noise” is sampled. But this approach has critical consequences, especially for filters with small number of particles, since they may be propagated too far from the real position. This issue could be overcome by choosing a more appropriate propagation noise distribution or by augmenting the number of particles and including the estimate of the currents in the state vector. However, our experience tells us that, for a number of particles between $n = 100$ and $n = 1000$, the performance remains similar. Therefore, it is expected that a much larger number is required. The inclusion of the currents velocity components would likely improve the estimate but a even larger number of particles would be needed.

On the other hand, figure 4.1(b) shows that the EKF converges to the vehicle true position, even with a relatively poor initialization. Some terms of the covariance matrix are above the pre-set threshold which makes the controller switch the approach side several times. Most simulations showed that the EKF approach provides the best results and the overall estimation is performed properly when it is initialized with the particle filter.

4.3.5.2 Initialization

The evolution of the PF algorithm is shown in figure 4.2. After having collected a set of consistent ranges, the particle filter is initialized by spreading the particles around a circumference with radius equal to the average of the collected range measurements ($t = 0s$). The density of particles suggests the possible lack of representativity at beginning: smaller number of particles would likely lead to lack of coverage to approximate the posterior in certain regions. Alternatively, the same would be verified if the number of particles is kept and the initial distance is augmented, which would result in a smaller density of particles over the circle.

The algorithm rapidly evolves and converge to the final estimate of the position. One can see that the particles are confined to a very small region at $t = 120s$ (deprivation). Space coverage becomes small and could lead to divergence after some “less consistent” measurements. It would be just a matter of time before PF estimate eventually diverge (Thrun et al., 2005). Two types of solutions would be possible to prevent this issue: introduction of randomly sampled particles

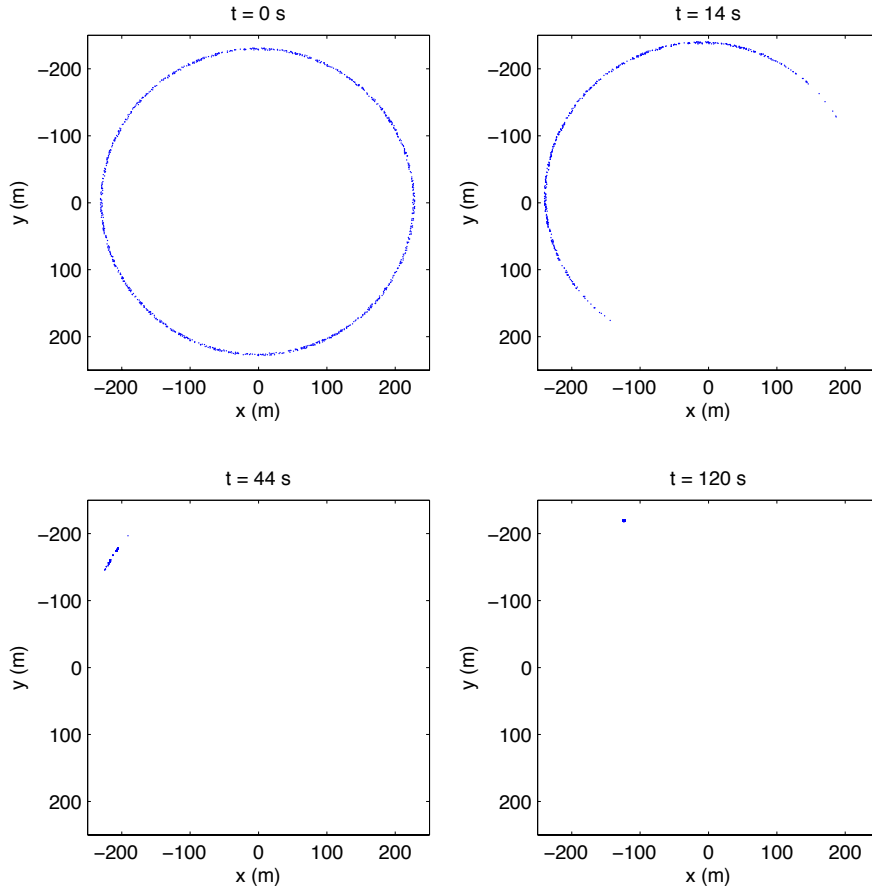


Figure 4.2: Evolution of the 1000 particles for an initialization with the vehicle starting at $(x, y) = (-150, -170)$. The vehicle velocity is $u = 1\text{m/s}$ and the currents are $(v_x, v_y) = (-0.2, 0.1)$.

in the set (Thrun et al., 2005), or; re-initialization after divergence by following the steps of the initialization procedure.

4.3.5.3 EKF approach

In what concerns convergence, the results shown above indicate that the EKF performs better than the particle filter. The use of the covariance matrix to infer about the confidence on the estimates provides to the system robustness and ability to take decisions. Re-initialization is specially appreciated in this context.

In the following simulation, the vehicle is set at $[x y]^T = [150 \ 150]^T$ with current velocity $[v_x \ v_y]^T = [0.2 \ -0.1]^T$. Figure 4.3 shows the position estimate along with that of the current component velocities. As can be seen, the estimation of the current is slow and erroneous for almost all time. Although erroneous, this shows that the correct estimation of this vector does not seem to be critical since the position estimate converges to the real position.

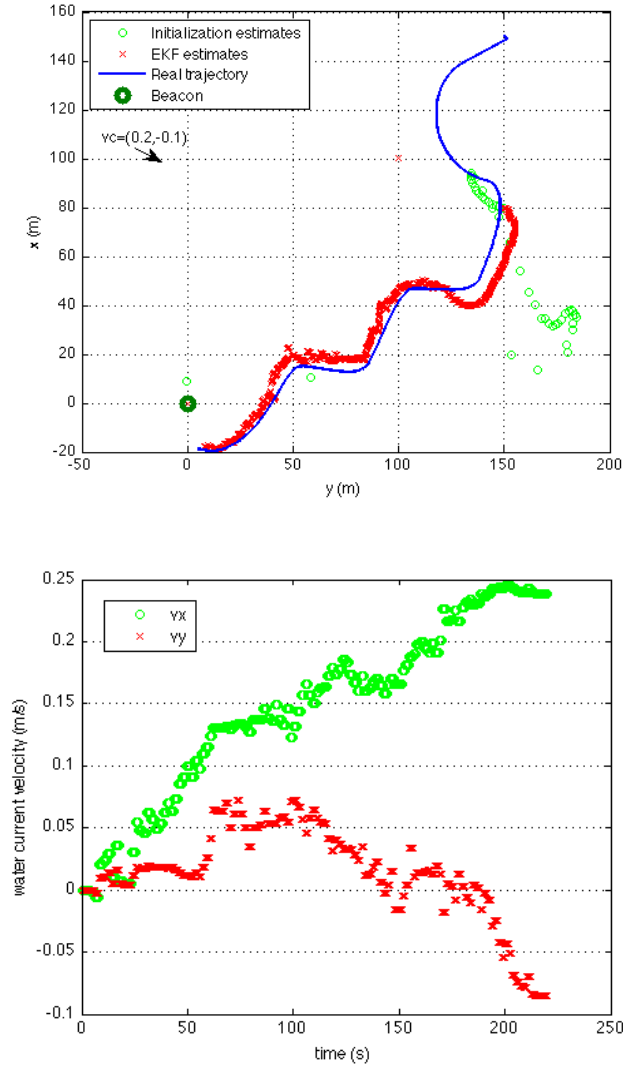


Figure 4.3: Position and current velocity estimations

In the present approach, the errors in the dead-reckoning model are reflected on the estimation of the current velocity. Imagine that the vehicle is moving in a straight line and the estimated forward velocity is inaccurate. The difference between the dead-reckoned and real forward velocities will be directly reflected on the estimate.

The results of another homing mission with different surge velocity ($u = 2\text{m/s}$) in the presence of voluntarily inserted model uncertainty and current $[v_x \ v_y]^T = [0.40]^T$ are shown in figure 4.4. The surge damping coefficient was set to be 30% less than its actual value. This fact, together with unmodeled current, naturally affect the initialization. In this case, the figure 4.4(b) shows that the initialization is made with an error of 43m. However, one can remark that the estimation of the EKF is capable of recovering from this error. The dashed line indicates the moment at which the approach side is switched for the first time ($\sim 45\text{s}$) and it can be seen that the observability is improved in such a way that the error decreases quickly. These corrections appear in figure 4.4(a)

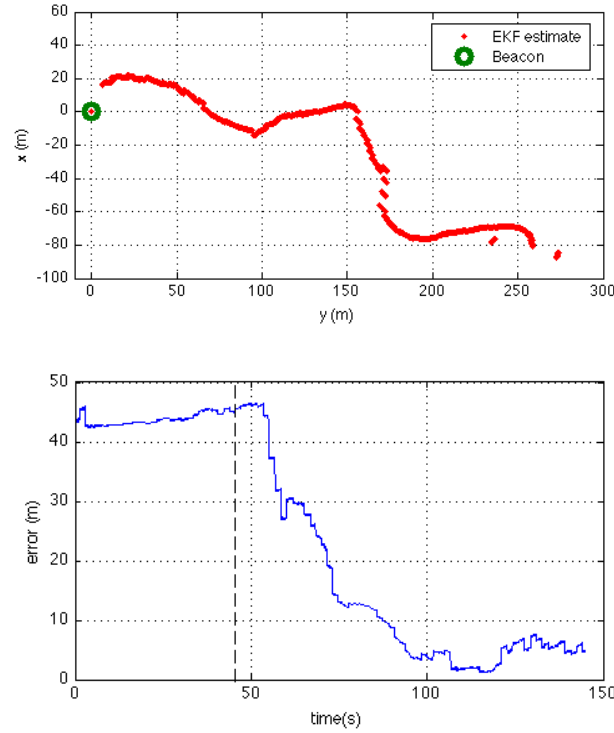


Figure 4.4: Homing at 2m/s

as larger corrections (“discontinuities”) after the first curve.

These results reveal that this approach is robust even in the presence of model uncertainties and possible inaccurate initializations.

In order to compare the effect of different parameters for direction switching, that is, approach side changes, the result of simulations with different values are presented next. The two tuning parameters are the minimum switching period and the maximum covariance. The former avoids the heading reference to switch at very high rates (chattering) while the second is a threshold used to change the approach side as a tentative to reduce the uncertainty of the position estimate. These parameters are denoted t_{thresh} and σ_{thresh} , respectively.

The trace of the 2-by-2 submatrix of P , P_p (the submatrix that is directly related with the $[x \ y]$ position covariance) is used as a measure of the uncertainty:

$$\text{trace}(P_p) = \sigma_{xx}^2 + \sigma_{yy}^2. \quad (4.20)$$

To better understand the performance of the EKF as a function of the two parameters aforementioned, several simulations were ran, varying σ_{thresh} and t_{thresh} . The resulting evolution of the measures of uncertainty is shown in figure 4.5, which must be analyzed along with the result in figure 4.6. It should be stressed that the observability degrades with the distance of the vehicle with respect to the beacon (see Bingham (2003) for an analysis on relative positioning in LBL localization systems). It can be seen from figure 4.6 that the initialization procedure feeds the EKF with

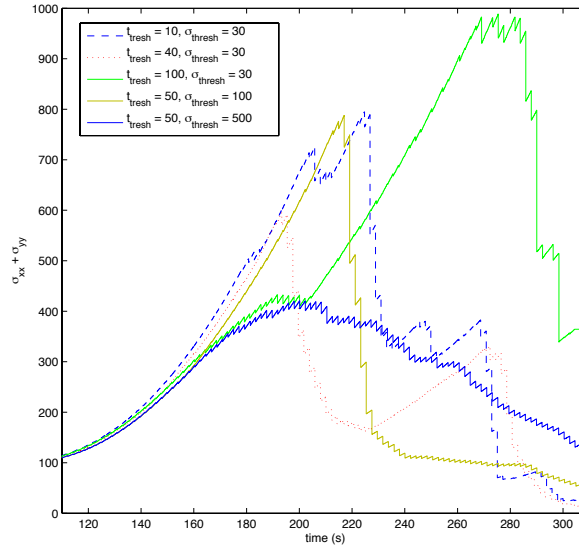


Figure 4.5: Evolution of the covariance as a function of the minimum switching period and of the switching covariance. The results were obtained from several simulations performed with the same initial conditions.

approximately the same initial position for all cases.

Two extreme cases can be observed from the plots:

- When σ_{thresh} is too small, that is, when $\sigma_{xx} > \sigma_{thresh}$ or $\sigma_{yy} > \sigma_{thresh}$ is verified for all time, the trajectory is driven by the minimum switching period, independently of the evolution of the covariance. The algorithm switches the approach side after every interval period t_{thresh} . The behavior corresponding to this situation can be seen in the simulations with $\sigma_{thresh} = 30$;
- When σ_{thresh} is too large, the approach side never switches and the algorithm becomes static, as for the case in which $\sigma_{thresh} = 500$. Still, for the example presented, the performance is relatively good due to the fact that the vehicle approaches the origin and the observability becomes better. Nevertheless, for larger distances and longest trajectories, the EKF uncertainty would grow much more and the estimation would possibly diverge.

For the analysis of the influence of t_{thresh} , suppose that the estimate is coincident with the actual position but the uncertainty is large and $\sigma_{xx} > \sigma_{thresh}$ or $\sigma_{yy} > \sigma_{thresh}$. If t_{thresh} is too small, the vehicle would describe a zig-zag trajectory about the line that joins the beacon and the initial position of the vehicle. For $t_{thresh} \rightarrow 0$, the trajectory would be coincident with the line. As stated earlier, the straight line trajectory to the origin lacks observability about the normal direction of the trajectory (in the 2-D plane), and consequently, the uncertainty about that axis would never stop growing. Alternatively, if t_{thresh} is too large the effect would be the same as for large σ_{thresh} .

Under these simulation conditions, values of t_{thresh} within the range $[30, 60]$ and of $\sigma_{thresh} \in [70, 200]$ provides satisfactory results. Nevertheless, it is expectable that the performances change

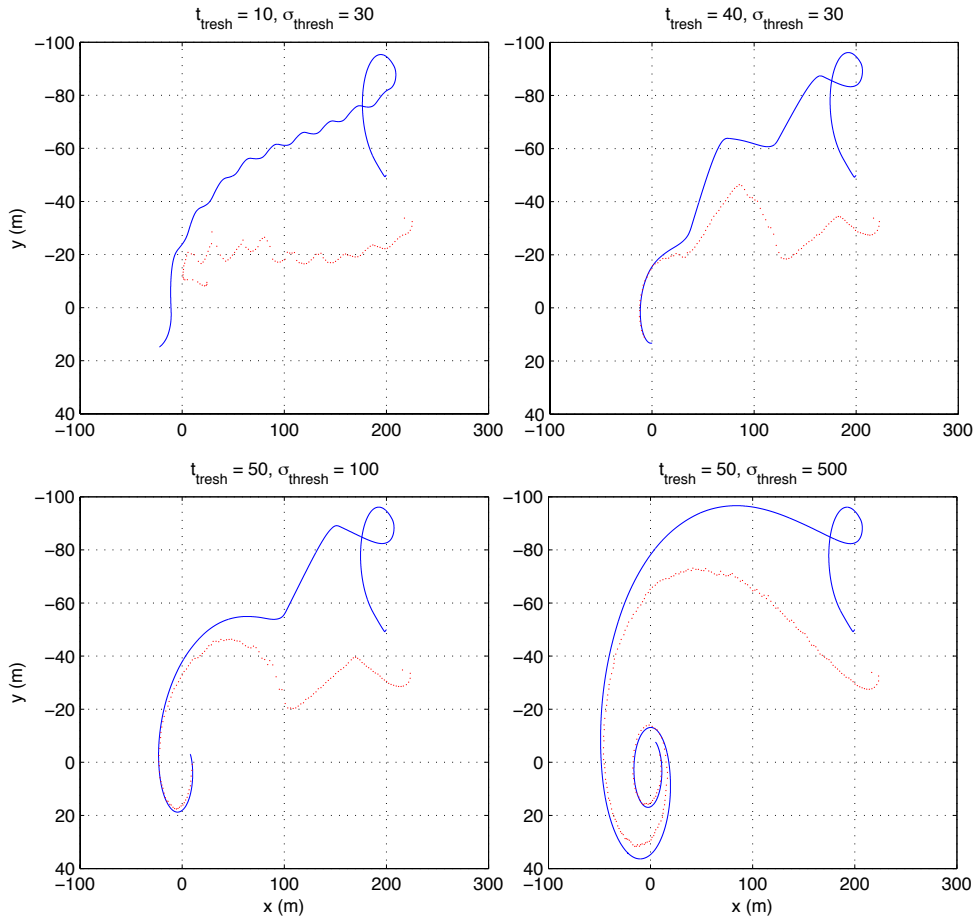


Figure 4.6: Ground truth (blue solid line) and estimated trajectories (red dots) as functions of the minimum switching period and of the switching covariance. Surge velocity reference is $u = 1\text{m/s}$ and the current velocity is $(v_x, v_y) = (-0.2, 0.1)$

according to the update rate, the measurement errors and the vehicle velocity. Hence, for different scenarios with different parameters, the same performances can not be granted. Therefore, the thresholds should be tuned according to the environment, sampling and velocity conditions.

4.4 Homing using a sensor-based approach

The previous method provided a complete approach for estimating the relative position of a robot with respect to a beacon as well as a control law that enables homing the robot to that reference. The approach relies on the position estimate to guide the robot.

The main goal of this section is to present an alternative way to home an underwater vehicle without resorting to localization algorithms. The main advantage behind this approach is the possibility of defining a totally predictable and deterministic behavior during the trajectory of the vehicle, while avoiding to rely on estimators which may diverge under unpredicted situations. Indeed, solving the localization problem would make it possible to decouple the navigation process

into control and position estimation but would be more demanding, more uncertain and may lead to wrong control decisions as the estimate is used to determine the desired heading.

In this section, a complete method to drive an AUV to a beacon based on ranges only is proposed. It is desired to keep the approach minimalistic not only in terms of computational complexity but also in terms of sensor/equipment requirements. The approach is constructed so that no state estimation is needed to robustly drive the AUV to a small neighborhood of the home (beacon) position. At the expense of imposing some constraints, the vehicle will be endowed with the ability to track a given gradient, while making the behavior completely predictable. It should be noted that precise localization methods surveyed earlier can complement the present work, in the vicinity of home for accurate positioning (e.g. docking). By applying Lyapunov nonlinear theory, a velocity control law is derived to conduct the vehicle toward the beacon without requiring initialization.

4.4.1 Control method

To begin with, some assumptions have to be made at this stage (some of them were already introduced in section 4.3.4)

1. An inner velocity loop allows for the robot to move at a constant forward speed u , independently of its angular velocity r (u and r can be manipulated separately)
2. When moving, the robot does not suffer from sideslip ($v = 0$), independently of the forward and angular velocities
3. The norm of the generalized horizontal drift vector $\mathbf{v}_c = [v_x, v_y]^T$, which includes the sum of the effects of the current, wind and waves is upper bounded, that is, $\|[v_x, v_y]^T\| = \|\mathbf{v}_c\| \leq \bar{v}_c$, where \bar{v}_c is a known nonnegative constant
4. The forward velocity is strictly greater than the current velocity $u > \bar{v}_c \geq \|\mathbf{v}_c\|$

Recall that the objective of the control law to be derived is to reduce the distance ρ to zero. Hence consider the system (4.15) and from assumption 2, let us re-write the system, for completeness,

$$\begin{aligned}\dot{\rho} &= u \cos(\psi - \psi_p) + v_x \cos \psi_p + v_y \sin \psi_p \\ \dot{\psi} &= r\end{aligned}\quad (4.21)$$

Clearly, beyond u , which is assumed to be constant, none of the variables is directly controllable. Keeping in mind that $u > \|\mathbf{v}_c\|$, assume that it is possible to set $\dot{\rho} = -\beta(\rho)$, where $\beta(\rho) : [0, \infty) \rightarrow [0, c_\beta]$ is a class \mathcal{K} function verifying $\lim_{\rho \rightarrow \infty} \beta(\rho) = c_\beta > 0$, for a given constant $0 < c_\beta < \infty$. Thus, the time derivative of the range would result negative in $\dot{\rho} < 0$.

Intuitively, the idea behind the introduction of β is simply that one aims at defining an approach rate to the origin. Its upper bound must obviously take into account the surge velocity u and the drift vector \mathbf{v}_c in order to make the approach to the origin possible, as it will be explained next.

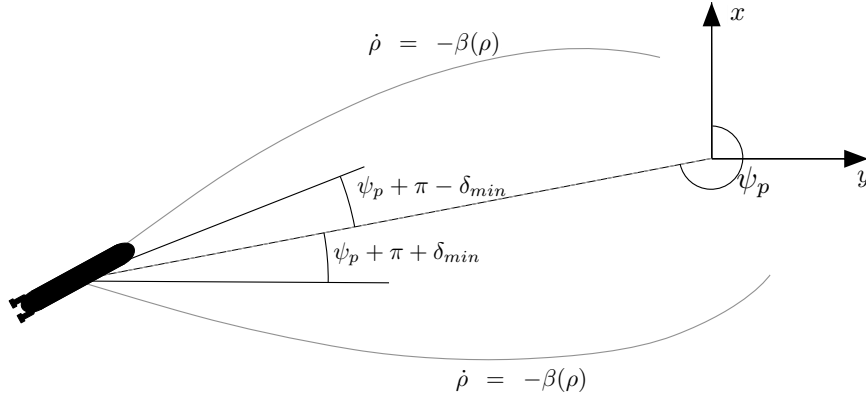


Figure 4.7: Homing method

4.4.1.1 Controller

The next developments use the Lyapunov direct method to derive a controller to home the vehicle to a reference. This method has been chosen since the solution directly results from the stability analysis, naturally granting convergence properties that other methods may fail to warrant.

Define the new error variable as $e_{\dot{\rho}} = \dot{\rho} + \beta$ and let the Lyapunov function be

$$V = V(\dot{\rho}) = \frac{1}{2}e_{\dot{\rho}}^2. \quad (4.22)$$

Note that the objective becomes tracking an approach gradient defined by β . Using (4.21), after algebraic manipulation, its time derivative results into

$$\dot{V} = e_{\dot{\rho}} \left(-u\dot{\psi} \sin(\psi - \psi_p) + \rho \dot{\psi}^2 + \dot{\beta} \right). \quad (4.23)$$

The control variable $r = \dot{\psi}$ appears now explicitly and, from assumption 1, suppose that it can be directly controlled although some considerations have to be taken into account, such as the smoothness properties, as it will be exposed later on.

The fact that only ρ is observable limits our approach. Indeed, if ψ_p would be known, the problem could be reduced to imposing the optimal time solution $\arg \min_{\psi} \dot{\rho} = \psi_p + \pi$. However, the approach follows a different way being motivated by robotics applications in which such variable is hard to observe or has to be estimated along with the current velocity vector v_c .

Intending to minimize the use of models at this stage, the second option is therefore discarded. Moreover, ψ must be different from $\psi_p + \pi$ to keep the term $u\dot{\psi} \sin(\psi - \psi_p)$ away from zero to ensure that the virtual control input $\dot{\psi}$ appears in (4.23). By appropriately choosing the new control variable β , it can be ensured that ψ remains away from $\psi_p + \pi$.

In order to assess the angle dynamics at equilibrium, consider that the gradient is being tracked

and consider the range dynamics in (4.21) and set it equal to $-\beta$:

$$\dot{\rho} = u \cos(\psi - \psi_p) + v_x \cos \psi_p + v_y \sin \psi_p = -\beta. \quad (4.24)$$

Taking $0 < \beta < u - \|v_c\| \leq u - k_{v_c}$, or equivalently $c_\beta = u - \|v_c\|$, at equilibrium ($e_\rho = 0$), it follows

$$\cos(\psi - \psi_p) > \frac{1}{u}(-u + k_{v_c} - v_x \cos \psi_p - v_y \sin \psi_p) \geq -1$$

These inequalities result from assumptions 3 and 4. Since $k_{v_c} \geq \|v_c\| > v_x \cos \psi_p - v_y \sin \psi_p$, $|\cos(\psi - \psi_p)| \neq 1 \Rightarrow \psi \neq \psi_p + n\pi, n \in \{0, 1\}$. In fact, the choice of β will directly influence the distance of ψ relatively to $\psi_p + \pi$, at equilibrium: the less the value of β , the bigger the difference between ψ and $\psi_p + \pi$.

One of the main benefits of the introduction of β is the possibility to keep the angle ψ away from $\psi_p - \pi$, at equilibrium, without knowing ψ_p explicitly, constituting therefore a major advantage in this approach. Let δ be the difference angle between ψ and $\psi_p - \pi$. Then

$$\begin{aligned} \delta &= \psi - \psi_p + \pi \\ &= \pm \arccos\left(\frac{1}{u}(-\beta - v_x \cos \psi_p - v_y \sin \psi_p)\right) \pm \pi. \end{aligned} \quad (4.25)$$

From the kinematics point of view, the fact that δ is different from zero means that the robot describes a curvilinear trajectory to the origin. By setting the upper bound of β , $c_\beta = u - \|v_c\| - \xi$, $0 < \xi < u - \|v_c\|$, at equilibrium, the minimum difference angle $\delta_{min} < \min_{v_c}(|\delta|)$ results

$$\delta_{min} = \pi + \arccos \frac{-u + \xi}{u}. \quad (4.26)$$

The definition of the upper bound of β leaves room to choose an approach side, that is, the equation (4.25) has two solutions $\psi = \psi_p \pm \arccos \frac{-u + \xi}{u} \pm \pi$, making possible to approach the homing point either by the right or the left hand sides (see figure 4.7). By constricting the robot heading angle ψ to lie exclusively in one set verifying $\psi - \psi_p > 0$ or $\psi - \psi_p < 0$, the ambiguity on the sign of $\sin(\psi - \psi_p)$ in (4.23) is lifted up. Henceforth, assume $\psi - \psi_p > 0$, and equivalently $\delta < 0$ and restrict our analysis and developments to that condition. Nevertheless, the results that follow can be very easily extended to the complementary case.

Clearly, from (4.24) and (4.25) the following implications hold:

$$\begin{aligned} \psi - \psi_p + \pi > \delta &\Rightarrow e_\rho = \dot{\rho} + \beta > 0, \\ \psi - \psi_p + \pi < \delta &\Rightarrow e_\rho = \dot{\rho} + \beta < 0, \\ \psi - \psi_p + \pi = \delta &\Rightarrow e_\rho = \dot{\rho} + \beta = 0. \end{aligned} \quad (4.27)$$

The control law follows:

$$\psi = r = ke_\rho + \frac{1}{u\rho \sin \delta_{min}} \left((u + k_{v_c})^2 + \frac{d\beta}{d\rho}(e_\rho) \right) h(e_\rho), \quad (4.28)$$

where

$$h(e_{\dot{\rho}}) = \begin{cases} 1, & \text{if } e_{\dot{\rho}} > 0, \\ 0, & \text{otherwise.} \end{cases} \quad (4.29)$$

The verification of asymptotic stability of the system under the control law (4.28) will be splitted into two parts: for $e_{\dot{\rho}} > 0$ and $e_{\dot{\rho}} \leq 0$.

1. $e_{\dot{\rho}} > 0$: firstly, one has to notice that $e_{\dot{\rho}} > 0 \Rightarrow \sin(\psi - \psi_p) > \sin \delta_{min}$, from (4.27) and (4.26). Since $|u \sin(\psi - \psi_p) - v_x \sin \psi_p + v_y \cos \psi_p| \leq (u + k_{v_c})$, it comes:

$$\begin{aligned} \dot{V} &= e_{\dot{\rho}} \dot{e}_{\dot{\rho}} \\ &= e_{\dot{\rho}} \left(-u \dot{\psi} \sin(\psi - \psi_p) + \frac{1}{\rho} (u \sin(\psi - \psi_p) - v_x \sin \psi_p + v_y \cos \psi_p)^2 + \frac{d\beta}{d\rho} (e_{\dot{\rho}} - \beta) \right) \end{aligned} \quad (4.30)$$

where the definition of β has been used to state $\dot{\beta} = \frac{d\beta}{d\rho} \frac{\partial \rho}{\partial t} = \frac{d\beta}{d\rho} (e_{\dot{\rho}} - \beta)$. Then, replacing (4.28) in the last expression yields

$$\dot{V} \leq -kue_{\dot{\rho}}^2 \sin(\psi - \psi_p) - e_{\dot{\rho}} \frac{d\beta}{d\rho} \beta \quad (4.31)$$

Since $\sin(\psi - \psi_p) > 0$, and, by definition $\frac{d\beta}{d\rho} \geq 0$, $\beta \geq 0$, it results

$$\dot{V} \leq -kue_{\dot{\rho}}^2 \sin(\psi - \psi_p) \forall \rho > 0, e_{\dot{\rho}} > 0.$$

2. $e_{\dot{\rho}} \leq 0$: as it has been seen for the complementary case, notice that $\dot{\beta} \leq 0$ along the trajectory. Still, β remains a virtual control input and can be handled to meet certain constraints. Thus, β can be designed such that its time derivative satisfy the following inequality:

$$\begin{aligned} \dot{\beta} = \frac{d\beta}{d\rho} \dot{\rho} &\geq -\frac{1}{\rho} (u \sin(\psi - \psi_p) - v_x \sin \psi_p + v_y \cos \psi_p)^2 \\ &\geq -\frac{1}{\rho} (u + \|v_c\|)^2 \end{aligned}$$

which, by verifying that $\dot{\rho} \leq -\beta$ for $e_{\dot{\rho}} \leq 0$, as seen in (4.27), implies

$$\frac{d\beta}{d\rho} \leq \frac{1}{\rho\beta} (u + \|v_c\|)^2 \leq \frac{1}{\rho\beta} (u + k_{v_c})^2. \quad (4.32)$$

The last result means that β has to vary slowly when ρ is large. This implies $\frac{1}{\rho} (u \sin(\psi - \psi_p) - v_x \sin \psi_p + v_y \cos \psi_p)^2 + \dot{\beta} \geq 0$. Then, from (4.23) straightforward algebra shows that

$$\begin{aligned} \dot{V} &= -kue_{\dot{\rho}}^2 \sin(\psi - \psi_p) + e_{\dot{\rho}} \left(\frac{1}{\rho} (u \sin(\psi - \psi_p) - v_x \sin \psi_p + v_y \cos \psi_p)^2 + \dot{\beta} \right) \\ &\leq -kue_{\dot{\rho}}^2 \sin(\psi - \psi_p). \end{aligned}$$

Hence, under the assumptions above, the origin is locally asymptotically stable for all $\psi \in (\psi_p - \pi, \psi_p)$.

Note that β plays the role of a virtual control input in this guidance law. It is designed so that it is possible for the vehicle to track the approach rate defined by the value that β takes. In practice, β defines a feasible approach rate for any given relative position of the vehicle with regard to the beacon. This function also enables accommodating the summation of drifts if a rough notion of its upper bound is known.

4.4.1.2 Constraint on yaw rate control

Up to now, it has been considered that the yaw rate r can be controlled directly. However, such assumption does not hold in real applications and an “inner loop” controller has to be included in order to obtain the desired velocity r_d . It is a common requirement for the reference to be sufficiently smooth (continuous and differentiable) which is not verified by the control law in (4.28), since $h(\cdot)$ is discontinuous. Therefore, the control law (4.28) has to be relaxed but influences on the convergence properties must be minimized. The argument is as follows.

Let replace h by

$$h'(e_{\dot{\rho}}) = \begin{cases} 0, & \text{if } e_{\dot{\rho}} < 0 \\ \alpha e_{\dot{\rho}}, & \text{if } \alpha e_{\dot{\rho}} < 1, \alpha \in (0, \infty). \\ 1, & \text{if } \alpha e_{\dot{\rho}} \geq 1 \end{cases} \quad (4.33)$$

The feedback control law in (4.28) results now continuous and differentiable. Recall that this function was introduced for $e_{\dot{\rho}} > 0$ and its effect is verified only in such situation. Using h' instead of h , from (4.30) allows to write

$$\dot{V} \leq -kue_{\dot{\rho}}^2 \sin(\psi - \psi_p) + \frac{1}{\rho} e_{\dot{\rho}} (1 - \alpha e_{\dot{\rho}}).$$

Although it is impossible to state that the time derivative of the Lyapunov function is negative definite, it is possible to guarantee that it tends to a positively invariant set, from theorem (Khalil, 2002, th. 4.18, pp.172). Its bound is directly related to α , diminishing as the value of α increases.

4.4.2 Stability analysis

The arguments above stand for a particular choice of approach rate β which must lie in a well known interval. Furthermore, the control law was derived based on the assumption that the vehicle heading lies in two specific quadrants: $\psi \in (\psi_p - \pi, \psi_p)$. However, this assumption can be relaxed and the stability of the control law can be proven for all the quadrants. The stability for all $\psi \in [-\pi, \pi)$ makes the overall system more robust and further increases the simplicity of the approach since no initialization procedure is required, in opposition to (Ferreira et al., 2010b; Baccou and Jouvencel, 2003; Bezruchko et al., 2011).

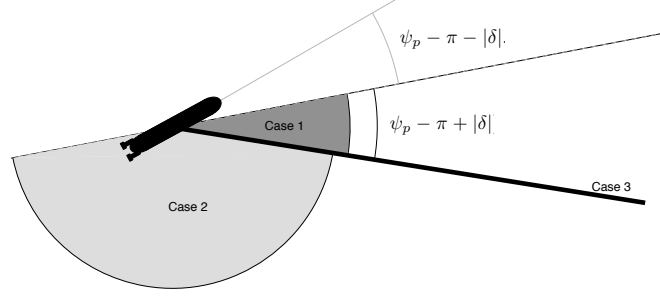


Figure 4.8: Illustration of the intervals of angles for stability analysis

In (4.25), it has been seen that the system with the control law given in (4.28) has two equilibrium points: $\psi = \psi_p - \pi \pm |\delta|$. Nevertheless, one of them is unstable ($\psi = \psi_p - \pi + |\delta|$) for the derivations above. There are three possible scenarios, which have now to be analyzed based on the control law (4.28). Consider the illustration given in figure 4.8.

- Case 1: When the vehicle moves with $\psi \in [\psi_p - \pi, \psi_p - \pi + |\delta|)$, one can verify $e_\rho < 0$ and therefore $\dot{\psi} < 0$, eventually reaching $\psi = \psi_p - \pi - |\delta|$.
- Case 2: Equivalently, for $\psi \in [0, \psi_p - \pi + |\delta|)$, $e_\rho > 0$ and consequently $\dot{\psi} > 0$ until stabilizing at $\psi = \psi_p - \pi - |\delta|$.
- Case 3: Furthermore, if $\psi = \psi_p - \pi + |\delta|$, from (4.5) it can be concluded that $\dot{\psi}_p \neq 0$, which will eventually make the heading diverge from the unstable equilibrium point. It is then possible to state that the system is stable since it can not stay forever in an invariant set other than the one previously derived.

These three conclusions enable concluding that the system is stable in the interval $[-\pi, \pi)$.

4.4.3 Homing with practical constraints on input

This section is devoted to finding upper bounds on the invariant set that the vehicle is able to reach for the method presented previously, considering the practical actuation constraints.

4.4.3.1 Upper bound on range

So far, it has been considered that the yaw rate r admits any value. However, this assumption does not hold for real vehicles since the viscous damping forces opposes the rotation of the vehicle and infinite angular velocity would imply infinite actuation, which is unrealistic. Still, one can verify in (4.28) that larger angular velocities - and consequently larger actuations - are only required close to the origin (note the effect of $1/\rho$ in the expression). Although the limited actuation $r \in [-\bar{r}, \bar{r}]$, where $\bar{r} > 0$ is the maximum absolute value of the actuation, prevents the approach to the origin with arbitrary small error, it is possible to derive an upper bound on the invariant set.

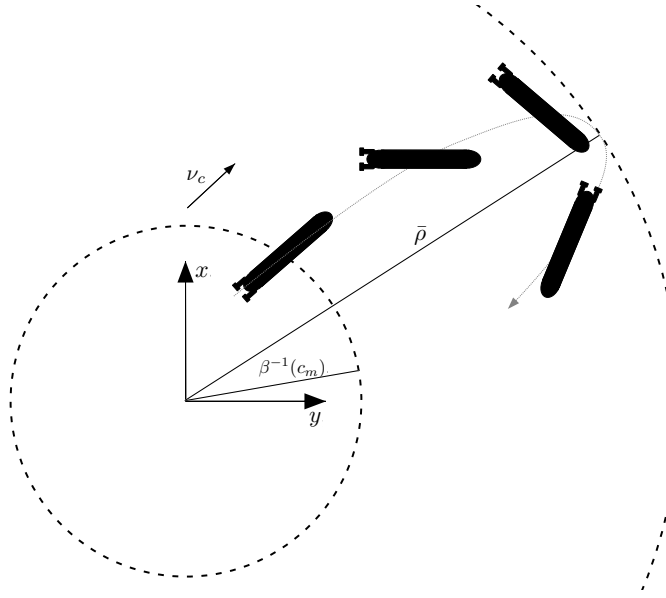


Figure 4.9: Upper bound of the invariant set

Note that, in steady state situation, the trajectory around the origin is periodical. Moreover, under such a condition, the angular velocity reaches its maximum absolute value $r = \bar{r}$.

Due to limited actuation, the vehicle trajectory, around the beacon, is an invariant set which adopts one of the following behaviors:

- Circular trajectory ($\dot{\rho} = 0$) when there is no current ($v_x, v_y = 0$)
- The range to the beacon decreases ($\dot{\rho} < 0$) and increases ($\dot{\rho} > 0$) alternate and periodically in the presence of constant currents

In both cases, it is obvious that the vehicle reaches the most distant point of the invariant set with $\dot{\rho} = 0$.

Let c_m be a positive constant. For any $c_m \in (0, c_\beta)$, assume that the gain k in (4.28) is chosen so that

$$\bar{r} = k c_m.$$

Denoting the inverse of the function $\beta(\cdot)$ as $\beta^{-1}(\cdot)$, this choice will ensure that the yaw rate will be saturated at distances $\rho \geq \beta^{-1}(c_m)$, when the vehicle is moving away from the beacon.

Hence, suppose that, at time t_0 , the vehicle reaches the distance $\rho(t_0) = \beta^{-1}(c_m)$ and consider the worst possible case: the vehicle has the same direction of the current ($\psi(t_0) = \angle(v_x, v_y)$). The equation for the range can be written as

$$\rho(t) = \int_{t_0}^{t_0+t} \dot{\rho}(\zeta) d\zeta + \rho(t_0). \quad (4.34)$$

Define τ to be given so that, for $t \in [t_0, t_0 + \tau]$, the range is increasing ($\dot{\rho} \geq 0$) and $\dot{\rho}(t_0 + \tau) = 0$, or, in other words, at time $t_0 + \tau$, the vehicle reaches the most distant point of the invariant trajectory.

In order to find the maximum range, let us first compute the maximum time interval τ : it is possible to show that, for the interval $[t_0, t_0 + \tau]$, the following assumption holds: the vehicle reaches the most distant point of the invariant set with $|r(t_0 + \tau)| = \bar{r}$ since $e_{\dot{\rho}}(t) = \dot{\rho}(t) + \beta(t) > c_m$ for $t \in [t_0, t_0 + \tau]$.

Moreover, by taking into account that $\psi(t_0) = \angle(v_x, v_y)$, one can verify that $\dot{\rho} \leq 0$ if $\psi(t) = \psi(t_0) + \pi, t \in [t_0, t_0 + \tau]$. In other words, this means that the distance starts decreasing before the heading verify $\psi(t) = \psi(t_0) + \pi$. The geometrical interpretation of this fact is that the range starts decreasing before the vehicle heading is in the opposite direction of the current vector. Hence, the maximum time interval is given by

$$\tau < \frac{\pi}{\bar{r}}. \quad (4.35)$$

It is now possible to derive an upper bound on the maximum range of the invariant trajectory. From (4.5) and (4.34), one verifies

$$\begin{aligned} \lim_{t \rightarrow \infty} \rho(t) &\leq \int_{t_0}^{t_0 + \tau} u + \|v_c\| dt + \beta^{-1}(c_m) \\ &= \frac{(u + \|v_c\|)\pi}{\bar{r}} + \beta^{-1}(c_m). \end{aligned}$$

Notice that the limit is independent of the approach rate β . While approaching the beacon, the vehicle is no longer able to maintain a constant gradient due to bounded actuation. Indeed, the mean value of $\dot{\rho}$ converges to zero as $t \rightarrow \infty$, that is $\lim_{t \rightarrow \infty} \int_0^t \dot{\rho} = 0$.

4.4.3.2 Effect of disturbances on upper bound

Not only the currents, but external, unpredicted disturbances can act on the vehicle body. These disturbances may result from unconsidered effects such as sideslip and/or from unpredicted motion of the beacon. In their presence, an upper bound can be determined. Still, particular attention must be given to disturbance magnitude in order to meet the constraints established in the previous section.

Suppose that $d = \sup \sum d_i$ is a constant that comprises the sum of the unconsidered/unknown effects d_i on the vehicle absolute velocity. Aiming at maintaining the control law (4.28) valid, β has to be redefined so that $\beta < u - \|v_c\| - d$ for all ρ . Hence, following the same argument as previously yields concluding that the upper bound of the invariant trajectory is given by:

$$\lim_{t \rightarrow \infty} \rho(t) \leq \frac{(u + \|v_c\| + d)\pi}{\bar{r}} + \beta^{-1}(c_m). \quad (4.36)$$

This result is specially interesting because it defines a circumference around the beacon where the vehicle is guaranteed to lie after having entered into it. From the practical point of view, such characteristic leaves room to explore scenarios in which the AUV homes to a moving beacon. Moreover, unconsidered effects or model uncertainties can be integrated in the constant d to find an ultimate bound of convergence around the beacon.

4.4.4 Results

In-water trials were carried out during the summer of 2011 with the MARES AUV in the Douro river. At that time, MARES measured 1.7 meters long. Along with the homing mission, several operations were planned for environmental sampling. Besides the sensors commonly used for environmental sampling, MARES carried an acoustic transducer to measure ranges to an acoustic beacon placed on a surface buoy. Range measurements are based on the TOF of acoustic pings of a TWTT system. The vehicle interrogates the beacon periodically with approximately 4 seconds of interval, which is a relatively low rate for the homing maneuver. Nevertheless, the results below show that the method can be applied to systems with such characteristics.

For the present results, MARES was arbitrarily placed in the open area at a typical distance of a few hundreds of meters, constrained only by the operational constraints (river width, line-of-sight). Figure 4.10 shows the results obtained for the homing maneuver when the vehicle was placed at an initial distance of approximately 200m. During the trajectory, the AUV was subjected to several disturbances due to the proximity of the surface which are mainly induced by wind and currents. Moreover, surge velocity was well below the expected value due to unconsidered protuberances as MARES was carrying a conductivity temperature depth (CTD) sensor at starboard, thus leading to considerable disturbances in both the surge and the yaw rate dynamics. Additionally, other unconsidered effects due to shape changes for integration of sensors induced significant inaccuracies on the model. Still, the behavior remained robust enough to drive MARES to the beacon. Note that β can be adjusted as a function of the confidence on the actual surge velocity. Indeed, if the vehicle was set to move at a constant velocity and its actual velocity is below the expected one, the control remains valid, as long as the assumptions made in section 4.4.1 hold, and the vehicle can be driven to home by reducing the approach rate β (or more formally, its upper bound c_β).

One can verify that MARES rapidly converges to negative range rates (approaching the beacon) after pointing away from the beacon, during the initial instants. An interesting behavior happens at time $t = 6150$ s: the AUV heading passes through the unstable equilibrium point $\psi = \theta - \pi + \delta$ and is no longer able to track the gradient, likely due to disturbances, stronger currents at the surface and chattering induced by discrete time measurements. Indeed, the range rate is obtained by the rather rough estimate $\dot{\rho} \approx (\rho_k - \rho_{k-1}) / (t_k - t_{k-1})$. Nevertheless, under this situation, it keeps turning in the clockwise direction until reaching the stable angle, as expected.

Subsequently, the range rate is maintained negative with chattering due to measurement discretization which makes the control law apply too prolonged corrections to the heading in some situations. The vehicle finishes reaching the neighborhood of the beacon and maintaining a distance below 20m.

In order to improve the performances of the overall system response, a rough estimation of the range rate has been implemented, given by:

$$\hat{\rho} = \dot{\rho}_k + \alpha_k \psi, \quad (4.37)$$

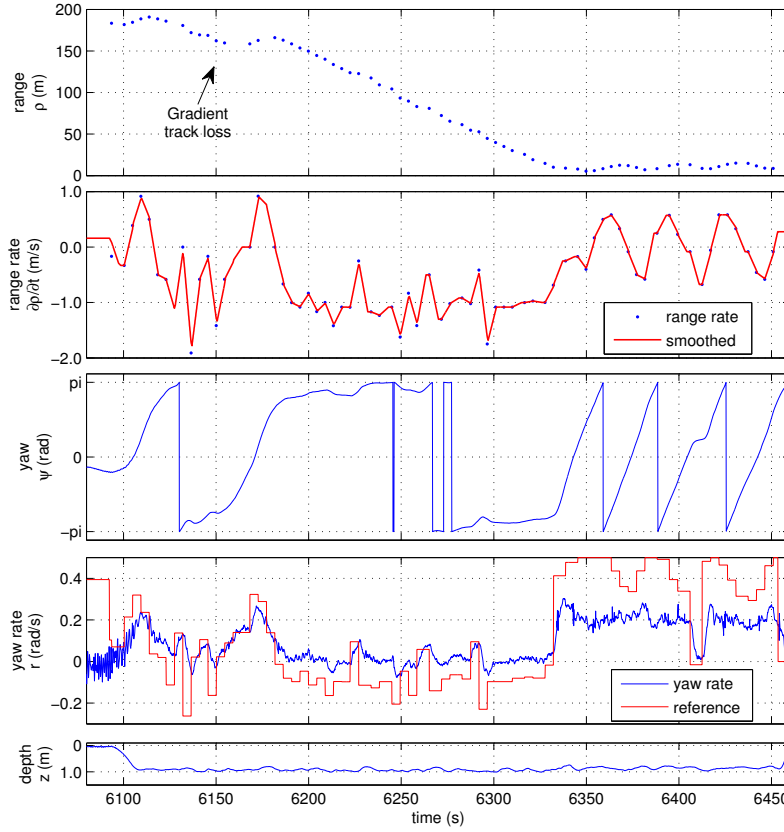


Figure 4.10: Results obtained for homing with surge velocity 1.0 meter per second (estimated) and desired approach rate $\beta = 0.6$ (log20110729142857)

where

$$\alpha_k = \begin{cases} l = \frac{\rho_k - \rho_{k-1}}{\psi(t_k) - \psi(t_{k-1})} & , \text{ if } \psi_k \neq \psi_{k-1} \wedge l \geq 0, \\ \alpha_{k-1} & , \text{ otherwise.} \end{cases}$$

The results of the homing maneuver including this last improvement are shown in figure 4.11. Note that the range rate becomes smoother during the approach and the maneuver ends with the vehicle in the vicinity of the beacon (below 10m). From (4.36), the maximum theoretical upper bound of the invariant set results $\lim_{t \rightarrow \infty} \rho(t) \leq 21$ meters for actual (estimated) surge velocity u of about 1.5 meters per seconds, current velocity $\|v_c\| = 0.25$ meters per second and disturbances d of about 0.2 meters per seconds, which includes unconsidered sway velocity and errors originated by discrete time measurements. The maximum yaw rate considered was the one observed in figure 4.10 ($\bar{r} \approx 0.25$ radians per second). The result is consistent with the logged data.

In both results, one can verify the absence of range measurements during some intervals or

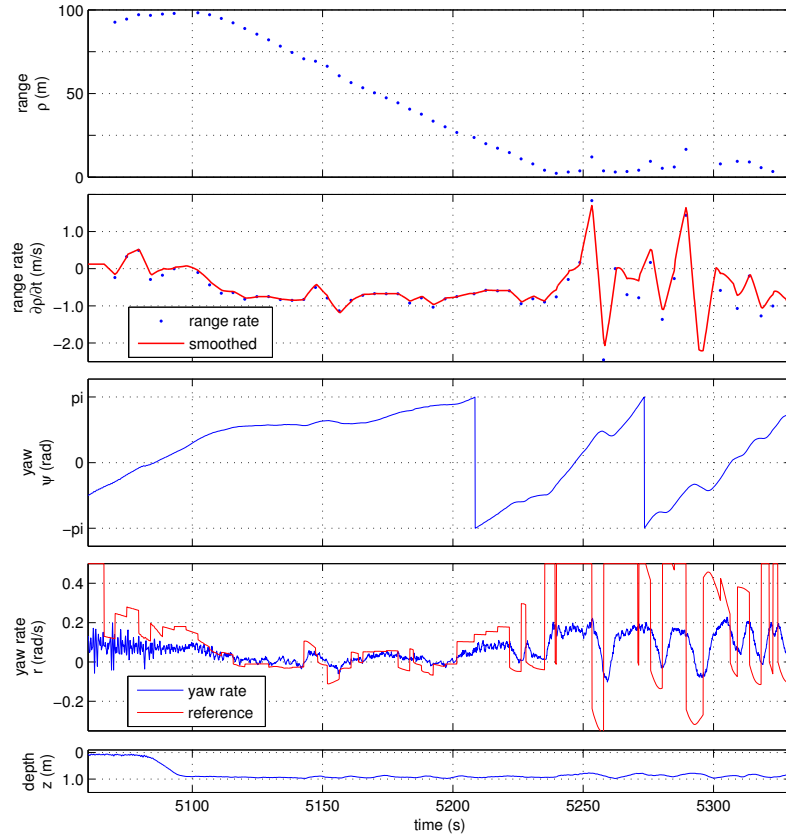


Figure 4.11: Results obtained for homing with surge velocity 1.5 meter per second (estimated) and desired approach rate $\beta = 0.7$ (log20110803142434)

even the presence of noisy measurements (outliers) originated by multipath reflections on the bottom, when MARES is close to the beacon (see figure 4.11). Still, the results show that the approach is capable of accommodating these sporadic erroneous measurements. Furthermore, it is expectable that the present approach is capable of handling hardly predictable offsets on the measurements coming from different properties of sound wave propagation. As an illustration, the difference in temperature and in density between two volumes of water (environments with different acoustic characteristics) would imply different speeds of propagation and, consequently, different range measurements for the same distance to the beacon. Since the range rate possesses the dominant role in the proposed control law, the effect of such property would be effective only on the transition from one to another environment. Furthermore, effects such as multipath and occlusions would make the vehicle behave in the same manner.

4.5 Conclusions

This chapter presented two different approaches to home a vehicle to a possibly varying position reference using ranges only. Firstly, the problem of localization was addressed by developing two estimators of different nature. The PFs are promising estimators that do not make assumptions on the noise. On the other hand, the EKF makes some assumptions on the kind of noise and need for initialization but it is generally less exigent in terms of computational requirements. A method using both filters was proposed: the PF estimates the initial position which is used afterwards by the EKF as the first estimate. Guidance questions could not be decoupled from estimation since observability is directly related with the trajectory. A guidance law was derived and posteriorly modified so that the trajectory changes according to the confidence on the estimate. For this part, the performances of the solutions were analyzed by means of realistic simulations. While the performances of the EKF approach demonstrated robustness and accuracy, the approach that only uses the particle filter frequently results in divergence of the estimate.

Then, a novel homing method for AUVs that are capable of measuring ranges to a given reference with unknown position was proposed. Driving the vehicle to home does not require solving the localization problem. Instead, coarse knowledge about disturbances is enough to enable an AUV to home. Having kept the approach simple and minimalistic, a specific control law has been derived and it has been demonstrated in both theory and practice that the homing method makes the vehicle converge to a reference even in the presence of significant disturbances and dynamics model inaccuracies. Moreover, the nature of the method makes it possible to derive upper bounds on the minimum distance that the vehicle is capable of reaching the beacon under different environmental conditions.

Although a specific type of vehicle was focused in this chapter, the derived control law is not limited to AUVs only and can also be applied to vehicles with controlled surge velocity and yaw rate. Further to the important role of the present method for missions of autonomous vehicles, the approach becomes particularly interesting for scenarios in which fault recovery or degraded mode navigation is required to home a vehicle with range-only measurements.

Besides the rather simple maneuver of homing, the method can also be extended to coordination problems (reference tracking) where an AUV or surface vessel is moving toward a moving reference and maintain a well known distance. Nonetheless, the maximum speed of the moving reference must be considered for the derivation of the control law.

Chapter 5

Local control for marine vehicles

Up to now, control and guidance have been proposed to endow autonomous marine vehicles to position themselves in uncommon modes of operation in chapter 3 or robustly approach a reference based on range measurements in chapter 4. These methods are *ad-hoc* solutions developed for specific purposes, which, in the latter case, assumed that the velocity could be controlled directly expecting that a lower level controller would solve the velocity tracking problem. In opposition to the previous chapters but also to complement the previous chapter, it is now intended to build a multilayer control architecture where different levels control different quantities, ultimately aiming at coordinating heterogeneous marine vehicles. The approach is similar to the inner-outer loop method presented in Fossen (1994). This chapter presents a solution for velocity control and target tracking for a broad class of marine vehicles.

Robotic systems are nonlinear. Therefore, high performance of robots requires nonlinear control techniques, otherwise leading to poorer, or even unstable, behaviors. Nonlinear control methods (see Khalil (2002)) include linearization, gain-scheduled, sliding mode control and backstepping (without being extensive). Linearization techniques take advantage of the vast results on linear control theory and are well suited for systems that operate at a nominal point of operation. Gain-scheduled control is a natural extension of the linearization technique by linearizing the systems at several points of operation and by interpolating the control laws. Sliding mode control and backstepping methods commonly result on nonlinear feedback control laws that typically employ a model of the dynamics. In the present work, the control laws for both underwater and surface robots were derived based on dynamics models.

Dynamics and kinematics control constitute the basic layer of our approach. It is important to keep the interaction with this layer simple and well defined while guaranteeing that the resulting behaviors can be versatile enough.

Besides velocity control and target tracking, special attention is given to modelling and measurement errors and on how they impact on reference tracking. Upper bounds on velocity error and on target tracking error are given.

5.1 Velocity control

Similarly to coordination problems, individual coherent and precise motion is desired in many robotic applications. The approach presented in this work requires bounded individual tracking errors. This section derives the low-level control laws that ensure such a bounded error.

5.1.1 Bounded velocity under bounded actuation

In many of the control problems, reduced models of vehicles are used to derive control laws and to infer about their stability but very few attention is given to the remaining degrees of freedom (DOFs). If their corresponding velocities become large, the system may become uncontrollable and unstable. Therefore, in the first part of this section, upper bounds are derived on the velocity of a marine (either underwater or surface) vehicle with limited actuation in order to support the derivation of the control laws.

Intuitively, one expects the velocity of marine vehicles to be limited under bounded actuation because of damping forces and moments. However, effects such as Coriolis and centripetal forces are less intuitive as they generally create several coupling forces and moments. The objective here is to verify bounded velocities and to determine such bounds.

To assess the dynamics under limited actuation, the first step is to define the set of the actuation vector and of the limited restoring forces and moments. Define the actuation vector to be component-wise bounded set, i.e., $\tau \in \Omega_\tau = \{\tau \in \mathbb{R}^{n_t} : |[\tau]_i| \leq \tau_{Mi}, i = 1, \dots, n_t\}$. Similarly, the vector of restoring forces and moments is considered to be bounded component-wise $g(\eta) \in \Omega_g = \{g(\eta) \in \mathbb{R}^6 : |[g(\eta)]_i| \leq g_{Mi}, i = 1, \dots, 6, \forall \eta(t)\}$. In the forthcoming analysis, we consider the matrix $|T| \in \mathbb{R}^{6 \times n_t}$ given by

$$|[T]|_{ij} = |[T]_{ij}|, \quad (5.1)$$

that is, $|T|$ is the matrix whose entries are the absolute values of the entries of T in (3.2).

The Lyapunov theory is used here to infer about the stability of the system. This widely used tool provides meaningful results on the behavior of dynamic systems and, therefore, constitutes a solid background for the upcoming developments. In addition to the analysis feature, the Lyapunov theory has naturally been applied in control law designs. Some examples are sliding mode control, the Lyapunov direct method and backstepping Khalil (2002).

Hence, the positive definite, radially unbounded Lyapunov function is defined as

$$V_b(v(t)) = \frac{1}{2} v(t)^T M v(t). \quad (5.2)$$

In order to assess the stability of the system, it is sufficient to determine its time-derivative:

$$\begin{aligned} \dot{V}_b(v(t)) &= v(t)^T M \dot{v} \\ &= v(t)^T (A(v(t))v(t) - h(\eta) + S\tau). \end{aligned}$$

Note that $A(\mathbf{v}(t)) = -C(\mathbf{v}(t)) - D(\mathbf{v}(t))$ and $\mathbf{v}(t)^T C(\mathbf{v}(t)) \mathbf{v}(t) = 0$ since $C(\mathbf{v}(t))$ is skew-symmetric. Moreover, for relatively large velocity, the quadratic terms of the damping forces and moment dominate in the presence of nonlinear skin friction and vortex shedding Fossen (1994). Nonetheless, it must be stressed that such simplification does not invalidate the following developments, as the remaining linear and nonlinear effects would contribute with more damping. Therefore, in many problems Fossen (1994); Ferreira et al. (2012, 2010), the viscous damping matrix takes the following representation $D(\mathbf{v}(t)) = D_1 \text{diag}(|\mathbf{v}(t)|)$, where $D_1 \in \mathbb{R}^{6 \times 6}$ and $\text{diag}(\cdot)$ denotes the diagonal matrix composed of the entries of its argument. Furthermore, define the positive definite matrix whose diagonal entries are positive and off-diagonal entries are non-positive that is:

$$D_c \in \mathbb{R}^{6 \times 6} : D_c > 0, [D_c]_{ii} > 0, [D_c]_{ij} \leq 0, i \neq j, \forall i, j = 1 \dots 6.$$

Additionally, assume that

$$D_c < D_1. \quad (5.3)$$

The idea behind defining this matrix is to reinforce the velocity bounds. In fact, as will be seen in the sequel, the upper bound the cross-coupling terms will subtract damping from the upper bound on the time derivative of the Lyapunov function (see (5.5)) and thus enabling the direct derivation of the velocity bounds for each DOF.

Hence, the time-derivative of the Lyapunov function results

$$\dot{V}_b(\mathbf{v}(t)) = \mathbf{v}(t)^T (-D_1 \text{diag}(|\mathbf{v}(t)|) \mathbf{v}(t) - g(\boldsymbol{\eta}) + T \boldsymbol{\tau}). \quad (5.4)$$

One can verify that the Lyapunov function time-derivative does not depend on the Coriolis and centripetal effects thus simplifying the determination of the bounds on the velocity vector. Using the facts that D_c is positive definite, the inequality in (5.3) and the equality $\mathbf{v}(t)^T \mathbf{v}(t) = |\mathbf{v}(t)|^T |\mathbf{v}(t)|$, the following upper bound is found for the Lyapunov function time derivative (5.4)

$$\dot{V}_b(\mathbf{v}(t)) \leq |\mathbf{v}(t)|^T (-D_c \text{diag}(|\mathbf{v}(t)|) |\mathbf{v}(t)| + g_M + |T| \boldsymbol{\tau}_M), \quad (5.5)$$

where $[g_M]_i = g_{Mi}$ and $[\boldsymbol{\tau}_M]_i = \tau_{Mi}$ are the vector whose entries are the upper bounds on the absolute values of the restoring forces and moments and actuation forces, respectively. Hence, the following implication holds:

$$[\text{diag}(\mathbf{v}(t)) \mathbf{v}(t)]_i > [(D_c)^{-1} (g_M + |T| \boldsymbol{\tau}_M)]_i, \forall i = 1, \dots, 6, \Rightarrow \dot{V}_b(\mathbf{v}(t)) < 0,$$

or, equivalently,

$$\dot{V}_b(\mathbf{v}(t)) < 0 \quad (5.6)$$

if

$$|[\mathbf{v}(t)]_i| \geq [v_M(t)]_i \left([(D_c)^{-1} (g_M + |T| \boldsymbol{\tau}_M)]_i \right)^{1/2}, \forall i = 1, \dots, 6, \quad (5.7)$$

According to this result, and recalling that the Lyapunov function $V_b(\mathbf{v}(t))$ is positive definite and

a radially unbounded function of the norm $\|\mathbf{v}(t)\|$, this implies that no solution can stay in the set $\{\mathbf{v}(t) \in \mathbb{R}^6 : |[\mathbf{v}(t)]_i| \geq ([(D_c)^{-1}(g_M + |T|\boldsymbol{\tau}_M)]_i)^{1/2}, \forall i = 1, \dots, 6\}$ for all time. The velocity vector eventually converges to an invariant set contained in a hyperrectangle that contains the origin and is defined by the entries of the vector $([(D_c)^{-1}(g_M + |T|\boldsymbol{\tau}_M)]_i)^{1/2}$ no matter what the actuation forces or the initial conditions are. The latter result is especially interesting and important since it individually bounds the velocities over each DOF. Both support common simplifications used in several problems, such as order reduction, by stating that the neglected DOFs are well behaved. Although this bound may seem conservative since the term

$$(-D_c \text{diag}(|\mathbf{v}(t)|)|\mathbf{v}(t)| + g_M + |T|\boldsymbol{\tau}_M)$$

in (5.5) is required to have positive entries, this yields component-wise bounds instead of more “classical” results that impose a bound to the norm of the vector. Nevertheless, these results can also be easily derived as follows, for completeness.

A similar though more conservative result can be extracted from these expressions using the concept of ultimate boundedness Khalil (2002). Take the maximum velocity component as

$$v_M = \max_i ([(D_c)^{-1}(g_M + |T|\boldsymbol{\tau}_M)]_i)^{1/2} \quad (5.8)$$

and define the smallest and largest eigenvalues of a generic matrix B as $\lambda_{\min}(B)$ and $\lambda_{\max}(B)$, respectively. Then, from (5.2), one can easily show that

$$\frac{1}{2} \lambda_{\min}(M) \|\mathbf{v}(t)\|^2 \leq V_b(\mathbf{v}(t)) \leq \frac{1}{2} \lambda_{\max}(M) \|\mathbf{v}(t)\|^2 \quad (5.9)$$

Since $|[\mathbf{v}(t)]_i| \geq v_M$ implies $\|\mathbf{v}(t)\| \geq \sqrt{6}v_M$, the time derivative of the Lyapunov function $V_b(\mathbf{v}(t))$ upper bounded

$$\dot{V}_b(\mathbf{v}(t)) \leq -W(\mathbf{v}(t)) = |\mathbf{v}(t)|^T (-D_c \text{diag}(|\mathbf{v}(t)|)|\mathbf{v}(t)| + g_M + |T|\boldsymbol{\tau}_M) \leq 0, \quad \forall \|\mathbf{v}(t)\| \geq \sqrt{6}v_M > 0.$$

Hence, the direct application of the theorem (Khalil, 2002, 4.18 pp.172) states that the velocity satisfies, for a time $T > 0$:

$$\|\mathbf{v}(t)\| \leq \sqrt{\frac{6\lambda_{\min}(M)}{\lambda_{\max}(M)}} v_M, \quad \forall t > T \quad (5.10)$$

that is, the velocity is globally ultimately bounded by $\sqrt{\frac{6\lambda_{\min}(M)}{\lambda_{\max}(M)}} v_M$ and reaches this bound in finite time. This result is more conservative than the one defined in (5.7) as the sphere defined by $\sqrt{\frac{6\lambda_{\min}(M)}{\lambda_{\max}(M)}} v_M$ contains all the corners of the hipercube implied in (5.7), since $\frac{\lambda_{\min}(M)}{\lambda_{\max}(M)} \geq 1$. However, this is connected to an important theory on perturbed systems and with widely used results on system analysis (see Khalil (2002)). A similar result can also be obtained in the context of input-to-state stability (ISS) with regard to the vector $g_M + |T|\boldsymbol{\tau}_M$.

It is important to highlight that the results presented still provide an upper bound on the velocity vector even neglecting the lower and higher order terms of damping. Since such terms are dissipative, they would contribute to a larger $D(\mathbf{v}(t))$ and consequently decrease the bounds, as suggested by the inverse of the matrix in (5.7).

5.1.2 Inner velocity loop

In the decoupled control architecture presented here, different loops are considered where different quantities are stabilized at desired, possibly time-varying, set points. The goal now is to stabilizing the velocity vector at a desired velocity $\mathbf{v}^*(t) : \mathbb{R} \rightarrow \mathbb{R}^n$, where $n \leq 6$. This vector, with a possibly lower dimension than the dynamics model (2.2), comes from the interest of controlling only part of the DOFs. In nonholonomic robots, the dimension of this vector is often equal to the number of DOFs, that is, the number of velocities that can be controlled directly. Sometimes, the dimension can be smaller than the degrees of DOFs, by neglecting some of them and using the fact that they are well-behaved or assuming that they are controlled independently (see, for example, Ferreira et al. (2010b)). The Lyapunov direct method will be used to derive the velocity control law.

Based on (2.2), consider the reduced order velocity vector $\bar{\mathbf{v}}(t) : \mathbb{R} \rightarrow \mathbb{R}^n$, whose dynamics is given by

$$\dot{\bar{\mathbf{v}}}(t) = P\bar{M}^\dagger (\bar{A}(\mathbf{v}(t))\mathbf{v}(t) - \bar{g}(\boldsymbol{\eta}(t)) + \bar{T}\boldsymbol{\tau}) \quad (5.11)$$

where the reduced order matrices and vectors are given by

$$\begin{aligned} \bar{\mathbf{v}}(t) &= P\mathbf{v}(t), \\ \bar{M} &= PM, \\ \bar{A}(\mathbf{v}(t)) &= PA(\mathbf{v}(t)), \\ \bar{g}(\boldsymbol{\eta}(t)) &= Pg(\boldsymbol{\eta}), \\ \bar{T} &= PT, \end{aligned}$$

with $P \in \mathbb{R}^{n \times 6}$ being a generic projection matrix, whose rows have norms equal to one and are mutually orthogonal. This matrix maps the overall system in a smaller dimension subspace considering only the relevant DOFs, by selecting the corresponding rows and columns.

Example 5.1. Suppose that the intention is to control the surge, heave and yaw velocities, that is, the linear velocities along the x -, z -axes and the angular velocity along the z -axis. Suppose that these are the only velocities considered. The choice for the projection matrix would then be

$$P = \begin{bmatrix} 1 & 0 & 0 & 0 & 0 & 0 \\ 0 & 0 & 1 & 0 & 0 & 0 \\ 0 & 0 & 0 & 0 & 0 & 1 \end{bmatrix}.$$

The first row captures the surge dynamics, the second captures the heave and the third captures the yaw one.

Note that the rows of the projection matrix P are orthogonal vectors. Moreover, the matrix $P\bar{M}^\dagger$ is square and has full rank in this case, which means that it is invertible.

It is important to note that all the states of the reduced model are controlled if \bar{T} has full row rank. This condition is assumed to be verified from now on.

Let us now focus on the derivation of a control to track a velocity reference. In order to find a suitable control law, the velocity error vector is defined as the difference between the actual and the desired velocities:

$$\tilde{\mathbf{v}}(t) = \bar{\mathbf{v}}(t) - \mathbf{v}^*(t).$$

Using (5.11), the time derivative of the error vector results

$$\dot{\tilde{\mathbf{v}}}(t) = P\bar{M}^\dagger (\chi(\mathbf{v}(t), \boldsymbol{\eta}(t)) + \bar{T}\boldsymbol{\tau}) - \dot{\mathbf{v}}^*(t), \quad (5.12)$$

where $\chi(\mathbf{v}(t), \boldsymbol{\eta}(t)) = \bar{A}(\mathbf{v}(t))\mathbf{v}(t) - \bar{g}(\boldsymbol{\eta}(t))$. Noting that $P\bar{M}^\dagger$ is invertible, this expression suggests the control law for the control input

$$\boldsymbol{\tau} = (\bar{T})^\dagger \left((P\bar{M}^\dagger)^{-1} \dot{\mathbf{v}}^*(t) - \chi(\mathbf{v}(t), \boldsymbol{\eta}(t)) - K_v \tilde{\mathbf{v}}(t) \right), \quad (5.13)$$

where $K_v \in \mathbb{R}^n$ is a positive definite matrix. This makes the error dynamics globally exponentially stable:

$$\dot{\tilde{\mathbf{v}}}(t) = -P\bar{M}^\dagger K_v \tilde{\mathbf{v}}(t).$$

Exponential stability is often desired as it provides superior tracking performances even in the presence of modelling errors when compared to asymptotically stable systems (Chung and Slotine, 2009).

Thus far, it has been assumed that the model is perfectly known which may be unrealistic in real applications. Actually, in robotics in general, and especially in marine robotics, exact models are very hard to obtain and, therefore, errors are naturally introduced. However, one may have a rough notion or a reasonable estimated upper bound on the introduced error, which in turn can be used in the controller design process to ensure stability and to meet the desired performances.

5.1.3 Error boundedness

In order to determine the necessary conditions to ensure convergence to the vicinity of the desired velocity and to assess the impact of the errors on the dynamics model, an analysis is provided considering a model error. To make the notation consistent with the previous developments, the notation $(\bar{\cdot})$ is used for the reduced order matrices and vectors, and denote the model terms as $(\cdot)_m$ and the errors terms as $(\cdot)_e$.

The analysis starts from (5.12), where it is assumed that the dynamics can be decomposed in two components: modelled and error components. More specifically, it is assumed that

$$\chi(\mathbf{v}(t), \boldsymbol{\eta}(t)) = \chi_m(\mathbf{v}(t), \boldsymbol{\eta}(t)) + \chi_e(\mathbf{v}(t), \boldsymbol{\eta}(t)), \quad (5.14)$$

where $\chi_m(\mathbf{v}(t), \boldsymbol{\eta}(t))$ and $\chi_e(\mathbf{v}(t), \boldsymbol{\eta}(t))$ stand for the modelled and error components, with

$$\begin{aligned}\chi_m(\mathbf{v}(t), \boldsymbol{\eta}(t)) &= \bar{A}_m(\mathbf{v}(t))\mathbf{v}(t) - \bar{g}_m(\boldsymbol{\eta}(t)) \\ \chi_e(\mathbf{v}(t), \boldsymbol{\eta}(t)) &= \bar{A}_e(\mathbf{v}(t))\mathbf{v}(t) - \bar{g}_e(\boldsymbol{\eta}(t)).\end{aligned}$$

As for $A(\mathbf{v}(t))$ and $\bar{A}(\mathbf{v}(t))$, the matrices above are defined as the sum of Coriolis and centripetal and damping components, respectively:

$$\begin{aligned}\bar{A}_m(\mathbf{v}(t)) &= P(C_m(\mathbf{v}(t)) + D_m(\mathbf{v}(t))) \\ \bar{A}_e(\mathbf{v}(t)) &= P(C_e(\mathbf{v}(t)) + D_e(\mathbf{v}(t))),\end{aligned}$$

where the inertia matrix is given by $M = M_m + M_e$ and the matrices $C_m(\mathbf{v}(t))$, $D_m(\mathbf{v}(t))$ and $C_e(\mathbf{v}(t))$, $D_e(\mathbf{v}(t))$ are the modelled and *error* Coriolis and damping matrices, respectively. As it is important for the forthcoming analysis, we highlight that, since $C_m(\mathbf{v}(t))$ and $C(\mathbf{v}(t))$ are skew-symmetric matrices and the subtraction (sum) of skew-symmetric matrices result in a skew-symmetric matrix, $C_e(\mathbf{v}(t))$ is also skew-symmetric.

Note that errors on $\dot{\mathbf{v}}^*(t)$ nor on \bar{T} (or, equivalently, T) have not been considered. This is reasonable for $\dot{\mathbf{v}}^*(t)$ since it is intrinsically given by the desired velocity reference, which is perfectly known. It is also fair to consider T with no error as it mostly depends on the relative positions of the actuators and of the center of gravity, which may be accurately determined using simple practical methods (see Ferreira et al. (2012), for example). Nonetheless, additional but generally small effects originated from torques induced by rotating propellers may be difficult to quantify. Moreover, the determination of exact forces exerted by the thrusters are also intricate, since they depend on the angular velocity of the thruster, on the propeller shape and on the relative velocity of the fluid passing by the propeller, which is obviously complex to measure. It is assumed here that these errors can be incorporated in the product $T\boldsymbol{\tau}$ by considering actuation errors only: suppose that the actuation vector is given by the sum of the modelled actuation $\boldsymbol{\tau}_m$ plus an error $\boldsymbol{\tau}_e$, that is, $\boldsymbol{\tau} = \boldsymbol{\tau}_m + \boldsymbol{\tau}_e$.

Provided that exact models are very difficult to obtain, instead of (5.13), a natural choice for the control law is

$$\boldsymbol{\tau}_m = (\bar{T})^\dagger \left((P\bar{M}_m^\dagger)^{-1} \dot{\mathbf{v}}^*(t) - \chi_m(\mathbf{v}(t), \boldsymbol{\eta}(t)) - K_v \tilde{\mathbf{v}}(t) \right). \quad (5.15)$$

Using (5.12) with (5.14) and (5.15) makes the error dynamics

$$\dot{\tilde{\mathbf{v}}}(t) = P\bar{M}^\dagger (\chi_e(\mathbf{v}(t), \boldsymbol{\eta}(t)) - K_v \tilde{\mathbf{v}}(t) + \bar{T} \boldsymbol{\tau}_e) + \left(P\bar{M}^\dagger (P\bar{M}_m^\dagger)^{-1} - I \right) \dot{\mathbf{v}}^*(t) \quad (5.16)$$

The Lyapunov theory background is used here to assess the stability of this closed-loop dynamics. Therefore, the radially unbounded, positive definite, Lyapunov function is defined as

$$V_v = \frac{1}{2} \tilde{\mathbf{v}}(t)^T (P\bar{M}^\dagger)^{-1} \tilde{\mathbf{v}}(t),$$

whose time derivative is given by

$$\dot{V}_v = \tilde{v}(t)^T (P\tilde{M}^\dagger)^{-1} \dot{\tilde{v}}(t).$$

Replacing (5.16) in the last expression yields

$$\dot{V}_v = \tilde{v}(t)^T \left[\chi_e(v(t), \eta(t)) - K_v \tilde{v}(t) + \bar{T} \tau_e + \left((P\tilde{M}_m^\dagger)^{-1} - (P\tilde{M}^\dagger)^{-1} \right) \dot{v}^*(t) \right]. \quad (5.17)$$

The intention is to prove that the error converges to a neighbourhood of the origin. An ultimate bound can be derived based on estimates of the errors introduced in the model. Some practical and realistic assumptions have to be made.

Assumption 5.1.1. *The time derivative of the desired velocity $v^*(t)$ is bounded so that $|\dot{v}^*(t)| \leq \delta_{\dot{v}^*} \in \mathbb{R}^n$.*

Assumption 5.1.2. *The error introduced in the modelled restoring forces and moments vector is bounded as $g_e(\eta(t)) \leq g_{eM} \in \mathbb{R}^n$, $\forall \eta(t)$.*

The idea now is to find bounds on the vectors $\chi_e(v(t), \eta(t))$ and M_e in order to come up with an ultimate bound on $\tilde{v}(t)$. Note that the time derivative of the Lyapunov function is upper bounded as

$$\dot{V}_v \leq |\tilde{v}(t)|^T \left[|\chi_e(v(t), \eta(t))| - K_v |\tilde{v}(t)| + |\bar{T}| |\tau_e| + \left| \left((P\tilde{M}_m^\dagger)^{-1} - (P\tilde{M}^\dagger)^{-1} \right) \dot{v}^*(t) \right| \right]. \quad (5.18)$$

Recall that $\chi_e(v(t), \eta(t)) = P(C_e(v(t)) + D_e(v(t)))v(t) - \bar{g}_e(\eta(t))$. Then, it is possible to write

$$|\tilde{v}(t)|^T |\chi_e(v(t), \eta(t))| \leq |\tilde{v}(t)|^T \left(|PC_e(v(t))v(t)| + |PD_e(v(t))v(t)| + |\bar{g}_e(\eta(t))| \right). \quad (5.19)$$

The following task is finding upper bounds on each term individually. From assumption 5.1.2 it is clear that

$$|\tilde{v}(t)|^T |g_e(\eta(t))| \leq |\tilde{v}(t)|^T P g_{eM}. \quad (5.20)$$

Using the fact that, for the maximum possible velocity $v(t) = v_M(t)$, the quadratic damping is dominant, or more generally, that it is possible to find a D_{eM} with non-negative entries, that is $D_{eM} = |D_{eM}|$, so that $D_e(v(t)) \leq D_{eM} \cdot \text{diag}(|v(t)|)$, it yields

$$\begin{aligned} |\tilde{v}(t)|^T |PD_e(v(t))v(t)| &\leq |\tilde{v}(t)|^T PD_{eM} \text{diag}(|v_M(t)|) |v(t)| \\ &\leq |\tilde{v}(t)|^T PD_{eM} \text{diag}(|v_M(t)|) v_M(t) \end{aligned} \quad (5.21)$$

for all $|v(t)| \leq |v_M(t)|$. In practice, $D_e(v(t))$ is the matrix of maximum estimated error, whose entries are non-negative. Although it is difficult to find accurate estimates of the errors, upper bounds can be estimated either in theory using a rough notion of neglected effects, or in practice by observing the navigation data, for example.

Finding an upper bound on $|\tilde{\mathbf{v}}(t)|^T |PC_e(\mathbf{v}(t))\mathbf{v}(t)|$ is slightly more difficult since it implies looking at the form of $C_e(\mathbf{v}(t))$. It is important to recall that $C_e(\mathbf{v}(t))$ is a skew-symmetric matrix, and that its entries are the dot product of two vectors (see Fossen (1994)), admitting the following representation:

$$C_e(\mathbf{v}(t)) = \begin{bmatrix} 0 & 0 & 0 & h_{14} & h_{15} & h_{16} \\ 0 & 0 & 0 & h_{24} & h_{25} & h_{26} \\ 0 & 0 & 0 & h_{34} & h_{35} & h_{36} \\ -h_{14} & -h_{24} & -h_{34} & 0 & h_{45} & h_{46} \\ -h_{15} & -h_{25} & -h_{35} & -h_{45} & 0 & h_{56} \\ -h_{16} & -h_{26} & -h_{36} & -h_{46} & -h_{56} & 0 \end{bmatrix}$$

with

$$h_{ij} = h_{ij}(\mathbf{v}(t)) = c_{ij}^T \mathbf{v}(t) \quad (5.22)$$

where $c_{ij} \in \mathbb{R}^6$, $i = 1, \dots, 5$, $j = 4, \dots, 6$. Using the Cauchy-Schwarz inequality, $c_{ij} \mathbf{v}(t) \leq \|c_{ij}\| \cdot \|\mathbf{v}_M(t)\|$, for all $|\mathbf{v}(t)| \leq |\mathbf{v}_M(t)|$. This yields

$$\begin{aligned} |\tilde{\mathbf{v}}(t)|^T |PC_e(\mathbf{v}(t))\mathbf{v}(t)| &\leq |\tilde{\mathbf{v}}(t)|^T PF(\{c_{ij}\}) \|\mathbf{v}_M(t)\| |\mathbf{v}(t)| \\ &\leq |\tilde{\mathbf{v}}(t)|^T PF(\{c_{ij}\}) \|\mathbf{v}_M(t)\| \|\mathbf{v}_M(t)\| \end{aligned} \quad (5.23)$$

where

$$F(\{c_{ij}\}) = \begin{bmatrix} 0 & 0 & 0 & \|c_{14}\| & \|c_{15}\| & \|c_{16}\| \\ 0 & 0 & 0 & \|c_{24}\| & \|c_{25}\| & \|c_{26}\| \\ 0 & 0 & 0 & \|c_{34}\| & \|c_{35}\| & \|c_{36}\| \\ \|c_{14}\| & \|c_{24}\| & \|c_{34}\| & 0 & \|c_{45}\| & \|c_{46}\| \\ \|c_{15}\| & \|c_{25}\| & \|c_{35}\| & \|c_{45}\| & 0 & \|c_{56}\| \\ \|c_{16}\| & \|c_{26}\| & \|c_{36}\| & \|c_{46}\| & \|c_{56}\| & 0 \end{bmatrix}.$$

This result is in agreement with results presented in Mulero-Martinez (2007).

For the remaining term, it is important to highlight that

$$|\tilde{\mathbf{v}}(t)|^T \left| \left((P\tilde{M}_m^\dagger)^{-1} - (P\tilde{M}^\dagger)^{-1} \right) \dot{\mathbf{v}}^*(t) \right| \leq |\tilde{\mathbf{v}}(t)|^T \left| (P\tilde{M}_m^\dagger)^{-1} - (P\tilde{M}^\dagger)^{-1} \right| |\dot{\mathbf{v}}^*(t)|, \quad (5.24)$$

and denote $M_{eM} \geq M_e$, the positive semi-definite matrix with non-negative entries. Hence, using assumption 5.1.1, it follows that

$$|\tilde{\mathbf{v}}(t)|^T \left| (P\tilde{M}_m^\dagger)^{-1} - (P\tilde{M}^\dagger)^{-1} \right| |\dot{\mathbf{v}}^*(t)| \leq |\tilde{\mathbf{v}}(t)|^T \left| (P\tilde{M}_m^\dagger)^{-1} - (P(PM_m + PM_{eM})^\dagger)^{-1} \right| |\delta_{\dot{\mathbf{v}}^*}|. \quad (5.25)$$

Finally, defining, for simplicity

$$\begin{aligned}
 \xi_1 &= |\bar{T}||\tau_e| \\
 \xi_2 &= P g_{eM} \\
 \xi_3 &= P D_{eM} \text{diag}(|v_M(t)|) v_M(t) \\
 \xi_4 &= P F(\{c_{ij}\}) |v_M(t)| v_M(t) \\
 \xi_5 &= \left| (P \bar{M}_m^\dagger)^{-1} - (P(PM_m + PM_{eM})^\dagger)^{-1} \right| |\delta_{\dot{v}^*}|,
 \end{aligned} \tag{5.26}$$

and using (5.18)-(5.25), it is possible to write the following implication

$$|[\tilde{v}(t)]_i| > [\tilde{v}_M]_i = [(K_v)^{-1} (\xi_1 + \xi_2 + \xi_3 + \xi_4 + \xi_5)]_i \Rightarrow \dot{V}_v \leq 0$$

Therefore, for any initial condition verifying $\tilde{v}(t) \leq \tilde{v}_M$, the velocity error vector will remain in the invariant set bounded by the entries of the vector \tilde{v}_M for all future times. Otherwise, the error vector will eventually converge to this invariant set.

As expected, the upper bound on the velocity error is a function of the inverse of the gain matrix K_v . One may note that the error can be made arbitrarily small by choosing a large K_v . Given an estimate on the error introduced in the model, this matrix can be tuned to meet a given velocity error. Nevertheless, this choice has to be balanced in practice as it will have a direct consequence on the response of the vehicle to velocity measurement noise, and may also lead to saturation of actuators for larger errors. This, in turn, does not guarantee the desired exponential stability. Moreover, this gain may be limited by the bandwidth of the actuators, whose nonlinear dynamics was not considered here, but remains valid when the response time of the actuators is fast enough when compared to the dynamics.

It was proven that under specific conditions, in the presence of model errors, the velocity error vector will remain bounded. It is possible to see from the last implication that the bound of the velocity error is directly proportional to the maximum time derivative of the desired velocity ($\dot{v}^*(t)$). This means that the references given by any higher level algorithm have to be smooth enough to bound the velocity tracking error.

Example 5.2. *To illustrate this section, the MARES AUV is considered as a case-study. Based on its model (see appendix C), the upper bound on the velocity vector is determined using the results obtained in section 5.1.1. The maximum velocity vector is bounded by the entries of v_M , which take the following values:*

$$v_M = \begin{bmatrix} u_M \\ v_M \\ w_M \\ p_M \\ q_M \\ r_M \end{bmatrix} = \begin{bmatrix} 2.5 \\ 0.13 \\ 0.62 \\ 8.4 \\ 1.1 \\ 0.52 \end{bmatrix}.$$

The first three entries stand for the maximum surge, sway and heave velocities (in meters per second) while the last three stand for the roll, pitch and yaw rate maximum angular velocities (in radians per second), respectively.

These are in agreement with those verified in practice. Nevertheless, the roll rate seems to be exaggerated. In fact, this value results from the very small damping on the roll motion, as well as from the fact that the upper bound on the restoring forces and moments vector g_M was considered for the worst possible case (vehicle rolled 90 degrees) thus inducing in g_M a moment on roll that is not verified in practice, unless it is forced by an external moment.

When determining hydrodynamic models for underwater vehicles, added mass and inertia terms can be determined quite accurately as they depend on the volume, shape and water density and mass and moment of inertia, respectively, which can all be accurately determined either using hydrodynamic theory or computational fluid dynamics (CFD). In opposition, viscous damping coefficients are generally difficult to obtain accurately since they depend on multiple parameters such as roughness, shape, Reynold's number, among others (White, 2003; Hoerner, 1965; Prestero, 2001). Additionally, most parameters are derived based on empirical formulas and typically result from truncated series. The set of DOFs composed of surge, heave, pitch and yaw has been considered. Using a matrix gain of the same order of magnitude as that used in practice and equal to $K_v = \text{diag}([100 \ 100 \ 100 \ 100])$, and assuming that the viscous damping coefficients and the inertia and added mass terms are both affected by an error of 10%, the maximum velocity tracking error is bounded by

$$\tilde{v}_M = \begin{bmatrix} \tilde{u}_M \\ \tilde{w}_M \\ \tilde{q}_M \\ \tilde{r}_M \end{bmatrix} = \begin{bmatrix} 0.45 \\ 0.50 \\ 0.40 \\ 0.36 \end{bmatrix},$$

for surge, heave, pitch rate and yaw rate, respectively. A 5% error on actuation and a bound $\delta_{v^*} = [1 \ 1 \ 1 \ 1]^T$ on the absolute time derivative of the desired velocity have been considered. Note that, for this result, it was considered that the roll rate is approximately null $[v_M]_4 \approx 0$ as it naturally is in typical operations.

5.1.4 Combinations of DOFs and guidance

The velocity control law defined in (5.13) enables controlling the entire set of DOFs of a vehicle through velocity references, which can be easily employed by guidance laws that feed the velocity controller. In order to unify the interaction with a set of heterogeneous vehicles, it might be interesting to define common maneuvers specially designed for the corresponding platform. Implementing a set of common maneuvers simplifies the interaction and the commands given by an operator or any high level algorithm to conceptually different vehicles, independently of their individual characteristics.

Moreover, the use of an inner velocity loop, enables decoupling the various DOFs of a vehicle. Such an approach allows for composed and decoupled elemental motion primitives. For example,

the depth reference can be set to a given, possibly time-varying, reference independently of the horizontal motion, which could be particularly appreciated under some scenarios such as bottom exploration.

This approach has been transversal to all the vehicles that served as assets in the work presented in this document. Hence, these robots can be commanded by setting

- the desired maneuver along with its parameters (for example, line-following and corresponding initial and final points);
- the desired pose or velocity reference(s).

Combinations of maneuvers with pose and velocity references are permitted.

Four types of *maneuvers* have been identified for marine vehicles: line-following, circle-following, waypoint and target tracking. The first two guarantee that each robot can follow any complex path, which can be approximated by concatenation of trimming paths such as simple lines and circles (Ghabcheloo et al., 2009). Waypoint and target-tracking allow versatile behaviors frequently desired in marine operations. Additionally, it might also be desirable that the robot can be operated in a "direct" manner through a fifth (free) mode that enables setting pose or velocity references explicitly to each DOF. Apart from the target tracking guidance, which has a special importance in the next chapters, the remaining maneuvers are not addressed in this thesis as several methods have already been proposed by several authors (some examples can be found in (Aguiar and Hespanha, 2007; Borhaug et al., 2007; Ghabcheloo, 2007; Ghabcheloo et al., 2009)).

As a simple exercise, consider the TriMARES AUV, which has been presented in section 2.6 and whose model parameters are given in D, in the next example.

Example 5.3. *As for the remaining vehicles, an inner velocity loop as described in section 5.1 has been developed and implemented for TriMARES.*

At the kinematics level a depth controller and a pitch controller, among others for the remaining DOFs, have been implemented. The heave, surge and pitch velocity references are generated according to the guidance laws:

$$u^*(t) = \frac{w s \theta}{c \theta} \quad (5.27)$$

$$w^*(t) = \frac{\zeta_z + u s \theta}{c \theta} \quad (5.28)$$

$$q^*(t) = -K_\theta \text{sat}(\theta - \theta^* - \dot{\theta}^*/K_\theta, \delta_\theta) \quad (5.29)$$

where

$$\zeta_z = -K_z \text{sat}(z - z^* - \dot{z}^*/K_z + \sigma_z/K_z, \delta_z)$$

and $K_\theta > 0$, $K_z > 0$ are scalar gains and $\delta_\theta > 0$, $\delta_z > 0$ are the saturation values. The term σ_z is used for asymptotic regulation (Singh and Khalil, 2005), providing integral action, and is given

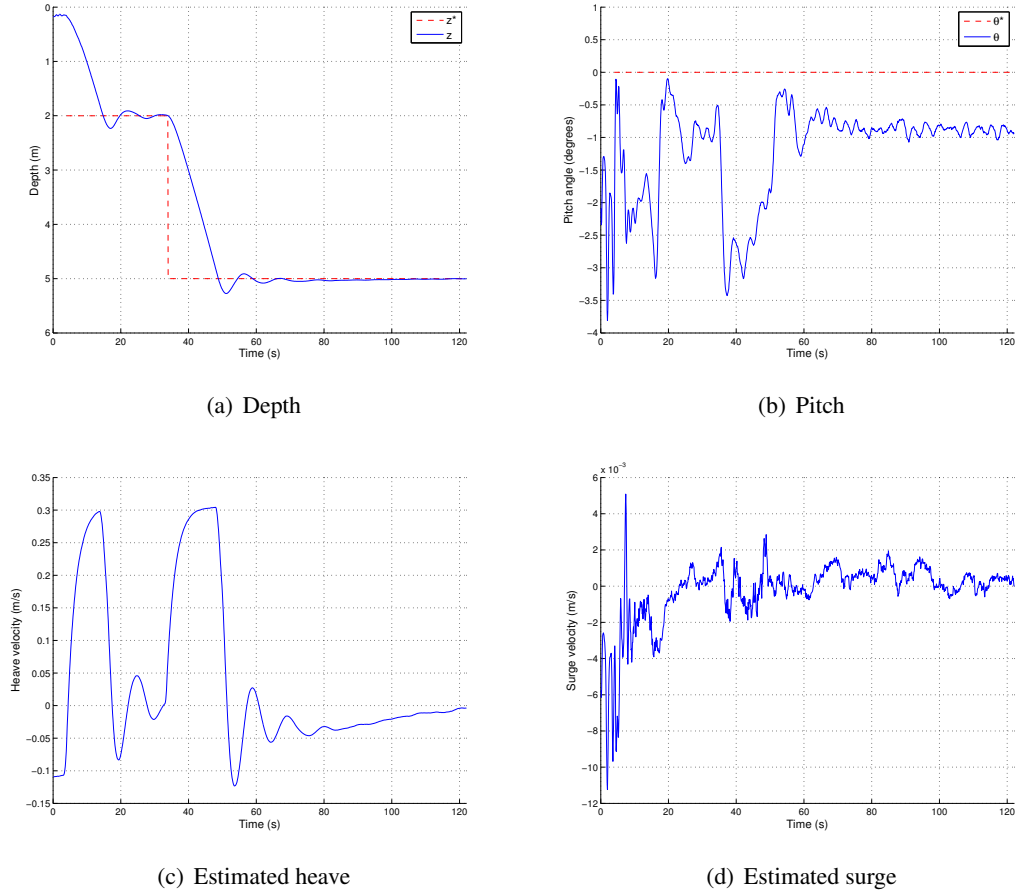


Figure 5.1: Controlled states during a hovering maneuver of TriMARES

by

$$\dot{\sigma}_z = -\gamma \sigma_z + \mu \text{sat}(z - z^*, \delta_\mu) \quad (5.30)$$

with $\gamma > 0$, $\mu > 0$ and $\delta_\mu > 0$.

During the first trials, its depth reference was set to $z^* = 2$ meters and posteriorly changed to $z^* = 5$ meters, by means of a mission script interpreted by the control software. The pitch angle reference was set null $\theta^* = 0$. The results of the depth and of the pitch control are depicted in figure 5.1. The plotted depth, pitch and heave demonstrate the performances of this implementation. The surge and heave velocities have been estimated on-line according to the model in D. Depth and pitch are obtained directly from sensor measurements. It can be seen that, although the pitch angle is not null over the entire operation, it remains close to zero. The largest deviations are caused by the heave motion. These deviations are likely caused by parameter mismatches and measurement offsets that make the state be in the vicinity of the reference but not coincident.

5.2 Target tracking and station keeping

Taking into account real practical problems such as model uncertainties, a target tracking problem built upon an inner-outer loop architecture is now addressed. In this topology the inner loop controller, derived in the previous section, stabilizes the velocity loop and a kinematic controller stabilizes the kinematic error. This approach provides superior degree of modularity, making it possible to modify the controllers in both loops independently. Successful implementations of this strategy have already been tested in different vehicles (Ferreira et al., 2010b, 2012, 2011) (Ferreira et al., 2010). Moreover, this approach makes it possible to treat the dynamics and the kinematics problems in a decoupled manner. In this section, a guidance law is derived for a class of nonholonomic vehicles with three DOFs. Extensions of this guidance to other vehicles with different DOFs are given in appendix A. The adaptation of the controllers to vehicles with less DOFs is trivial. Special attention must be given to individual tracking performances (velocity and position) and therefore an analysis of the errors is provided.

Further to the mobile target tracking problem, it is important to stress the relevance of the station-keeping problem. As motivated in Pereira et al. (2008), station-keeping behaviors for autonomous marine vehicles are desired in several applications, in which the vehicles act as aid assets in field experiments. Holding the position even in the presence of disturbances originated by wind, current and waves is of particular importance since it makes it possible, in several applications, to minimize the counteracting forces exerted by the vehicle and thus minimize the amount of energy applied. To our best knowledge, few works have addressed the station-keeping problem for nonholonomic marine vehicles. Fossen and Strand (2001) have derived a *weather optimal positioning control* for a ship with surge, sway and yaw DOFs. In their approach, a control law was derived to control the vehicle on a circle with predefined radius and further extended to include an integral term by using an estimate of the mean disturbance force. Riedel and Healey (1998) use a sliding mode controller while relying on the estimate of a periodic wave disturbance and on a DVL. Cao and Morse (2007) propose a controller for station-keeping of a holonomic vehicle capable of ranging to at least two beacons. The method employs an estimator of the error and switching logic hybrid system to adjust the *gain* matrix in the control law. Also using the hybrid systems framework with a multi-operation, multi-controller autopilot, the work by Nguyen et al. (2008) proposes a structure to control marine vessels in transit and in station-keeping maneuvers. Further contributions were presented in Matos and Cruz (2008) for the control of small underactuated ASVs. The control method implements a proportional-integral controller to make the ASV hold a constant position under water current and wind disturbances. The experimental results have provided very motivating results. Nonetheless, the discontinuous nature of the heading reference may lead to chattering when the vehicle is close to the reference point.

The main difficulty in stabilizing non-holonomic marine vehicles on a position reference is related with the impact of the disturbances induced by wind, currents and waves on the transversal axis of the vehicle (normally coincident with the sway direction). The only way to remain stationary on a given position is to align with the disturbance vector. In a significant part of the

works, *ad-hoc* control laws are derived for this particular purpose but they generally are parametric, depending on “empirical” control expressions. As a result, their proof of stability is difficult to obtain. In the remainder of this section, a guidance law is proposed to stabilize non-holonomic vehicles on a desired position assuming a general disturbance vector that incorporates the effects of the wind, currents and waves. It will become clear that the tracking error (distance to the reference position) is dictated by the actuation capabilities, namely on the dynamics of the orientation and more specifically on the rapidity to track a given orientation.

Since the adaptation of the control law for two-dimensional can be trivially derived from the next developments, it is not addressed here.

It is assumed that the desired position is uniquely defined by the vector

$$\eta_l^*(t) = \begin{bmatrix} x^*(t) & y^*(t) & z^*(t) \end{bmatrix}^T \in \mathbb{R}^3.$$

and its time-derivative is given by

$$\dot{\eta}_l^*(t) = v^*(t) \begin{bmatrix} c\psi^*(t)c\theta^*(t) \\ s\psi^*(t)c\theta^*(t) \\ -s\theta^*(t) \end{bmatrix}, \quad (5.31)$$

where $v^*(t) \geq 0$ is the speed, $\psi^*(t)$ and $\theta^*(t)$ are the orientation angles of the desired velocity.

Marine vehicles that do not have actuation on sway nor roll are considered here. This class represent a large part of vehicles found in literature. Examples can be found in Cruz and Matos (2008); Cruz et al. (2007); Allen et al. (1997). These vehicles are commonly designed so that they are stable on the uncontrolled axes, implying that the corresponding velocities are negligible. Therefore, in the following steps, it will be assumed that $v = 0$ and $p = 0$. Assuming so is not realistic in practice but the corresponding effect of these velocities can be considered disturbances.

It is assumed that the vehicle kinematics is affected by drifts, typically induced by currents and wind, in practice. The drift vector takes the following representation:

$$v_D(t) = v_D(t) \begin{bmatrix} c\psi_D(t)c\theta_D(t) \\ s\psi_D(t)c\theta_D(t) \\ -s\theta_D(t) \end{bmatrix} \in \mathbb{R}^3,$$

where $v_D(t) \geq 0$ is the magnitude of the drift vector, $\theta_D(t)$ and $\psi_D(t)$ are the orientation angles of the drift.

The evolution of the actual vehicle position (kinematics) is given as a function of its velocity

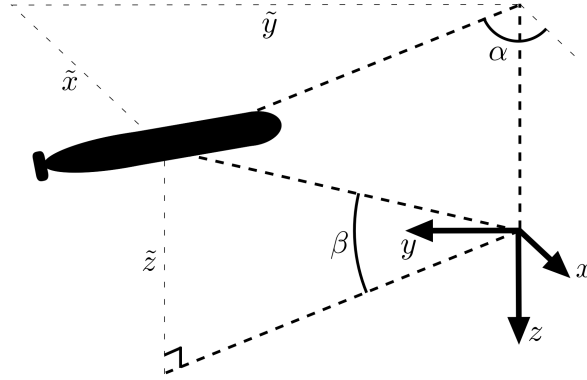


Figure 5.2: Position errors and relative angles

components, surge $u(t)$ and heave $w(t)$, and of the drift induced velocities:

$$\begin{aligned}\dot{\eta}_l(t) &= J_l(\eta_a(t))v_l(t) + v_D(t) \\ &= \begin{bmatrix} u(t)c\psi(t)c\theta(t) + w(t)c\psi(t)s\theta(t) \\ u(t)s\psi(t)c\theta(t) + w(t)s\psi(t)s\theta(t) \\ -u(t)s\theta(t) + w(t)c\theta(t) \end{bmatrix} + v_D(t) \begin{bmatrix} c\psi_D(t)c\theta_D(t) \\ s\psi_D(t)c\theta_D(t) \\ -s\theta_D(t) \end{bmatrix},\end{aligned}$$

where $v_l(t)$ is the vector of linear velocities, that is, $v_l(t) = [I_{3 \times 3} \ 0_{3 \times 3}]v(t) = [u(t) \ v(t) \ w(t)]^T$, where it is assumed that sway is null, $v(t) = 0$.

The problem can be stated as the problem of stabilizing the position $\eta_l(t)$ at the desired position $\eta_l^*(t)$. Therefore, the error vector is introduced:

$$\tilde{\eta}(t) = \begin{bmatrix} \tilde{x}(t) & \tilde{y}(t) & \tilde{z}(t) \end{bmatrix}^T = \eta_l(t) - \eta_l^*(t),$$

which is aimed to be reduced to zero. It will not be possible to drive the error vector to the origin, since the control law is undefined for such a situation. Nevertheless, it is possible to guarantee that it reaches its vicinity with a bounded error. Furthermore, depending on the vehicle dynamics (admissible angular acceleration), the error can be made arbitrarily small.

A more convenient representation can be obtained considering the spherical coordinates. Therefore, the distance between the vehicle and the target is defined as

$$\rho(t) = (\tilde{\eta}(t)^T \tilde{\eta}(t))^{1/2} \in \mathbb{R}.$$

The relative angles, expressed in the inertial frame and depicted in figure 5.2, are given by the horizontal azimuth $\alpha(t) = \angle(\tilde{x}(t), \tilde{y}(t))$ and vertical elevation $\beta(t) = \angle(\sqrt{\tilde{x}(t)^2 + \tilde{y}(t)^2}, -\tilde{z}(t))$. Note that $\alpha(t)$ is undefined for $\tilde{x}(t) = \tilde{y}(t) = 0$ and $\beta(t)$ is undefined for $\tilde{x}(t) = \tilde{y}(t) = \tilde{z}(t) = 0$.

The error vector takes the following representation:

$$\tilde{\eta}(t) = \rho(t) \begin{bmatrix} c\alpha(t)c\beta(t) \\ s\alpha(t)c\beta(t) \\ -s\beta(t) \end{bmatrix}.$$

The time derivative of the distance between the target and the vehicle is thus written as

$$\begin{aligned} \dot{\rho}(t) &= \frac{1}{\rho(t)} \tilde{\eta}(t)^T \dot{\tilde{\eta}}(t) \\ &= \vartheta + \vartheta_D + \vartheta^* \end{aligned} \quad (5.32)$$

where

$$\begin{aligned} \vartheta &= u(c\psi \cos \alpha + s\psi s\alpha)c\theta c\beta + w(c\psi c\alpha + s\psi s\alpha)s\theta c\beta + (us\theta - wc\theta)s\beta \\ &= uc(\psi - \alpha)c\theta c\beta + wc(\psi - \alpha)s\theta c\beta + (us\theta - wc\theta)s\beta \\ \vartheta_D &= v_D(c\psi_D c\alpha + s\psi_D s\alpha)c\theta_D c\beta + v_D s\theta_D s\beta \\ &= v_D(c(\psi_D - \alpha)c\theta c\beta + s\theta_D s\beta) \\ \vartheta^* &= -v^*(c\psi^* c\alpha + s\psi^* s\alpha)c\theta^* c\beta + v^* s\theta^* s\beta \\ &= -v^*(c(\psi^* - \alpha)c\theta c\beta + s\theta^* s\beta). \end{aligned}$$

Note that the dependence on time was dropped for clarity. These variables can be seen as the projections of the velocities on the axis resulting from the segment that joins the desired position and the vehicle position. The contribution of the vehicle velocity is given by ϑ , the drift induced velocity component is given by ϑ_D while the contribution of the desired reference position velocity appears in ϑ^* .

5.2.1 Guidance law

The definition of this framework makes it possible to determine guidance laws for the vehicle using the velocity references to drive the vehicle towards its reference point. Taking into account a large set of marine vehicles found in the literature, four combinations of DOFs can be considered, in general:

1. Surge, pitch rate and yaw rate (u, q, r)
2. Surge, heave and yaw rate (u, w, r)
3. Heave, pitch rate and yaw rate (w, q, r)
4. Surge, heave, pitch rate and yaw rate (u, w, q, r)

The inner velocity control loop is used to stabilize the velocity error. To this effect, the control law in (5.13) is used to abstract from the lower level dynamics and it is assumed that the virtual

control inputs are now $u, w, \dot{\theta}(t) = q$ and $\dot{\psi}(t) = r$. Assuming that the tracking error is negligible, it is possible to assume that $u \approx u^*, w \approx w^*, q \approx q^*, r \approx r^*$ after a finite time, since the velocity error dynamics is made globally exponentially stable, using the control law in (5.13). These assumptions will be relaxed and the impact of imperfect velocity tracking will be analyzed afterwards.

In the following derivations, no assumption is made on the uncontrolled velocities.

Controlled surge, pitch and yaw

Assuming that the drift velocity and the desired position evolution are known, the aim is to derive a suitable control law that uses ϑ and its control inputs, to drive the distance between the vehicle and the position to the vicinity of zero. The reason for not driving the vehicle to the exact desired position, is that the α and β are undefined, and rapidly vary in the presence of disturbances when the vehicle is in the vicinity of the desired position. A closer look at the dynamics of the angles α and β in the section 5.2.2 shows that their time derivatives are functions of the inverse of $\rho(t)$. In turn, this implies the non-existence of *regular feedback* (Sontag, 1998). Nevertheless, it does not preclude asymptotic controllability but some effects may arise:

- Disturbance sensitiveness: under unpredicted disturbances, the vehicle may deviate from the desired reference point, thus inducing a large variation on α and β ;
- Measurement error sensitiveness: as for the disturbances, measurement errors on the position may impact on the azimuth and elevation angles causing large variations;
- Infinite actuation or *divergent maneuvers*: depending on the guidance method, deviations from the reference point would either cause infinite actuation (see section 5.2.2) or maneuvers that would make the vehicle diverge first and then converge again (see the nonholonomic cart example moving on an *invariant circle* in Sontag (1998)).

For these reasons, the guidance objective is loosen so that the vehicles reach the vicinity of the reference and regular feedback can be used. An analysis of the steady-state behavior will show that the vehicle position converges to an invariant set defined by the surface of a sphere with an arbitrary radius. In practice, this radius is lower bounded by the actuation capability.

Choose the following guidance laws for the rate of the angles:

$$q^* = -K_\theta(\theta + \beta) - \dot{\beta}, \quad (5.33)$$

$$r^* = (-K_\psi(\psi - \alpha + \pi) + \dot{\alpha}) c(\theta), \quad (5.34)$$

where K_θ and K_ψ are constant positive scalars. The convergence of the angles is therefore exponential. The solution of the differential equation $\dot{\theta}(t) = q^*$ and $\dot{\psi}(t) = r^*/c\theta$ are

$$\begin{aligned} \theta &= (\theta_0 + \beta_0)e^{-K_\theta t} - \beta \\ \psi &= (\psi_0 - \alpha_0 + \pi)e^{-K_\psi t} + \alpha - \pi. \end{aligned}$$

where $\theta_0 = \theta(t_0)$, $\beta_0 = \beta(t_0)$, $\psi_0 = \psi(t_0)$ and $\alpha_0 = \alpha(t_0)$.

Hence, as time grows, the projection of the vehicle velocity verifies

$$\begin{aligned} \lim_{t \rightarrow \infty} \vartheta &= uc\pi c(-\beta)c\beta + wc\pi s(-\beta)c\beta + (us(-\beta) - wc(-\beta))s\beta \\ &= -u. \end{aligned}$$

Choosing

$$u^* = \vartheta_D + \vartheta^* + K_\rho(\rho(t) - \delta), \quad (5.35)$$

where $\delta > 0$ is the desired distance from the reference position and $K_\rho > 0$ is a scalar gain, yields from (5.32)

$$\begin{aligned} \lim_{t \rightarrow \infty} \dot{\rho}(t) &= -u^* + \vartheta_D + \vartheta^* \\ &= -K_\rho(\rho(t) - \delta) \end{aligned} \quad (5.36)$$

Therefore, it is possible to conclude that the vehicle position converges to a ball of radius δ around the desired position $\hat{\eta}_l^*(t)$.

As previously seen, the bounded actuation restricts the vehicle velocity. Therefore, instead of (5.35), a control law of the type

$$u^* = \vartheta_D + \vartheta^* + K_\rho \text{sat}(\rho(t) - \delta, \mu_\rho) \quad (5.37)$$

would be more appropriate, where $\text{sat}(\cdot, \cdot) : \mathbb{R} \times \mathbb{R}^+ \rightarrow \mathbb{R}$ is the saturation function defined as

$$\text{sat}(\lambda, \mu) = \begin{cases} \lambda, & \text{if } |\lambda| \leq \mu \\ \frac{\lambda}{\|\lambda\|} \mu, & \text{else} \end{cases}.$$

In this case, it is convenient to choose the saturation value μ_ρ so that the product $K_\rho \mu_\rho$ does not exceed the maximum surge velocity, that is $K_\rho \mu_\rho \leq [v_M(t)]_1$, in order not to saturate the actuators. However, this may not be sufficient since $v_M(t)$ provides an upper bound on the vehicle velocity but may not be coincident with its maximum. Actually, the sum in (5.37) should not exceed the maximum value allowed for the surge velocity.

The control laws of the remaining combinations of DOFs follow the same reasoning presented above. Therefore, their derivation is almost limited to the presentation of the control expressions. These are given in appendix A. Furthermore, note that the guidance law in (5.35) makes the vehicle move in the opposite direction if its heading points in the opposite direction. This might be inefficient and thus an alternative is proposed in appendix B.

5.2.2 Steady state orientation for station keeping

The final orientation of the vehicle is analyzed when performing a station keeping maneuver ($v^* = 0$). It is important to stress that it is not necessary to know the magnitude or the orientation of the

drift vector in order to verify the forthcoming results.

Recall that the azimuth angle is given by

$$\alpha = \angle(\tilde{x}, \tilde{y}).$$

After simple algebra, its time derivative results into

$$\dot{\alpha} = \frac{\tilde{y}\dot{\tilde{x}} - \tilde{x}\dot{\tilde{y}}}{\tilde{x}^2 + \tilde{y}^2}.$$

Expressing this in spherical coordinates gives

$$\begin{aligned} \dot{\alpha} = & -\frac{1}{(\rho(t)c\alpha c\beta)^2 + (\rho(t)s\alpha c\beta)^2} \\ & [\rho(t)s\alpha c\beta (uc\psi c\theta + wc\psi s\theta + v_D c\psi_D c\theta_D) \\ & - \rho(t)c\alpha c\beta (us\psi c\theta + ws\psi s\theta + v_D s\psi_D c\theta_D)] \end{aligned}$$

By recalling that $\lim_{t \rightarrow \infty} \psi = \alpha - \pi$, after some simplifications, it finally yields

$$\lim_{t \rightarrow \infty} \dot{\alpha} = -\frac{v_D c\theta_D s(\alpha - \psi_D)}{\rho(t)c\beta}.$$

For $\rho(t) \neq 0$ and $c\theta_D/c\beta > 0$, there are two equilibrium points: $\alpha = \psi_D$ and $\alpha = \psi_D - \pi$. The first is a stable equilibrium point while the second is an unstable equilibrium point. To prove that the equilibrium point $\alpha = \psi_D - \pi$ is unstable, it suffices to verify that

$$\begin{aligned} \alpha \in (\psi_D, \psi_D + \pi) & \Rightarrow \dot{\alpha} < 0 \\ \alpha \in (\psi_D - \pi, \psi_D) & \Rightarrow \dot{\alpha} > 0, \end{aligned}$$

Therefore, it follows that, for any t and any $\alpha(t) \neq \psi_D - \pi$, the vehicle azimuth angle will converge to $\lim_{t \rightarrow \infty} \psi = \lim_{t \rightarrow \infty} \alpha - \pi = \psi_D - \pi$. Intuitively, to hold a given position, the solution is to *face* and compensate the drifts. This last results demonstrates mathematically such a requirement

Turning now our attention to the elevation, recall that the corresponding angle is given by

$$\beta = \angle\left(\sqrt{\tilde{x}^2 + \tilde{y}^2}, -\tilde{z}\right).$$

Computing its time derivative yields the following expression:

$$\dot{\beta} = \frac{-\dot{\tilde{z}}\sqrt{\tilde{x}^2 + \tilde{y}^2} + \tilde{x}\dot{\tilde{z}}\tilde{x}/\sqrt{\tilde{x}^2 + \tilde{y}^2} + \tilde{z}\dot{\tilde{y}}\tilde{y}/\sqrt{\tilde{x}^2 + \tilde{y}^2}}{\sqrt{\tilde{x}^2 + \tilde{y}^2 + \tilde{z}^2}}.$$

Expressed in spherical coordinates, after straightforward simplifications, it results

$$\begin{aligned}\dot{\beta} = \frac{1}{\rho(t)} [& -c\beta(-us\theta + wc\theta - v_D s\theta_D) \\ & -s\beta c\alpha(uc\psi c\theta + wc\psi s\theta + v_D c\psi_D c\theta_D) \\ & -s\beta s\alpha(us\psi c\theta + ws\psi s\theta + v_D s\psi_D c\theta_D)].\end{aligned}$$

Recalling that the guidance law in (5.33) makes $\lim_{t \rightarrow \infty} \theta(t) = -\beta$, as time tends to infinity, this differential equation simplifies into

$$\lim_{t \rightarrow \infty} \dot{\beta} = \frac{1}{\rho(t)} (-w - v_D (c\beta \sin \theta - s\beta c\theta (c\alpha c\psi_D + s\alpha s\psi_D))).$$

Furthermore, note that it was proven that $\lim_{t \rightarrow \infty} \alpha = \psi_D$, and thus

$$\lim_{t \rightarrow \infty} \dot{\beta} = \frac{1}{\rho(t)} (-w - v_D s(\beta - \theta_D)).$$

It is necessary to verify that $|w| < v_D$ to stabilize β . If this occurs, the elevation angle has two equilibrium points $\beta = \arcsin(-w/v_D) + \theta_D$ and $\beta = \arcsin(-w/v_D) + \theta_D + \pi$. Again, the second is an unstable equilibrium point and therefore it is possible to conclude that $\lim_{t \rightarrow \infty} \theta(t) = \lim_{t \rightarrow \infty} -\beta = -\arcsin(-w/v_D) - \theta_D$.

As stated before, both azimuth and elevation angle rates are functions of the inverse of the distance $\rho(t)$. In practice, this means that small positional disturbances or noisy measurements of the position induce large variations on the angles α and β , when the vehicle is close to the reference position. Moreover, such angles are undefined for $\rho(t) = 0$ and consequently this situation must be avoided, thus the inclusion of the constant δ in (5.35), (5.37), and in the guidance laws proposed in appendix (A.7), (A.9), (A.10), (B.1), (B.2).

5.2.3 Target tracking under unknown drifts and velocity errors

Motivated by real implementations of the control laws, an analysis is now provided both on error boundedness and on the final orientation in the presence of unknown and bounded drifts. Integration of sensors to measure the drift velocity and its orientation may be expensive and imply an additional effort in their integration. Here, it is shown that suitable performances can be obtained even in the absence of such measurements.

It is now intended to assess the tracking error under unknown drifts and velocity errors for the control law derived in section 5.2.1. The derivations for the remaining cases presented in appendix A can be easily extrapolated. As previously seen, the presence of model uncertainties may induce velocity tracking errors whose absolute values are bounded by the entries of the vector \tilde{v}_M . Therefore, it is considered that the surge, pitch rate and yaw rate are affected by errors, as

follows:

$$\begin{aligned} u &= u^* + \tilde{u} \\ q &= q^* + \tilde{q} \\ r &= r^* + \tilde{r} \end{aligned}$$

where $|\tilde{u}| \leq [\tilde{v}_M]_1$, $|\tilde{q}| \leq [\tilde{v}_M]_5$, $|\tilde{r}| \leq [\tilde{v}_M]_6$.

As a result, the angles will not be perfectly tracked. To prove this, the guidance laws (5.33) and (5.34) are used to write:

$$\begin{aligned} q &= -K_\theta(\theta + \beta) - \dot{\beta} + \tilde{q}, \\ r &= (-K_\psi(\psi - \alpha + \pi) + \dot{\alpha} + \tilde{r}) c(\theta). \end{aligned}$$

Therefore, it becomes clear that the desired angles will be tracked with errors as time tends to infinity:

$$\lim_{t \rightarrow \infty} \theta = -\beta + \tilde{\theta} \quad (5.38)$$

$$\lim_{t \rightarrow \infty} \psi = \alpha - \pi + \tilde{\psi}, \quad (5.39)$$

where $|\tilde{\theta}| \leq \frac{|\tilde{q}|}{K_\theta}$ and $|\tilde{\psi}| \leq \frac{|\tilde{r}|}{K_\psi}$ are the angle errors in steady state.

Before introducing the effect of the surge velocity tracking error, let us infer about the impact of the angle errors in the approach rate $\dot{\rho}(t)$. Hence, using a step-by-step development, the azimuth error $\tilde{\psi}$ is firstly introduced, then the altitude error $\tilde{\theta}$, and finally the surge velocity error in order to derive an upper bound on the tracking error.

Using the definition of ϑ in (5.32) and the limit (5.39), it is possible to obtain

$$\lim_{t \rightarrow \infty} \vartheta = u(-c\tilde{\psi}c\theta c\beta + s\theta s\beta) + w(-c\tilde{\psi}s\theta c\beta - c\theta s\beta).$$

Using now (5.38) and noting that $c(-\beta + \tilde{\theta}) = c\beta c\tilde{\theta} + s\beta s\tilde{\theta}$, $s(-\beta + \tilde{\theta}) = -s\beta c\tilde{\theta} + c\beta s\tilde{\theta}$, the last expression is rewritten as

$$\begin{aligned} \lim_{t \rightarrow \infty} \vartheta &= u(-c\tilde{\psi}(c\beta c\tilde{\theta} + s\beta s\tilde{\theta})c\beta + (-s\beta c\tilde{\theta} + c\beta s\tilde{\theta})s\beta) \\ &\quad + w(-c\tilde{\psi}(-s\beta c\tilde{\theta} + c\beta s\tilde{\theta})c\beta - (c\beta c\tilde{\theta} + s\beta s\tilde{\theta})s\beta). \end{aligned}$$

Moreover, the trigonometric relationships $s\beta c\beta = 1/2 s(2\beta)$, $c^2\beta + s^2\beta = 1$, make it possible to write

$$\begin{aligned} \lim_{t \rightarrow \infty} \vartheta &= u(-c\tilde{\theta} + (1 - c\tilde{\psi})(c^2\beta c\tilde{\theta} + 1/2 s(2\beta) s\tilde{\theta})) \\ &\quad + w(-c\tilde{\psi}s\tilde{\theta} - (1 - c\tilde{\psi})(s^2\beta s\tilde{\theta} + 1/2 s(2\beta) c\tilde{\theta})). \end{aligned}$$

Finally, it is easy to prove that $(c^2\beta c\tilde{\theta} + 1/2s(2\beta)s\tilde{\theta}) = c(\beta - \tilde{\theta}/2)$ and $(s^2\beta s\tilde{\theta} + 1/2s(2\beta)c\tilde{\theta}) = c(-\beta + \tilde{\theta}/2 + \pi/4)$, yielding

$$\begin{aligned} \lim_{t \rightarrow \infty} \vartheta = & u(-c\tilde{\theta} + (1 - c\tilde{\psi})c(\beta - \tilde{\theta}/2)) \\ & + w(-c\tilde{\psi}s\tilde{\theta} - (1 - c\tilde{\psi})c(-\beta + \tilde{\theta}/2 + \pi/4)). \end{aligned}$$

Consider that there is a surge velocity tracking error, that is $u = u^* + \tilde{u}$, and suppose that ϑ_D is not measured. Hence, a natural choice for the surge control law would be

$$u^* = \begin{cases} \zeta(c(\psi - \alpha)c\theta c\beta + s\theta s\beta) \\ \quad \text{if } c(\psi - \alpha)c\theta c\beta + s\theta s\beta \leq 0 \\ 0, \quad \text{else} \end{cases} \quad (5.40)$$

as in (B.1) but this time the drift component is not considered: $\zeta = -\vartheta^* - K_\rho \text{sat}(\rho(t) - \delta, \mu_\rho)$. Assuming that $|\tilde{\psi}| < \pi/2$, the desired velocity becomes

$$\lim_{t \rightarrow \infty} u^* = \zeta(-c\tilde{\theta} + (1 - c\tilde{\psi})c(\beta - \tilde{\theta}/2)) \quad (5.41)$$

In steady state, the time derivative of the distance to the reference becomes, from (5.32),

$$\begin{aligned} \lim_{t \rightarrow \infty} \dot{\rho}(t) = & (u^* + \tilde{u})(-c\tilde{\theta} + (1 - c\tilde{\psi})c(\beta - \tilde{\theta}/2)) \\ & + w(-c\tilde{\psi}s\tilde{\theta} - (1 - c\tilde{\psi})c(-\beta + \tilde{\theta}/2 + \pi/4)) + \vartheta_D + \vartheta^*. \end{aligned}$$

Replacing u^* by its expression, the final distance to the target is upper bounded as follows:

$$\begin{aligned} \lim_{t \rightarrow \infty} \dot{\rho}(t) \leq & (-K_\rho(\rho - \delta) - v^*)(|c\tilde{\theta} + c\tilde{\psi}| - 1)^2 \\ & + |\tilde{u}|(|c\tilde{\theta}| + 1 - c\tilde{\psi}) + |w|(|c\tilde{\psi}s\tilde{\theta}| + 1 - c\tilde{\psi}) + v_D + v^*. \end{aligned}$$

Thus, the ultimate tracking error is bounded by

$$\begin{aligned} \lim_{t \rightarrow \infty} \rho(t) \leq & \rho_M \\ = & \frac{1}{K_\rho(|c\tilde{\theta} + c\tilde{\psi}| - 1)^2} (|\tilde{u}|(|c\tilde{\theta}| + 1 - c\tilde{\psi}) \\ & + |w|(|c\tilde{\psi}s\tilde{\theta}| + 1 - c\tilde{\psi}) + v_D + v^*) - \frac{v^*}{K_\rho} + \delta. \end{aligned} \quad (5.42)$$

Throughout this subsection, it has been considered that the error in the angle tracking was induced by errors in the velocity loop. Nonetheless, the result given above remains valid when the angle errors include velocity loop errors as well as biased measurement of angles.

5.3 Experimental results

Several tests have been conducted in real environment. The objective of the missions was to validate the developed methods. Next, the operation setup will be described and the results will be presented, preserving the same order as the outline of this chapter.

5.3.1 Setup description

In this experiment, the Gama ASV has been used as a test asset. Besides GPS receivers, which supply position and velocity data to the controllers, the vehicles are fitted with inertial measurement units feeding back the velocity and position controllers, running on a local PC, with the angles and angular rates. In the absence of velocity measurements with regard to the fluid, the velocity provided by the GPS was used as a rough approximation of the vehicle velocity with regard to the water. This obviously introduces an error in the velocity control loop that can be of the same magnitude of the drift. Nevertheless, the controllers are expected to be robust enough to accommodate this error and successfully track their references under bounded drifts below their maximum achievable velocities. Furthermore, it is expected that the performances presented below can be improved with the inclusion of drift and body velocity with regard to the fluid.

The reason for using these vehicles rather than underwater vehicles is related to the fact that more accurate measurements on the position can be obtained. In fact, with the current GPS equipment, it is possible to achieve about 1.5 meters of absolute, geo-referenced accuracy and measurement updates at 10 hertz.

The control and guidance loops in the vehicles have been configured to run with a constant period of one hundred milliseconds. In the following results, the position of the base station was defined to be the origin. These are shown with no filtering as results of the *raw* data output from the sensors.

5.3.2 Static target tracking and station-keeping

In order to assess the performances of the control scheme, a static reference point was set for Gama ASV. Arbitrarily placed in the operation area, the vehicle must track the referred point and hold the position according to the guidance laws derived earlier in this chapter.

Several tests were performed in several days with slightly different conditions, namely in terms of wind speed and direction. Figure 5.3 depicts an example of the path travelled by Gama during a tracking task. An arbitrary constant reference position was set, depicted by the red cross on the plot, at a distance of about 100 meters from the vehicle initial position. The trajectory is naturally curvilinear not only because of the line-of-sight-like control law but also due to disturbances. This effect is emphasized by the arrows that represent vehicle heading: the vehicle heading does not coincide with the tangent to the trajectory due to a lateral velocity induced by the current. As described in section 5.2.2, in the vicinity of the reference, the vehicle faces the mean orientation

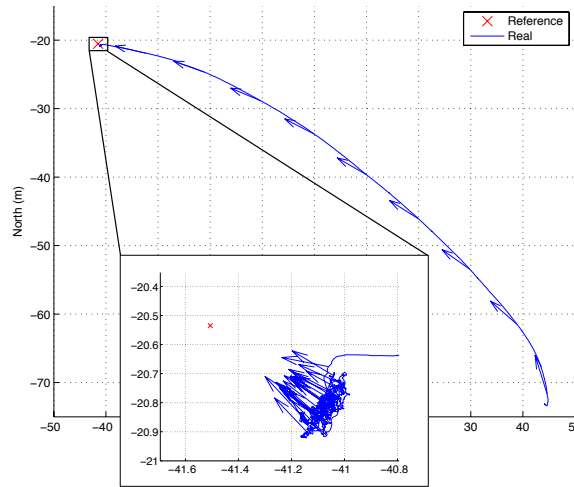


Figure 5.3: Target tracking trajectory. The arrows show the heading of the vehicle plotted at intervals of 10 seconds.

of disturbances, *sliding* on a circle (bidimensional case for ASVs) with a radius equal to $\delta = 0.5$ meters.

Figure 5.4 shows the evolution of the north and east components of the position referred to the local origin. The evolution of the error over time is shown in figure 5.5 (blue solid line for the error referred to the CG), which demonstrates that the center of gravity of the vehicle remains with an expected error equal to δ . It is important to emphasize that this error remains bounded between 0.5 and 0.6 meters in these results even in the presence of drifts such as wind and currents, which have been estimated to be about 0.2 to 0.3 meters per second, according to a test in which Gama was left to drift. A rough estimate was then computed based on the difference of positions and the corresponding elapsed time. As the drift can not be measured because of the absence of sensors, it is not feedforwarded in the guidance law. As such, this impacts as an unpredicted disturbance on the system.

This target tracking guidance law is especially interesting for applications that require accurate static positioning of on board sensors. Some examples include transponders for LBL localization or cameras to statically record a sequence on a given area, for instance. Carefully placing the

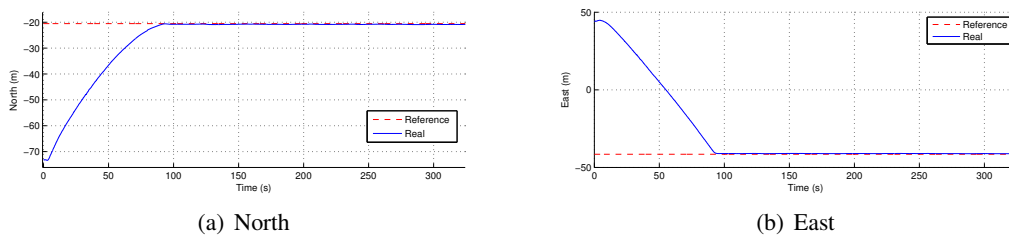


Figure 5.4: Evolution of the horizontal coordinates

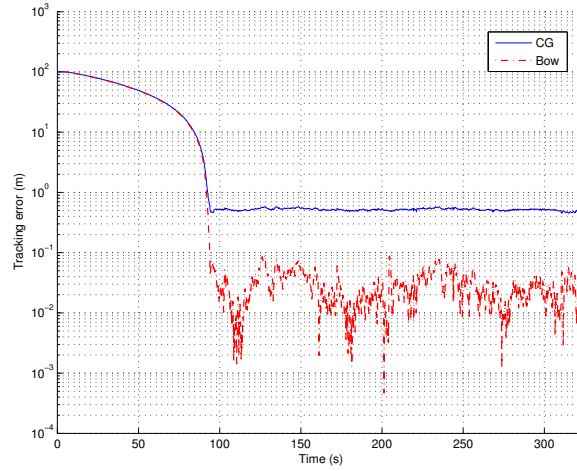


Figure 5.5: Tracking error: center of gravity (CG) and bow relative distances

sensors on the vehicle body may provide even better results. For this guidance law, the bow is the most appropriate position. Additionally, the radius of the ball that the vehicle tends to can be adjusted according to the dimensions of the vehicle. More specifically, it was proven in the previous section that the vehicle attitude points towards the reference position. After stabilization, the center of gravity of the vehicle *slides* over a ball of radius δ because of disturbances. As the attitude of the vehicle points to the reference, any point on the body that is inside the ball of radius δ is trivially closer to the reference. If this point is chosen so that it is on the longitudinal axis of the vehicle and at a positive offset $\delta_B = \delta$ with regard to the center of gravity (see figure 5.6), then this point is coincident with the reference position in steady state, when the vehicle slides on the circle with radius δ .

In this case, the radius was chosen δ so that it is approximately equal to the distance between the center of gravity and the bow. The distance between the bow central point and the reference point is depicted in figure 5.5 (red dashed line). This distance is about five times smaller than the vehicle tracking error. Interestingly enough, the guidance and control loops have proved to be robust and accurate even in the presence of small waves and variable wind and currents always found in uncontrolled environments such as the river.

Figure 5.7 shows the vehicle heading versus time. It is possible to see the effect of the disturbances and their variability: After stabilization at the reference point, the heading changes over time to compensate lateral drifts mostly induced by currents and wind.

5.4 Conclusions

This chapter presented a complete framework for guiding autonomous marine vehicles subjected to unpredictable disturbances originated by drift or model and measurement errors. For the velocity and position layers, suitable feedback control laws were derived to drive the vehicles to velocity

reference and possibly moving, position references. This rather simple control topology is often used in practice but very few works formalize its implementation by abstracting from the lower layers errors. Using this type of hierarchical and modular control topology introduces a main advantage: it is possible to modify the upper layers without changing the lower ones, thus allowing several combinations of control layers rather than deriving *ad-hoc* control laws. Here, special attention has been given to tracking errors in both velocity and position control loops, and the results presented provide a systematic method for similar implementations considering modular control layers.

Using nonlinear control tools, it was possible to derive dynamics and kinematics controllers, which have provided satisfactory performances in the target tracking task performed by an ASVs. The results from tracking of mobile targets is left to chapter 6 where virtual references are generated for several coordinated vehicles.

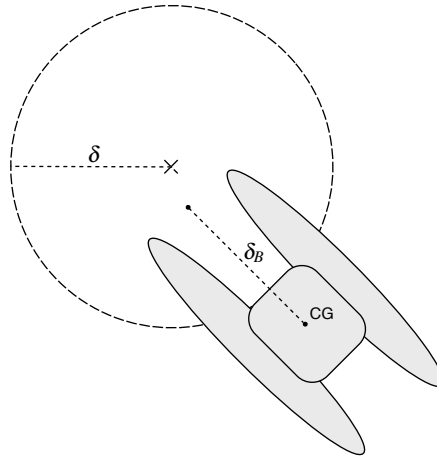


Figure 5.6: Relative position of the vehicle (CG) and relative position of bow with regard to the position reference

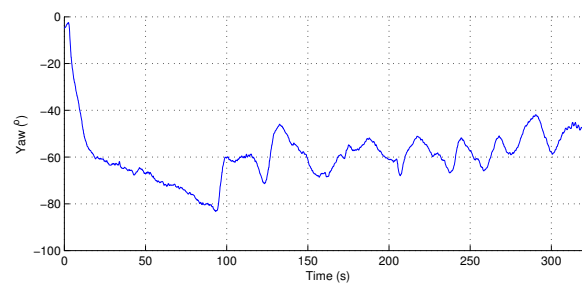


Figure 5.7: Yaw angle

Chapter 6

Coordination of marine vehicles

Accurate positioning and coordination of marine vehicles require suitable automatic control schemes as they typically suffer from a set of external disturbances that are difficult to predict and to anticipate. Following the line presented in the previous chapter, the control problem is addressed at three levels: velocity stabilization, position stabilization and coordination. In the velocity loop, the controller stabilizes the vehicle velocity around a given time varying reference. The position controller is then responsible to generate velocity references to stabilize the vehicle on a possibly varying position reference, which is subsequently used by a central coordination scheme that keeps the vehicles in formation. This chapter focuses on this last level.

Autonomous marine vehicles, both surface and underwater, have received special attention from the scientific and military communities, motivated by the challenges and the opportunities present in marine environments. Along with this interest, there has been a common trend in robotics to develop distributed systems. Rather than having a single, powerful, robot, distributed solutions contemplating cooperating robots can significantly improve the performance, robustness, reliability and operational costs (Cao et al., 1997; Fukuda and Nakagawa, 1988; Parker, 2008).

In the following sections, the main concepts, tools and techniques used in robotic coordination are exposed. There are different studies in this domain and the intention is not to cover the entire literature. Instead, the idea is to expose the concepts and the research related to coordination of marine vehicles. Then the coordination method is described and extended to accommodate undesirable errors and communication constraints when the vehicles are moving in formation.

6.1 Related works and motivation

Inspired by the cells of living creatures, the early study by Fukuda and Nakagawa (1988) has led to a new concept in robotics through the understanding of the capabilities of a set of cooperative robots, as opposed to using a single one. By taking the industrial robotics as background, the main idea was to conceive a manipulator from elementary robotic components (cells): joints, branches and work (tool) cells. Cells are described as “fundamental components of the structure and mechanism” (Fukuda and Nakagawa, 1988) that perform elementary tasks and are capable of working

independently but cooperate with the entire cell group. When they are combined, it is possible to obtain a versatile manipulator. Other than this feature, the theoretical flexibility, robustness and fault tolerance in redundant systems are identified as the main advantages of cooperative systems.

Researchers have answered to different needs and requirements presenting several robotic solutions. As a result, thousands of different robots have been engineered. Coordination is a way of taking advantage of the features of every robot in a team and it has been common to find heterogeneous teams of robots in several works. In opposition to homogeneous teams (see, for example, Kube and Bonabeau (2000)), using heterogeneous robots usually requires different control methods, and individual characteristics and performances (Ducatelle et al., 2011) have to be carefully handled in a cooperative team.

For an overview on architecture and hierarchical models for cooperative systems, we refer to the work by Farinelli et al. (2004) and Cao et al. (1997). These provide a comprehensive overview on multirobot systems and define key concepts in this domain.

At this point, it is important to differentiate between *cooperation* and *coordination*. These very close terms are frequently used in the multirobot literature and may lead to misconception. According to the embracing work in (Farinelli et al., 2004) on the taxonomy on this subject, it is considered that the cooperation is the capability of several robots to work together to achieve a common goal. Coordination is a cooperative task in which the states of the coordinated robots (for example, actions, positions, etc.) are taken into account to obtain coherency and high performances. The present work deals with the coordination of marine vehicles and more precisely with formation control.

Farinelli et al. (2004) provide a comprehensive picture for classification of cooperative multi-robot systems by identifying four hierarchical levels: cooperation level, knowledge level, coordination level and organization level, following a top-down perspective. Some of the definitions can also be found in the previous survey by Cao et al. (1997). In order to make it clear, some concepts and definitions in the context of coordinated systems are introduced. The coordination level regards how the actions of each robot influence the remaining ones. A system is said to be coordinated if the actions of the team robots are performed such that the overall operation is carried out in a performing and coherent fashion. They are defined as strongly coordinated if they possess a set of rules for interacting between them. Otherwise, if they do not have such a set of rules, they are said to be weakly coordinated. At the organization level, the system is said to be centralized when the group architecture is characterized by a single robot. In other words, an architecture is centralized when the decisions depends on a single robot (commonly referred to as leader) which is in charge of generating references to the other team mates (commonly referred to as followers). Moreover a system is said to be strongly centralized when decisions are taken only by a single element. It is said to be weakly centralized when more than one robot can take decisions over the operation. In opposition, a decentralized architecture presents no such leader: each robot is autonomous on its decisions. Due to practical and design constraints, a physical leader may not exist in a centralized organization. Instead, a virtual leader can act as an element of the team that is free of, or at least less subject to, undesired effects present in the physical ones.

6.1.1 Coordinated control

According to the interesting survey by Murray (2007) on cooperative control of multiple vehicles, there are three main types of approaches to formation control problems: Potential-field based (Leonard and Fiorelli, 2001; Horner and Healey, 2004; Vail and Veloso, 2003; Egerstedt and Hu, 2001; Ogren et al., 2002), optimization-based (Defoort et al., 2009; Dunbar and Murray, 2006; Schwager et al., 2011, 2009) and swarm behaviors (Sahin, 2005; Leonard and Fiorelli, 2001; Kube and Bonabeau, 2000; Ducatelle et al., 2011). Additionally, consensus-based algorithms have also been applied in the context of formation control (see, for example, (Ghabcheloo, 2007; Ghabcheloo et al., 2009; Ren and Atkins, 2007; Fax and Murray, 2004; Sun et al., 2009; Chung and Slotine, 2009)). Next, a brief overview on some interesting contribution in the literature is provided.

6.1.1.1 Potential field based coordination

The use of virtual potential fields is a way of formally deriving control laws based on the environment and goals. Environment variables gathered by the robots are integrated into a formal potential field which is afterwards used to define their motion. Artificial potential fields are typically generated according to the idea that obstacles, or more generally undesired states, generate a repelling force while navigation goals (desired states) generate an attractive force. Robots are driven in a way that the potential energy is minimized along their trajectories. This approach has been applied to different types of scenarios from simple schooling schemes to highly dynamic environments such as robotic soccer (Vail and Veloso, 2003). Leonard and Fiorelli (2001) present strongly and weakly centralized coordination of vehicles using potential fields, exploring on multiple-vehicle control for different topologies and their stability and focusing on the derivation of potential field functions and the corresponding control law for fully actuated vehicles. Another application of virtual potential fields is also presented in (Horner and Healey, 2004) to drive an unmanned aerial vehicle (UAV) to an area in order to collect data from other vehicles. The potential field is derived upon the the signal strength measured from wireless communication devices. Egerstedt and Hu (2001) presented a solution to keep in formation a team with n elements. The approach conceptually considers $n+1$ virtual robots and is very interesting in the sense that the individual dynamics are decoupled from the formation dynamics using a *formation constraint function*, that can be seen as a potential function. Within the same context, Ogren et al. (2002) presented a method for formation keeping along arbitrary paths defined by a virtual leader, and formation geometries. Ihle et al. (2006) also proposed an elegant and generic formulation resorting to Lagrangian multipliers to reduce constraint functions, which measure general positioning errors, to zero. The approach is also extended to underactuated ships.

6.1.1.2 Optimization based coordination

Control problems can be solved in an optimization framework where it is necessary to minimize a given cost function while considering constraints. Optimization based methods in the context of

robotic coordination mainly contemplate model predictive control (MPC), also known as receding horizon control. Clearly, the literature is more limited than for the remaining methods presented in this section.

One of the major advantages of the MPC is the direct manipulation of input constraints, such as saturation. In fact, when using other control design tools, the control laws are commonly derived based on the assumption that the required actuation effort does not reach saturation. This, in turn, may introduce undesired effects in the dynamics if the combinations of gains and errors are not handled properly. However, the MPC approach is generally computationally demanding and it is not suitable for many robotics applications. In order to reduce the computational requirements, some authors proposed variants of the MPC algorithm with a randomized optimization by using Monte Carlo sampling (Tanner and Piovesan, 2010) and hybrid particle swarm optimization (Vaccarini and Longhi, 2009).

Under the obstacle avoidance scenario, Defoort et al. (2009) developed a decentralized algorithm for optimal coordinated collision avoidance. After discretization, at each time step, the optimal trajectory to the goal is computed by each robot using an MPC method while taking into account possible collision with other robots moving in vicinity. In the presence of a conflict (possible collision), the robots dynamically adjust their trajectories.

Another method that uses MPC for formation keeping was developed by Dunbar and Murray (2006). Their approach is decentralized but assumes that each robot knows the predicted states of the team mates for the subsequent time step, obtained by means of communications. Using a similar approach, the work by Nascimento (2012) addresses the coordination of ground robots using a cost function, optimized using MPC, where predicted states, control actions and obstacles are taken into account.

Besides MPC, optimization based cooperation also includes optimal coverage by robots. Schwager et al. (2011) proposed a common problem formulation to compare some methods used in coverage (see Schwager et al. (2009) for an application to coverage). A group of robots is used to cover an area of interest and some points have to be visited by one or more robots, depending on its significance.

6.1.1.3 Swarm behaviors

Swarm behaviors constitutes another approach to coordinated control. Sahin (2005) provides an overview on swarm robotics, defining it as “the study of how large a number of relatively simple physically embodied agents can be designed such that a desired collective behavior emerges from the local interactions among agents and between the agents and the environment”. Swarm behaviors, generally employ decentralized methods at the coordination level and are commonly characterized by simple and yet powerful control laws imitating animal behaviors. One of the most famous work is the paper by Reynolds (1987), on the imitation of the behaviors of animals flocking or schooling. Many studies within this context consider a biologic background to inspire control laws such as in (Leonard and Fiorelli, 2001) and in (Kube and Bonabeau, 2000).

Based on the pheromone mediated navigation of ants, Ducatelle et al. (2011) discuss the guidance of swarms of wheeled robot in constrained environments. Two types of robots are used: eye-bots and foot-bots. The eye-bots are distributed over the area of interest and provide direction information (policy) to foot-bots while regarding their area. By analogy with pheromone based navigation of ants in trails, the authors argue that the process follows the biology-inspired phenomenon: the foot-bots make use of the information on direction provided by the eye-bots (pheromone effect, by analogy). Eye-bots are capable of learning from the trajectory followed by the foot-bots by interpreting their directions and adjusting the policies according to their behaviors.

6.1.1.4 Consensus algorithm applied to formation keeping

Cooperation, and coordination in particular, implicitly assume that there is interaction between the team mates. Such an interaction, achieved either by explicit communication, sensing or modification of the environment, is used to infer about the state of the remaining team mates. In this domain, graph theory has been used to model the interaction between elements and has assumed an important role in several studies (Ghabcheloo, 2007; Ren and Atkins, 2007; Fax and Murray, 2004), where *Laplacian matrices* capture the interactions between the coordinated robots. The properties of the resulting Laplacian matrix have been explored to solve the average-consensus problem¹, while capturing the network topology. The work by Olfati-Saber and Murray (2004) has induced a significant part of the average-consensus and graph theory based solutions in robotics. The paper provides an overview on the graph theory and contributes with several important results, which are then applied to the consensus of a simple integrator systems (in the same issue of the journal, the work by Fax and Murray (2004) addressed the stabilization of more general linear system using graph theory).

A relevant work was also conducted by Ghabcheloo (Ghabcheloo et al., 2009; Ghabcheloo, 2007), who took advantage of graph theory and nonlinear control theory to address the problem of coordinating a team of robots along predefined parallel paths (trimming paths). Moreover, important issues arising from delays and communication losses are addressed in order to infer about the stability and convergence of the systems. A similar approach was also followed by Borhaug et al. (2007) and Almeida et al. (2012).

A relevant work in time-varying formation keeping was developed and tested by Sun et al. (2009) in a ring communication topology, also known as a cycle topology (the i th robot knows the position of the $(i-1)$ th robot). The authors formulated the problem of synchronous trajectory tracking adopting a decoupled translational and angular framework.

By adopting a very interesting kinematic error representation, Dong and Farrell (2008) presented a method for achieving coordination of multiple nonholonomic robots. In their work, a canonical, chained form is adopted to solve two problems: formation keeping and trajectory

¹consensus problems are concerned with the agreement of state of subsystems, that is, making the state variables converge to the same values ($\lim_{t \rightarrow \infty} x_i(t) = \lim_{t \rightarrow \infty} x_j(t)$ for all robots $i, j, i \neq j$ in the formation, where x are the state one want to make agree)

tracking while keeping in formation. The approach was similarly explored in Dong and Farrell (2009).

Although not directly related to formation keeping problems, Chung and Slotine (2009) have presented a suitable control law to reach consensus on the state of generic robots within the context of synchronization. The assumptions implicitly state that the robots are holonomic. By using modified Laplacian matrices and the contraction theory, the work presents several results on tracking and synchronization.

6.1.2 Biased comparison of methods

This chapter concentrates on precise positioning of coordinated marine robots. In this context, potential-field-, consensus- and optimization-based approaches are the most promising choices. Optimization-based methods, using MPC for example, require prediction of future states in a finite horizon. A model for this prediction may be difficult to obtain, since unpredictable disturbances (wind, waves, currents) typically affect marine vehicles during their missions and optimization-based methods may fall ill-suited. Furthermore, optimization-based methods are usually demanding and their computational requirements significantly increase with the number of state variables considered, and consequently with the number of vehicles in the formation. In contrast, agreement on a given state through average-consensus is expected to be considerably less intensive in computational terms and individual tracking errors can be treated locally without requiring predictions (Chung and Slotine, 2009; Ghabcheloo et al., 2009), resulting in a more natural approach comparatively to optimization. Nevertheless, the theoretical framework behind average-consensus algorithms generally originate specific solutions, such as consensus on an along-path scalar variable (Ghabcheloo et al., 2009) or relative positions while tracking a geometrically changing formation shape (Sun et al., 2009). For these reasons, a solution based on potential-field is the most promising approach for the work presented in this thesis since it establishes a simple and yet powerful base framework that can also incorporate new behaviors (such as obstacle avoidance, changing geometry formations, etc.) in a more straightforward manner comparatively to optimization- and consensus-based approaches.

6.2 Formation keeping

The coordination algorithm presented in this work is based on the work by Egerstedt and Hu (2001). This centralized approach assumes the existence of a virtual leader, which can be coincident with one of the robots, and an unlimited number of followers. The leader collects the positions of the different followers and instructs them on the position references in order to keep the desired formation. One of the main advantages of this method is that, under individual bounded errors, the formation is guaranteed to be stable, that is, each vehicle will eventually reach its relative position in the formation. This is especially important since it makes it possible to abstract from the lower level control layers, and therefore disregard the individual errors caused by control parameter mismatches or drifts, for example, as long as they remain bounded. Though this coordination

algorithm provides versatile behaviors and interesting performances, there is room for extensions, so that it is possible to explicitly handle motion constraints or communication limitations. An alternative mathematical construction of the method can make the formation tolerant to communication losses and delays. As long as bounded delays and periodical exchanges of feedback data and commands are guaranteed, the formation can be maintained and a smooth evolution can be obtained.

The next subsection presents a brief summary of the key concepts in Egerstedt and Hu (2001), which are subsequently generalized, extended and adapted to the problem of marine vehicle coordination under communication constraints.

6.2.1 Background

In order to make the forthcoming analysis easier and to self-contain the present section, the variables used throughout the following developments are introduced and the main ideas behind the work in (Egerstedt and Hu, 2001) are summarized.

Consider N vehicles moving in formation. The (possibly reduced order) position of the i th vehicle is denoted $\eta_i(t) \in \mathbb{R}^m$, $i = 1, \dots, N$, with $m \leq 3$. Similarly, the position of the virtual leader is given by $\eta_0(t) \in \mathbb{R}^m$, which is continuous and differentiable. Hereafter, the subscript $(\cdot)_0$ is used to denote the vectors or scalars corresponding to the virtual leader. The idea of considering a virtual leader instead of a real one is advantageous because it is not affected by real disturbances, which could degrade the overall performances of the formation.

Consider a continuous and differentiable path $p_0(s_0(t)) : \mathbb{R} \rightarrow \mathbb{R}^m$, parametrized by a scalar function $s_0(t) : \mathbb{R} \rightarrow \mathbb{R}$, that defines the virtual leader position at instant t : $\eta_0(t) = p_0(s_0(t))$. Each real vehicle (follower) should assume a specific position in the formation, with regard to the virtual leader. Therefore, a change of coordinates is appropriate. The desired relative position of a vehicle with regard to the virtual leader is given by $\tilde{\eta}_i^*(t) = \eta_i^*(t) - \eta_0(t)$, where $\eta_i^*(t)$ is the desired vehicle position expressed in an absolute inertial frame. Similarly, the position of the vehicle is also expressed with regard to the leader as $\tilde{\eta}_i(t) = \eta_i(t) - \eta_0(t)$.

The desired positions of the vehicles are given by $\tilde{\eta}_i^d(t) \in \mathbb{R}^m$, also defined with regard to the virtual leader position. These vectors, which can be seen as the vector defining the position of virtual followers, make it possible for the vehicles to follow a time-varying reference that is not rigidly coupled to the position of the virtual leader. Instead, its dynamics can be assigned so that it converges to $\tilde{\eta}_i^*(t)$, as intended, but still considering the individual tracking errors defined by the difference between this virtual follower position and the corresponding real vehicle position.

To drive the individual references $\tilde{\eta}_i^d(t)$ to their respective desired final positions $\tilde{\eta}_i^*(t)$, a *formation constraint function* is used

$$F : \mathbb{R}^m \times \dots \times \mathbb{R}^m \rightarrow \mathbb{R}^+. \quad (6.1)$$

It is assumed that this function is differentiable and strictly convex, and the solution of

$$F(\tilde{\eta}_1^d(t), \dots, \tilde{\eta}_n^d(t)) = 0$$

is uniquely determined by $(\tilde{\eta}_1^*(t), \dots, \tilde{\eta}_n^*(t))$, or equivalently $F^{-1}(0) = (\tilde{\eta}_1^*(t), \dots, \tilde{\eta}_n^*(t))$. This formation constraint function is actually a positive definite potential-field function that creates a measure of the distance between all the reference positions $\tilde{\eta}_i^d(t)$ and their respective desired final positions $\tilde{\eta}_i^*(t)$.

As for the virtual leader, suppose that the evolution of the individual references are determined by paths $p_i(s_i(t)) : \mathbb{R} \rightarrow \mathbb{R}^m$ that can be designed so that $\tilde{\eta}_i^d(t)$ converges to $\tilde{\eta}_i^*(t)$. Take

$$\tilde{\eta}_i^d(t) = p_i(s_i(t)), \quad (6.2)$$

which, differentiating with respect to time, results

$$\dot{\tilde{\eta}}_i^d(t) = \frac{dp_i(s_i(t))}{ds_i(t)} \dot{s}_i(t), \quad i = 1, \dots, N. \quad (6.3)$$

Choosing

$$\frac{dp_i(s_i(t))}{ds_i(t)} = -\nabla_{\tilde{\eta}_i^d(t)} F, \quad (6.4)$$

and

$$\dot{s}_i(t) = c_i e^{-\alpha_i \rho_i(t)}, \quad (6.5)$$

for all $i = 1, \dots, N$, where $c_i, \alpha_i > 0$ and $\rho_i(t) = \|\tilde{\eta}_i(t) - \tilde{\eta}_i^d(t)\|$ makes the reference $\tilde{\eta}_i^d(t)$ converge to $\tilde{\eta}_i^*(t)$ under bounded error $\rho_i(t)$ (see the theorems in (Egerstedt and Hu, 2001)).

It is still necessary to define the evolution of the virtual leader over its path. Similarly, the time derivative of the evolution rate is given by

$$\dot{s}_0(t) = \frac{c_0 e^{-\alpha_0 \sum_{i=1}^N \rho_i(t)}}{\left\| \frac{dp_0(s_0(t))}{ds_0(t)} \right\|}, \quad (6.6)$$

which takes into account the sum of all the vehicle tracking errors, and where $c_0, \alpha_0 > 0$. Of course, it is supposed that $\left\| \frac{dp_0(s_0(t))}{ds_0(t)} \right\| \neq 0$ for all $s_0(t)$, which means that the path of the virtual leader has no *stationary points*.

6.2.2 Generalization

The method presented is suitable for most robotic applications with vehicles that are not strongly affected by communication latency and intermittence. The only requirement for the algorithm to work properly is ensuring individual bounded tracking errors. This construction is powerful but may be limited when it comes to practical implementation. For example, note that in a faulty formation, with a vehicle that cannot move or that is unable to communicate its position to the virtual leader, this latter will continue evolving since $\dot{s}_0(t) > 0, \forall \rho_i(t) \in \mathbb{R}^+$ (see (6.6)). Depending

on the requirements, it may be preferable to stop the formation, that is, the virtual leader holds its position and so do all real and virtual followers vehicles operating properly, if one of the vehicles is unable to reach its position reference or is unable to communicate. Furthermore, the construction above does not allow static formations, that is, formations holding position.

This set of reasons leads us to present a more general construction for this centralized coordination problem. Some changes to the control scheme are proposed. Firstly, and following the same sequence as above, the direction of the path does not necessarily need to follow the steepest descent direction. Instead of (6.4), the use of continuous functions of the type $f_i(F) : \mathbb{R} \rightarrow \mathbb{R}^m$ that verify

$$(\nabla_{\tilde{\eta}_i^d(t)} F)^T \cdot f_i(F) < 0, \quad \forall F \neq 0,$$

and

$$f_i(0) = \mathbf{0}.$$

is proposed. Then, the path is chosen so that it obeys the following relationship:

$$\frac{dp_i(s_i)}{ds_i} = f_i(F), \quad i = 1, \dots, N. \quad (6.7)$$

Furthermore, the proposed path evolution parameters s_i are given by

$$\dot{s}_i = g_i(\rho_i(t)), \quad i = 1, \dots, N, \quad (6.8)$$

where $g_i(\rho_i(t)) : \mathbb{R}^+ \rightarrow \mathbb{R}^+$ are continuous non-increasing functions.

Finally, the leader path evolution is dictated by the product

$$\dot{s}_0 = \lambda_0 \prod_{i=1}^N \alpha_i g_i(\rho_i(t)), \quad (6.9)$$

where λ_0 and α_i are positive constants.

Note that $\dot{s}_i = 0$ and $\dot{s}_0 = 0$ if $g_i(\rho_i(t)) = 0$, for any $i = 1, \dots, N$. This means that both the vehicle (virtual) reference and the virtual leader hold their positions, awaiting for the vehicle i to track its reference so that $g_i(\rho_i(t)) > 0$, and so do the remaining references after having tracked their desired positions in the formation with respect to the virtual leader. This is also valid when there are more than one vehicle whose tracking errors imply $g_i(\rho_i(t)) = 0$.

The rest of the proof of convergence follows the same steps as in (Egerstedt and Hu, 2001). Suppose that each vehicle is able to track its reference in finite time so that $g_i(\rho_i(t))$ is non null,

that is, there exists a time t' , that verifies $g_i(\rho_i(t)) > 0, \forall t > t'$. Then, it follows that

$$\begin{aligned}\dot{F} &= \sum_{i=0}^N (\nabla_{\tilde{\eta}_i^d(t)} F)^T \dot{\tilde{\eta}}_i^d(t) \\ &= \sum_{i=0}^N (\nabla_{\tilde{\eta}_i^d(t)} F)^T \frac{dp_i(s_i)}{ds_i} \dot{s}_i \\ &= \sum_{i=0}^N (\nabla_{\tilde{\eta}_i^d(t)} F)^T f_i(F) \dot{s}_i, \quad \forall t > t'.\end{aligned}$$

Since, by definition, $(\nabla_{\tilde{\eta}_i^d(t)} F)^T f_i(F) < 0, \forall F > 0$, and $\dot{s}_i = g_i(\rho_i(t)) > 0$ and consequently $\dot{s}_0 > 0$, for all $t > t'$, it yields

$$\dot{F} < 0, \forall t > t', \forall F > 0.$$

This proves that the formation converges to the desired shape and position. In contrast to (6.6), note that no assumption was made on the leader path. This makes it possible to handle both dynamically changing paths, as well as stationary points and, as a result, station-keeping behaviors can be obtained.

6.2.3 Particular method

For a scenario with limited communication bandwidth, limited range and intermittence, there are special concerns regarding the relative vehicle placement and the behavior of the formation in case of faults, which include communication losses or malfunctioning vehicles. In such cases, it may be preferable to make the formation hold its position, waiting for the *missing(s) vehicle(s)*². Furthermore, supposing that a given geometry configuration allows robust communication links, it may be desirable that such a configuration is achieved. Nevertheless, the scheme proposed in (Egerstedt and Hu, 2001) can not guarantee that the vehicles converge to their desired position $\tilde{\eta}_i^*(t), i = 1, \dots, N$ in the formation since $\dot{s}_i > 0, i = 0, \dots, N$ if they have bounded velocity.

Next, a particular implementation is proposed based on the generalization presented above. Any other choice of function meeting the conditions above would be valid as well. Here, a focus on limited formation errors and rigid formations is given. Empirically, the aim is to guarantee that the vehicles do not deviate too much from their position references in the formation.

The objective is to reduce the distance between the desired and the reference positions. Therefore, define the proposed formation constraint function to be given by

$$F = \sum_{i=1}^N \|\tilde{\eta}_i^d(t) - \tilde{\eta}_i^*(t)\|^2, \quad (6.10)$$

²missing vehicles are seen here as vehicles that are above a predefined threshold distance from their respective references (virtual follower) or that can not communicate with the virtual leader

which is strictly convex and positive definite. As real marine vehicles have bounded velocities, the functions $f_i(F)$ are defined to be a bounded function of the gradient of F :

$$f_i(F) = -\text{sat}\left(\nabla_{\tilde{\eta}_i^d(t)} F, \Gamma_i\right), \quad (6.11)$$

where Γ_i are positive constants and $\text{sat}(\cdot, \cdot) : \mathbb{R}^n \times \mathbb{R} \rightarrow \mathbb{R}^n$ is the saturation function now defined as in (5.37). This definition obviously meets the condition $(\nabla_{\tilde{\eta}_i^d(t)} F)^T f_i(F) < 0$. Note that decreasing the constants Γ_i makes it possible to evolve the position references more slowly.

The next step is to define the functions $g_i(\rho_i(t))$. The aim is to achieve a *rigid* formation where possible failures in both tracking performances and/or communication links cause the formation to stop (virtual leader holding its position and vehicles holding their positions in the formation). This will allow the *missing vehicles* to join the formation before it continues evolving over the desired path. Henceforth, the choice is a simple piecewise linear and nonnegative function as follows:

$$g_i(\rho_i(t)) = \begin{cases} \Lambda_i - \lambda_i \rho_i(t), & \text{if } 0 \leq \rho_i(t) \leq \frac{\Lambda_i}{\lambda_i}, \\ 0, & \text{otherwise} \end{cases}, \quad (6.12)$$

where $\Lambda_i, \lambda_i > 0$ are positive constants.

This definition implies that the formation evolves only if $\rho_i(t) < \frac{\Lambda_i}{\lambda_i}$ for all $i = 1, \dots, N$. Otherwise, the formation will end up stopping, because the virtual leader stops. Hence the *rigidity* of the formation, that is, the error tolerance for the vehicles to track their respective references, is dictated by the ratio $\frac{\Lambda_i}{\lambda_i}$. This can be used to design rigid formations where the positions in the formation are maintained as precisely as desired. This, however, may come at the expense of a slower formation evolution.

Additionally, as Λ_i is the maximum value of $g_i(\rho_i(t))$, the evolution rate is directly defined by this constant: the greater the value of Λ_i , the faster the evolution of the i th position reference along the path that conducts the vehicle to the desired position in the formation.

6.2.4 Convergence under bounded tracking error and communication constraints

The overall stability and convergence of the formation can be assessed through the leader evolution variable s_0 . It has been clear that the formation converges to the desired position, that is, the virtual leader converges to its reference position and so do the virtual followers, whenever the condition $\dot{s}_0 > 0$ is verified (see (6.8), (6.9) and (6.12)). This condition means that all the vehicles are tracking their respective references with a bounded error. Therefore, it suffices to prove that $\dot{s}_0 > 0$ in order to demonstrate the convergence of the formation.

Hence, choose Λ_i and λ_i so that

$$g_i(\rho_i(t)) > 0 \Leftrightarrow \rho_{Mi} < \frac{\Lambda_i}{\lambda_i}. \quad (6.13)$$

Recall that ρ_{Mi} is the upper bound on the target tracking error (see (5.42)). If this is satisfied for all $i = 1, \dots, N$, then using the convergence properties derived in (5.42), it follows that there is a finite time t' that ensures

$$\dot{s}_0 = \lambda_0 \prod_{i=1}^N \alpha_i g_i(\rho_i(t)) > 0, \quad \forall t > t'. \quad (6.14)$$

Obviously, the time t' depends on the initial vehicle poses and disturbances.

Hereafter, the discrete nature of the communications is explicitly addressed while the intermittence is addressed implicitly. Suppose that the vehicle i reports its tracking error vector $\tilde{\eta}_i(t_k)$ to the virtual leader at time t_k . In the absence of new data, the virtual leader assumes that the position of the i th vehicles remains constant until the new position is reported at time t_{k+1} . The intention is to analyze how the position reference for the vehicle i evolves between two consecutive transmissions of the position. What follows is valid for any $i = 1, \dots, N$. Without loss of generality, assume first that $\rho_i(t_k) < \frac{\Lambda_i}{\lambda_i}$. Moreover, it is assumed that the leader transmits the position reference somewhere in the interval $[t_k, t_{k+1}]$.

Supposing that $\tilde{\eta}_{li}(t) = \tilde{\eta}_i(t_k)$, that is, the position of position error of the vehicle i seen by the the leader is constant in the interval $t_k < t < t_{k+1}$, the aim is to determine how the position reference evolves. The time derivative of the estimated distance between the reference and the estimated position of the vehicle $\tilde{\eta}_i(t_k)$, which is denoted $\hat{\rho}_i = \|\tilde{\eta}_i^d(t) - \tilde{\eta}_i(t_k)\|$, is given by

$$\frac{d\hat{\rho}_i}{dt} = \frac{\partial \hat{\rho}_i}{\partial \tilde{\eta}_i^d(t)} \frac{d\tilde{\eta}_i^d(t)}{dt} + \frac{\partial \hat{\rho}_i}{\partial \tilde{\eta}_i(t_k)} \frac{d\tilde{\eta}_i(t_k)}{dt}.$$

Since $\frac{d\tilde{\eta}_i(t_k)}{dt} = 0$, it yields:

$$\begin{aligned} \frac{d\hat{\rho}_i}{dt} &= - \frac{(\tilde{\eta}_i^d(t) - \tilde{\eta}_i(t_k))^T}{\hat{\rho}_i} f_i(F) g_i(\hat{\rho}_i) \\ &= - \frac{(\tilde{\eta}_i^d(t) - \tilde{\eta}_i(t_k))^T}{\hat{\rho}_i} f_i(F) (\Lambda_i - \lambda_i \hat{\rho}_i) \\ &\leq \Gamma_i (\Lambda_i - \lambda_i \hat{\rho}_i). \end{aligned}$$

By the comparison lemma (Khalil, 2002), it is possible to obtain

$$\hat{\rho}_i \leq \frac{\Lambda_i}{\lambda_i} - \frac{\Lambda_i - \lambda_i \hat{\rho}_i(t_k)}{\lambda_i} e^{-\lambda_i \Gamma_i (t - t_k)}.$$

The case where $\hat{\rho}_i(t_k) \geq \frac{\Lambda_i}{\lambda_i}$ is straightforward: because $g_i(\hat{\rho}_i) = 0$, $\forall t \in [t_k, t_{k+1})$, $\frac{d\hat{\rho}_i}{dt} = 0$. In other words, the reference does not evolve and neither does the virtual leader as long as all the real vehicles have not tracked their references with error distances below $\rho_i(t) < \frac{\Lambda_i}{\lambda_i}$.

Since the vehicles are able to track their references with errors $\rho_i(t) < \frac{\Lambda_i}{\lambda_i}$ in a finite time, and assuming that the vehicles are able to communicate in a bi-directional way with the virtual leader with bounded communication periods, which may be constant or not, it is possible to conclude

that

$$\lim_{t \rightarrow \infty} \frac{1}{t - t_0} s_0 = \lim_{t \rightarrow \infty} \left(\frac{1}{t - t_0} \int_{t_0}^t \prod_{i=1}^N \alpha_i g_i(\rho_i(t)) dt + s_0(t_0) \right) > 0. \quad (6.15)$$

Hence s_0 continues increasing over time, thus guaranteeing that the formation evolves along its path.

6.3 Experimental results

Several experiments have been carried out at the river and at sea. The results presented next have been carried out in the Douro river, close to Porto, Portugal and in the Mediterranean Sea, in La Spezia, Italy. The setup description is borrowed from section 5.3. The formation has been operating both with radio (WiFi) communications and acoustics communications to validate the approach for underwater operations and still keep accuracy of surface vehicles for data analysis. On shore, the virtual leader was running on a local computer for direct feedback on the vehicles positions and on the performances of the algorithm. The update rate for the virtual leader was set equal to the local control rate in the vehicles (10 Hz). When operating over radio communications, the communication rate was also set to this rate. For acoustic communications, the communication rate has been imposed by the acoustic channel.

This section is divided according to the communication means used to exchange data between the leader and the followers. In the first part, a high data rate, using radio communications, is considered. To assess the performances of the method under nominal and degraded modes, two different types of missions are presented. In degraded mode operation, the local control of a vehicle has been *degraded* by attaching sensors on the vehicle body which have not been considered in the vehicle dynamics model. In the second part, the formation-keeping control scheme is tested over acoustic links provided by underwater acoustic modems attached to the vehicles.

Although only two vehicles were used, it has been demonstrated in the previous section that the coordination scheme is expandable to as many vehicles as desired, as long as the communication means has the capability to handle all the transmissions of the vehicles states to the virtual leader and of the references to the vehicles. Henceforth, if this is verified, similar results are expected with formations incorporating more vehicles. The use of low data rates is still possible in this context, but at the cost of obtaining poorer performances and slower motions. The parameters Λ_i and λ_i introduced in section 6.2.3 can be tuned to balance data rate and desired performances.

6.3.1 Operation using radio communications

6.3.1.1 The “perfect” case

Zarco and Gama were deployed on the La Spezia shore, Italy. Apart from navigation sensors and dry body parts, the vehicles had the same body configuration. In the operation area, natural disturbances impacted on the motion of the vehicles. Namely, the presence of wind, small currents and waves were the main causes for deviations. The position references of the vehicles were set to

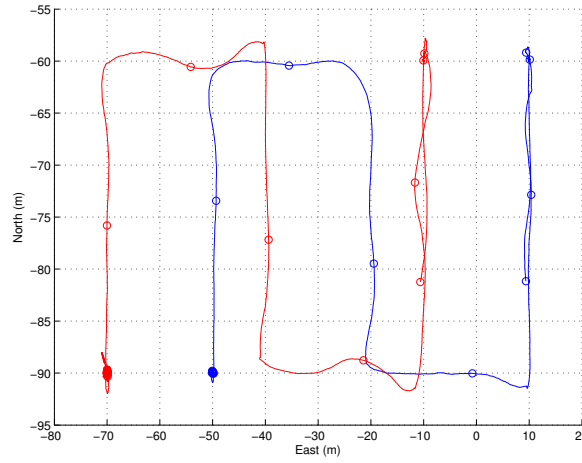


Figure 6.1: Coordinated mission of Zarco and Gama in La Spezia

follow the leader with offsets in the eastward direction. Specifically, Zarco position reference, with regard to the leader, was set to $\tilde{\eta}_Z^*(t) - \tilde{\eta}_0^*(t) = [0, 10]^T$, while Gama's was set $\tilde{\eta}_G^*(t) - \tilde{\eta}_0^*(t) = [0, -10]^T$. Therefore, their relative position should be $\tilde{\eta}_Z^*(t) - \tilde{\eta}_G^*(t) = [0, 20]^T$ along all the path, if perfect tracking was possible. The starting position of the leader was $[-60, 0]^T$

A short mission composed of 6 waypoints separated by 30 meters was ran. To assess the impact of the parameters λ_i and Λ_i on the formation, the parameter λ_i has been varied to change the *rigidity* of the formation. The parameter Λ_i was kept constant over this experiment and set to $\Lambda_i = 1.7$, while λ_i was set first to $\lambda_i = \frac{1}{2}$, $i = Z, G$. The virtual leader parameter was set to $\lambda_0 = 1.2$.

Figure 6.1 depicts the trajectories of Zarco and Gama. The maximum *allowed* deviation before the formation “stops” is $\Lambda_i/\lambda_i = 3.4$ meters. Note that the necessary condition for the virtual leader to track the next waypoint is to approach the current waypoint with a distance below one meter.

For further rigidity in the formation, the parameters λ_i , $i = Z, G$ were reduced to 1. Hence, the formation ultimately stops if a vehicle deviates more than $\Lambda_i/\lambda_i = 1.7$ meters from its reference. The resulting figure 6.2 shows the trajectories of the vehicles. These show accurate motions of the vehicles even in the presence of disturbances induced by wind, small waves and currents. Similarly, the relative positions of the vehicles show to be precise, as it can be seen from the circles on the plot, which indicate the positions of the vehicles at the same instants of time. Note that the trajectories deviate much less from the segments that join two adjacent waypoints. This is due to the reduced error tolerance and consequent slightly slower formation evolution. The norm of the relative position error is shown in figure 6.3. It is possible to notice that the error remains below one meter for most of the time, which is below the GPS measurement standard deviation (1.5 meters, announced by the manufacturer). The largest peak ($t \approx 270$ seconds) happens after Gama has lost communication which makes it hold its position after a short time, as it can be seen at position $[x, y] \approx [-62, -70]^T$ and later at position $[x, y] \approx [-72.5, -70]^T$.

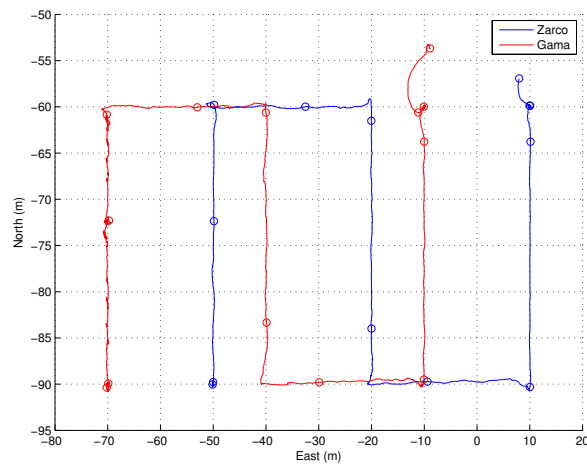


Figure 6.2: Positions of Zarco and Gama resulting from the coordinated mission in La Spezia. The circles indicate the positions of the vehicles at intervals of 30 seconds.

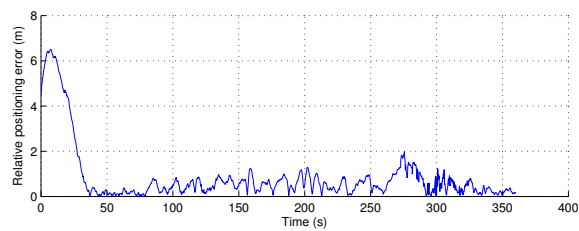


Figure 6.3: Relative positioning error between Zarco and Gama for the trajectory of figure 6.2

6.3.1.2 The “not-so-perfect” case

In March 2013, both vehicles were deployed in the Douro river for a set of tasks including bathymetry and acoustic signal recording. Both vehicles were equipped with minimal navigation setup, but differed on the protuberances originated by external devices carried on board as Zarco was equipped with an echosounder and a sidescan. Furthermore, each ASV carried an appended acoustic transponder. The dynamics models of the vehicles were not adapted to their new configurations in order to assess the robustness of the velocity control law, guidance and coordination scheme.

Therefore, it is expected that the damping of Zarco is significantly larger than in its basic configuration and thus the velocity control loop will suffer from severe errors. The same happens with Gama, though the effect of the added transducer is much less significant than the effect of the combined sensors added to Zarco. This impacts on the formation, as the desired velocities generated by the guidance law will be tracked with larger errors. In turn, the reference positions will be tracked more slowly and will naturally present larger tracking errors for non-static position references.

Figure 6.4 depicts the trajectories of Zarco and Gama along a path defined by eight waypoints. These eight waypoints define seven legs sequentially perpendicular with 100 meters and 30 meters of length, respectively. The necessary condition for the virtual leader to track the next waypoint is to approach the current waypoint with a distance below one meter. The virtual leader is initially placed at point $[-50, -50]$, Zarco must hold a relative position $[-5, 0]$ and the relative position of Gama was set to $[5, 0]$ with regard to the leader. These relative positions are expressed in a frame with the same directions of the inertial frame (NE).

The figure shows that the trajectory of Zarco is smoother than that of Gama. This is a result of the tracking errors: because Zarco moves slower due to unconsidered damping effects, its position is *delayed* with regard to Gama. As such, during transitions, when the virtual leader moves toward to the next waypoint, the reference position of Zarco changes its direction, thus inducing a heading change.

The circle indicates the positions of the vehicles every 30 seconds since the starting time. Note that the trajectory of the virtual leader has not been included for clarity.

Based on the desired relative positions of the ASVs, if the position references were perfectly tracked, a distance of 10 meters between the vehicles would be expected. However, the neglected additional damping and the disturbances originate an error on the relative distance as displayed in figure 6.5. The relative distance appears to be larger than expected in almost the entire path. This was due to the non-modelled added damping on Zarco, which is delayed with regard to Gama. It is possible to see that the distance between the vehicle decreases when following the smallest legs in the path. Here, Gama clearly follows a longer path than Zarco as it tracks its reference with smaller error than Zarco. Since the virtual leader reference changes from one corner to the following before Zarco reaches the corner, the trajectory of this latter is made shorter and *smoother*. The direct correspondence of the circles in figure 6.4 with the figure 6.5 shows that the

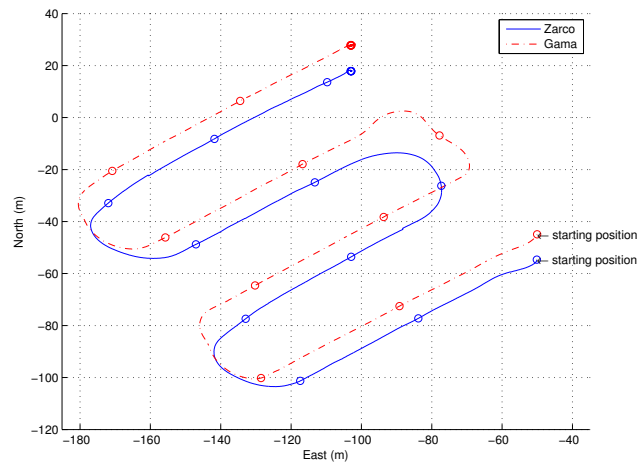


Figure 6.4: Coordinated mission of Zarco and Gama

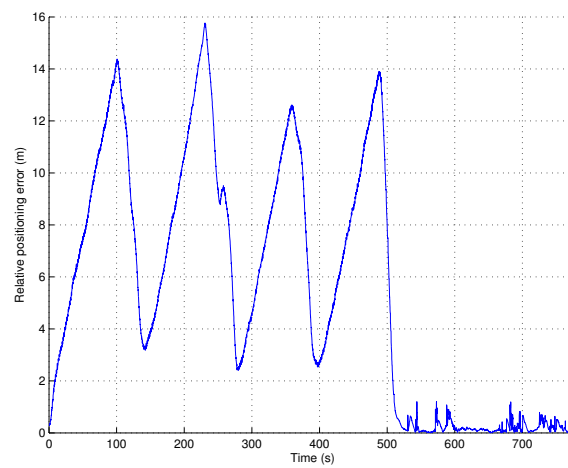


Figure 6.5: Relative distance error of Zarco and Gama along the coordinated operation

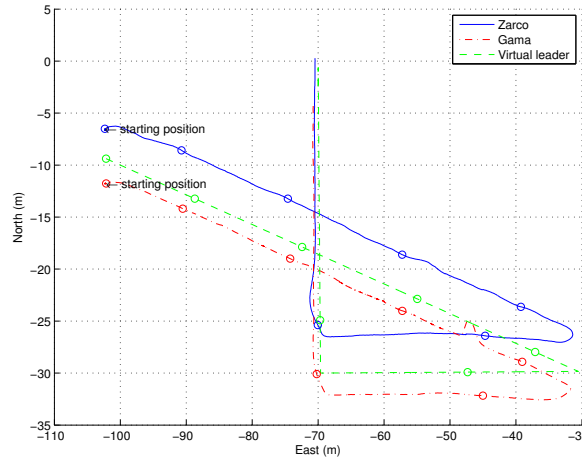


Figure 6.6: Coordinated mission of Zarco and Gama

vehicles get closer when following the smallest legs of the path.

These results show that the vehicles can maintain the formation with a limited error and that the vehicles are able to track their references under disturbances and even when mismatching model parameters are used. However, the vehicles ability to accurately track their position references can be further exploited by penalizing more the tracking errors in the formation. Therefore, by appropriately tuning the parameters λ_i and Λ_i , more rigid formations can be obtained.

Hence, the value of alpha was reduced to $\lambda_i = \frac{1}{5}$, $i = 1, 2$ and left $\Lambda_i = 1.7$. This implies that the formation stops if any vehicles presents a tracking error above $\frac{\Lambda_i}{\lambda_i} = 8.5$ meters. For the previous results, the parameters used were $\lambda_i = \frac{1}{15}$ implying that the formation stops evolving whenever a vehicle presents a tracking errors above 25.5 meters.

The results of this second mission are shown in figure 6.6. As in the previous case, the vehicles are required to maintain a relative distance on the north axis. This time, the vehicles were set to be at relative positions $[2.5, 0]$ (Zarco) and $[-2.5, 0]$ (Gama) with regard to the position of the virtual leader. The plot shows that the trajectories do not seem to hold this exact distance with to the virtual leader. Gama is closer to the virtual leader than desired, while Zarco is farther. The vehicles slightly deviate from their desired positions because of drift, whose direction is clearly in the first quadrant (0 to 90°). Along its path, Gama trajectory shows a discontinuity caused by wrong a GPS fix ($[x \ y] \approx [-26, -48]$), which is quickly handled by the controller moving Gama to its predefined path.

This discontinuity can also be seen in the figure 6.7, where the relative distance of the ASVs is shown, at time $t \approx 180$ (the first peak). The second peak at time $t \approx 300$ seconds is caused by an abrupt change in the direction of the formation after the virtual leader reached the position $[-70, -30]$. At this time, the vehicles rotate with with a relatively small forward motion as the control law in (B.1) dictates. The vehicles are subjected to unpredicted disturbances and their relative positions vary. A similar behavior has also happened in the first abrupt change at $[-70, -30]$, but this time, the trajectory followed by the two vehicles was more consistent

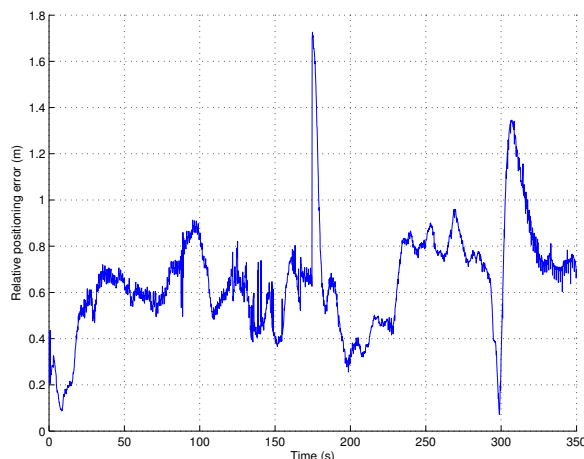


Figure 6.7: Relative distance error of Zarco and Gama along the coordinated operation

These results demonstrate that the formation rigidity can be tuned at will. Of course, disturbances and vehicle capabilities have to be taken into consideration and may hinder relative positioning accuracy. Nevertheless, vehicles are able to keep in formation with a relative error below 1.5 meters, which is of the same order of magnitude as the GPS accuracy.

6.3.2 Operation using acoustic communications

Further experiments have been conducted using acoustic communications. The main objective was to explore and to validate the overall control scheme in more constrained conditions. For this purpose, two ASVs equipped with acoustic modems have been employed and a base station that acted as the virtual leader on shore. This base station was also equipped with an acoustic modem. The status of the two ASVs and of the virtual leader was visualized in real-time and the desired position of the virtual leader was dynamically set by means of an user interface running on the base station. A short mission was run in a small area where the communications were constrained by the environment, having encountered several transmission failures, intrinsic delays and low bandwidth.

As the main objective of the experiment was to assess the robustness of the method, no efforts have been made to tune the acoustic modems to improve the communication channel. As a consequence, during the mission, a relatively large variability of transmission success was found and the time between two consecutive transmissions was large (tens of seconds in some cases). Moreover, this variability was different for the two ASVs. The resulting trajectory is depicted in figure 6.8. It is important to highlight that both the references and the reported positions had their resolution reduced to one meter. The figure shows the real references (circles) and the evolution of the position of the ASVs.

Here, the robustness of the method was assessed by comparing the reference relative positions of the ASVs with their real relative positions in figure 6.9. It is possible to observe that the real

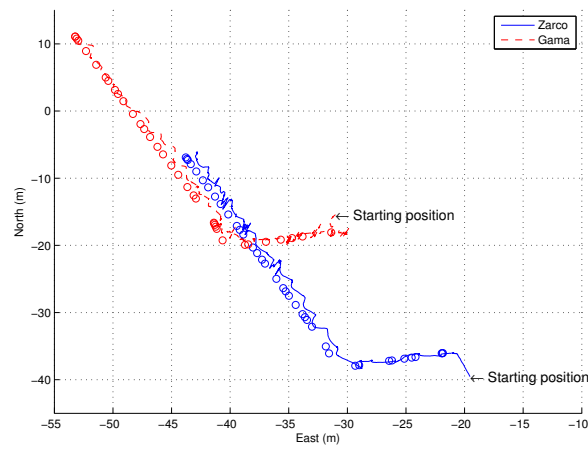


Figure 6.8: Discrete position references and trajectories of the two ASVs. The circles indicate the position references.

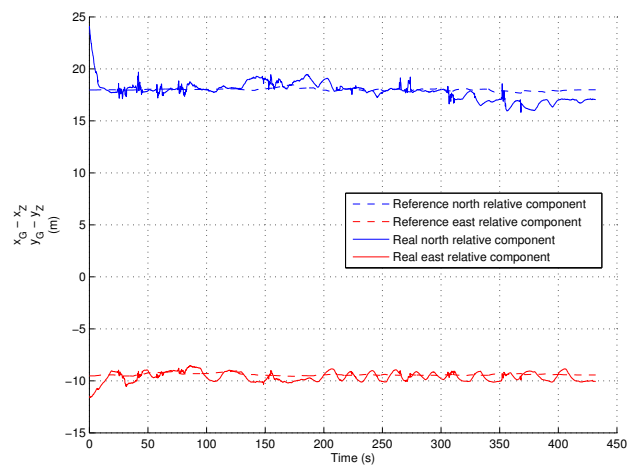


Figure 6.9: Real and reference relative positions of the two ASVs. Upper: North component. Lower: East component.

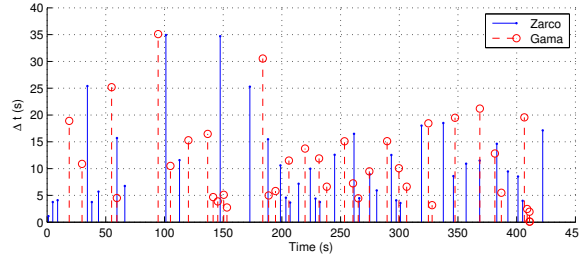


Figure 6.10: Time difference between two consecutive successful transmissions of state to the virtual leader

north and east components of the relative positions differ less than two meters from the desired ones, even in the presence of large and variable intermittences, as it can be seen in figure 6.10. Obviously, the decrease of resolution in both position feedback and references to one meter have also impacted on the performances of the formation.

From figure 6.8, it is possible to verify that both the vehicles had to hold their positions, facing the mean disturbance vector. The causes for that can be twofold: a vehicle does not receive new references for a large amount of time or is receiving the same reference (this happens when the formation stops); the other vehicle in the formation has not reached its reference and has caused the formation to stop, or the position report has not been transmitted to the virtual leader. From the plots, it is clear that these behaviors were caused by large delays on communications, which forced the evolution of the virtual leader to slow.

The trajectories of the vehicles in figure 6.8 are much less smooth as compared to the trajectories using radio links (figure 6.2). This is a consequence of the lower bandwidth and larger intermittences and delays but, if no drifts influenced the vehicles trajectories, they would be similar. From figure 6.8, and from our empirical verification, the drift was mainly induced by eastward wind. It is possible to conclude that the trajectory may have been rougher if the direction of the trajectory was in the same as that of the drift vector, as the vehicle would have to turn 180° to face the drift in order to hold the position.

6.4 Conclusions

Motivated by several sensor fusion applications that are intrinsically centralized, a centralized coordination scheme have utilized the target tracking algorithm developed in chapter 5 to drive the vehicles coherently. With the lower level target tracking algorithm, no pre-established paths have to be known *a priori*. Depending on the technology used for communications, the data exchange may suffer from significant delays (acoustic communications, for instance). By construction, the formation keeping method can become tolerant to delays with very small or ultimately no effort on parameter tuning. Of course, for optimal performances according to a given metric, some parameters may have to be modified but the convergence of the vehicles to their positions in the formation and the convergence of the entire formation remain guaranteed. Additionally, as a result

of the control scheme presented in the current and in the previous chapter, it is possible to obtain both mobile and static formations.

The experiments conducted in real conditions have provided very encouraging results, allowing the vehicles to behave robustly under drifts induced by wind and currents as well as communication limitations.

Using the results presented here, a natural extension of this chapter would be a weakly centralized formation where several virtual leaders would be dictating their local formation in a macro formation composed of several sub-formations. Furthermore, using roles and higher level protocols and methods, one can obtain very versatile and fault tolerant formations where the composition of the sub-formation can be obtained as a function of the overall state of the formation or as a function of the on-going task.

Chapter 7

Cooperative localization and tracking

As introduced in chapter 2, underwater localization and positioning is still a considerable challenge due to environmental and technological constraints. Such limitations have been restraining the growth of autonomous robotic systems in such environments and therefore the localization of underwater targets, including mobile robots, has attracted the interest of several researchers over the last years (Whitcomb et al., 1999; Cruz et al., 2001; Bahr et al., 2009; Vaganay et al., 2004; Kussat et al., 2005; Aparicio et al., 2011; Casey et al., 2007; Eustice et al., 2011). In this chapter, the three-dimensional positioning of time-of-arrival (TOA) sensors to track and optimally estimate the three-dimensional position of an underwater sound source is addressed. Firstly, an unconstrained case, in which sensors can be placed anywhere in space, is addressed to find the optimal configuration. Subsequently, motivated by real applications, the same problem is tackled for the plane-constrained case. Although instigated by underwater applications, the work presented here has applications in general networks of distributed sensors that make use of TOA measurements to estimate the position of a source.

7.1 Related works and motivation

Underwater localization solutions predominantly include two types of methods: range-based and combined angle/range-based. Range based solutions use trilateration to determine the position of an active transmitter underwater. The long baseline (LBL) has been employed in many georeferentiation applications for which bounded error localization is required (Whitcomb et al., 1999; Cruz et al., 2001; Bahr et al., 2009; Vaganay et al., 2004). LBL systems require precise synchronization between the transmitters and the receivers for one-way travel time (OWTT) (Eustice et al., 2011). In opposition, two-way travel time (TWTT) based systems do not need synchronization (Cruz et al., 2001). While the former can be composed of two sets of sensors (active transmitters and passive receivers), the second scheme must use both in each beacon or use transducers that accumulate the two roles.

The ultra-short baseline (USBL) systems (see, for example, Gadre et al. (2008)) use the bearing and ranging capabilities of acoustic receivers and transmitters. Receivers are placed closely and

measure the time-differences-of-arrival (TDOAs), thus making it possible to compute the angle of arrival. The range measurements are obtained similarly to LBL.

As seen in chapter 2, self-localization can still be achieved from integration over time of inertial measurements only but recall that this does not ensure bounded error on the position estimate for unlimited time.

All these techniques have been used in several self-localization problems, which are a fundamental part of autonomous vehicle navigation. In order to estimate its position, a vehicle measures its relative ranges or angles to one or more beacons, whose positions are known. Complementary, tracking techniques typically have to measure variables in different places in order to infer the position of the target object. This is the case of tracking using TOA sensors. Under some conditions, LBL and USBL systems can also be used for target tracking.

Optimal sensor positioning for tracking purposes has recently attracted the attention of several researchers (Bishop et al., 2010; Martinez and Bullo, 2006; Meng et al., 2012; Dette, 1997; Zhao et al., 2012b; Yang et al., 2011; Ray and Mahajan, 2002; Dai et al., 2013). Numerous algorithms have been developed for estimation. The most recurrent in the literature are the Kalman filter (Kalman, 1960), the particle filter and least-squares estimation methods. In several problems, and as seen in chapter 4, the estimate variance depends on the state itself and some works have tackled the problem so that the state is guaranteed to be in the vicinity of the optimal observability points. The Cramer-Rao lower bound (CRLB), which provides a measure of the achievable performance of an efficient estimator, has been used in several works to assess such a *measure of observability* (see, for example, (Martinez and Bullo, 2006; Bishop et al., 2010; Bingham, 2003)). Mostly based on the analysis of the Fisher information matrix (FIM), whose determinant is the inverse of the CRLB, several results have been developed for multiple scenarios, including two- and three-dimensional problems with homogeneous and heterogeneous sensors. Different types of sensors that provide measurements on bearing, range, received signal strength (RSS), TOA, TDOA have been considered. Significant contributions have been given in (Bishop et al., 2010; Martinez and Bullo, 2006; Zhao et al., 2012b) and two common approaches are considered in the literature: minimization of the average of the variances (A-optimality) or minimization of the volume of the confidence regions (D-optimality) (refer to Dette (1997) for further details).

Aiming at minimizing the volume of the confidence regions, Bishop et al. (2010) present a summary of the main results for bearing, ranging, TOA and TDOA. The sensors are considered to be homogeneous with same variance. The authors provide interesting results presenting the necessary conditions for optimal positions of the sensors in two-dimensional problems.

The optimal positioning of TDOA sensors has also been considered in Meng et al. (2012), where the A-optimality criterion was used to optimize the average variance of the estimate for homogeneous sensors in 2D scenarios. A solution considering an extended Kalman filter (EKF) and a nonlinear programming problem to find the optimal trajectories of the sensor illustrate the work with interesting simulation results.

Using a transversal approach for three different optimization problems, Zhao et al. (2012b) provide an overview on range-only, bearing-only and RSS-only optimal positioning, in two- and

three-dimensional spaces, extending the work in Zhao et al. (2012a). Beyond the unification of the theory for the three methods, the extension of the localization problem to three-dimensional space constitutes the main contribution of the work.

In the absence of theory supporting the optimal placement of TOA sensors in three-dimensional spaces, Ray and Mahajan (2002) propose a genetic algorithm to solve a geometrically constrained optimization problem, assuming that the position of the sound source is known. The results obtained from simulation are very interesting and are in agreement with the result presented later on in this chapter.

Other works also include the analysis for bearing-only and combined bearing/ranging optimal positioning of sensors in Yang et al. (2011) and range-only in Dai et al. (2013). Martinez and Bullo (2006) present an optimal positioning algorithm for a network of ranging sensors that uses an extended Kalman filter (EKF) and a decentralized control method to drive the sensors towards their optimal positions.

As mentioned in previous works (Zhao et al., 2012b; Ray and Mahajan, 2002), the extension of the optimal positioning of sensor to 3D is not trivial. Motivated by marine applications, in this chapter, results in the context of TOA-only sound source localization are presented for both unconstrained three-dimensional and plane-constrained positioning.

7.2 Unconstrained optimal positioning of sensors

7.2.1 Background

As seen before, several methods can be used for the localization of a sound source underwater. Our interest focuses now on the TOA-based estimation problem, for which a minimum of four sensors is required to solve the problem of position estimation since, in addition to the position, the time of emission is unknown. Next, the main theoretical background is presented, including the measurement model and the specific FIM used afterwards to find the optimal relative positions of the sensors, with respect to the target, in order to obtain the best possible estimate, that is, with the least possible uncertainty.

7.2.1.1 Time-of-arrival measurements

Consider a set of N sensors. Let us write the vector of observations as

$$\hat{\mathbf{t}} = \begin{bmatrix} \hat{t}_1 \\ \hat{t}_2 \\ \vdots \\ \hat{t}_N \end{bmatrix} = \boldsymbol{\tau} + \mathbf{w}_s = \begin{bmatrix} \tau_1 \\ \tau_2 \\ \vdots \\ \tau_N \end{bmatrix} + \begin{bmatrix} w_{s1} \\ w_{s2} \\ \vdots \\ w_{sN} \end{bmatrix}, \quad (7.1)$$

where $\boldsymbol{\tau} \in \mathbb{R}^N$ is a vector, whose entries are the TOAs, which is corrupted by a noise vector $\mathbf{w}_s = [w_{s1} \ w_{s2} \ \dots \ w_{sN}]^T \in \mathbb{R}^N$.

Note that w_{s_i} are variable and depend on several quantities such as the temperature along the water column, which also varies according to the horizontal position, and the positions of both emitter and receivers. Moreover, effects such as multipath or occlusions influence the distribution followed by w_{s_i} , as seen in chapter 2. In this chapter, it is assumed that, due to the proximity of the sensors to the target, such effects are negligible and that the noise variables can be drawn from a normal distributions $w_{s_i} \sim \mathcal{N}(0, \sigma_i^2)$, where σ_i^2 are the variances. It is also assumed that the noise variables w_{s_i} are uncorrelated.

Let the vector $\eta_t = [x_t \ y_t \ z_t]^T$ define the position of the target. Similarly, define $\eta_{s_i} = [x_{s_i} \ y_{s_i} \ z_{s_i}]^T$, $i = 1, \dots, N$, where $N \geq 4$ in the present case, to be the position of the i -th TOA sensor. Therefore, the relative positions are given by

$$\tilde{\eta}_i = \eta_{s_i} - \eta_t, \ i = 1, \dots, N. \quad (7.2)$$

Given the sound speed, c_s , and assuming a linear propagation of acoustic waves, the entries of the vector τ simply result:

$$\tau_i = \|\tilde{\eta}_i\|/c_s + \tau_t. \quad (7.3)$$

The position $\tilde{\eta}_i$ and the time of emission τ_t are unknown, thus the need for at least four sensors to determine the three-dimensional position of the target.

7.2.1.2 The Fisher information matrix

Define the measurement likelihood function $f_t(\hat{\tau}, \tau(\eta_t))$. The entries of the FIM, $I(\eta_t) \in \mathbb{R}^{4 \times 4}$, then result (see (Bishop et al., 2010) and (Martinez and Bullo, 2006)):

$$[I(\eta_t)]_{kl} = E \left\{ \frac{\partial}{\partial (\eta_t)_k} \ln \left(f_t(\hat{\tau}, \tau(\eta_t)) \right) \cdot \frac{\partial}{\partial (\eta_t)_l} \ln \left(f_t(\hat{\tau}, \tau(\eta_t)) \right) \right\},$$

where $E\{\cdot\}$ denotes the expected value and recall that the notation $[\cdot]_{ij}$ is used to identify the matrix entry in the i -th row and j -th column. Similarly, the notation $(\cdot)_i$ is used to denote the i -th element of a vector.

By assuming that the likelihood $f_t(\hat{\tau}, \tau(\eta_t))$ is a Gaussian function, one can show that the FIM results into

$$I(\eta_t) = (J_t(\eta_t))^T \Sigma^{-1} J_t(\eta_t), \quad (7.4)$$

where $J_t(\eta_t)$ is the Jacobian of the vector $\tau(\eta_t)$ and $\Sigma = \text{diag}(\sigma_1^2, \sigma_2^2, \dots, \sigma_N^2)$ is the covariance matrix.

The Jacobian of $\tau(\eta_t)$ can be written as

$$J_t(\eta_t) = -\frac{1}{c_s} \begin{bmatrix} \tilde{\eta}_1^T / \|\tilde{\eta}_1\| & c_s \\ \tilde{\eta}_2^T / \|\tilde{\eta}_2\| & c_s \\ \vdots & \vdots \\ \tilde{\eta}_N^T / \|\tilde{\eta}_N\| & c_s \end{bmatrix}$$

and, after some algebra, the FIM follows:

$$I(\eta_t) = \frac{1}{c_s^2} \begin{bmatrix} \sum_{i=1}^N \frac{\tilde{\eta}_i \tilde{\eta}_i^T}{\sigma_i^2 \|\tilde{\eta}_i\|^2} & -c_s \sum_{i=1}^N \frac{\tilde{\eta}_i}{\sigma_i^2 \|\tilde{\eta}_i\|} \\ -c_s \sum_{i=1}^N \frac{\tilde{\eta}_i^T}{\sigma_i^2 \|\tilde{\eta}_i\|} & \sum_{i=1}^N \frac{c_s^2}{\sigma_i^2} \end{bmatrix}. \quad (7.5)$$

In the next section, the necessary conditions to minimize the volume of the confidence region are derived.

7.2.2 Unconstrained optimal 3D localization

This section presents the analysis and the conditions to obtain the best achievable performance of an efficient estimator tracking the position of a sound source using TOA measurements. For the sake of illustration, the figure (7.1) and (7.2) show the optimal positions of the sensors and the corresponding FIM determinant, respectively.

7.2.2.1 Coordinates and metric

Let us decompose the FIM (7.5) as

$$I(\eta_t) = \frac{1}{c_s^2} \begin{bmatrix} I_1(\eta_t) & I_2(\eta_t) \\ I_3(\eta_t) & I_4(\eta_t) \end{bmatrix}, \quad (7.6)$$

where

$$\begin{aligned} I_1(\eta_t) &= \sum_{i=1}^N \tilde{\eta}_i \tilde{\eta}_i^T / (\sigma_i^2 \|\tilde{\eta}_i\|^2) \\ I_2(\eta_t) &= I_3(\eta_t)^T = -c_s \sum_{i=1}^N \tilde{\eta}_i / (\sigma_i^2 \|\tilde{\eta}_i\|) \\ I_4(\eta_t) &= c_s^2 \sum_{i=1}^N \frac{1}{\sigma_i^2}. \end{aligned}$$

In order to explore the FIM under the relative angular position of the target and of the sensors, express the matrix in spherical coordinates:

$$\begin{cases} \tilde{x}_i &= \|\tilde{\eta}_i\| s\theta_i c\psi_i \\ \tilde{y}_i &= \|\tilde{\eta}_i\| s\theta_i s\psi_i \\ \tilde{z}_i &= \|\tilde{\eta}_i\| c\theta_i \end{cases}, \quad (7.7)$$

where it is recalled that $s\cdot = \sin(\cdot)$ and $c\cdot = \cos(\cdot)$.

The submatrices of the FIM thus become

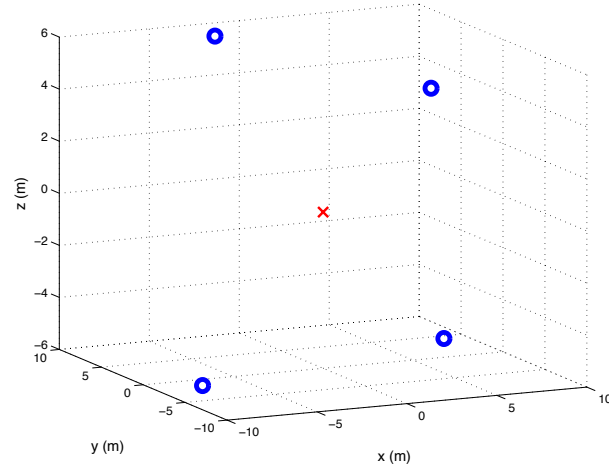


Figure 7.1: Optimal positions of receivers (circles). The target (cross) is located at the origin. The parameters considered are $\sigma_i = 10^{-4} \text{ s } \forall i$.

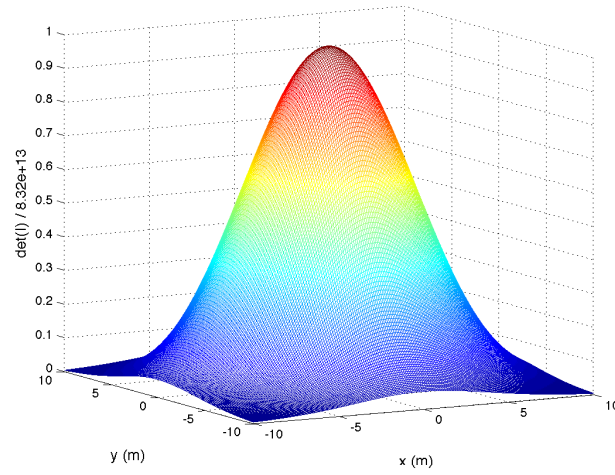


Figure 7.2: Metric value as a function of target position as a function of the target position in the plane defined by $z_t = 0$. The parameters considered are $c_s = 1500 \text{ m/s}$, $\sigma_i = 10^{-4} \text{ s } \forall i \in \{1, \dots, N\}$.

$$I_1(\eta_t) = \sum_{i=1}^N \frac{1}{\sigma_i^2} \begin{bmatrix} s\theta_i^2 c\psi_i^2 & s\theta_i^2 c\psi_i s\psi_i & s\theta_i c\theta_i c\psi_i \\ s\theta_i^2 c\psi_i s\psi_i & s\theta_i^2 s\psi_i^2 & s\theta_i c\theta_i s\psi_i \\ s\theta_i c\theta_i c\psi_i & s\theta_i c\theta_i s\psi_i & c\theta_i^2 \end{bmatrix}$$

$$I_2(\eta_t) = I_3(\eta_t)^T = -c_s \sum_{i=1}^N \frac{1}{\sigma_i^2} \begin{bmatrix} s\theta_i c\psi_i \\ s\theta_i s\psi_i \\ c\theta_i \end{bmatrix}$$

$$I_4(\eta_t) = c_s^2 \sum_{i=1}^N \frac{1}{\sigma_i^2}$$

It is interesting to note that, under this scenario, the FIM does not depend on the range between the sensors and the target but only on the relative angles.

In order to find the optimal position of the sensors to observe the target, choose the determinant of the FIM as the metric M for this scenario:

$$M = \det(I(\eta_i)). \quad (7.8)$$

This metric quantifies the *amount of information* given by a set of measurements collected by the sensors, which is aimed at being maximized. Therefore our problem is reduced to finding the set of angles θ_i and ψ_i that maximizes M . The D-optimality criterion is used to derive the optimal positions of the sensors so that the volume of the uncertainty ellipsoid is minimized (Dette, 1997). Mathematically, it is desired to find the pairs

$$\{\theta_i^*, \psi_i^*\} \in \underset{\substack{\{\theta_i, \psi_i\} \\ i=1, \dots, N}}{\operatorname{argmax}} M(\{\theta_i, \psi_i\}). \quad (7.9)$$

7.2.2.2 Optimal positions

Firstly, note that the FIM is symmetric. Hence, using the Schur complement as in (Bishop et al., 2010), the metric M , that is, the determinant of the matrix can be written in an alternative form as

$$\det(I(\{\theta_i, \psi_i\})) = \frac{1}{c_s^8} \det(I_4) \det(I_1 - I_2 I_4^{-1} I_3), \quad (7.10)$$

where the arguments of the matrix I_k , $k = 1, \dots, 4$, were dropped for clarity.

Since I_4 is a positive scalar, $\det(I_4) = I_4$, note that $I_2 I_4^{-1} I_3 \geq 0$ (the proof is simply based on the fact that, for any $x \in \mathbb{R}^3$, $x^T I_2 I_4^{-1} I_3 x = I_4^{-1} x^T I_2 I_2^T x = I_4^{-1} \|x^T I_2\|^2 \geq 0$ which, in turn, implies that $I_2 I_4^{-1} I_3$ is positive semi-definite) and therefore

$$\begin{aligned} M(\{\theta_i, \psi_i\}) &= \frac{1}{c_s^8} I_4 \det(I_1 - I_2 I_4^{-1} I_3) \\ &\leq \frac{1}{c_s^8} I_4 \det(I_1). \end{aligned} \quad (7.11)$$

Hence, it is possible to conclude that the equality is achieved when $I_2 = I_3^T = \mathbf{0}$ or equivalently

$$\sum_{i=1}^N \frac{s\theta_i c\psi_i}{\sigma_i^2} = 0, \quad \sum_{i=1}^N \frac{s\theta_i s\psi_i}{\sigma_i^2} = 0, \quad \sum_{i=1}^N \frac{c\theta_i}{\sigma_i^2} = 0, \quad (7.12)$$

Let us focus now our attention on the determinant of I_1 . Similarly to the previous step, decompose the matrix in blocks as follows:

$$I_1 = \begin{bmatrix} A & B \\ C & D \end{bmatrix} \quad (7.13)$$

with

$$A = \sum_{i=1}^N \frac{1}{\sigma_i^2} \begin{bmatrix} s\theta_i^2 c\psi_i^2 & s\theta_i^2 c\psi_i s\psi_i \\ s\theta_i^2 c\psi_i s\psi_i & s\theta_i^2 s\psi_i^2 \end{bmatrix},$$

$$B = C^T = \sum_{i=1}^N \frac{1}{\sigma_i^2} \begin{bmatrix} s\theta_i c\theta_i c\psi_i \\ s\theta_i c\theta_i s\psi_i \end{bmatrix},$$

$$D = \sum_{i=1}^N \frac{1}{\sigma_i^2} c\theta_i^2.$$

Under the assumption that $I_2 = I_3^T = \mathbf{0}$, it comes

$$M(\{\theta_i, \psi_i\}) = \frac{1}{c_s^8} I_4 \det(D) \det(A - BD^{-1}C). \quad (7.14)$$

Using the same reasoning as above and noting that D is a positive scalar, the verification that $BD^{-1}C \geq 0$ is straightforward. Therefore, the choice

$$B = C^T = \sum_{i=1}^N \frac{1}{\sigma_i^2} \begin{bmatrix} s(2\theta_i) c\psi_i \\ s(2\theta_i) s\psi_i \end{bmatrix} = \mathbf{0}$$

or, equivalently,

$$\sum_{i=1}^N \frac{s(2\theta_i) c\psi_i}{\sigma_i^2} = 0, \quad \sum_{i=1}^N \frac{s(2\theta_i) s\psi_i}{\sigma_i^2} = 0, \quad (7.15)$$

maximizes the metric M over $B = C^T$. Note that the fact that $s\theta_i c\theta_i = 1/2s(2\theta_i)$ has been used. Under this condition, the metric M becomes

$$M(\{\theta_i, \psi_i\}) = \frac{1}{c_s^8} I_4 D \det(A) \quad (7.16)$$

Let us concentrate now on maximizing $\det(A)$. Using the equalities $c\psi_i^2 = (1 + c(2\psi_i))/2$ and $s\psi_i^2 = (1 - c(2\psi_i))/2$, rewrite the matrix A as

$$A = \sum_{i=1}^N \frac{1}{\sigma_i^2} \begin{bmatrix} s\theta_i^2 (\frac{1}{2} + \frac{c(2\psi_i)}{2}) & s\theta_i^2 c\psi_i s\psi_i \\ s\theta_i^2 c\psi_i s\psi_i & s\theta_i^2 (\frac{1}{2} - \frac{c(2\psi_i)}{2}) \end{bmatrix}$$

whose determinant becomes

$$\det(A) = \left(\sum_{i=1}^N \frac{1}{2\sigma_i^2} s\theta_i^2 \right)^2 - \left(\sum_{i=1}^N \frac{1}{2\sigma_i^2} \frac{s\theta_i^2 c(2\psi_i)}{2} \right)^2 - \left(\sum_{i=1}^N \frac{1}{2\sigma_i^2} s\theta_i^2 s(2\psi_i) \right)^2$$

Hence, setting

$$\sum_{i=1}^N \frac{s\theta_i^2 c(2\psi_i)}{\sigma_i^2} = 0, \quad \sum_{i=1}^N \frac{s\theta_i^2 s(2\psi_i)}{\sigma_i^2} = 0, \quad (7.17)$$

maximizes the determinant of A over these terms.

Finally, if the conditions (7.12), (7.15) and (7.17) are satisfied, the metric is given by

$$M = \frac{1}{c_s^8} c_s^2 \sum_{i=1}^N \frac{1}{\sigma_i^2} \sum_{i=1}^N \frac{1}{\sigma_i^2} c \theta_i^2 \left(\sum_{i=1}^N \frac{1}{2\sigma_i^2} s \theta_i^2 \right)^2,$$

which can be rewritten as

$$M = \frac{1}{c_s^8} c_s^2 \sum_{i=1}^N \frac{1}{\sigma_i^2} \sum_{i=1}^N \frac{1}{\sigma_i^2} c \theta_i^2 \left(\sum_{i=1}^N \frac{1}{2\sigma_i^2} - \sum_{i=1}^N \frac{1}{2\sigma_i^2} c \theta_i^2 \right)^2.$$

Define $\xi = \sum_{i=1}^N \frac{1}{\sigma_i^2} c \theta_i^2$, the constant $\alpha = \sum_{i=1}^N \frac{1}{\sigma_i^2}$ and write, by substitution,

$$M = \frac{1}{c_s^6} \alpha \xi \left(\frac{1}{2} \alpha - \frac{1}{2} \xi \right)^2.$$

Note that $\xi \in [0, \alpha]$. It can be shown (by finding the roots of the derivative with respect to ξ) that the maximal value of M is reached when $\xi = \frac{\alpha}{3}$, or equivalently

$$\sum_{i=1}^N \frac{c \theta_i^2}{\sigma_i^2} = \frac{1}{3} \sum_{i=1}^N \frac{1}{\sigma_i^2}. \quad (7.18)$$

To summarize, the determinant of the FIM, $M(\cdot)$, reaches its maximum value, which is equal to $M^* = \frac{1}{27c_s^6} \left(\sum_{i=1}^N \frac{1}{\sigma_i^2} \right)^4$ when the following conditions are simultaneously satisfied:

$$\begin{aligned} \sum_{i=1}^N \frac{s \theta_i c \psi_i}{\sigma_i^2} &= 0, \quad \sum_{i=1}^N \frac{s \theta_i s \psi_i}{\sigma_i^2} = 0, \quad \sum_{i=1}^N \frac{c \theta_i}{\sigma_i^2} = 0, \\ \sum_{i=1}^N \frac{s(2\theta_i) c \psi_i}{\sigma_i^2} &= 0, \quad \sum_{i=1}^N \frac{s(2\theta_i) s \psi_i}{\sigma_i^2} = 0, \\ \sum_{i=1}^N \frac{s \theta_i^2 c(2\psi_i)}{\sigma_i^2} &= 0, \quad \sum_{i=1}^N \frac{s \theta_i^2 s(2\psi_i)}{\sigma_i^2} = 0, \\ \sum_{i=1}^N \frac{c \theta_i^2}{\sigma_i^2} &= \frac{1}{3} \sum_{i=1}^N \frac{1}{\sigma_i^2}. \end{aligned}$$

7.2.3 Positioning and estimation

In the previous section, it has been considered that the target position is perfectly known, which is very unlikely in most real estimation problems. In this section, an algorithm is proposed for estimation and positioning. The estimation algorithm is based on a nonlinear Newton's method to solve a nonlinear least-square formulated problem.

The algorithm is composed of two sequential steps that are iteratively ran whenever a new measurement set is available:

1. Estimation: given a set of TOA measurements, the position of the target is estimated using a least-squares method. Since the problem is nonlinear, a Newton's method is used to

iteratively estimate the position and the time of emission until the difference between the new estimate and the previous is less than a pre-set threshold value or exceeds a maximum number of iterations;

2. Positioning: given the estimate, the receivers are moved towards their (estimated) optimal relative positions. A gradient descent algorithm is employed to iteratively compute the directions to follow. The algorithm stops after a predefined number of iterations.

The convergence issues are not addressed here, since they have a large coverage in specialized literature. Nevertheless, one can anticipate that the overall speed performances and number of iterations that the algorithm requires to obtain an equivalent estimate uncertainty and positioning depend on the gains used in the Newton's and gradient descent methods.

7.2.3.1 Estimation

In order to estimate the target position, the estimation problem is formulated as a nonlinear least-square problem. The Newton's method is then applied to find the optimal point that minimizes a given error function.

Define the state estimate as the concatenation of the position vector and of the time of emission estimates:

$$\hat{X}_k = [\hat{\eta}_t(k)^T \hat{\tau}_t(k)]^T \in \mathbb{R}^4, \quad (7.19)$$

where $k \in \mathbb{N}$.

Recall that the relative positions of the receivers are given by $\tilde{\eta}_i = \eta_{s_i} - \eta_t$ and that the TOAs are given by $\tau = [\tau_1, \dots, \tau_N]$ and define the *error* vector as

$$g(\eta_t, \tau) = \begin{bmatrix} ||\tilde{\eta}_1||^2 - c_s^2(\tau_1 - \tau_t)^2 \\ \vdots \\ ||\tilde{\eta}_N||^2 - c_s^2(\tau_N - \tau_t)^2 \end{bmatrix}. \quad (7.20)$$

Given an initial guess estimate of the state \hat{X}_0 and a set of measurements composing the entries of $\hat{\tau} = [\hat{\tau}_1, \dots, \hat{\tau}_N]$, the state estimate is recursively estimated, until a given criterion is met, by the Newton's method applied to multidimensional nonlinear equations:

$$\hat{X}_{k+1} = \hat{X}_k - K(J_g(\hat{X}_k))^\dagger g(\hat{\eta}_t(k), \hat{\tau}_t(k)), \quad (7.21)$$

where $K > 0$ is a scalar gain, $J_g(\hat{X}_k)$ stands for the Jacobian of g evaluated at \hat{X}_k for the set of measured times of arrival, which is given by

$$J_g(\hat{X}_k) = 2 \cdot \begin{bmatrix} -\tilde{\eta}_1^T & c_s^2(\hat{\tau}_1 - \tau_t) \\ \vdots & \vdots \\ -\tilde{\eta}_N^T & c_s^2(\hat{\tau}_N - \tau_t) \end{bmatrix} \Big|_{\tilde{\eta}_i = \eta_{s_i} - \hat{\eta}_t(k), \tau_t = \hat{\tau}_t(k)}.$$

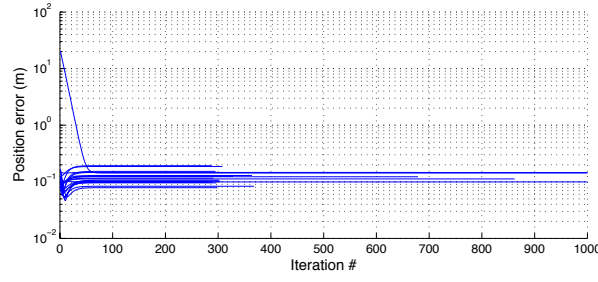


Figure 7.3: Error evolution

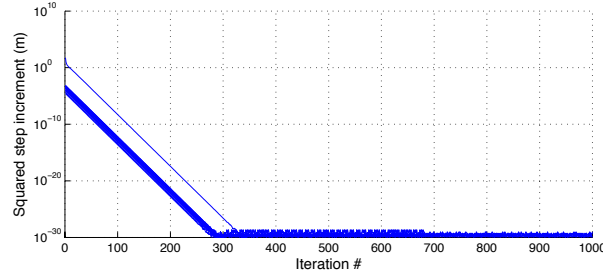


Figure 7.4: Step increment

7.2.3.2 Positioning algorithm

A very simple positioning algorithm can be obtained by applying a gradient descent algorithm to a function that takes into account the individual errors of the constraints in (7.12), (7.15), (7.17) and (7.18). For this purpose, define the error functions e_i as the square of the conditions above, that is,

$$e_1 = \left(\sum_{i=1}^N \frac{1}{\sigma_i^2} s \theta_i c \psi_i \right)^2, e_2 = \left(\sum_{i=1}^N \frac{1}{\sigma_i^2} s \theta_i s \psi_i \right)^2, e_3 = \left(\sum_{i=1}^N \frac{1}{\sigma_i^2} c \theta_i \right)^2, e_4 = \left(\sum_{i=1}^N \frac{1}{\sigma_i^2} s (2\theta_i) c \psi_i \right)^2,$$

$$e_5 = \left(\sum_{i=1}^N \frac{1}{\sigma_i^2} s (2\theta_i) s \psi_i \right)^2, e_6 = \left(\sum_{i=1}^N \frac{1}{\sigma_i^2} s \theta_i^2 c (2\psi_i) \right)^2, e_7 = \left(\sum_{i=1}^N \frac{1}{\sigma_i^2} s \theta_i^2 s (2\psi_i) \right)^2, e_8 = \left(\sum_{i=1}^N \frac{1}{\sigma_i^2} c \theta_i^2 - \frac{1}{3} \sum_{i=1}^N \frac{1}{\sigma_i^2} \right)^2$$

Then, the problem can be formulated using a potential function

$$V(\eta_{s_1}, \dots, \eta_{s_N}) = \sum_{i=1}^8 e_i(\eta_{s_1}, \dots, \eta_{s_N}), \quad (7.22)$$

which is used to iteratively to update the receiver positions using the straightforward gradient descent algorithm:

$$\begin{bmatrix} \eta_{s_1}(l+1) \\ \vdots \\ \eta_{s_N}(l+1) \end{bmatrix} = \begin{bmatrix} \eta_{s_1}(l) \\ \vdots \\ \eta_{s_N}(l) \end{bmatrix} + K_V \begin{bmatrix} \nabla_{\eta_{s_1}} V \\ \vdots \\ \nabla_{\eta_{s_N}} V \end{bmatrix} \Big|_{\eta_{s_i} = \eta_{s_i}(l)}, \quad (7.23)$$

where $K_V > 0$ is a scalar gain and $\nabla_v(\cdot)$ denotes the gradient of a function with respect to a vector v .

7.2.4 Results

Simulations have been conducted to validate the approach. For the results presented next, it is assumed that the variances are equal for all the sensors, that is $\sigma_i = \sigma$ for all i , and the gains have been set as follows: $K = 10^{-1}$ and $K_V = 10^{-1} \cdot \sigma^4$.

The initial positions of the receivers were generated randomly within a cube of side equal to 100 meters. To ensure that the position is observable, it has been considered that the initial configurations must verify $M \geq \underline{M}$, where $0 < \underline{M} < M^*$ is a constant. Otherwise, the estimation algorithm can originate poor estimates, which could lead to divergence. For the simulations, a uniform distribution in the interval $[-\sigma, \sigma]$ was employed instead of a Gaussian distribution as assumed in the model. The reason for this choice was to show by means of simulation that the algorithms perform properly even under unmatched assumptions on noise. Two cases are considered: $\sigma = 10^{-4}$ s and $\sigma = 10^{-2}$ s. In underwater environments, the former value is realistic when using digital signal processing. The latter was exaggerated in order to assess the robustness of the method.

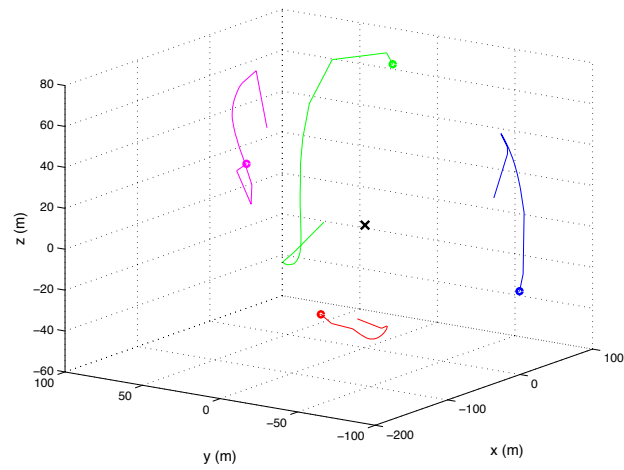
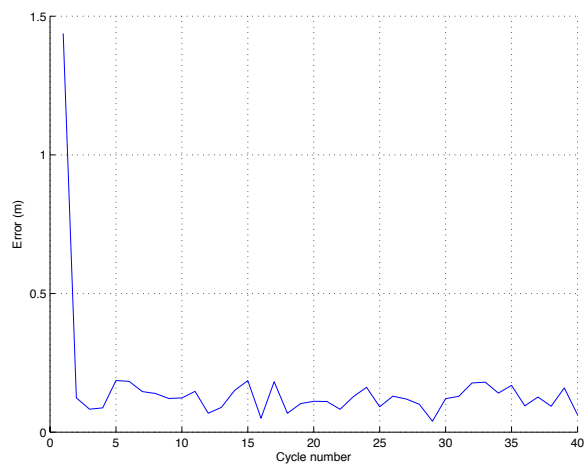
For each *epoch*, a new set of TOAs is drawn, which is subsequently used to estimate the target position. For what concerns optimal placement of sensors, the positioning algorithm is iterated five times at each epoch, after the estimate has been computed. The recursive estimation algorithm is stopped after the sum of the squared increment verifies

$$K(J_g(\hat{X}_k))^{-1}g)^T(K(J_g(\hat{X}_k))^{-1}g) < 10^{-30} \quad (7.24)$$

(see (7.21) and note that $J_g(\hat{X}_k)^\dagger = J_g(\hat{X}_k)^{-1}$ for $N = 4$) or has been iterated more than one thousand times. These values have been selected after resorting to simulations and are justified in figure (7.3) and figure (7.4), where the evolution of the estimate error and the respective estimate increment are depicted for a simulation considering $\sigma = 10^{-4}$ s. In figure (7.3), the plot shows that most of the estimation steps do not use more than five hundred iterations because the increments become small and satisfy the first condition.

Figure 7.5 depicts the trajectories (lines) and the final positions (circles) of the mobile receivers for $\sigma = 10^{-4}$ s. The cross (at the origin) indicates the sound source position. The trajectories are smooth and remain stable after tracking the sound source. In figure 7.8, the position estimate error resulting from the estimation algorithm is shown. The estimate error rapidly decreases from the first to the second epoch and remains around 0.1 meters.

Figure 7.7 shows the evolution of the trajectories of the receivers. The lines show coarser trajectories than in the previous case. This is the result of a larger noise that originates coarser estimates that vary more significantly. The optimal positions of the sensors are adjusted after each new estimate and consequently become noisier. Larger relative distances would make the trajectory smoother as the sensitivity of a change on the estimate would become smaller, that is, the corresponding angles $\{\theta_i, \psi_i\}$ would suffer less from estimate variance.

Figure 7.5: Optimal positioning ($\sigma = 10^{-4}$ s)Figure 7.6: Estimate error ($\sigma = 10^{-4}$ s)

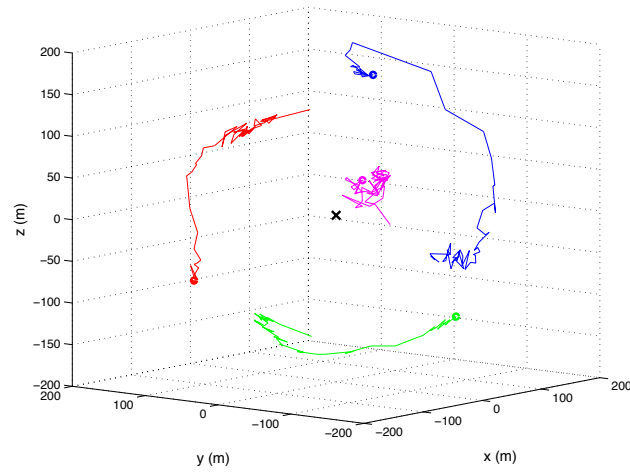


Figure 7.7: Optimal positioning ($\sigma = 10^{-2}$ s)

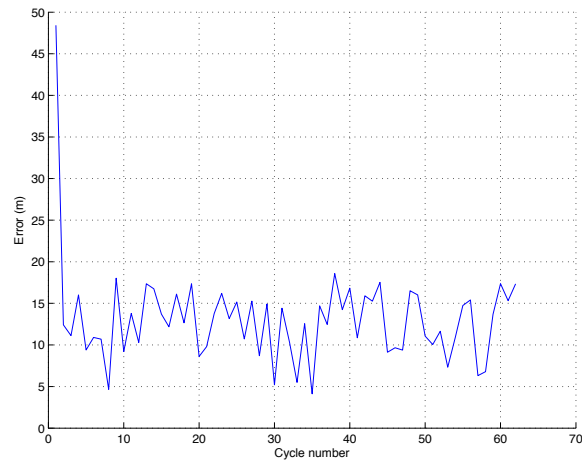


Figure 7.8: Estimate error ($\sigma = 10^{-2}$ s)

7.3 Plane-constrained optimal 3D localization

Motivated by real applications of *optimal* localization of an acoustic source using surface vehicles, this section provides the necessary conditions to obtain the best possible estimate.

Recall the definition of the FIM in section 7.2.1.2 and re-define the composing matrices I_i , $i = 1, \dots, 4$ in Cartesian coordinates, as follows:

$$I(\eta_t) = \frac{1}{c_s^2} \begin{bmatrix} I_1(\eta_t) & I_2(\eta_t) \\ I_3(\eta_t) & I_4 \end{bmatrix} \quad (7.25)$$

with

$$I_1(\eta_t) = \sum_{i=1}^N \frac{1}{\sigma_i^2 \|\tilde{\eta}_i\|^2} \begin{bmatrix} \tilde{x}_i^2 & \tilde{x}_i \tilde{y}_i & \tilde{x}_i \tilde{z}_i \\ \tilde{x}_i \tilde{y}_i & \tilde{y}_i^2 & \tilde{y}_i \tilde{z}_i \\ \tilde{x}_i \tilde{z}_i & \tilde{y}_i \tilde{z}_i & \tilde{z}_i^2 \end{bmatrix},$$

$$I_2(\eta_t) = I_3^T(\eta_t) = -c_s \sum_{i=1}^N \frac{1}{\sigma_i^2 \|\tilde{\eta}_i\|} \begin{bmatrix} \tilde{x}_i \\ \tilde{y}_i \\ \tilde{z}_i \end{bmatrix},$$

$$I_4 = c_s^2 \sum_{i=1}^N \frac{1}{\sigma_i^2}.$$

The problem can be formulated as follows: given the target position η_t , find the relative horizontal positions of the sensors $[\tilde{x}_i, \tilde{y}_i]$ that maximize the metric $M(\{\tilde{x}_i, \tilde{y}_i\})$, or, mathematically,

$$\{\tilde{x}_i, \tilde{y}_i\}_{i=1}^N \in \underset{\{\tilde{x}_i, \tilde{y}_i\}_{i=1}^N}{\operatorname{argmax}} M(\{\tilde{x}_i, \tilde{y}_i\}). \quad (7.26)$$

7.3.1 Plane constrained optimal positions

It is clear from (7.5) that the relative positions of the sensors with regard to the source impact on the FIM and consequently on the objective function M in (7.8). The idea is to find a set of conditions that ensure optimal positioning of the sensors for *optimal* estimation. In the forthcoming developments, the solution that maximizes M is derived. In what follows, it is considered that $\tilde{z}_i = z > 0$ for all $i = 1, \dots, N$, that is, the sensors are at the same vertical position and are not coplanar with the target.

Consider (7.25) and note that I_4 is invertible. Applying the Schur complement to $I(\eta_t)$, as in (Bishop et al., 2010) and as in the previous section, the objective function results into

$$M(\{\tilde{x}_i, \tilde{y}_i\}) = \frac{1}{c_s^8} \det(I_4) \det(I_1 - I_2 I_4^{-1} I_3), \quad (7.27)$$

where the argument of the matrix functions were dropped for clarity.

Again, note that I_4 is a scalar. Since $I_4 > 0$ and $I_2 = I_3^T$, $I_2 I_4^{-1} I_3$ is positive semi-definite, as shown previously. Moreover, by the matrix determinant lemma (see (Ding and Zhou, 2007), for example), assuming that I_1 is invertible, it is possible to write

$$M(\{\tilde{x}_i, \tilde{y}_i\}) = \frac{1}{c_s^8} I_4 [(1 - I_4^{-1} I_3 I_1^{-1} I_2) \det(I_1)],$$

and it becomes clear that, in order to maximize M , the term $I_4^{-1} I_3 I_1^{-1} I_2$ has to be minimized. To this end, suppose that it is possible to set the horizontal positions of the sensors at will and choose

$$\sum_{i=1}^N \frac{\tilde{x}_i}{\sigma_i^2 \|\tilde{\eta}_i\|} = \sum_{i=1}^N \frac{\tilde{y}_i}{\sigma_i^2 \|\tilde{\eta}_i\|} = 0. \quad (7.28)$$

It is important to note that the vertical position of the sensors with respect to the target can not be controlled and hence, unlike section 7.2.2, the last entry of the vectors I_2 and I_3 can not be set to zero.

Based on (7.27) and assuming that the condition in (7.28) is verified, define the matrix

$$\begin{aligned} A &= I_1 - I_2 I_4^{-1} I_3 \\ &= \begin{bmatrix} A_1 & A_2 \\ A_3 & A_4 \end{bmatrix} \end{aligned} \quad (7.29)$$

where

$$\begin{aligned} A_1 &= \sum_{i=1}^N \frac{1}{\sigma_i^2 \|\tilde{\eta}_i\|^2} \begin{bmatrix} \tilde{x}_i^2 & \tilde{x}_i \tilde{y}_i \\ \tilde{x}_i \tilde{y}_i & \tilde{y}_i^2 \end{bmatrix}, \\ A_2 &= A_3^T = \sum_{i=1}^N \frac{1}{\sigma_i^2 \|\tilde{\eta}_i\|^2} \begin{bmatrix} \tilde{x}_i \tilde{z}_i \\ \tilde{y}_i \tilde{z}_i \end{bmatrix}, \\ A_4 &= \sum_{i=1}^N \frac{\tilde{z}_i^2}{\sigma_i^2 \|\tilde{\eta}_i\|^2} - \frac{1}{\sum_{i=1}^N \frac{1}{\sigma_i^2}} \left(\sum_{i=1}^N \frac{\tilde{z}_i}{\sigma_i^2 \|\tilde{\eta}_i\|} \right)^2. \end{aligned}$$

Following the same reasoning as above and using again the Schur complement, the objective function can be rewritten as

$$M(\{\tilde{x}_i, \tilde{y}_i\}) = \frac{1}{c_s^8} I_4 A_4 \det(A_1 - A_2 A_4^{-1} A_3).$$

Since the product $A_2 A_4^{-1} A_3$ is positive semi-definite (note that supposing that A_4 is negative contradicts the fact that the determinant of the FIM is non-negative), it has to be minimized. Hence, suppose that it can be imposed that $A_2 = \mathbf{0}$, or equivalently

$$\sum_{i=1}^N \frac{\tilde{x}_i \tilde{z}_i}{\sigma_i^2 \|\tilde{\eta}_i\|^2} = \sum_{i=1}^N \frac{\tilde{y}_i \tilde{z}_i}{\sigma_i^2 \|\tilde{\eta}_i\|^2} = 0, \quad (7.30)$$

the metric results

$$M(\{\tilde{x}_i, \tilde{y}_i\}) = \frac{1}{c_s^8} I_4 A_4 \det(A_1).$$

The maximization of the metric proceeds with the maximization of the determinant of the matrix A_1 . Thus, it is easy to verify that

$$\det(A_1) = \sum_{i=1}^N \frac{\tilde{x}_i^2}{\sigma_i^2 \|\tilde{\eta}_i\|^2} \sum_{i=1}^N \frac{\tilde{y}_i^2}{\sigma_i^2 \|\tilde{\eta}_i\|^2} - \left(\sum_{i=1}^N \frac{\tilde{x}_i \tilde{y}_i}{\sigma_i^2 \|\tilde{\eta}_i\|^2} \right)^2, \quad (7.31)$$

which leads to an additional condition in order to maximize the metric: by verifying that the last term is non-negative, suppose that it can be imposed that

$$\sum_{i=1}^N \frac{\tilde{x}_i \tilde{y}_i}{\sigma_i^2 \|\tilde{\eta}_i\|^2} = 0. \quad (7.32)$$

Additionally, by noting that

$$\sum_{i=1}^N \frac{\tilde{x}_i^2}{\sigma_i^2 \|\tilde{\eta}_i\|^2} \sum_{i=1}^N \frac{\tilde{y}_i^2}{\sigma_i^2 \|\tilde{\eta}_i\|^2} = \frac{1}{4} \left[\left(\sum_{i=1}^N \frac{\tilde{x}_i^2 + \tilde{y}_i^2}{\sigma_i^2 \|\tilde{\eta}_i\|^2} \right)^2 - \left(\sum_{i=1}^N \frac{\tilde{x}_i^2 - \tilde{y}_i^2}{\sigma_i^2 \|\tilde{\eta}_i\|^2} \right)^2 \right]$$

and imposing

$$\sum_{i=1}^N \frac{\tilde{x}_i^2 - \tilde{y}_i^2}{\sigma_i^2 \|\tilde{\eta}_i\|^2} = 0 \quad (7.33)$$

gives

$$\begin{aligned} \det(A_1) &= \frac{1}{4} \left(\frac{\tilde{x}_i^2 + \tilde{y}_i^2}{\sigma_i^2 \|\tilde{\eta}_i\|^2} \right)^2 \\ &= \frac{1}{4} \left(\sum_{i=1}^N \frac{1}{\sigma_i^2} - \frac{\tilde{z}_i^2}{\sigma_i^2 \|\tilde{\eta}_i\|^2} \right)^2, \end{aligned}$$

where the relationship $\tilde{x}_i^2 + \tilde{y}_i^2 = \|\tilde{\eta}_i\|^2 - \tilde{z}_i^2$ has been used.

Assuming that the conditions (7.28), (7.30), (7.32) and (7.33) hold, expanding the metric function results into

$$\begin{aligned} M(\{\tilde{x}_i, \tilde{y}_i\}) &= \frac{1}{c_s^8} c_s^2 \sum_{i=1}^N \frac{1}{\sigma_i^2} \cdot \left(\sum_{i=1}^N \frac{\tilde{z}_i^2}{\sigma_i^2 \|\tilde{\eta}_i\|^2} - \frac{1}{\sum_{i=1}^N \frac{1}{\sigma_i^2}} \left(\sum_{i=1}^N \frac{\tilde{z}_i}{\sigma_i^2 \|\tilde{\eta}_i\|} \right)^2 \right) \cdot \frac{1}{4} \left(\sum_{i=1}^N \frac{1}{\sigma_i^2} - \frac{\tilde{z}_i^2}{\sigma_i^2 \|\tilde{\eta}_i\|^2} \right)^2 \\ &= \frac{1}{4c_s^6} \cdot m_1(\tilde{\eta}_i) \cdot m_2(\tilde{\eta}_i) \end{aligned} \quad (7.34)$$

where

$$m_1(\tilde{\eta}_i) = \left(\sum_{i=1}^N \frac{\tilde{z}_i^2}{\sigma_i^2 \|\tilde{\eta}_i\|^2} \sum_{i=1}^N \frac{1}{\sigma_i^2} - \left(\sum_{i=1}^N \frac{\tilde{z}_i}{\sigma_i^2 \|\tilde{\eta}_i\|} \right)^2 \right)$$

$$m_2(\tilde{\eta}_i) = \left(\sum_{i=1}^N \frac{1}{\sigma_i^2} - \sum_{i=1}^N \frac{\tilde{z}_i^2}{\sigma_i^2 \|\tilde{\eta}_i\|^2} \right)^2.$$

It is clear that $m_2(\tilde{\eta}_i) \geq 0$ and $m_1(\tilde{\eta}_i) \geq 0$ since, from the definition of the metric, $M \geq 0$. From m_1 and m_2 , it is possible to verify that the metric depends only on the relative distances of the sensor with regard to the target, that is, the norm of the vectors $\tilde{\eta}_i$. In order to find a clearer representation and to maximize the objective function, let us expand the function m_1 as follows:

$$m_1(\tilde{\eta}_i) = \sum_{i=1}^N \frac{\tilde{z}_i^2}{\sigma_i^4 \|\tilde{\eta}_i\|^2} + \sum_{i=1}^N \sum_{j \neq i}^N \frac{\tilde{z}_i^2}{\sigma_i^2 \sigma_j^2 \|\tilde{\eta}_i\|^2} - \sum_{i=1}^N \frac{\tilde{z}_i^2}{\sigma_i^4 \|\tilde{\eta}_i\|^2} - \sum_{i=1}^N \sum_{j \neq i}^N \frac{\tilde{z}_i^2}{\sigma_i^2 \sigma_j^2 \|\tilde{\eta}_i\| \|\tilde{\eta}_j\|}$$

$$= \sum_{i=1}^N \sum_{j \neq i}^N \frac{\tilde{z}_i^2}{\sigma_i^2 \sigma_j^2 \|\tilde{\eta}_i\|^2} - \sum_{i=1}^N \sum_{j \neq i}^N \frac{\tilde{z}_i^2}{\sigma_i^2 \sigma_j^2 \|\tilde{\eta}_i\| \|\tilde{\eta}_j\|}$$

For each sensor i , define the set of the remaining sensors that are at the same distance from the target, that is, $\Omega_i = \{j = 1, 2, \dots, N, \tilde{\eta}_j \in \mathbb{R}^3 : j \neq i, \|\tilde{\eta}_j\| = \|\tilde{\eta}_i\|\}$. Similarly, for each sensor i , the complement of Ω_i is denoted $\bar{\Omega}_i$. Hence, m_1 can be decomposed and simplified as follows:

$$m_1(\tilde{\eta}_i) = \sum_{i=1}^N \sum_{j \in \Omega_i}^N \frac{\tilde{z}_i^2}{\sigma_i^2 \sigma_j^2 \|\tilde{\eta}_i\|^2} + \sum_{i=1}^N \sum_{j \in \Omega_i}^N \frac{\tilde{z}_i^2}{\sigma_i^2 \sigma_j^2 \|\tilde{\eta}_i\|^2}$$

$$- \sum_{i=1}^N \sum_{j \in \bar{\Omega}_i}^N \frac{\tilde{z}_i^2}{\sigma_i^2 \sigma_j^2 \|\tilde{\eta}_i\| \|\tilde{\eta}_j\|} - \sum_{i=1}^N \sum_{j \in \Omega_i}^N \frac{\tilde{z}_i^2}{\sigma_i^2 \sigma_j^2 \|\tilde{\eta}_i\|^2}$$

$$= \sum_{i=1}^N \sum_{j \in \bar{\Omega}_i}^N \frac{\tilde{z}_i^2}{\sigma_i^2 \sigma_j^2 \|\tilde{\eta}_i\|^2} - \sum_{i=1}^N \sum_{j \in \bar{\Omega}_i}^N \frac{\tilde{z}_i^2}{\sigma_i^2 \sigma_j^2 \|\tilde{\eta}_i\| \|\tilde{\eta}_j\|}. \quad (7.35)$$

Some conclusions can be drawn at this point: 1) sensors that are equally distant from the target do not impact on the m_1 function; 2) the complement of Ω_i , $\bar{\Omega}_i$, can not be null, otherwise m_1 is null and so is the objective function M , in other words, there must be at least one sensor whose distance from the target must be different from the others; 3) since m_2 is non-negative, the second term of m_1 in (7.35) has to be minimized in order to maximize the objective function.

The change of variables $\gamma_i = \frac{\tilde{z}_i}{\|\tilde{\eta}_i\|}$ and $\lambda_i = \frac{1}{\sigma_i^2}$ is now adopted. Henceforth, by noting that $\tilde{z}_i = \tilde{z}_j = z \forall i, j = 1, \dots, N$, the function m_1 can be rewritten as

$$m_1(\tilde{\eta}_i) = \sum_{i=1}^N \sum_{j \in \bar{\Omega}_i}^N \lambda_i \lambda_j \gamma_i^2 - \sum_{i=1}^N \sum_{j \in \bar{\Omega}_i}^N \lambda_i \lambda_j \gamma_i \gamma_j. \quad (7.36)$$

It is important to observe that $\gamma_i = 1$ implies that $\|\tilde{\eta}_i\| = \tilde{z}_i$ and $\gamma_i \rightarrow 0$ implies $\tilde{\eta}_i \rightarrow \infty$. Assume that the distance to the target can be made so large that $\gamma_i \in [0, 1]$. According to the expression

of m_1 , the second term is intended to be minimized. Without loss of generality, suppose that the sensors can be organized in two complementary sets according to their distance to the target: the set Γ_0 groups the sensors that are at an infinite distance $\Gamma_0 = \{i = 1, \dots, N, \gamma_i \in [0, 1] : \gamma_i = 0\}$ and $\bar{\Gamma}_0 = \{i = 1, \dots, N, \gamma_i \in [0, 1] : \gamma_i \neq 0\}$ is its complement.

Suppose that the placement of the sensors verifies the condition

$$\sum_{i=1}^N \sum_{j \in \bar{\Omega}_i}^N \lambda_i \lambda_j \gamma_i \gamma_j = 0. \quad (7.37)$$

Hence, using (7.34), (7.36) and (7.37), the metric finally results

$$M(\{\tilde{x}_i, \tilde{y}_i\}) = \frac{1}{4c_s^6} \left(\sum_{i \in \bar{\Gamma}_0} \lambda_i \gamma_i \sum_{j \in \bar{\Omega}_i} \lambda_j \right) \left(\sum_{i=1}^N \lambda_i - \sum_{i \in \bar{\Gamma}_0} \lambda_i \gamma_i^2 \right)^2. \quad (7.38)$$

The maximization of this last expression is not trivial since it admits several local maxima and the different combinations in the organizations of the sets Γ_0 and $\bar{\Gamma}_0$ may lead to different discrete solutions that have to be individually analyzed in practice. Hereafter, the case with four sensors is addressed.

7.3.2 Case with four sensors and same noise variance

In order to exemplify and to assess the optimal sensor configuration, a problem considering four sensors is now addressed. Recall that this is the minimum number of sensors required to estimate the position of a target whose time of emission is unknown. Consider that $\lambda_i = \lambda$, $\forall i = 1, \dots, 4$ and that the sensor $\{1\}$ belongs to the set $\bar{\Gamma}_0$, that is, its distance from the target is finite, while the remaining sensors, $\{2, 3, 4\}$ belong to Γ_0 . Therefore, it is easy to verify that the metric function becomes

$$\begin{aligned} M(\{\tilde{x}_i, \tilde{y}_i\}) &= \frac{1}{4c_s^6} (\lambda \gamma_1^2 \cdot 3\lambda) (4\lambda - \lambda \gamma_1^2)^2 \\ &= \frac{3}{4c_s^6} \lambda^3 \gamma_1^2 (4 - \gamma_1^2)^2. \end{aligned}$$

Interestingly, for the domain of γ_1 , the maximum value of the metric is reached when $\gamma_1 = 1$, that is, when the sensor $\{1\}$ is above the target.

Hence, setting

$$\begin{aligned} \tilde{\eta}_1 &= [0, 0, \tilde{z}_1]^T \\ \tilde{\eta}_i &= \begin{bmatrix} \rho \cos\left(\frac{2\pi(i-2)}{3} + \psi_0\right) \\ \rho \sin\left(\frac{2\pi(i-2)}{3} + \psi_0\right) \\ \tilde{z}_i \end{bmatrix}, \quad i = 2, \dots, 4 \end{aligned} \quad (7.39)$$

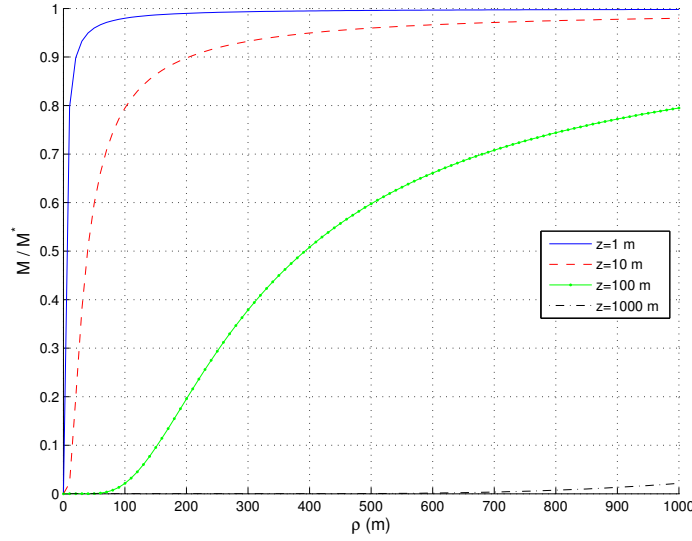


Figure 7.9: Influence of ρ on the metric

with $\rho = \infty$ and ψ_0 being any angular offset, verifies the conditions (7.28), (7.30), (7.32), (7.33) and (7.37). Therefore, the metric M is maximized over the horizontal positions of the sensors. The offset ψ_0 was added only to emphasize the independence of the metric with regard to the rotation of the overall configuration of sensors.

Impact of bounded distances from the target

In practice, infinite distances from the target are obviously impossible. Therefore, it is important to understand how the bounded distances between the vehicles impact on the metric M . As seen in (7.38), if the optimal angular configuration is satisfied and the distance obey (7.39), the metric becomes a function of the variances σ_i and of the division of the depth by the distance between each sensor and the target, $\frac{z_i}{\|\tilde{\eta}_i\|}$. By contemplating the scenario with four sensors and same variances, figure 7.9 depicts the metric M normalized by the optimal value M^* , that is, obtained from M when $\rho = \infty$. Although the metric depends only on the quotients of the depth by the distances to the target, the plot shows the results for several depth, for clarity.

For the present case with four sensors with same variance and under the assumption that the distance to the target is bounded, that is, for a fixed $\gamma_i = \gamma, i = 2, 3, 4$, from (7.38) and (7.34), it can be proven that

$$M^* = \frac{27\lambda^4}{4c_s^6}$$

$$M(\{\tilde{x}_i, \tilde{y}_i\}) = \frac{27\lambda^4}{4c_s^6} (\gamma - 1)^2 (1 - \gamma^2)$$

respectively. The quotient then becomes

$$\frac{M(\{\tilde{x}_i, \tilde{y}_i\})}{M^*} = (\gamma - 1)^2 (1 - \gamma^2)^2$$

In practice, from this last expression, and also from the figure, it is possible to conclude that the metric reaches about 20% of the optimal value M^* when ρ is two times the depth and about 90% when ρ is twenty times the value of the depth. It is clear that small ρ , with regard to the depth, can considerably degrade the estimate. This has to be taken into account when designing the tracking algorithm.

7.4 Coordinated placement of sensors

Given the target location, the optimal positions of the sensors and hence of the vehicles are uniquely determined up to a formation rotation. Using this important feature, the formation of vehicles can be guided so that the observation of the target is maintained optimal even under motion of the target. A two-step iterative procedure, similar to the one that has been proposed in section 7.2.3, contemplating estimation and positioning steps is implemented. For formation keeping, the centralized coordination scheme presented in chapter 6 is employed. A brief explanation of the methods used is now provided.

7.4.1 Coordination of autonomous vehicles

Coherent motion and formation keeping of vehicles has been achieved by means of a centralized coordination algorithm that guides the vehicles as exposed in chapter 6. The virtual leader position, along with relative positions of the references of the vehicles with regard to this latter, uniquely define the formation. The inclusion of a virtual leader is advantageous in this scenarios since it does not suffer from external disturbances, measurement or positioning errors, in opposition to real vehicles, and thus prevents the propagation of these undesired effects in the formation.

According to the optimal configuration (7.39), the formation is set so that it satisfies the final angular configuration, that is, vehicle $\{1\}$ on the center of a circle of radius ρ_f where the remaining three vehicles are placed so that

$$\eta_{s_i} - \eta_{s_1} = \begin{bmatrix} \rho_f \cos\left(\frac{2\pi(i-2)}{3} + \psi_0\right) \\ \rho_f \sin\left(\frac{2\pi(i-2)}{3} + \psi_0\right) \\ 0 \end{bmatrix}, \quad i = 2, \dots, 4$$

The radius of the formation ρ_f is varied according to the behavior adopted: during homing, that is, the approach to the target, the formation is maintained *small* and thus ρ_f is small. After having approached the target, the formation must grow to improve the estimate confidence and thus ρ_f is made larger.

7.4.2 Homing to target

As previously seen, and strengthened in this chapter, the relative positions of the sensors have a strong impact on the expected variance of the estimate. For simulations of the optimal unconstrained positioning case presented in section 7.2.4, it has been considered that the initial value of the metric was above a pre-defined threshold, which would guarantee that the system is *sufficiently observable* in order to obtain a sufficiently precise initial estimate of the position from the TOA measurements. In reality, exploring different configurations at different positions is obviously impracticable. Additionally, as the confidence on the estimate depends on the relative positions, it might be insensate to position the formation of vehicles equipped with the sensors based on any estimate, regardless of the observability of the target. Therefore, alternative behaviors should be adopted to drive the vehicles to a near optimal configuration to subsequently start positioning based on the estimate of the target. Hereafter, the positions of the sensors are considered to be coincident with the vehicles that carry them.

Using the same principle as in USBL systems, it is possible to determine the direction of the target with a relatively *tight* and carefully placed set of sensors. By making use of the formation of vehicles already in their final angular configuration, at each epoch, the direction is determined and subsequently used to drive the formation towards the target. Let $\bar{\eta} = \frac{1}{N} \sum_{i=1}^N \eta_{s_i}$ be the mean position of the sensors and $\bar{\tau} = \frac{1}{N} \sum_{i=1}^N \hat{\tau}_i$ be the mean TOA. The direction to which the formation is driven is determined as

$$\zeta = - \frac{\sum_{i=1}^N (\eta_{s_i} - \bar{\eta}) (\hat{\tau}_i - \bar{\tau})}{\left\| \sum_{i=1}^N (\eta_{s_i} - \bar{\eta}) (\hat{\tau}_i - \bar{\tau}) \right\|}. \quad (7.40)$$

This direction is provided to the virtual leader, which subsequently generates the path of the formation.

7.4.3 Estimation-based positioning

Estimation

The position of the target is estimated whenever a new set of coherent measurements has been reported by the vehicles to a central estimation algorithm. It is considered that coherent measurements are those that, given the distances between the vehicles in the formation, do not differ more than a given user-defined threshold, which obviously depends on the desired distances between the sensors and the target. By combining the positions of the sensors to the TOAs, the position of the target is estimated using a Newton's method applied to multidimensional nonlinear equations as described in section 7.2.3.1

Positioning

As stated earlier, positioning the formation based on the estimate may lead to poor performances. Two criteria have been adopted to switch the behavior of the formation from homing to estimation-based positioning:

1. The Newton's algorithm converges in a limited number of iterations;
2. The horizontal position estimate is sufficiently close to the horizontal center of mass (mean position) of the formation.

Given a successful estimate of the target position, the virtual leader drives the formation towards the target at each epoch. The second criterion ensures that the formation is in an appropriate position to estimate the target position. If these two criteria are simultaneously met, the *outer* vehicles can *enlarge* the formation by placing themselves farther apart from the target and thus improving the estimation confidence by augmenting the metric M according to the derivations of the previous section. In practice, the largest radius of the formation must be limited because of the attenuation of the acoustic signal and, in some scenarios, because of the bounds of the operation area.

7.5 Field trials

Field trials have been carried out in the Douro river. The operation is described and the collected data is analyzed next.

7.5.1 Assets

In order to compute the TOAs of a signal sent by an acoustic target underwater, a set composed of acoustic transducers and signal processing boards has been used. These signal processing boards are responsible to compute, by using matching filters tuned to detect the desired signal, and report the TOAs over a serial port to the local computer running aboard the vehicle. The boards require synchronization between them to report the collected TOAs with regard to a common time basis. After computation of the TOA, the local computer is responsible to forward the relevant information to a central estimator that estimates the target position on-line.

The four heterogeneous autonomous surface vehicles (ASVs) described in 2.6 and depicted in figure 7.10 have been used to estimate and optimally position themselves according to the TOA measurements and to the corresponding estimate. The vehicles were equipped with general



Figure 7.10: Formation of four heterogeneous vehicles

positioning system (GPS) devices and compasses or inertial measurement units (IMUs). The formers were providing precise time information to the acoustic receivers enclosed aboard the vehicles. The coordination algorithm has been ran on a computer on the margin interacting with the vehicles by means of radio communications. The overall operation ran autonomously.

An acoustic pinger emitting a signal of 35 kHz lasting 11 milliseconds has been anchored in the river, in the water column, which has a maximum depth of about 10 meters at the deployment location. As the pinger was not rigidly attached to the bottom nor any structure, it is impossible to provide ground-truth information about its position. Nonetheless, it is expected that the vehicles can track the pinger and estimate its position. Moreover, the convergence of the formation to a given point would suggest that the algorithm can track and estimate the position of the target successfully.

7.5.2 Operation

The vehicles were placed in formation at an arbitrary point in the operation area. This point was chosen to be $[x, y] = [-35, -115]$. According to section 7.4, the formation must first approach the target using the homing method. To do this, the radius of the formation was set to $\rho_f = 20$ meters. For practical reasons, the radius adopted for the estimation-based positioning behavior was set to $\rho_f = 50$ meters because of bounded operation area. According to the section 7.3.2, the expected metric value should be higher than 60% of the optimal value, provided that the maximum depth is 10 meters.

Over the entire operation, the estimation algorithm was continuously ran to decide when the formation should switch from homing behavior to estimation-based positioning. The results are presented and discussed hereafter. It must be highlighted that some incoherent GPS fixes occurred on two vehicles during the operation, conducting to poor positioning and to poor estimates during some instants. These malfunctions were observed in the field via an interface providing feedback on the positions of the vehicles in real time. As it is not trivial to filter them at this point, the results presented include these occurrences, which were robustly accommodated by the algorithm though, as the results hereafter demonstrate.

7.5.3 Performances

The estimated coordinates of the target over time are depicted in figure 7.11. The results shown in this figure have been computed using the last 60 estimates of the target to smooth the obtained results. Incoherent estimates caused by the divergence of the estimator have been filtered. All the estimates that were not contained in a cube with 2000 meters side length and centered at the origin were removed to avoid results biased by incoherent estimates. Nevertheless, it should be noted that these were only two over 537 estimates. The standard deviations of these estimates are shown in figure 7.12. It is important to note that the mean estimate converges to a constant

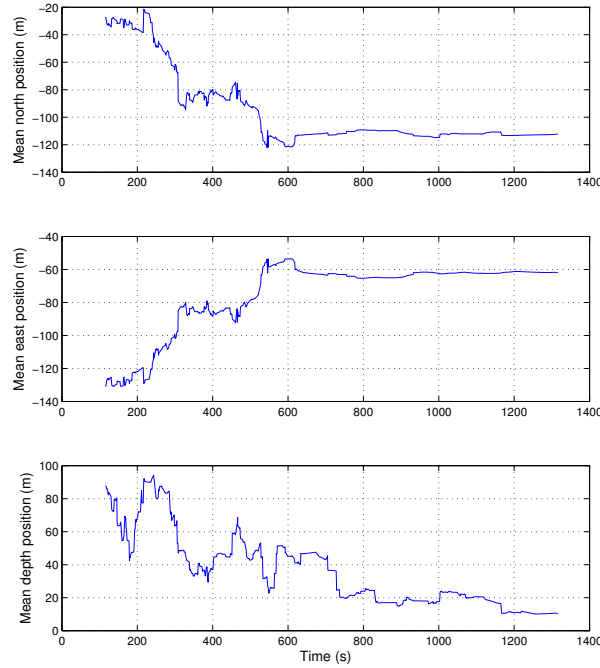


Figure 7.11: Mean estimated position over a window of 60 sequential estimates

value, suggesting a successful tracking and position estimation of the target. Moreover, the standard deviation of the estimate generally shows a decreasing trend although it was affected by the erroneous measurements of the positions of the vehicles.

Figure 7.13 depicts the mean position of the formation as well as the final estimated target position. For the sake of clarity, the trajectories of the vehicles have not been included. Note that there are several discontinuities in the mean position of the formation. These are caused by the erroneous GPS fixes, which also have impacted on the estimate during some intervals of time. From the figure, it is clear that the center of mass of the formation ends over a small region very close to the mean estimated position of the target.

7.6 Conclusions

In this chapter, the solution for optimal placement of TOA sensors in three-dimensional spaces has been presented. Based on the FIM, the necessary conditions have been derived to minimize the volume of the confidence region and consequently reduce the estimate uncertainty. Using the geometric properties of the optimal sensor positions, simulation results illustrated an approach that contemplates a two-step algorithm that sequentially considers estimation and placement. Concerning unconstrained three-dimensional positioning, the real implementation of this approach into real robots would require special attention on sensor motions. In particular, the limited speed of the vehicles and the precision on positioning would constitute the main constraints. A proper

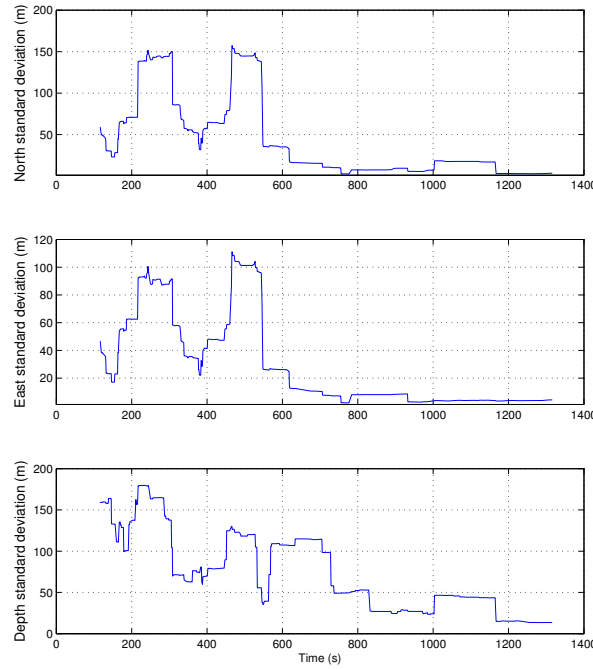


Figure 7.12: Standard deviation of the estimate

tuning of gain and/or saturating the position increments would surely solve the former. The second constraint implies that robotic platform equipped with precise navigation sensors and control laws have to be employed to improve the localization. Nonetheless, very accurate positioning may not be available for underwater robots in an unlimited volume of operation.

The optimal positioning of sensors was further explored to the plane-constrained case and the optimal positions of the sensors were derived. The special case with four sensors was explored and the results presented here are in agreement with the work in Ray and Mahajan (2002), in a slightly different formulation where the difference TOA problem was considered. Through genetic algorithm simulation, the results have provided a similar configuration with a central receiver and three other placed on the vertices of an equilateral triangle. Nonetheless, in Ray and Mahajan (2002), by construction the receivers were constrained to move in a circle with bounded radius. The optimal solution found in this chapter indicates that the outside receivers should be placed as far as possible. For practical reasons this bound is finite and must be carefully considered during the placement of receivers. The coordinated placement of sensors was subsequently implemented on a formation of four ASVs. The first field trials have provided very motivating results that still require tuning to accelerate the tracking task and to improve the estimate by means of more precise positioning of vehicles in the formation. Although the malfunction of some GPS devices influenced the overall performances of the formation and of the estimation, the results obtained for the position estimate, and namely its standard deviation, have demonstrated the proof of concept of this novel coordinated localization method.

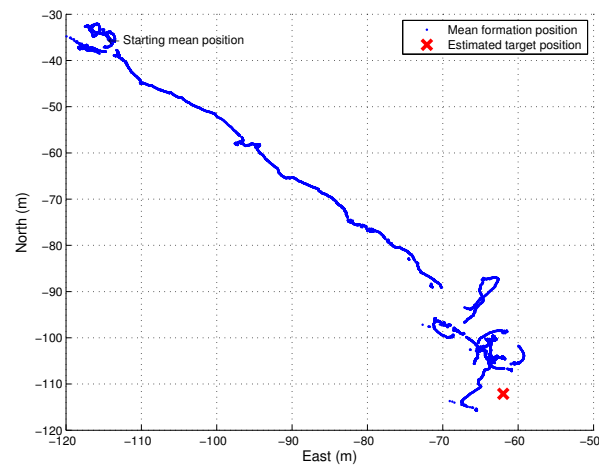


Figure 7.13: Mean position of the formation and estimated position of the target

Chapter 8

Conclusions

This thesis addressed the control and the coordination of a broad family of marine vehicles. A theoretical framework based on the Lyapunov theory has been used in most of the thesis to derive control and guidance laws and to assess the stability of the controllers. The general dynamics and kinematics models were introduced to support the control and guidance laws derivations and the related control methods were presented. An example on how models and control tools can be applied to control a hovering autonomous underwater vehicle (AUV) in the vertical pose was given. Two control laws were developed to stabilize the vehicle vertically and to drive it to a horizontal position reference by taking advantage of the heave degree of freedom (DOF). At the kinematics level, a very simple and basic exercise of coordination was then presented. In order to home the vehicle to a possibly moving beacon, estimation-based and sensor-based approaches were developed for a scenario where only ranges can be measured. The proposed guidance laws for homing presumed the existence of a lower level velocity control loop, which was subsequently formalized in chapter 5 for generic marine vehicles. This velocity control loop was further exploited and a target tracking and station-keeping guidance law was developed for several types of underactuated marine vehicles with different DOFs. This additional loop was then employed by a coordination scheme for marine vehicles under potential communication constraints. All these control loops building blocks, from the very low-level velocity controller to the formation control method, were used in an application contemplating coordinated localization and tracking of a sound source underwater. A solution to drive a team of heterogeneous vehicles carrying time-of-arrival (TOA) sensors was proposed to optimally estimate the position of a target underwater, that is, with the least possible uncertainty.

8.1 Main contributions

A list of contributions, organized by chapter, is summarized below.

Chapter 3

- Development of a control law based on the backstepping method to stabilize a hovering AUV in the vertical pose.
- Derivation of a guidance law to drive the vehicle horizontally when the vehicle is pitching up or down. The vehicle periodically rotates due to torques originated by the thrusters actuation when keeping the depth constant. By exploring such a rotation, the heave motion was exploited to guide the vehicle to a given horizontal position reference.

Chapter 4

- Development of an estimation-based approach to home a vehicle to a possibly moving reference based on range measurements only. The resulting estimate then feeds a guidance law that adjusts the vehicle heading while assuming that the surge velocity is constant.
- Implementation of an extended Kalman filter (EKF) and a particle filter (PF) for relative localization and comparison of their performances. In general, the EKF performs better than the PF for the parameters (modelled covariances for the EKF and approximation of the likelihood for the PF) and the scenario considered. For EKF initialization, a combined implementation of both filters was implemented to take advantage of the straightforward initialization of the PF.
- Design of an alternative, sensor-based, guidance law to home the vehicle using range-only measurements. It was demonstrated that homing does not require estimation and a guidance law that only uses range measurements was derived. The guidance law makes the vehicle track a defined gradient that has to take into account the vehicle velocity and the drift vector. Actually, only a rough notion of their absolute values is needed to drive the vehicle towards the reference point. The robustness of the approach was demonstrated by means of experimental data that validated the guidance law.

Chapter 5

- Derivation and formalization of a velocity control loop for generic marine vehicles. Additionally, the tracking performances of the velocity control loop were assessed by a focused analysis of the error under model uncertainties.
- Development of a simple architecture (inner/outer loop) enabling straightforward implementation of guidance laws granting versatility of the approach, as demonstrated in the implementation on TriMARES.
- Design of a target tracking and station-keeping guidance law for several types of underactuated marine vehicles with different DOFs. An analysis on the tracking errors has also been performed for this guidance law.

Chapter 6

- Generalization of the control scheme by Egerstedt and Hu (2001) for centralized formation control, while keeping the convergence properties.
- Particularization of the method to accommodate communication constraints, which include intermittence, non-periodic exchange of data. Additionally, the control scheme makes the formation tolerant to communication faults by holding its position in the case of prolonged lack of feedback from one or more vehicles in the formation.
- Validation of the approach in real conditions using two coordinated autonomous surface vehicle (ASV) and under different communication scenarios: high rate radio-based communications on the surface and low rate underwater acoustics communications.

Chapter 7

- Derivation of the optimal positions of TOA sensors that minimize the volume of the uncertainty of an estimate by using the determinant of the Fisher information matrix (FIM), which served as a metric to quantify the *amount of information* carried on each set of measurements. The optimal position were derived for an unconstrained case, where the sensors can be placed anywhere in three-dimensional space, and to the plane constrained case, where the vehicles are constrained to lie in a plane to estimate the three-dimensional position of the target.
- Design of a coordinated optimal solution to track and estimate the position of an acoustic target underwater. The building blocks derived in the previous chapter have been used to carry TOA sensors on a team of coordinated robots in a formation whose geometry uses the results obtained from the derivation of the optimal positions of sensors.
- Validation of the target tracking and localization approach using a team of four heterogeneous ASVs.

8.2 Publications

The developments of the present thesis have naturally originated some publications. A list of publications related to the work presented in this thesis and written during the Ph.D. program is given below. Other publications less related to this thesis have been omitted. This list contains both published and submitted publications. After each entry, a brief description of the paper is provided.

Conference papers

- Bruno M. Ferreira, Aníbal Matos, Helder S. Campos, Nuno A. Cruz. Localization of a sound source: optimal positioning of sensors carried on autonomous surface vehicles. Proceedings of the MTS/IEEE Oceans 2013 Conference, San Diego, CA, September 2013.

This work presents the results on plane constrained optimal positioning of TOA sensors addressed in chapter 7. This paper has been selected to be part of the student poster competition held at the conference.

- Miguel Pinto, Bruno Ferreira, Heber Sobreira, Aníbal Matos, Nuno Cruz. Spline Navigation and Reactive Collision Avoidance with COLREGs for ASVs. Proceedings of the MTS/IEEE Oceans 2013 Conference, San Diego, CA, September 2013.

This work proposes a collision avoidance method using splines and reactive behaviors that are based on the local automatic controllers presented in chapter 5.

- B. Ferreira, A. Matos, N. Cruz. Optimal positioning of autonomous marine vehicles for underwater acoustic source localization using TOA measurements. Proceedings of 2013 IEEE International Underwater Technology Symposium (UT13).

This paper reports the results obtained for optimal positioning of TOA sensors in three-dimensional space (unconstrained). Most of the developments are based on the first part of the chapter 7.

- N. Cruz, A. Matos, B. Ferreira. Modular Building Blocks for the Development of AUVs – from MARES to TriMARES. Proceedings of 2013 IEEE International Underwater Technology Symposium (UT13).

The modular architecture adopted in both the mechanical structure and in the software designs is described in this paper. More concretely, the use of dynamic models and controllers than can be adapted (off-line) is addressed and the method employed to “port” the control software is explained.

- B. Ferreira, A. Matos, N. Cruz, R. Almeida. Towards cooperative localization of an acoustic pinger. Proceedings of the MTS/IEEE Oceans 2012 Conference, Hampton Roads, VA, USA, October 2012.

A preliminary study on the effect of the relative positions of the TOA sensors, with regard to the acoustic target, is presented. The study essentially employs simulations to come up with some conclusions on where the target should be, given the positions of the TOA sensors. This study also served as a motivation to chapter 7. This paper was also selected to

be inserted in the student poster competition held at the conference and awarded the second place.

- B. Ferreira, J. Jouffroy, A. Matos, N. Cruz. Control and guidance of a hovering AUV pitching up or down. Proceedings of the MTS/IEEE Oceans 2012 Conference, Hampton Roads, VA, USA, October 2012.

The control and guidance laws adopted to stabilize a hovering AUV in the vertical pose and drive it horizontally at the same time are presented in this paper. Most the content is based on chapter 3.

- N. Cruz, B. Ferreira, A. Matos, Chiara Petrioli, Roberto Petrocchia, Daniele Spaccini. Implementation of an Underwater Acoustic Network using Multiple Heterogeneous Vehicles. Proceedings of the MTS/IEEE Oceans 2012 Conference, Hampton Roads, VA, USA, October 2012.

This joint work with researchers from La Sapienza University, Rome, Italy, reports the preliminary implementation and tests of a mobile underwater acoustic network. Based on the control and guidance laws proposed in 5, underwater and surface vehicles were commanded over the acoustic channel.

- B. Ferreira, A. Matos. Design of a framework for cooperative marine robots. Proceedings of the StudECE - First PhD Student Conference on Electrical and Computers Engineering, Porto, Portugal, June 2012.

Beyond the control solution proposed in 5, this short paper gives an overview on the control architecture to achieve versatile maneuvers and on how to use it to coordinate autonomous vehicles.

- Bruno M. Ferreira, Aníbal C. Matos, Nuno A. Cruz. Modeling and control of TriMARES AUV. Proceedings of the Robotica 2012 Conference, Guimarães, Portugal, April 2012.

This paper mostly presents the model derived for the TriMARES AUV and its control architecture, adapted from 5. Preliminary tests from field trials are also presented.

- Nuno A. Cruz, Aníbal C. Matos, Rui M. Almeida, Bruno M. Ferreira, Nuno Abreu. TriMARES - A hybrid AUV/ROV for dam inspection. Proceedings of the MTS/IEEE Oceans 2011 Conference, Kona, Hawaii, pp.1-7, 19-22 Sept. 2011.

The design process of the TriMARES AUV is presented in this paper.

- Bruno M. Ferreira, Aníbal C. Matos, Nuno A. Cruz (2011). Automatic reconfiguration and control of the MARES AUV in the presence of a thruster fault. Proceedings of the IEEE Oceans 2011 Conference, Santander, Spain, 4-6 June 2011.

An approach to detect, identify and accommodate possible thruster faults is proposed. The detection and the identification are based on an EKF that utilizes a dynamics model to predict the state. Two alternative control laws are proposed to control the MARES AUV with one vertical thruster only, that is, assuming that the other is malfunctioning.

- Bruno M. Ferreira, Aníbal C. Matos, Nuno A. Cruz (2010). Single beacon navigation: localization and control of the MARES AUV. Proceedings of the IEEE Oceans 2010 Conference, Sydney, Australia, 2010.

The estimation approach to home an AUV to a beacon using range-only measurements presented in chapter 4 is presented in this paper.

Journal papers and book chapter

- Bruno M. Ferreira, Aníbal C. Matos, Nuno A. Cruz, A. P. Moreira. Robust coordination of multiple marine robots. Submitted, December 2013, IEEE Journal of Oceanic Engineering.

This article encompasses the coordination scheme extension in chapter 6.

- Nuno A. Cruz, Bruno M. Ferreira, Aníbal C. Matos. Ocean Observation With Coordinated Robotic Platforms. *Sea Technology*, vol. 54, no. 5, May 2013.

This short paper summarizes the goals related with the use of coordinated autonomous marine vehicles as well as some of the main achievements already accomplished.

- Nuno A. Cruz, Bruno M. Ferreira, Oleksiy Kebkal, Aníbal C. Matos, Chiara Petrioli, Roberto Petroccia, Daniele Spaccini. Investigation of Underwater Acoustic Networking Enabling the Cooperative Operation of Multiple Heterogeneous Vehicles. *Marine Technology Society Journal*, vol. 47, no. 2, March/April 2013.

This is an extension of the conference paper Cruz et al. (2012) where the coordination scheme proposed in chapter 6 has been used over acoustic communications and the performances of the combined control solution and communication technology has been assessed by means of data from field trials and simulations.

- Bruno M. Ferreira, Aníbal C. Matos, Nuno A. Cruz. Fault Tolerant Depth Control of the MARES AUV. *Challenges and Paradigms in Applied Robust Control*, Andrzej Bartoszewicz (ed.), ISBN: 978-953-307-33, October 2011.

This book chapter is an extension of the conference paper to detect, identify and accommodate possible faults in vertical thrusters of MARES AUV.

- Bruno M. Ferreira, Aníbal C. Matos, Nuno A. Cruz, A. P. Moreira. Homing a robot with range-only measurements under unknown drifts. Submitted, August 2011, Re-submitted in revised form, August 2013, Robotics and Autonomous Systems, Elsevier.

The sensor-based approach to home an AUV, as proposed in 4, is presented in this paper. A brief comparison with the estimation-based approach is also carried out.

- Bruno M. Ferreira, Aníbal C. Matos, Nuno A. Cruz. Estimation approach for AUV navigation using a single acoustic beacon. Sea Technology, vol.51, no.12, December 2010.

The main ideas and the achievements obtained in the conference paper Ferreira et al. (2010a) were summarized in this brief paper.

- Bruno M. Ferreira, Aníbal C. Matos, Nuno A. Cruz, Miguel A. Pinto. Modeling and Control of the MARES Autonomous Underwater Vehicle. Marine Technology Society Journal, vol. 44, no. 2, March/April 2010.

This paper presents the preliminary design of the control laws and architecture of the control and guidance layer posteriorly adapted on MARES.

8.3 Future work

Several avenues have been identified to further exploit the work presented in this thesis. Concerning vertical pose control, it would be very interesting to control the roll angle so that the vehicle direction can be controlled for all time. This would yield precise positioning which could be used for docking using precise relative localization, for example. Such a precise docking could be complemented with a prior homing to a docking-station, possibly using range measurements. Regarding homing, there is room for exploring the impact of the parameters used in both EKF and PF as well as the distribution approximation used by the PF. Moreover, the augmented estimate vector including the drift vector in the PF would certainly improve the estimate.

Concerning the coordination of vehicles, an interesting avenue would be the implementation of a weakly centralized method, with several virtual leaders and sub-formations. Furthermore, the employment of roles and tasks assignment as used in several robotic applications such as robotic soccer would permit versatile formations of vehicles and would improve robustness by taking decisions according to the state of the formation, the goals of the mission and each vehicle performances. Additionally, different implementations of the formation constraint function could enable introducing new behaviors such as collision avoidance.

Finally, the coordinated tracking and localization of underwater sound sources has a tremendous potential in underwater navigation applications. Using acoustics communications, the localization of an AUV equipped with an acoustic pinger and navigating underwater can be obtained using a formation of vehicles on the surface, which subsequently can communicate to the passively listening AUV its position accurately, while following it. This enables bounded localization error no matter where the AUV is nor the travelled distance, at the cost of being accompanied by a formation of vehicles at the surface. Moreover, if communications are established between the AUV and one of the ASVs and communications are guaranteed by means of radio to the ASV, then a less intermittent and faster link can be obtained from the AUV to any external entity. In a different but close context, the benefits of using the vertical channel to guarantee a communication link between an AUV and an ASV have been identified by Pascoal et al. (2000). The results obtained in the last two chapters could be further exploited to coordinate and to improve the navigation of an AUV: as seen in chapter 7, the optimal solution to localize an acoustic source using TOA sensors at the surface is to have a sensor on the vertical line and the remaining distributed on a circle. In the case where ASVs are used to cooperatively localize the AUV, the “central” ASV may also compile the role of a communication and navigation aid (CNA) asset (see also Vaganay et al. (2004)) that grants a communication link to the AUV and sends information on the AUV externally estimated position or any other kind of relevant information during the mission.

Appendix A

Guidance laws for other DOFs combinations

A.1 Controlled surge, heave and yaw rate

Choose r^* as in (5.34). As $t \rightarrow \infty$, the vehicle velocity component projected in the frame defined by the positions of the target and of the vehicle, becomes

$$\lim_{t \rightarrow \infty} \vartheta = -uc(\theta + \beta) - ws(\theta + \beta)$$

Define ζ as a virtual velocity control input and take

$$u^* = \zeta c(\theta + \beta) \tag{A.1}$$

$$w^* = \zeta s(\theta + \beta). \tag{A.2}$$

The vehicle velocity component results

$$\lim_{t \rightarrow \infty} \vartheta = -\zeta$$

and, similarly to (5.37), choose

$$\zeta = \vartheta_D + \vartheta^* + K_\rho \text{sat}(\rho(t) - \delta, \mu_\rho) \tag{A.3}$$

which makes the distance dynamics

$$\begin{aligned} \lim_{t \rightarrow \infty} \dot{\rho}(t) &= -\zeta + \vartheta_D + \vartheta^* \\ &= -K_\rho \text{sat}(\rho(t) - \delta, \mu_\rho). \end{aligned} \tag{A.4}$$

Clearly, the vehicle linearly converges to the desired position for $\rho(t) \geq \mu_\rho$ and then exponentially converges to a sphere of radius δ around the desired position for $\rho(t) < \mu_\rho$.

A.2 Controlled heave, pitch rate and yaw rate

The resulting control law is similar to the one presented for the case of controlled surge, pitch rate and yaw rate. However, we will see that the heave direction will have to point towards the desired position.

The yaw rate r^* guidance law is taken as in (5.34) and the pitch rate control law as

$$q^* = K_\theta(\theta + \beta - \frac{\pi}{2}) - \dot{\beta} \quad (\text{A.5})$$

which makes the convergence of θ to $-\beta + \frac{\pi}{2}$ exponential:

$$\theta = (\theta_0 + \beta_0 - \frac{\pi}{2})e^{-K_\theta t} - \beta + \frac{\pi}{2}. \quad (\text{A.6})$$

Hence, it yields

$$\lim_{t \rightarrow \infty} \vartheta = w.$$

Thus, setting

$$w^* = -\vartheta_D - \vartheta^* - K_\rho \text{sat}(\rho(t) - \delta, \mu_\rho) \quad (\text{A.7})$$

and substituting into (5.32), the distance time derivative becomes

$$\lim_{t \rightarrow \infty} \dot{\rho}(t) = -K_\rho \text{sat}(\rho(t) - \delta, \mu_\rho). \quad (\text{A.8})$$

A.3 Controlled surge, heave, pitch rate and yaw rate

With four DOFs, any of the control laws presented above can be applied, while leaving one of the DOFs *inactive*. However a more suitable control law can be derived. Using the pitch rate and the yaw rate control laws in (5.33) and (5.34), respectively and setting

$$u^* = \zeta(c(\psi - \alpha)c\theta c\beta + s\theta s\beta) \quad (\text{A.9})$$

$$w^* = \zeta(c(\psi - \alpha)s\theta c\beta + c\theta s\beta) \quad (\text{A.10})$$

with

$$\zeta = -\vartheta_D - \vartheta^* - K_\rho \text{sat}(\rho(t) - \delta, \mu_\rho).$$

This control law makes $\lim_{t \rightarrow \infty} \dot{\rho}(t)$ equal to (A.4). In addition to the combined control of surge and heave, minor differences are introduced in this guidance law comparatively to (5.37) and (A.7): in these control laws, the surge and heave velocities take the same magnitude of $\vartheta_D + \vartheta^* + K_\rho \text{sat}(\rho(t) - \delta, \mu_\rho)$ regardless of the azimuth and of the altitude. This means that initially the vehicle may move in the opposite direction of the target during a short interval of time. With the control law in (A.9)-(A.10) this is avoided, making the vehicle move *backwards* during the corresponding instants. This raises some questions related to efficiency, which will be addressed next.

Appendix B

Efficiency considerations

In the kinematic guidance laws presented thus far, the surge and heave velocities (u^* and w^*) may be chosen so that the vehicle trajectory is shorter, which means that a *less curvilinear* trajectory can be obtained during the initial time. For example, consider the guidance law (5.37). It is easy to verify that the surge velocity is independent of the relative angle to the target. Hence, if the vehicle points in the opposite direction of the target, it will move with positive surge velocity though it is enlarging the distance from the target. Note that, without affecting the convergence properties, the surge velocity can be set equal to (A.9) instead of (5.37) or (5.35), allowing *backward* motion if the vehicle orientation points to the opposite direction of the target. The same applies to the heave velocity, for which the control law in (A.10) can be used instead of (A.7).

Furthermore, backward motion may be undesired for marine vehicles as many thrusters are asymmetric and consequently make the motion in one direction (supposed to be frontwards) much more efficient than in the opposite. Therefore, without affecting the convergence of the vehicle, an appropriate choice would be

$$u^* = \begin{cases} \zeta (c(\psi - \alpha) c\theta c\beta + s\theta s\beta) & \text{if } c(\psi - \alpha) c\theta c\beta + s\theta s\beta \leq 0 \\ 0, & \text{else} \end{cases} \quad (\text{B.1})$$

$$w^* = \begin{cases} \zeta (c(\psi - \alpha) s\theta c\beta + c\theta s\beta) & \text{if } c(\psi - \alpha) s\theta c\beta + c\theta s\beta \leq 0 \\ 0, & \text{else} \end{cases} \quad (\text{B.2})$$

with $\zeta = -\vartheta_D - \vartheta^* - K_\rho \text{sat}(\rho(t) - \delta, \mu_\rho)$, instead of (5.37) or (A.9) and (A.7) or (A.10), respectively.

Example B.1. *In order to illustrate the control laws and their alternatives, the results of the simulation considering the control laws in (5.37), (A.9) and (B.1) are presented. It was considered that the heave is null $w = w^* = 0$ and that surge, pitch and yaw are controlled. The trajectories are depicted in the figure B.1 for the vehicle starting at the position $[x \ y \ z]_{t=t_0} = [2 \ 2 \ 2]$ with initial*

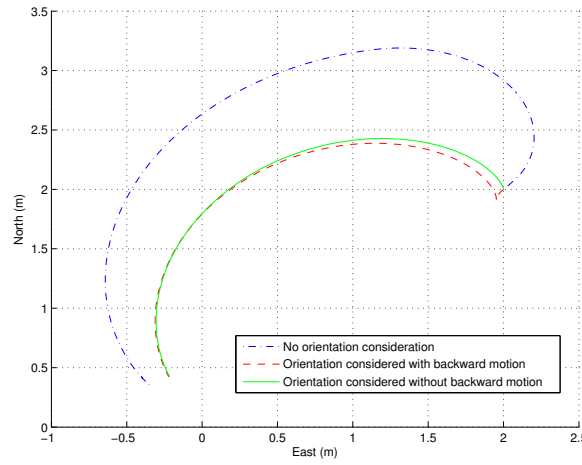


Figure B.1: Comparison of trajectories for control law variants

orientation $[\theta \ \psi]|_{t=t_0} = [\pi/4 \ \pi/4]$. The gains considered are $K_\rho = 1$, $K_\psi = K_\theta = 0.5$ and the offset constant $\delta = 0.5$.

The plot shows that when the orientation is not taken into consideration, the trajectory may be larger than in the other cases. During the first instants, it is possible to confirm that allowing the vehicle to move in the backwards, using (5.37), causes the trajectory not to coincide with that obtained when the vehicle cannot move backwards as a result of using the control law in (B.1). Although very similar, allowing backward motion may be inefficient for certain vehicles.

Appendix C

MARES model

The current reduced model of MARES is given in this section. The vehicle can have different configurations resulting in different mathematical models (Cruz and Matos, 2008; Cruz et al., 2013). Hence, here, the mathematical model for the configuration with a module that includes an altimeter, a beam attenuation meter and a camera is presented. Since common configuration changes mainly result in modifications of the length, weight and buoyancy, the model remains similar, that is, in terms of non-null entries of the matrices, with changes on the values of the parameters only. The values of the parameters shown hereafter are based on theoretical and semi-empirical formulas. The reader is referred to (Hoerner, 1965; White, 2003; Fossen, 1994; Prestero, 2001) for further details.

It is assumed that the origin of the body-fixed frame coincides with the center of gravity of the vehicles for all the forthcoming derivations. The reduced-order combined inertia and added mass matrix M is given in (C.1). The derivation of the matrix of centripetal and Coriolis terms $C(\cdot)$, resulting from the sum of the terms from rigid-body from inertia matrix and from added mass, is straightforward from Fossen (1994) and is given in (C.2).

$$M = \begin{bmatrix} m - X_{\ddot{u}} & 0 & 0 & 0 & -X_{\dot{q}} & 0 \\ 0 & m - Y_{\ddot{v}} & 0 & -Y_{\dot{p}} & 0 & -Y_{\dot{r}} \\ 0 & 0 & m - Z_{\ddot{w}} & 0 & -Z_{\dot{q}} & 0 \\ 0 & -K_{\dot{v}} & 0 & I_{xx} - K_{\dot{p}} & 0 & 0 \\ -M_{\ddot{u}} & 0 & -M_{\ddot{z}} & 0 & I_{yy} - M_{\dot{q}} & 0 \\ 0 & -N_{\dot{v}} & 0 & 0 & 0 & I_{zz} - N_{\dot{r}} \end{bmatrix} \quad (\text{C.1})$$

$$C(v) = \begin{bmatrix} 0 & -mr & mq \\ mr & 0 & -mp \\ -mq & mp & 0 \\ 0 & -Z_{\dot{w}}w - Z_{\dot{q}}q & +Y_{\dot{v}}v + Y_{\dot{p}}p + Y_{\dot{r}}r \\ +Z_{\dot{w}}w + Z_{\dot{q}}q & 0 & -X_{\dot{u}}u - X_{\dot{q}}q \\ -Y_{\dot{v}}v - Y_{\dot{p}}p - Y_{\dot{r}}r & +X_{\dot{u}}u + X_{\dot{q}}q & 0 \\ 0 & -Z_{\dot{w}}w - Z_{\dot{q}}q & +Y_{\dot{v}}v + Y_{\dot{p}}p + Y_{\dot{r}}r \\ +Z_{\dot{w}}w + Z_{\dot{q}}q & 0 & -X_{\dot{u}}u - X_{\dot{q}}q \\ -Y_{\dot{v}}v - Y_{\dot{p}}p - Y_{\dot{r}}r & +X_{\dot{u}}u + X_{\dot{q}}q & 0 \\ 0 & I_{zz}r - Y_{\dot{r}}v - N_{\dot{r}}r & -I_{yy}q + X_{\dot{q}}u + Z_{\dot{q}}w + M_{\dot{q}}q \\ -I_{zz}r + Y_{\dot{r}}v + N_{\dot{r}}r & 0 & I_{xx}p - Y_{\dot{p}}v - K_{\dot{p}}p \\ I_{yy}q - X_{\dot{q}}u - Z_{\dot{q}}w - M_{\dot{q}}q & -I_{xx}p + Y_{\dot{p}}v + K_{\dot{p}}p & 0 \end{bmatrix} \quad (C.2)$$

$$D(v) = - \begin{bmatrix} X_{u|u}|u| & 0 & 0 & 0 & X_{q|q}|q| & 0 \\ 0 & Y_{v|v}|v| & 0 & Y_{p|p}|p| & 0 & Y_{r|r}|r| \\ 0 & 0 & Z_{w|w}|w| & 0 & Z_{q|q}|q| & 0 \\ 0 & K_{v|v}|v| & 0 & K_{p|p}|p| & 0 & 0 \\ M_{u|u}|u| & 0 & M_{w|w}|w| & 0 & M_{q|q}|q| & 0 \\ 0 & N_{v|v}|v| & 0 & 0 & 0 & N_{r|r}|r| \end{bmatrix} \quad (C.3)$$

$$g(\eta) = g(\eta_a) = \begin{bmatrix} (W - B) \sin \theta \\ -(W - B) \cos \theta \sin \phi \\ -(W - B) \cos(\theta) \cos \phi \\ y_B B \cos \theta \cos \phi - z_B B \cos \theta \sin \phi \\ -z_B B \sin \theta - x_B B \cos \theta \cos \phi \\ x_B B \cos \theta \sin \phi + y_B B \sin \theta \end{bmatrix}, \quad (C.4)$$

$$P = \begin{bmatrix} d_1 & \dots & d_{n_a} \\ r_1 \times d_1 & \dots & r_{n_a} \times d_{n_a} \end{bmatrix} = \begin{bmatrix} 1 & 1 & 0 & 0 \\ 0 & 0 & 0 & 0 \\ 0 & 0 & 1 & 1 \\ 0 & 0 & 0 & 0 \\ z_1 & z_2 & x_3 & x_4 \\ -y_1 & -y_2 & 0 & 0 \end{bmatrix} \quad (C.5)$$

Regarding the viscous damping matrix, it is assumed that linear components of damping are negligible for the velocity under consideration. Similarly, the terms higher than second order are also considered to be small enough to be neglected. Therefore, the resulting nonlinear viscous damping matrix is expressed in (C.3).

The matrix mapping the forces exerted by the thrusters in the vector of forces and moments expressed in the body-fixed frame is given in C.5.

Table C.1: Added mass coefficients

| Coefficient | Value | Units |
|--------------------------------------------------------|-----------------------|------------------------|
| $X_{\dot{u}}$ | $-2.64 \cdot 10^0$ | kg |
| $Y_{\dot{v}}, Z_{\dot{w}}$ | $-4.81 \cdot 10^1$ | kg |
| $K_{\dot{p}}$ | $-1.56 \cdot 10^{-2}$ | kg·m ² /rad |
| $M_{\dot{q}}, N_{\dot{r}}$ | $-9.61 \cdot 10^0$ | kg·m ² /rad |
| $Y_{\dot{p}}, K_{\dot{v}}$ | $3.07 \cdot 10^{-3}$ | kg·m/rad, kg·m |
| $Y_{\dot{r}}, -Z_{\dot{q}}, -M_{\dot{w}}, N_{\dot{v}}$ | $1.20 \cdot 10^0$ | kg·m/rad, kg·m |
| $X_{\dot{q}}, M_{\dot{u}}$ | $-3.07 \cdot 10^{-3}$ | kg·m/rad, kg·m |

Table C.2: Viscous damping coefficients

| Coefficient | Value | Units |
|-------------|-----------------------|-------------------------------------|
| $X_{u u }$ | $-1.02 \cdot 10^1$ | kg/m |
| $Y_{v v }$ | $-1.34 \cdot 10^2$ | kg/m |
| $Z_{w w }$ | $-1.29 \cdot 10^2$ | kg/m |
| $K_{p p }$ | $-2.52 \cdot 10^{-2}$ | kg·m ² /rad ² |
| $M_{q q }$ | $-1.72 \cdot 10^1$ | kg·m ² /rad ² |
| $N_{r r }$ | $-1.80 \cdot 10^1$ | kg·m ² /rad ² |
| $X_{q q }$ | $4.37 \cdot 10^{-3}$ | kg·m/rad |
| $Y_{p p }$ | $-4.37 \cdot 10^{-3}$ | kg·m/rad |
| $Y_{r r }$ | $-1.44 \cdot 10^0$ | kg·m/rad |
| $Z_{q q }$ | $1.32 \cdot 10^0$ | kg·m/rad |
| $K_{v v }$ | $1.85 \cdot 10^{-1}$ | kg |
| $M_{u u }$ | $-1.85 \cdot 10^{-1}$ | kg |
| $M_{w w }$ | $-2.07 \cdot 10^0$ | kg |
| $N_{v v }$ | $-2.17 \cdot 10^0$ | kg |

Table C.3: Parameters

| Parameter | Value | Units |
|-------------|-----------------------|-------|
| m | $3.61 \cdot 10^1$ | kg |
| W | $3.54 \cdot 10^2$ | N |
| B | $3.56 \cdot 10^2$ | N |
| x_B, y_B | 0 | m |
| z_B | $-3.63 \cdot 10^{-3}$ | m |
| z_1, z_2 | $-3.63 \cdot 10^{-3}$ | m |
| $y_1, -y_2$ | $-1.09 \cdot 10^{-1}$ | m |
| x_3 | $-4.32 \cdot 10^{-1}$ | m |
| x_4 | $4.38 \cdot 10^{-1}$ | m |

The vector of restoring forces and moments is given in Fossen (1994), and is easily reduced to (C.4), where W and B denote the weight and the buoyancy forces, respectively.

The values of the parameters of the Coriolis and centripetal matrix and of the damping matrix are listed in tables C.1 and C.2, respectively. The remaining coefficients of the added mass matrix and of the restoring forces and moments vector are given in table C.3

Table C.4: Inertia tensors

| Parameter | Value | Units |
|-----------|----------------------|--------------------|
| I_{xx} | $2.04 \cdot 10^{-1}$ | kg· m ² |
| I_{yy} | $8.96 \cdot 10^0$ | kg· m ² |
| I_{zz} | $8.96 \cdot 10^0$ | kg· m ² |

Appendix D

TriMARES model

Apart from the matrix that maps the forces exerted by the thrusters on the body-fixed frame axes, which is given in (D.1), the model of TriMARES takes the same form as the model of MARES, given in C. Therefore, this specific model differs only on the values of the parameters, which are listed below in the corresponding tables.

$$P = \begin{bmatrix} 1 & 1 & 1 & 1 & 0 & 0 & 0 \\ 0 & 0 & 0 & 0 & -1 & 0 & 0 \\ 0 & 0 & 0 & 0 & 0 & 1 & 1 \\ 0 & 0 & 0 & 0 & 0 & 0 & 0 \\ z_1 & z_2 & z_3 & z_4 & 0 & x_6 & x_7 \\ y_1 & y_2 & y_3 & y_4 & -x_5 & 0 & 0 \end{bmatrix} \quad (\text{D.1})$$

Table D.1: Added mass coefficients

| Coefficient | Value | Units |
|--------------------------------------------------------|--------------------|------------------------|
| $X_{\dot{u}}$ | $-5.87 \cdot 10^0$ | kg |
| $Y_{\dot{v}}, Z_{\dot{w}}$ | $-1.11 \cdot 10^2$ | kg |
| $K_{\dot{p}}$ | $-1.90 \cdot 10^2$ | kg·m ² /rad |
| $M_{\dot{q}}, N_{\dot{r}}$ | $-1.26 \cdot 10^1$ | kg·m ² /rad |
| $Y_{\dot{p}}, K_{\dot{v}}$ | $-5.59 \cdot 10^1$ | kg·m/rad, kg·m |
| $Y_{\dot{r}}, -Z_{\dot{q}}, -M_{\dot{w}}, N_{\dot{v}}$ | $-5.00 \cdot 10^0$ | kg·m/rad, kg·m |
| $X_{\dot{q}}, M_{\dot{u}}$ | $3.02 \cdot 10^0$ | kg·m/rad, kg·m |

Table D.2: Viscous damping coefficients

| Coefficient | Value | Units |
|-------------|----------------------|-------------------------------------|
| $X_{u u }$ | $-3.24 \cdot 10^1$ | kg/m |
| $Y_{v v }$ | $-3.03 \cdot 10^2$ | kg/m |
| $Z_{w w }$ | $-3.27 \cdot 10^2$ | kg/m |
| $K_{p p }$ | $-1.22 \cdot 10^0$ | kg·m ² /rad ² |
| $M_{q q }$ | $-1.75 \cdot 10^1$ | kg·m ² /rad ² |
| $N_{r r }$ | $-1.64 \cdot 10^1$ | kg·m ² /rad ² |
| $X_{q q }$ | $9.52 \cdot 10^{-2}$ | kg·m/rad |
| $Y_{p p }$ | $-6.32 \cdot 10^0$ | kg·m/rad |
| $Y_{r r }$ | $-5.87 \cdot 10^0$ | kg·m/rad |
| $Z_{q q }$ | $7.20 \cdot 10^0$ | kg·m/rad |
| $K_{v v }$ | $1.92 \cdot 10^{-1}$ | kg |
| $M_{u u }$ | $7.27 \cdot 10^{-1}$ | kg |
| $M_{w w }$ | $1.31 \cdot 10^1$ | kg |
| $N_{v v }$ | $-1.08 \cdot 10^1$ | kg |

Table D.3: Parameters

| Parameter | Value | Units |
|-------------|-----------------------|-------|
| m | $1.1 \cdot 10^2$ | kg |
| W | $7.84 \cdot 10^2$ | N |
| B | $7.87 \cdot 10^2$ | N |
| x_B, y_B | 0 | m |
| z_B | $-3.50 \cdot 10^{-2}$ | m |
| z_1, z_2 | $-4.69 \cdot 10^{-2}$ | m |
| z_3, z_4 | $9.97 \cdot 10^{-2}$ | m |
| $y_1, -y_2$ | $2.29 \cdot 10^{-1}$ | m |
| $y_3, -y_4$ | $7.67 \cdot 10^{-2}$ | m |
| x_3 | $-4.32 \cdot 10^{-1}$ | m |
| x_4 | $4.38 \cdot 10^{-1}$ | m |
| x_7 | $-4.38 \cdot 10^{-1}$ | m |

Table D.4: Inertia tensors

| Parameter | Value | Units |
|-----------|-------------------|-------------------|
| I_{xx} | $5.68 \cdot 10^0$ | kg·m ² |
| I_{yy} | $1.03 \cdot 10^1$ | kg·m ² |
| I_{zz} | $1.23 \cdot 10^1$ | kg·m ² |

Appendix E

Zarco and Gama model

Since Zarco and Gama are very similar vehicles, their model is assumed to be the same. Structurally, the model is similar to the one presented for MARES in C. Besides the dissimilar values that the parameters take, for Zarco and Gama, the restoring forces and moments vector are considered to be null and some cross-coupling effects are considered negligible. In particular, the coupling between sway and roll, heave and sway and surge and pitch are considered null. For completeness, the matrices composing the model are presented next.

$$M = \begin{bmatrix} m - X_{\dot{u}} & 0 & 0 & 0 & 0 & 0 \\ 0 & m - Y_{\dot{v}} & 0 & 0 & 0 & -Y_{\dot{r}} \\ 0 & 0 & m - Z_{\dot{w}} & 0 & 0 & 0 \\ 0 & 0 & 0 & I_{xx} - K_{\dot{p}} & 0 & 0 \\ 0 & 0 & 0 & 0 & I_{yy} - M_{\dot{q}} & 0 \\ 0 & -N_{\dot{v}} & 0 & 0 & 0 & I_{zz} - N_{\dot{r}} \end{bmatrix} \quad (\text{E.1})$$

$$C(v) = \begin{bmatrix} 0 & -mr & mq \\ mr & 0 & -mp \\ -mq & mp & 0 \\ 0 & -Z_{\dot{w}}w & +Y_{\dot{v}}v + Y_{\dot{r}}r \\ +Z_{\dot{w}}w & 0 & -X_{\dot{u}}u \\ -Y_{\dot{v}}v - Y_{\dot{r}}r & +X_{\dot{u}}u & 0 \\ 0 & -Z_{\dot{w}}w & +Y_{\dot{v}}v + Y_{\dot{r}}r \\ +Z_{\dot{w}}w & 0 & -X_{\dot{u}}u \\ -Y_{\dot{v}}v - Y_{\dot{r}}r & +X_{\dot{u}}u & 0 \\ 0 & I_{zz}r - Y_{\dot{r}}v - N_{\dot{r}}r & -I_{yy}q + M_{\dot{q}}q \\ -I_{zz}r + Y_{\dot{r}}v + N_{\dot{r}}r & 0 & I_{xx}p - K_{\dot{p}}p \\ I_{yy}q - M_{\dot{q}}q & -I_{xx}p + K_{\dot{p}}p & 0 \end{bmatrix} \quad (\text{E.2})$$

Table E.1: Added mass coefficients

| Coefficient | Value | Units |
|--------------------------------------------------------|--------------------|------------------------|
| $X_{\dot{u}}$ | $-5.5 \cdot 10^0$ | kg |
| $Y_{\dot{v}}, Z_{\dot{w}}$ | $-6.74 \cdot 10^1$ | kg |
| $K_{\dot{p}}$ | $-1.08 \cdot 10^1$ | kg·m ² /rad |
| $M_{\dot{q}}, N_{\dot{r}}$ | $-1.39 \cdot 10^1$ | kg·m ² /rad |
| $Y_{\dot{p}}, K_{\dot{v}}$ | $-5.59 \cdot 10^1$ | kg·m/rad, kg·m |
| $Y_{\dot{r}}, -Z_{\dot{q}}, -M_{\dot{w}}, N_{\dot{v}}$ | $3.36 \cdot 10^0$ | kg·m/rad, kg·m |
| $X_{\dot{q}}, M_{\dot{u}}$ | $3.02 \cdot 10^0$ | kg·m/rad, kg·m |

$$D(v) = - \begin{bmatrix} X_{u|u}|u| & 0 & 0 & 0 & 0 & 0 \\ 0 & Y_{v|v}|v| & 0 & 0 & 0 & Y_{r|r}|r| \\ 0 & 0 & Z_{w|w}|w| & 0 & 0 & 0 \\ 0 & 0 & 0 & K_{p|p}|p| & 0 & 0 \\ 0 & 0 & 0 & 0 & M_{q|q}|q| & 0 \\ 0 & N_{v|v}|v| & 0 & 0 & 0 & N_{r|r}|r| \end{bmatrix} \quad (\text{E.3})$$

$$P = \begin{bmatrix} 1 & 1 \\ 0 & 0 \\ 0 & 0 \\ 0 & 0 \\ 0 & 0 \\ -y_1 & -y_2 \end{bmatrix} \quad (\text{E.4})$$

The parameters of the matrices are given in tables E.1, E.2, E.3 and E.4.

Table E.2: Viscous damping coefficients

| Coefficient | Value | Units |
|-------------|--------------------|-------------------------------------|
| $X_u u $ | $-3.07 \cdot 10^1$ | kg/m |
| $Y_v v $ | $-1.29 \cdot 10^2$ | kg/m |
| $Z_w w $ | $-3.32 \cdot 10^2$ | kg/m |
| $K_p p $ | $-2.32 \cdot 10^1$ | kg·m ² /rad ² |
| $M_q q $ | $-2.20 \cdot 10^1$ | kg·m ² /rad ² |
| $N_r r $ | $-1.17 \cdot 10^1$ | kg·m ² /rad ² |
| $Y_r r $ | $-7.12 \cdot 10^0$ | kg·m/rad |
| $N_v v $ | $-1.12 \cdot 10^0$ | kg |

Table E.3: Parameters

| Parameter | Value | Units |
|-------------|-----------------------|-------|
| m | $5.5 \cdot 10^1$ | kg |
| z_1, z_2 | $5.00 \cdot 10^{-1}$ | m |
| $y_1, -y_2$ | $-2.45 \cdot 10^{-1}$ | m |

Table E.4: Inertia tensors

| Parameter | Value | Units |
|-----------|---------------------|-------------------|
| I_{xx} | $5.5 \cdot 10^{-1}$ | kg·m ² |
| I_{yy} | $8.28 \cdot 10^0$ | kg·m ² |
| I_{zz} | $7.73 \cdot 10^0$ | kg·m ² |

Appendix F

BASV model

Because of their similar design in terms of actuators and symmetries, the BASV and Zarco have similar models, taking the same forms of model matrices. In this thesis, it was considered that only the coefficients varied. As such, the matrices composing the model will not be exposed again. Only the parameters are given hereafter.

Table F.1: Added mass coefficients

| Coefficient | Value | Units |
|--------------------------------------------------------|-----------------------|------------------------|
| $X_{\dot{u}}$ | $-1.1 \cdot 10^0$ | kg |
| $Y_{\dot{v}}, Z_{\dot{w}}$ | $-1.24 \cdot 10^1$ | kg |
| $K_{\dot{p}}$ | $-5.8 \cdot 10^{-2}$ | kg·m ² /rad |
| $M_{\dot{q}}, N_{\dot{r}}$ | $-4.24 \cdot 10^{-1}$ | kg·m ² /rad |
| $Y_{\dot{p}}, K_{\dot{v}}$ | $-5.59 \cdot 10^1$ | kg·m/rad, kg·m |
| $Y_{\dot{r}}, -Z_{\dot{q}}, -M_{\dot{w}}, N_{\dot{v}}$ | $-1.77 \cdot 10^{-1}$ | kg·m/rad, kg·m |
| $X_{\dot{q}}, M_{\dot{u}}$ | $3.02 \cdot 10^0$ | kg·m/rad, kg·m |

Table F.2: Viscous damping coefficients

| Coefficient | Value | Units |
|-------------|-----------------------|-------------------------------------|
| $X_u u $ | $-7.81 \cdot 10^0$ | kg/m |
| $Y_v v $ | $-4.94 \cdot 10^1$ | kg/m |
| $Z_w w $ | $-2.31 \cdot 10^2$ | kg/m |
| $K_p p $ | $-9.86 \cdot 10^0$ | kg·m ² /rad ² |
| $M_q q $ | $-4.41 \cdot 10^0$ | kg·m ² /rad ² |
| $N_r r $ | $-2.38 \cdot 10^{-1}$ | kg·m ² /rad ² |
| $X_q q $ | $9.52 \cdot 10^{-2}$ | kg·m/rad |
| $Y_p p $ | $-6.32 \cdot 10^0$ | kg·m/rad |
| $Y_r r $ | $-2.79 \cdot 10^{-1}$ | kg·m/rad |
| $Z_q q $ | $7.20 \cdot 10^0$ | kg·m/rad |
| $K_v v $ | $1.92 \cdot 10^{-1}$ | kg |
| $M_u u $ | $7.27 \cdot 10^{-1}$ | kg |
| $M_w w $ | $1.31 \cdot 10^1$ | kg |
| $N_v v $ | $-1.98 \cdot 10^0$ | kg |

Table F.3: Parameters

| Parameter | Value | Units |
|-------------|-----------------------|-------|
| m | $1.1 \cdot 10^1$ | kg |
| W | $7.84 \cdot 10^2$ | N |
| B | $7.87 \cdot 10^2$ | N |
| x_B, y_B | 0 | m |
| z_B | $-3.50 \cdot 10^{-2}$ | m |
| z_1, z_2 | $0 \cdot 10^{-1}$ | m |
| $y_1, -y_2$ | $-1.48 \cdot 10^{-1}$ | m |
| x_3 | $-4.32 \cdot 10^{-1}$ | m |
| x_4 | $4.38 \cdot 10^{-1}$ | m |

Table F.4: Inertia tensors

| Parameter | Value | Units |
|-----------|----------------------|-------------------|
| I_{xx} | $3.3 \cdot 10^{-1}$ | kg·m ² |
| I_{yy} | $5.08 \cdot 10^{-1}$ | kg·m ² |
| I_{zz} | $3.98 \cdot 10^{-1}$ | kg·m ² |

Appendix G

LASV model

As for the BASV, the model is assumed to be similar to the presented in appendix E. Only the parameters and coefficients differ. These are listed in the following tables.

Table G.1: Added mass coefficients

| Coefficient | Value | Units |
|--------------------------------------------------------|-----------------------|-----------------------------------------------------------------|
| $X_{\dot{u}}$ | $-2.8 \cdot 10^0$ | kg |
| $Y_{\dot{v}}, Z_{\dot{w}}$ | $-2.93 \cdot 10^1$ | kg |
| $K_{\dot{p}}$ | $-1.08 \cdot 10^1$ | $\text{kg} \cdot \text{m}^2/\text{rad}$ |
| $M_{\dot{q}}, N_{\dot{r}}$ | $-3.49 \cdot 10^0$ | $\text{kg} \cdot \text{m}^2/\text{rad}$ |
| $Y_{\dot{p}}, K_{\dot{v}}$ | $-5.59 \cdot 10^1$ | $\text{kg} \cdot \text{m}/\text{rad}, \text{kg} \cdot \text{m}$ |
| $Y_{\dot{r}}, -Z_{\dot{q}}, -M_{\dot{w}}, N_{\dot{v}}$ | $-2.51 \cdot 10^{-1}$ | $\text{kg} \cdot \text{m}/\text{rad}, \text{kg} \cdot \text{m}$ |
| $X_{\dot{q}}, M_{\dot{u}}$ | $3.02 \cdot 10^0$ | $\text{kg} \cdot \text{m}/\text{rad}, \text{kg} \cdot \text{m}$ |

Table G.2: Viscous damping coefficients

| Coefficient | Value | Units |
|-------------|----------------------|-------------------------------------|
| $X_{u u }$ | $-7.23 \cdot 10^0$ | kg/m |
| $Y_{v v }$ | $-1.28 \cdot 10^2$ | kg/m |
| $Z_{w w }$ | $-1.77 \cdot 10^2$ | kg/m |
| $K_{p p }$ | $-2.32 \cdot 10^1$ | kg·m ² /rad ² |
| $M_{q q }$ | $-9.74 \cdot 10^0$ | kg·m ² /rad ² |
| $N_{r r }$ | $-7.22 \cdot 10^0$ | kg·m ² /rad ² |
| $X_{q q }$ | $9.52 \cdot 10^{-2}$ | kg·m/rad |
| $Y_{p p }$ | $-6.32 \cdot 10^0$ | kg·m/rad |
| $Y_{r r }$ | $1.19 \cdot 10^0$ | kg·m/rad |
| $Z_{q q }$ | $7.20 \cdot 10^0$ | kg·m/rad |
| $K_{v v }$ | $1.92 \cdot 10^{-1}$ | kg |
| $M_{u u }$ | $7.27 \cdot 10^{-1}$ | kg |
| $M_{w w }$ | $1.31 \cdot 10^1$ | kg |
| $N_{v v }$ | $5.22 \cdot 10^0$ | kg |

Table G.3: Parameters

| Parameter | Value | Units |
|-------------|-----------------------|-------|
| m | $2.8 \cdot 10^1$ | kg |
| W | $7.84 \cdot 10^2$ | N |
| B | $7.87 \cdot 10^2$ | N |
| x_B, y_B | 0 | m |
| z_B | $-3.50 \cdot 10^{-2}$ | m |
| z_1, z_2 | $0 \cdot 10^{-1}$ | m |
| $y_1, -y_2$ | $-1.48 \cdot 10^{-1}$ | m |
| x_3 | $-4.32 \cdot 10^{-1}$ | m |
| x_4 | $4.38 \cdot 10^{-1}$ | m |

Table G.4: Inertia tensors

| Parameter | Value | Units |
|-----------|-------------------|-------------------|
| I_{xx} | $1.41 \cdot 10^0$ | kg·m ² |
| I_{yy} | $3.12 \cdot 10^0$ | kg·m ² |
| I_{zz} | $2.54 \cdot 10^0$ | kg·m ² |

References

- ACSA. Acsa underwater gps: Gib-lite, December 2011a. URL <http://www.underwater-gps.com/images/dynproduits/g41.pdf>.
- ACSA. Acsa underwater gps: Gib plus, December 2011b. URL <http://www.underwater-gps.com/images/dynproduits/g418.pdf>.
- A. P. Aguiar and A. M. Pascoal. Dynamic positioning and way-point tracking of underactuated auvs in the presence of ocean currents. *International Journal of Control*, 80(7):1092–1108, 2007. doi: 10.1080/00207170701268882. URL <http://www.tandfonline.com/doi/abs/10.1080/00207170701268882>.
- A.P. Aguiar and J.P. Hespanha. Trajectory-tracking and path-following of underactuated autonomous vehicles with parametric modeling uncertainty. *Automatic Control, IEEE Transactions on*, 52(8):1362–1379, aug. 2007. ISSN 0018-9286. doi: 10.1109/TAC.2007.902731.
- Corporation Airmar Technology. Cs4500 —ultrasonic speed sensor, 12 2011a. URL <http://www.airmartechonology.com/2009/products/marine-product.asp?prodid=68&manf=All>.
- Corporation Airmar Technology. St850 —thru-hull, smart sensor, December 2011b. URL <http://www.airmartechonology.com/2009/products/marine-product.asp?prodid=58&manf=All>.
- AI Al-Shamma’a, A Shaw, and S Saman. Propagation of electromagnetic waves at MHz frequencies through seawater. *IEEE Transactions on Antennas And Propagation*, 52(11):2843–2849, NOV 2004. ISSN 0018-926X. doi: {10.1109/TAP.2004.834449}.
- B. Allen, R. Stokey, T. Austin, N. Forrester, R. Goldsborough, M. Purcell, and C. von Alt. Remus: a small, low cost auv; system description, field trials and performance results. In *OCEANS ’97. MTS/IEEE Conference Proceedings*, volume 2, pages 994–1000 vol.2, oct 1997. doi: 10.1109/OCEANS.1997.624126.
- J. Almeida, C. Silvestre, and A. M. Pascoal. Cooperative control of multiple surface vessels with discrete-time periodic communications. *International Journal of Robust and Nonlinear Control*, 22(4):398–419, 2012. ISSN 1099-1239. doi: 10.1002/rnc.1698. URL <http://dx.doi.org/10.1002/rnc.1698>.
- Gianluca Antonelli, Thor I. Fossen, and Dana R. Yoerger. Underwater robotics. In *Springer Handbook of Robotics*, pages 987–1008. 2008.
- J. Aparicio, F.J. Alvarez, A. Jimenez, C. De Marziani, J. Urena, and C. Diego. Underwater channel modeling for a relative positioning system. In *OCEANS, 2011 IEEE - Spain*, pages 1–7, june 2011. doi: 10.1109/Oceans-Spain.2011.6003515.

- A. A. Argyros, K. E. Bekris, S. C. Orphanoudakis, and L. E. Kavraki. Robot homing by exploiting panoramic vision. *Autonomous Robots*, 19(1):7–25, 2005.
- M. S. Arulampalam, S. Maskell, N. Gordon, and T. Clapp. A tutorial on particle filters for online nonlinear/non-Gaussian Bayesian tracking. *IEEE Transactions on Signal Processing*, 50(2): 174–188, February 2002. ISSN 1053-587X.
- P. Baccou and B. Jouvencel. Homing and navigation using one transponder for auv, postprocessing comparisons results with long base-line navigation. In *Robotics and Automation, 2002. Proceedings. ICRA '02. IEEE International Conference on*, volume 4, pages 4004 – 4009 vol.4, 2002. doi: 10.1109/ROBOT.2002.1014361.
- P. Baccou and B. Jouvencel. Simulation results, post-processing experimentations and comparisons results for navigation, homing and multiple vehicles operations with a new positioning method using on transponder. In *IROS 2003: Proceedings of the 2003 IEEE/RSJ International Conference on Intelligent Robots and Systems, Vols 1-4*, pages 811–817, 2003.
- Alexander Bahr, John J. Leonard, and Maurice F. Fallon. Cooperative Localization for Autonomous Underwater Vehicles. *International journal of Robotics Research*, 28(6):714–728, June 2009. ISSN 0278-3649. doi: {10.1177/0278364908100561}. 10th International Symposium on Experimental Robotics (ISER), Rio de Janeiro, BRAZIL, JUL 06-12, 2006.
- S. Barkby, S. B. Williams, O. Pizarro, and M. V. Jakuba. A featureless approach to efficient bathymetric slam using distributed particle mapping. *Journal of Field Robotics*, 28(1):19–39, 2011.
- P. Batista, C. Silvestre, and P. Oliveira. A time differences of arrival-based homing strategy for autonomous underwater vehicles. *International Journal of Robust and Nonlinear Control*, 20(15):1758–1773, 2010.
- Fedor Bezruchko, Igor Burdinsky, and Anton Myagotin. Global extremum searching algorithm for the auv guidance toward an acoustic buoy. In *OCEANS'11 - Oceans of Energy for a Sustainable Future*, Santander, Spain, 2011. IEEE.
- Brian Bingham. *Precision Autonomous Underwater Navigation*. PhD thesis, Massachusetts Institute of Technology, Massachusetts, May 2003.
- Adrian N. Bishop, Baris Fidan, Brian D.O. Anderson, Kutluyil Dogancay, and Pubudu N. Pathirana. Optimality analysis of sensor-target localization geometries. *Automatica*, 46(3): 479 – 492, 2010. ISSN 0005-1098. doi: 10.1016/j.automatica.2009.12.003. URL <http://www.sciencedirect.com/science/article/pii/S0005109809005500>.
- E. Borhaug, A. Pavlov, and K.Y. Pettersen. Straight line path following for formations of under-actuated underwater vehicles. In *Decision and Control, 2007 46th IEEE Conference on*, pages 2905 –2912, dec. 2007. doi: 10.1109/CDC.2007.4434733.
- M. Boutayeb, H. Rafaralahy, and M. Darouach. Convergence analysis of the extended kalman filter used as an observer for nonlinear deterministic discrete-time systems. *Automatic Control, IEEE Transactions on*, 42(4):581–586, Apr 1997. ISSN 0018-9286. doi: 10.1109/9.566674.
- M. Cao and A.S. Morse. Station keeping in the plane with range-only measurements. In *American Control Conference, 2007. ACC '07*, pages 5419–5424, 2007. doi: 10.1109/ACC.2007.4282748.

- Y. U. Cao, A. S. Fukunaga, and A. B. Kahng. Cooperative mobile robotics: Antecedents and directions. *Autonomous Robots*, 4(1):7–27, 1997. ISSN 0929-5593. doi: {10.1023/A:1008855018923}.
- T. Casey, B. Guimond, and J. Hu. Underwater vehicle positioning based on time of arrival measurements from a single beacon. In *OCEANS 2007*, pages 1 –8, 29 2007-oct. 4 2007. doi: 10.1109/OCEANS.2007.4449186.
- H. T. Choi, A. Hanai, S. K. Choi, and J. Yuh. Development of an underwater robot, odin-iii. In *Intelligent Robots and Systems, 2003. (IROS 2003). Proceedings. 2003 IEEE/RSJ International Conference on*, volume 1, pages 836 – 841 vol.1, October 2003. doi: 10.1109/IROS.2003.1250733.
- Soon-Jo Chung and J.-J.E. Slotine. Cooperative robot control and concurrent synchronization of lagrangian systems. *IEEE Transactions on Robotics*, 25(3):686 –700, June 2009. ISSN 1552-3098. doi: 10.1109/TRO.2009.2014125.
- N. Cruz, L. Madureira, A. Matos, and F.L. Pereira. A versatile acoustic beacon for navigation and remote tracking of multiple underwater vehicles. In *OCEANS, 2001. MTS/IEEE Conference and Exhibition*, volume 3, pages 1829 –1834 vol.3, 2001. doi: 10.1109/OCEANS.2001.968124.
- N. A. Cruz and A. C. Matos. The MARES AUV, a modular autonomous robot for environment sampling. In *OCEANS 2008*, pages 1–6, 2008.
- N.A. Cruz, B.M. Ferreira, A.C. Matos, C. Petrioli, R. Petroccia, and D. Spaccini. Implementation of an underwater acoustic network using multiple heterogeneous vehicles. In *Oceans, 2012*, pages 1–10, 2012. doi: 10.1109/OCEANS.2012.6405107.
- Nuno Cruz, Aníbal Matos, Sérgio Cunha, and Sérgio Silva. Zarco - an autonomous craft for underwater surveys. In *Proceedings of the 7th Geomatic Week, Barcelona, Spain, February 2007.*, 2007.
- Nuno A. Cruz, Anibal C. Matos, Rui M. Almeida, Bruno M. Ferreira, and Nuno Abreu. Trimares - a hybrid auv/rov for dam inspection. In *OCEANS 2011*, pages 1 –7, September 2011.
- Nuno A. Cruz, Aníbal C. Matos, and Bruno M. Ferreira. Modular building blocks for the development of auvs – from mares to trimares. In *Proceedings of 2013 IEEE International Underwater Technology Symposium (UT13)*, 2013.
- James B. Dai, Qi Fu, and Neville K. S. Lee. Beacon placement strategies in an ultrasonic positioning system. *IIE Transactions*, 45(5):477–493, 2013. doi: 10.1080/0740817X.2011.649387. URL <http://www.tandfonline.com/doi/abs/10.1080/0740817X.2011.649387>.
- Michael Defoort, Jorge Palos, Annemarie Kokosy, Thierry Floquet, and Wilfrid Perruquetti. Performance-based reactive navigation for non-holonomic mobile robots. *Robotica*, 27:281–290, March 2009. ISSN 0263-5747. doi: {10.1017/S0263574708004700}.
- S. Desset, R. Damus, J. Morash, and C. Bechaz. Use of GIBs in AUVs for underwater archaeology. *Sea Technology Magazine*, 44(12):22+, December 2003. ISSN 0093-3651.
- Holger Dette. Designing experiments with respect to ‘standardized’ optimality criteria. *Journal of the Royal Statistical Society: Series B (Statistical Methodology)*, 59(1):97–110, 1997.

- ISSN 1467-9868. doi: 10.1111/1467-9868.00056. URL <http://dx.doi.org/10.1111/1467-9868.00056>.
- James Diebel. Representing attitude: Euler angles, unit quaternions, and rotation vectors, 2006.
- Jiu Ding and Aihui Zhou. Eigenvalues of rank-one updated matrices with some applications. *Applied Mathematics Letters*, 20(12):1223 – 1226, 2007. ISSN 0893-9659. doi: <http://dx.doi.org/10.1016/j.aml.2006.11.016>. URL <http://www.sciencedirect.com/science/article/pii/S0893965907000614>.
- Mari Carmen Domingo. Overview of channel models for underwater wireless communication networks. *Physical Communication*, 1(3):163 – 182, 2008. ISSN 1874-4907. doi: 10.1016/j.phycom.2008.09.001.
- Wenjie Dong and J.A. Farrell. Cooperative control of multiple nonholonomic mobile agents. *Automatic Control, IEEE Transactions on*, 53(6):1434 – 1448, July 2008. ISSN 0018-9286. doi: 10.1109/TAC.2008.925852.
- Wenjie Dong and Jay A. Farrell. Decentralized cooperative control of multiple nonholonomic dynamic systems with uncertainty. *Automatica*, 45(3):706–710, March 2009. ISSN 0005-1098. doi: {10.1016/j.automatica.2008.09.015}.
- Frederick Ducatelle, Gianni A. Di Caro, Carlo Pinciroli, and Luca M. Gambardella. Self-organized cooperation between robotic swarms. *Swarm Intelligence*, 5(2):73–96, June 2011. ISSN 1935-3812. doi: {10.1007/s11721-011-0053-0}.
- W. B. Dunbar and R. M. Murray. Distributed receding horizon control for multi-vehicle formation stabilization. *Automatica*, 42(4):549–558, April 2006. ISSN 0005-1098. doi: {10.1016/j.automatica.2005.12.008}.
- M. Egerstedt and Xiaoming Hu. Formation constrained multi-agent control. *Robotics and Automation, IEEE Transactions on*, 17(6):947 – 951, December 2001. ISSN 1042-296X. doi: 10.1109/70.976029.
- R. M. Eustice, L. L. Whitcomb, H. Singh, and M. Grund. Experimental results in synchronous-clock one-way-travel-time acoustic navigation for autonomous underwater vehicles. In *Proceedings of the 2007 IEEE International Conference on Robotics and Automation, Vols 1-10*, pages 4257–4264, 2007.
- Ryan M. Eustice, Hanumant Singh, and Louis L. Whitcomb. Synchronous-Clock, One-Way-Travel-Time Acoustic Navigation for Underwater Vehicles. *Journal of Field Robotics*, 28(1, SI):121–136, January 2011. ISSN 1556-4959. doi: {10.1002/rob.20365}.
- O. M. Faltinsen. *Hydrodynamics of high-speed marine vehicles*. Cambridge University Press, 2005.
- A. Farinelli, L. Locchi, and D. Nardi. Multirobot systems: A classification focused on coordination. *IEEE Transactions on Systems Man And Cybernetics Part B-Cybernetics*, 34(5):2015–2028, October 2004. ISSN 1083-4419. doi: {10.1109/TSMCB.2004.832155}.
- J. A. Fax and R. M. Murray. Information flow and cooperative control of vehicle formations. *IEEE Transactions on Automatic Control*, 49(9):1465–1476, September 2004. ISSN 0018-9286. doi: {10.1109/TAC.2004.834433}.

- H. J. S. Feder, J. J. Leonard, and C. M. Smith. Adaptive mobile robot navigation and mapping. *International Journal of Robotics Research*, 18(7):650–668, July 1999. ISSN 0278-3649.
- M. D. Feezor, F. Y. Sorrell, P. R. Blankinship, and J. G. Bellingham. Autonomous underwater vehicle homing/docking via electromagnetic guidance. *IEEE Journal of Oceanic Engineering*, 26(4):515–521, 2001.
- J. Ferguson. Under-ice seabed mapping with auvs. In *OCEANS 2009 - Europe, Vols 1 and 2*, pages 1434–1439, 2009.
- B. Ferreira, A. Matos, and N. Cruz. Single beacon navigation: Localization and control of the mares auv. In *OCEANS 2010*, 2010a.
- B. Ferreira, A. Matos, and N. Cruz. Single beacon navigation: Localization and control of the mares auv. In *OCEANS 2010*, pages 1 –9, September 2010b. doi: 10.1109/OCEANS.2010.5664518.
- Bruno Ferreira, Anibal Matos, Nuno Cruz, and Miguel Pinto. Modeling and Control of the MARES Autonomous Underwater Vehicle. *Marine Technology Society journal*, 44(2, SI):19–36, March-April 2010. ISSN 0025-3324.
- Bruno M. Ferreira, Aníbal C. Matos, and Nuno A. Cruz. Fault tolerant depth control of the mares auv. In Andrzej Bartoszewicz, editor, *Challenges and Paradigms in Applied Robust Control*, chapter 3. InTech, 2011.
- Bruno M. Ferreira, Aníbal C. Matos, and Nuno A. Cruz. Modeling and control of trimares auv. In Estela Bicho, Fernando Ribeiro, and Luis Louro, editors, *Robotica 2012: 12th International Conference on Autonomous Robot Systems and Competitions*, pages 57–62, Guimarães, 2012. Universidade do Minho.
- A. Folk, B. Armstrong, E. Wolbrecht, H.F. Grip, M. Anderson, and D. Edwards. Autonomous underwater vehicle navigation using moving baseline on a target ship. In *OCEANS 2010*, pages 1 –7, September 2010. doi: 10.1109/OCEANS.2010.5664462.
- T. I. Fossen. *Guidance and control of ocean vehicles*. Wiley, 1994. ISBN 9780471941132.
- Thor I. Fossen and Jann Peter Strand. Nonlinear passive weather optimal positioning control (wopc) system for ships and rigs: experimental results. *Automatica*, 37(5):701 – 715, 2001. ISSN 0005-1098. doi: [http://dx.doi.org/10.1016/S0005-1098\(01\)00006-1](http://dx.doi.org/10.1016/S0005-1098(01)00006-1). URL <http://www.sciencedirect.com/science/article/pii/S0005109801000061>.
- Toshio Fukuda and Seiya Nakagawa. Approach to the dynamically reconfigurable robotic system. *Journal of Intelligent & Robotic Systems*, 1:55–72, 1988. ISSN 0921-0296. 10.1007/BF00437320.
- A. S. Gadre, D. K. Maczka, D. Spinello, B. R. McCarter, D. J. Stilwell, W. Neu, M. J. Roan, and J. B. Hennage. Cooperative localization of an acoustic source using towed hydrophone arrays. In *Autonomous Underwater Vehicles, 2008. AUV 2008. IEEE/OES*, pages 1 –8, October 2008. doi: 10.1109/AUV.2008.5290529.
- A. Gelb. *Applied optimal estimation*. MIT Press, 1999. ISBN 9780262570480.

- R. Ghabcheloo, A. P. Aguiar, A. Pascoal, C. Silvestre, I. Kaminer, and J. Hespanha. Coordinated path-following in the presence of communication losses and time delays. *SIAM journal on control and optimization*, 48(1):234–265, 2009. ISSN 0363-0129. doi: {10.1137/060678993}.
- Reza Ghabcheloo. *Coordinated path following of multiple autonomous vehicles*. PhD thesis, Instituto Superior Técnico, Technical University of Lisbon, 2007.
- F. Gustafsson, F. Gunnarsson, N. Bergman, U. Forssell, J. Jansson, R. Karlsson, and P. J. Nordlund. Particle filters for positioning, navigation, and tracking. *IEEE Transactions On Signal Processing*, 50(2):425–437, February 2002. ISSN 1053-587X.
- O. Hegrenaes, K. Gade, O. K. Hagen, and P. E. Hagen. Underwater transponder positioning and navigation of autonomous underwater vehicles. In *OCEANS 2009, Vols 1-3*, pages 831–837, 2009.
- S. F. Hoerner. *Fluid-dynamic drag: practical information on aerodynamic drag and hydrodynamic resistance*. Hoerner Fluid Dynamics, 1965.
- Jeroen D. Hol, Thomas B. Schön, and Fredrik Gustafsson. Modeling and calibration of inertial and vision sensors. *International Journal of Robotics Research*, 29:231–244, February 2010. ISSN 0278-3649. doi: <http://dx.doi.org/10.1177/0278364909356812>.
- D. P. Horner and A. J. Healey. Use of artificial potential fields for uav guidance and optimization of wlan communications. In *Autonomous Underwater Vehicles, 2004 IEEE/OES*, pages 88 – 95, june 2004. doi: 10.1109/AUV.2004.1431198.
- I.-A.F. Ihle, J. Jouffroy, and T.I. Fossen. Formation control of marine surface craft: A lagrangian approach. *Oceanic Engineering, IEEE Journal of*, 31(4):922–934, 2006. ISSN 0364-9059. doi: 10.1109/JOE.2006.880426.
- Teledyne RD Instruments. Teledyne rdi navigation products, December 2011. URL http://www.rdinstruments.com/nav_products.aspx.
- P. Jantapremjit and P. A. Wilson. Control and guidance for homing and docking tasks using an autonomous underwater vehicle. In *2007 IEEE/RSJ International Conference on Intelligent Robots and Systems, Vols 1-9*, pages 3678–3683, 2007.
- J. Jouffroy and J. Reger. An algebraic perspective to single-transponder underwater navigation. In *Computer Aided Control System Design, 2006 IEEE International Conference on Control Applications, 2006 IEEE International Symposium on Intelligent Control, 2006 IEEE*, pages 1789–1794, 2006. doi: 10.1109/CACSD-CCA-ISIC.2006.4776912.
- J. Jouffroy, Qiuyang Zhou, and O. Zielinski. Towards selective tidal-stream transport for lagrangian profilers. In *OCEANS 2011*, pages 1 –6, September 2011.
- R. E. Kalman. A new approach to linear filtering and prediction problems. *Journal Of Basic Engineering*, 82(Series D):35–45, 1960.
- T. Katayama. *Subspace Methods for System Identification*. Communications and Control Engineering. Springer, 2005. ISBN 9781852339814. URL <http://books.google.pt/books?id=kTf1Xqdcv4QC>.
- H. K. Khalil. *Nonlinear systems*. Prentice Hall, 2002. ISBN 9780130673893.

- C. R. Kube and E. Bonabeau. Cooperative transport by ants and robots. *Robotics And Autonomous Systems*, 30(1-2):85–101, January 2000. ISSN 0921-8890. doi: {10.1016/S0921-8890(99)00066-4}.
- N. H. Kussat, C.D. Chadwell, and R. Zimmerman. Absolute positioning of an autonomous underwater vehicle using gps and acoustic measurements. *Oceanic Engineering, IEEE Journal of*, 30(1):153 – 164, January 2005. ISSN 0364-9059. doi: 10.1109/JOE.2004.835249.
- N. E. Leonard and E. Fiorelli. Virtual leaders, artificial potentials and coordinated control of groups. In *Decision and Control, 2001. Proceedings of the 40th IEEE Conference on*, volume 3, pages 2968 –2973 vol.3, 2001. doi: 10.1109/2001.980728.
- Linkquest. Linkquest DVLs, 12 2011. URL http://www.link-quest.com/html/models_nq.htm.
- S. Martinez and F. Bullo. Optimal sensor placement and motion coordination for target tracking. *Automatica*, 42(4):661–668, April 2006. ISSN 0005-1098. doi: {10.1016/j.automatica.2005.12.018}.
- A. Matos and N. Cruz. Positioning control of an underactuated surface vessel. In *OCEANS 2008*, pages 1–5, 2008. doi: 10.1109/OCEANS.2008.5152091.
- Wei Meng, Lihua Xie, and Wendong Xiao. Optimal sensor pairing for tdoa based source localization and tracking in sensor networks. In *Information Fusion (FUSION), 2012 15th International Conference on*, pages 1897 –1902, July 2012.
- J. I. Mulero-Martinez. Uniform bounds of the coriolis/centripetal matrix of serial robot manipulators. *IEEE Transactions on Robotics*, 23(5):1083 –1089, October 2007. ISSN 1552-3098. doi: 10.1109/TRO.2007.903820.
- Richard M. Murray. Recent research in cooperative control of multivehicle systems. *Journal of dynamic systems measurement and control-transactions of the asme*, 129(5):571–583, September 2007. ISSN 0022-0434. doi: {10.1115/1.2766721}. International Conference on Advances in Control and Optimization of Dynamical Systems, Bangalore, INDIA, FEB 01-02, 2007.
- Tiago Nascimento. *Coordinated Multi-Robot Formation Control*. PhD thesis, FEUP, December 2012.
- A. Negre, C. Pradalier, and M. Dunbabin. Robust vision-based underwater homing using self-similar landmarks. *Journal of Field Robotics*, 25(6-7):360–377, 2008.
- Paul Newman and John J. Leonard. Pure range-only subsea slam. In *Proceedings of the IEEE International Conference on Robotics and Automation*, Taiwan, September 2003.
- Trong Dong Nguyen, A.J. Sorensen, and Ser Tong Quek. Multi-operational controller structure for station keeping and transit operations of marine vessels. *Control Systems Technology, IEEE Transactions on*, 16(3):491–498, 2008. ISSN 1063-6536. doi: 10.1109/TCST.2007.906309.
- P. Ogren, M. Egerstedt, and X. M. Hu. A control Lyapunov function approach to multiagent coordination. *IEEE Transactions On Robotics And Automation*, 18(5):847–851, October 2002. ISSN 1042-296X. doi: {10.1109/TRA.2002.804500}.

- R. Olfati-Saber and R. M. Murray. Consensus problems in networks of agents with switching topology and time-delays. *IEEE Transactions on Automatic Control*, 49(9):1520–1533, September 2004. ISSN 0018-9286. doi: {10.1109/TAC.2004.834113}.
- E. Olson, J. Leonard, and S. Teller. Robust range-only beacon localization. In *Autonomous Underwater Vehicles, 2004 IEEE/OES*, pages 66 – 75, 2004. doi: 10.1109/AUV.2004.1431195.
- Edwin Olson, John J. Leonard, and Seth Teller. Robust range-only beacon localization. *IEEE Journal of Oceanic Engineering*, 31(4):949 –958, October 2006. ISSN 0364-9059. doi: 10.1109/JOE.2006.880386.
- Oxford Dictionaries. "coordination". oxford dictionaries. dictionaries. URL [definition/american_english/](http://definition.american_english/).
- Lynne E. Parker. Multiple mobile robot systems. In *Springer Handbook of Robotics*, pages 921–941. 2008.
- A. Pascoal, P. Oliveira, C. Silvestre, L. Sebastiao, M. Rufino, V. Barroso, J. Gomes, G. Ayela, P. Coince, M. Cardew, A. Ryan, H. Braithwaite, N. Cardew, J. Trepte, N. Seube, J. Champeau, P. Dhaussy, V. Sauce, R. Moitie, R. Santos, F. Cardigos, M. Brussieux, and P. Dando. Robotic ocean vehicles for marine science applications: the european asimov project. In *OCEANS 2000 MTS/IEEE Conference and Exhibition*, volume 1, pages 409–415 vol.1, 2000. doi: 10.1109/OCEANS.2000.881293.
- A. Pereira, J. Das, and G. Sukhatme. An experimental study of station keeping on an underactuated asv. In *Intelligent Robots and Systems, 2008. IROS 2008. IEEE/RSJ International Conference on*, pages 3164–3171, 2008. doi: 10.1109/IROS.2008.4650991.
- Jan Petrich and Daniel J. Stilwell. Robust control for an autonomous underwater vehicle that suppresses pitch and yaw coupling. *Ocean Engineering*, 38(1):197 – 204, 2011. ISSN 0029-8018. doi: 10.1016/j.oceaneng.2010.10.007. URL <http://www.sciencedirect.com/science/article/pii/S0029801810002222>.
- M. Pfingsthorn, A. Birk, and H. Bulow. An efficient strategy for data exchange in multi-robot mapping under underwater communication constraints. In *Intelligent Robots and Systems (IROS), 2010 IEEE/RSJ International Conference on*, pages 4886 –4893, October 2010. doi: 10.1109/IROS.2010.5650270.
- Max Pfingsthorn, Andreas Birk, Narunas Vaskevicius, and Kaustubh Pathak. Cooperative 3d mapping under underwater communication constraints. In *OCEANS'11 Santander*, Santander, Spain, 2011. IEEE.
- T. Prestero. Verification of a six-degree of freedom simulation model for the remus autonomous underwater vehicle. Master's thesis, Massachusetts Institute of Technology, 2001.
- Probir Kumar Ray and Ajay Mahajan. A genetic algorithm-based approach to calculate the optimal configuration of ultrasonic sensors in a 3d position estimation system. *Robotics and Autonomous Systems*, 41(4):165 – 177, 2002. ISSN 0921-8890. doi: 10.1016/S0921-8890(02)00292-0. URL <http://www.sciencedirect.com/science/article/pii/S0921889002002920>.
- Wei Ren and Ella Atkins. Distributed multi-vehicle coordinated control via local information exchange. *International Journal of Robust and Nonlinear Control*, 17(10-11):1002–1033, July 2007. ISSN 1049-8923. doi: {10.1002/rnc.1147}.

- Craig W. Reynolds. Flocks, herds and schools: A distributed behavioral model. *SIGGRAPH Comput. Graph.*, 21(4):25–34, August 1987. ISSN 0097-8930. doi: 10.1145/37402.37406. URL <http://doi.acm.org/10.1145/37402.37406>.
- D. Ribas, N. Palomeras, P. Ridao, M. Carreras, and A. Mallios. Girona 500 auv: From survey to intervention. *IEEE/ASME Transactions on Mechatronics*, 17(1):46–53, February 2012. ISSN 1083-4435. doi: 10.1109/TMECH.2011.2174065.
- J. S. Riedel and A. J. Healey. Shallow water station keeping of auvs using multi-sensor fusion for wave disturbance prediction and compensation. In *OCEANS '98 Conference Proceedings*, volume 2, pages 1064–1068 vol.2, 1998. doi: 10.1109/OCEANS.1998.724399.
- Gao Rui and M. Chitre. Cooperative positioning using range-only measurements between two auvs. In *OCEANS 2010 IEEE - Sydney*, pages 1–6, May 2010. doi: 10.1109/OCEANSSYD.2010.5603615.
- E. Sahin. Swarm robotics: From sources of inspiration to domains of application. In Sahin, E and Spears, WM, editor, *Swarm Robotics*, volume 3342 of *Lecture Notes In Computer Science*, pages 10–20, Heidelberger Platz 3, D-14197 Berlin, Germany, 2005. Springer-Verlag Berlin. ISBN 3-540-24296-1. Workshop on Swarm Robotics, Santa Monica, CA, JUL 17, 2004.
- Mac Schwager, Daniela Rus, and Jean-Jacques Slotine. Unifying geometric, probabilistic, and potential field approaches to multi-robot deployment. *International Journal of Robotics Research*, 30:371–383, March 2011. ISSN 0278-3649. doi: <http://dx.doi.org/10.1177/0278364910383444>.
- Mac Schwager, James McLurkin, Jean-Jacques E. Slotine, and Daniela Rus. From Theory to Practice: Distributed Coverage Control Experiments with Groups of Robots. In Khatib, O and Kumar, V and Pappas, GJ, editor, *Experimental Robotics*, volume 54 of *Springer Tracts in Advanced Robotics*, pages 127–136, HEIDELBERGER PLATZ 3, D-14197 BERLIN, GERMANY, 2009. European Robot Res Network, Springer-Verlag Berlin. ISBN 978-3-642-00195-6. 11th International Symposium on Experimental Robotics (ISER), Athens, GREECE, JUL 13-16, 2008.
- S. Sgorbini, A. Peirano, S. Cocito, and M. Morgigni. An underwater tracking system for mapping marine communities: an application to *Posidonia oceanica*. *Oceanologica Acta*, 25(3-4):135–138, May-July 2002. ISSN 0399-1784. doi: {10.1016/S0399-1784(02)01188-X}.
- Abhyudai Singh and Hassan K. Khalil. Regulation of nonlinear systems using conditional integrators. *International Journal of Robust and Nonlinear Control*, 15(8):339–362, 2005. ISSN 1099-1239. doi: 10.1002/rnc.996. URL <http://dx.doi.org/10.1002/rnc.996>.
- H. Singh, J. G. Bellingham, F. Hover, S. Lerner, B. A. Moran, K. von der Heydt, and D. Yoerger. Docking for an autonomous ocean sampling network. *IEEE Journal of Oceanic Engineering*, 26(4):498–514, 2001.
- J.-J. E. Slotine and W. Li. *Applied nonlinear control*. Prentice Hall, 1991. ISBN 9780130408907.
- Eduardo D. Sontag. Stability and stabilization: discontinuities and the effect of disturbances, in “Nonlinear analysis, differential equations and control”, 1998.

- S. W. Squyres, R. E. Arvidson, J. F. Bell, J. Bruckner, N. A. Cabrol, W. Calvin, M. H. Carr, P. R. Christensen, B. C. Clark, L. Crumpler, D. J. Des Marais, C. d'Uston, T. Economou, J. Farmer, W. Farrand, W. Folkner, M. Golombek, S. Gorevan, J. A. Grant, R. Greeley, J. Grotzinger, L. Haskin, K. E. Herkenhoff, S. Hviid, J. Johnson, G. Klingelhofer, A. Knoll, G. Landis, M. Lemmon, R. Li, M. B. Madsen, M. C. Malin, S. M. McLennan, H. Y. McSween, D. W. Ming, J. Moersch, R. V. Morris, T. Parker, J. W. Rice, L. Richter, R. Rieder, M. Sims, M. Smith, P. Smith, L. A. Soderblom, R. Sullivan, H. Wanke, T. Wdowiak, M. Wolff, and A. Yen. The Spirit Rover's Athena Science Investigation at Gusev Crater, Mars. *Science*, 305(5685):794–799, August 2004. ISSN 0036-8075. doi: {10.1126/science.3050794}.
- M. Stojanovic, L. Freitag, J. Leonard, and P. Newmarr. A network protocol for multiple auv localization. In *OCEANS 2002 MTS/IEEE Conference & Exhibition, Vols 1-4, Conference Proceedings*, pages 604–611, 2002.
- Dong Sun, Can Wang, Wen Shang, and Gang Feng. A Synchronization Approach to Trajectory Tracking of Multiple Mobile Robots While Maintaining Time-Varying Formations. *IEEE Transactions on Robotics*, 25(5):1074–1086, October 2009. ISSN 1552-3098. doi: {10.1109/TRO.2009.2027384}.
- Herbert G. Tanner and Jorge L. Piovesan. Randomized Receding Horizon Navigation. *IEEE Transactions on Automatic Control*, 55(11):2640–2644, November 2010. ISSN 0018-9286. doi: {10.1109/TAC.2010.2063291}.
- Sebastian Thrun, Wolfram Burgard, and Dieter Fox. *Probabilistic Robotics (Intelligent Robotics and Autonomous Agents)*. The MIT Press, 2005. ISBN 0262201623.
- Massimo Vaccarini and Sauro Longhi. Formation Control of Marine Vehicles via Real-Time Networked Decentralized MPC. In *MED: 2009 17th Mediterranean Conference On Control & Automation, Vols 1-3*, pages 428–433, 345 E 47TH ST, NEW YORK, NY 10017 USA, 2009. IEEE. ISBN 978-1-4244-4684-1. 17th Mediterranean Conference on Control and Automation, Thessaloniki, GREECE, JUN 24-26, 2009.
- J. Vaganay, P. Baccou, and B. Jouvencel. Homing by acoustic ranging to a single beacon. In *OCEANS 2000 MTS/IEEE - Where Marine Science and Technology Meet, Vols 1-3, Conference Proceedings*, pages 1457–1462, 2000.
- J. Vaganay, J.J. Leonard, J.A. Curcio, and J.S. Willcox. Experimental validation of the moving long base-line navigation concept. In *Autonomous Underwater Vehicles, 2004 IEEE/OES*, pages 59 – 65, June 2004. doi: 10.1109/AUV.2004.1431194.
- D. Vail and M. Veloso. Dynamic multi-robot coordination. In Schultz, AC and Parker, LE and Schneider, FE, editor, *Multi-Robot Systems: From Swarms To Intelligent Automata, Vol Ii*, pages 87–98, PO BOX 17, 3300 AA DORDRECHT, NETHERLANDS, 2003. Springer. ISBN 1-4020-1185-7. 2nd International Workshop on Multi-Robot Systems, NAVAL RES LAB, WASHINGTON, D.C., MAR, 2003.
- Kenneth Waldron and James Schmiedeler. Kinematics. In *Springer Handbook of Robotics*, pages 9–33. Springer, 2008.
- Louis L. Whitcomb, Dana R. Yoerger, and Hanumant Singh. Combined doppler/lbl based navigation of underwater vehicles. In *In: Proceedings of the the 11th International Symposium on Unmanned Untethered Submersible Technology*, 1999.

F. M. White. *Fluid mechanics*. McGraw-Hill, 2003.

Xsens. Xsens mti: Miniature ahrs - attitude and heading sensor, December 2011. URL <http://www.xsens.com/en/general/mti>.

Chun Yang, L. Kaplan, E. Blasch, and M. Bakich. Optimal placement of heterogeneous sensors in target tracking. In *Information Fusion (FUSION), 2011 Proceedings of the 14th International Conference on*, pages 1 –8, July 2011.

S. Zhao and J. Yuh. Experimental study on advanced underwater robot control. *IEEE Transactions on Robotics*, 21(4):695 – 703, August 2005. ISSN 1552-3098. doi: 10.1109/TRO.2005.844682.

Shiyu Zhao, B. M. Chen, and T. H. Lee. Optimal placement of bearing-only sensors for target localization. In *American Control Conference (ACC), 2012*, pages 5108 –5113, June 2012a.

Shiyu Zhao, Ben M. Chen, and Tong H. Lee. Optimal sensor placement for target localization and tracking in 2d and 3d. Available online: <http://arxiv.org/abs/1210.7397>, October 2012b.